

MEASUREMENTS OF TIME-DEPENDENT CP VIOLATION IN B MESON
DECAYS TO $\psi(2S)K_S^0$ AND $\phi K_S^0\gamma$

A DISSERTATION SUBMITTED TO THE GRADUATE DIVISION OF THE
UNIVERSITY OF HAWAII IN PARTIAL FULFILLMENT
OF THE REQUIREMENTS FOR THE DEGREE OF

DOCTOR OF PHILOSOPHY

IN

PHYSICS

DECEMBER 2010

By

Himansu Bhusan Sahoo

Dissertation Committee:

Thomas Browder, Chairperson

Stephen Olsen

Sandip Pakvasa

John Madey

Thomas Schroeder

Copyright 2010

by

Himansu Bhusan Sahoo

To my family and friends

with the best gratitude

Acknowledgements

I would like to express my deep gratitude to many individuals involved in different stages towards the successful completion of this thesis work. My deepest appreciation goes to my thesis supervisor, Professor Tom Browder for providing me this nice opportunity to work in the Belle experiment. He has always been very patient with me and given enough freedom to work independently. I am thankful to my teacher Professor Niranjana Barik and Dr. Sanjay Swain for promoting me towards graduate studies at University of Hawaii. Special thanks goes to Dr. Karim Trabelsi for his encouragements and supportive discussions throughout my graduate career.

I am very thankful to my dissertation committee members, Tom Browder, Stev Olsen, Sandip Pakvasa, Jahn Madey, and Thomas Schroeder. I would like to thank my Belle referees P. Krizan, T. Kawasaki, J. Dalseno, Y. Ushiroda, G. Mohanty and Y. Onuki for showing interest in my analysis and helping me towards publication of my result.

I would like to thank the faculty members at University of Hawaii for their wonderful lectures. I thank to Gary Varner for giving me a chance to work in hardware. Many thanks to UH Belle group members Mike Peter, Mike Jones, Fang Fang, Marlon, Li Jin, Herbert, Eric, Hulya, Kirika, Kurtis, Jamal, Larry, Mike for their help and discussions. Special thanks to Margie, Karen, Jan, Jossie, Peter, Dian and Jacky for their support. I would like to thank my friends Sanjay, Shailesh, Duc, Andrew, Sandip, Kishore, Dhiren, Ashwin, Saumya, Bibhu for being always with me.

I wish to thank every member of the Belle Collaboration and KEKB for their hard work for smooth running of the experiment. Special thanks to Yoshihide Sakai, Nishida Sohei, Toru Tsuboyama, Kenkichi Miyabayashi, Tagir Aushev, Ishino, Sumisawa for guiding and helping me as a group member. During my stay at KEK, I enjoyed friendship with Manmohan, Debabrat, Tapas, Seema, Rajeev, Nikhil, Abinash, Vishal, Vipin, Puneet. I would like to thank Belle secretaries Imai Chihiro, Atsuko Naka, Tomoka Yokoyama and Shinobu Oishi for their support during my long stay at KEK.

Finally, I can't forget the love and support of my family members. My parents have always been a constant source of inspiration and encouragement throughout my life.

ABSTRACT

In this dissertation, we report improved measurements of time-dependent CP violation parameters for $B^0(\overline{B}^0) \rightarrow \psi(2S)K_S^0$. This analysis is based on a data sample of 657×10^6 $B\overline{B}$ pairs collected at the $\Upsilon(4S)$ resonance with the Belle detector at the KEKB asymmetric-energy e^+e^- collider. One neutral B meson is fully reconstructed in the $\psi(2S)K_S^0$ CP -eigenstate decay channel, and the flavor of the accompanying B meson is identified as either B^0 or \overline{B}^0 from its decay products. CP violation parameters are obtained from the asymmetries in the distributions of the proper-time intervals between the two B decays: $\mathcal{S}_{\psi(2S)K_S^0} = +0.72 \pm 0.09(\text{stat}) \pm 0.03(\text{syst})$, $\mathcal{A}_{\psi(2S)K_S^0} = +0.04 \pm 0.07(\text{stat}) \pm 0.05(\text{syst})$.

We also report the first observation of the radiative decay $B^0 \rightarrow \phi K_S^0 \gamma$ using a data sample of 772×10^6 $B\overline{B}$ pairs. We observe a signal of 37 ± 8 events with a significance of 5.4 standard deviations including systematic uncertainties. The measured branching fraction is $\mathcal{B}(B^0 \rightarrow \phi K^0 \gamma) = (2.74 \pm 0.60 \pm 0.32) \times 10^{-6}$, where the uncertainties are statistical and systematic, respectively. We also precisely measure $\mathcal{B}(B^+ \rightarrow \phi K^+ \gamma) = (2.48 \pm 0.30 \pm 0.24) \times 10^{-6}$. The observed $M_{\phi K}$ mass spectrum differs significantly from that expected in a three-body phase-space decay.

The radiative $B \rightarrow \phi K \gamma$ mode is sensitive to new physics from right-handed currents, which could affect the CP asymmetry. Here, we report the first measurement of time-dependent CP violation parameters in the $B^0 \rightarrow \phi K_S^0 \gamma$ mode: $\mathcal{S} = +0.74_{-1.05}^{+0.72}(\text{stat})_{-0.24}^{+0.10}(\text{syst})$, $\mathcal{A} = +0.35 \pm 0.58(\text{stat})_{-0.10}^{+0.23}(\text{syst})$. We also report a feasibility study for the radiative decay $B \rightarrow \omega K \gamma$.

Contents

Acknowledgements	iv
Abstract	v
List of Tables	x
List of Figures	xii
List of Acronyms	xvi
1 Introduction	1
1.1 The Standard Model	1
1.2 CP Violation	3
1.3 The discovery of CP violation in the kaon system	3
1.4 CP violation in the Standard Model	5
1.5 Phenomena of B^0 - \bar{B}^0 mixing and CP violation in B decays	7
1.6 Types of CP violation in B decays	9
1.7 $B^0 \rightarrow \psi(2S)K_S^0$ decay	10
1.8 The $b \rightarrow s\gamma$ decays	12
1.9 Probe for New Physics	13
1.10 Experimental Technique	15
1.11 Thesis Outline	16
2 The Belle Experiment	17
2.1 Overview of the Belle Experiment	17
2.2 The KEKB Accelerator	17
2.2.1 The Crab Cavities	19
2.3 The Belle Detector	21
2.3.1 Silicon Vertex Detector (SVD)	22
2.3.2 Central Drift Chamber (CDC)	25
2.3.3 Aerogel Cerenkov Counter System (ACC)	27
2.3.4 Time-of-Flight Counters (TOF)	29
2.3.5 Electromagnetic Calorimeter (ECL)	30
2.3.6 Superconducting Solenoid Magnet	31
2.3.7 K_L^0 and Muon Detection System (KLM)	31

2.3.8	Extreme Forward Calorimeter (EFC)	33
2.4	Trigger System (TRG)	33
2.5	Data Acquisition System (DAQ)	34
2.6	Offline Software and Computing	35
3	Measurements of time-dependent CP violation in $B^0 \rightarrow \psi(2S)K_S^0$	37
3.1	Introduction	37
3.2	Hadronic Event Selection	37
3.3	Signal Reconstruction	38
3.3.1	Reconstruction of J/ψ and $\psi(2S)$ from di-leptons	39
3.3.2	K_S^0 Reconstruction	40
3.3.3	Reconstruction of $\psi(2S)$ from $J/\psi\pi^+\pi^-$	41
3.3.4	B Candidate Selection	42
3.3.5	Reconstruction Efficiency	43
3.4	Background Suppression	45
3.5	Mass Difference Sideband Study	49
3.5.1	Discrepancy between MC and data sidebands	50
3.6	Branching Fraction Checks	51
3.7	$B^0 \rightarrow \psi(2S)K_S^0$ Signal Extraction	52
3.7.1	Vertex Reconstruction	52
3.7.2	Flavor Tagging	53
3.7.3	Fitting Procedure	54
3.8	Determination of CP Asymmetries	55
3.8.1	Signal Fraction Estimation	57
3.8.2	Signal PDF	57
3.8.3	Peaking Background PDF	58
3.8.4	Combinatorial Background PDF	60
3.8.5	Final PDF for CP fitting	60
3.9	Validation Checks	62
3.9.1	Cross-check with $J/\psi K_S^0$ fitter	62
3.9.2	CP Linearity Test	62
3.9.3	Fit Bias	62
3.9.4	Lifetime Fit	63
3.9.5	CP Fit in Control Sample	63
3.10	Systematic Uncertainty	65
3.11	CP Fit Results in $B^0 \rightarrow \psi(2S)K_S^0$	68
4	Observation of $B^0 \rightarrow \phi K_S^0 \gamma$	71
4.1	Introduction	71
4.2	Event Selection	71
4.2.1	$\phi(1020)$ meson reconstruction	72
4.2.2	Radiative γ reconstruction	72
4.2.3	B meson reconstruction	73
4.2.4	Best Candidate Selection (BCS)	74
4.3	Continuum Suppression	74

4.3.1	ROOKSFW	74
4.3.2	$\cos \theta_B$	76
4.3.3	Likelihood Ratio (LR)	76
4.4	Generic B Backgrounds	78
4.5	Reconstruction Efficiency	80
4.6	Rare B Backgrounds	80
4.6.1	ϕ mass sideband study in MC	82
4.6.2	Parameterization of the Rare Background	83
4.6.3	ϕ mass sideband study in Data	84
4.7	Signal Extraction Procedure	85
4.7.1	Correlation between ΔE and M_{bc}	85
4.7.2	Fitter Tests	87
4.7.3	Signal PDF Calibration	90
4.8	$B \rightarrow \phi K \gamma$ Signal	92
4.9	$M(\mathbf{X}_s)$ Efficiency Calibration	94
4.9.1	$M(\mathbf{X}_s)$ mass dependence of the efficiency	94
4.9.2	$M(\mathbf{X}_s)$ mass distribution in data	95
4.10	Systematic Errors	96
4.11	Branching Fraction and Significance	101
5	Measurements of time-dependent CP violation in $B^0 \rightarrow \phi K_S^0 \gamma$	103
5.1	Introduction	103
5.2	Selection Criteria	103
5.2.1	r -bin dependent LR cut	104
5.2.2	Endcap photons and Signal box	104
5.3	Parameters for time-dependent Study	106
5.3.1	Signal and background fractions	106
5.3.2	Continuum parameters from data sideband	106
5.3.3	Effective lifetime of $B\bar{B}$ backgrounds	107
5.4	Ensemble Test	109
5.5	Validation Checks	110
5.5.1	CP fit in Signal MC	111
5.5.2	CP Linearity Check	111
5.5.3	Lifetime fit in Signal MC	111
5.5.4	Vertex Resolution	112
5.5.5	Lifetime and CP fit in $B^0 \rightarrow K^{*0} \gamma$	113
5.5.6	Lifetime and CP fit in $B^+ \rightarrow \phi K^+ \gamma$	114
5.5.7	Lifetime fit in $B^0 \rightarrow \phi K_S^0 \gamma$	114
5.5.8	CP fit to Sideband events	115
5.5.9	Random Flavor Tagging	116
5.5.10	CP fit to four Random Control Samples	116
5.6	CP Fit Results in $B^0 \rightarrow \phi K_S^0 \gamma$	117
5.7	Checks after box opening	119
5.7.1	Toy MC with Measured parameters	119
5.7.2	Katayama Scan	119

5.7.3	Likelihood Scan	120
5.8	Systematic Uncertainty	120
5.9	Statistics Issues in $B^0 \rightarrow \phi K_S^0 \gamma$	122
5.10	Charge Asymmetry in $B^+ \rightarrow \phi K^+ \gamma$	123
6	Search for $B \rightarrow \omega K \gamma$ decays	125
6.1	Introduction	125
6.2	Event Selection	125
6.2.1	π^0 meson reconstruction	125
6.2.2	$\omega(782)$ meson reconstruction	126
6.2.3	B meson reconstruction	126
6.3	Continuum Suppression	127
6.4	Generic B Backgrounds	127
6.5	Rare B backgrounds	130
6.6	Correlation between ΔE and M_{bc}	131
7	Conclusions	132
7.1	Measurements of time-dependent CP violation in $B^0 \rightarrow \psi(2S)K_S^0$	132
7.2	Observation of $B^0 \rightarrow \phi K_S^0 \gamma$ and Measurements of time-dependent CP violation	133
A	Particle Identification	136
A.1	K/π Identification	136
A.2	Electron Identification	138
A.3	Muon Identification	139
B	$B^0 \rightarrow \psi(2S)K_S^0$ Signal using $772 \times 10^6 B\bar{B}$ pairs	141
B.1	$B^0 \rightarrow \psi(2S)K_S^0$ Signal Extraction using Belle's Full data sample	141
C	Publications	143
	Bibliography	160

List of Tables

1.1	The standard model fundamental particles with their mass and charge . . .	2
1.2	The properties of fundamental forces and their mediators	2
2.1	Geometrical parameters of the ECL	31
3.1	The K_S^0 selection criteria in three momentum ranges	41
3.2	Typical resolutions in the mass distributions, ΔE and M_{bc} from signal MC for the $B^0 \rightarrow \psi(2S)K_S^0$ decay mode	42
3.3	Reconstruction efficiency from signal MC for the $B^0 \rightarrow \psi(2S)K_S^0$ mode . . .	45
3.4	Reconstruction efficiency from signal MC for the control sample $B^+ \rightarrow \psi(2S)K^+$ mode	45
3.5	Individual background modes in the signal region for $B^0 \rightarrow \psi(2S)(J/\psi\pi^+\pi^-)K_S^0$ mode	47
3.6	The six sideband regions in the mass difference plot	49
3.7	Background estimated from mass difference sidebands	50
3.8	Branching fractions for $B^+ \rightarrow \psi(2S)K^+$ mode	51
3.9	Branching fractions for $B^0 \rightarrow \psi(2S)K^0$ mode	52
3.10	The PDFs used to model each component in the 2D fit for $B^0 \rightarrow \psi(2S)K_S^0$ mode	55
3.11	Signal yield in data for each subsample	56
3.12	Events in the signal box in data: before and after tagging and vertexing, and for time-dependent fit	56
3.13	Signal fractions in individual r -bins for $B^0 \rightarrow \psi(2S)K_S^0$ mode	58
3.14	Wrong tag fractions, w_l and wrong tag fraction differences, Δw_l in MC for each r -interval	59
3.15	Wrong tag fractions, w_l and wrong tag fraction differences, Δw_l in data for each r -interval	59
3.16	The background shape parameters from data sideband for the $B^0 \rightarrow \psi(2S)K_S^0$ mode	61
3.17	Checks for fit bias in \mathcal{S} and \mathcal{A} in signal MC for $B^0 \rightarrow \psi(2S)K_S^0$ mode . . .	62
3.18	Lifetime fit in data for $B^\pm \rightarrow \psi(2S)K^\pm$ mode	65
3.19	Lifetime fit in data for $B^0 \rightarrow \psi(2S)K_S^0$ mode	65
3.20	CP fit in data for $B^\pm \rightarrow \psi(2S)K^\pm$ mode	65
3.21	Summary of the Systematic Uncertainties for $B^0 \rightarrow \psi(2S)K_S^0$ mode	67
3.22	Systematic Uncertainties in Vertexing for $B^0 \rightarrow \psi(2S)K_S^0$ mode	68

3.23	CP fit results in data with different subsamples for the $B^0 \rightarrow \psi(2S)K_S^0$ decay mode	68
4.1	The amount of non-resonant component from rare MC (signal region), rare MC (sideband) and data sideband	86
4.2	The PDFs used to model each component in the 2D fit for $B \rightarrow \phi K \gamma$ mode	87
4.3	The fudge factor corrections from the $B^0 \rightarrow K^* \gamma$ for exp07 to exp31 sample	91
4.4	The fudge factor corrections from the $B^0 \rightarrow K^* \gamma$ for exp33 to exp65 sample	91
4.5	Signal shape parameters from the weighted MC sample for two different datasets in $B^+ \rightarrow \phi K^+ \gamma$ mode	92
4.6	Signal shape parameters from the weighted MC sample for exp07-65	92
4.7	The signal yields, efficiencies, ratio and systematics using the $B^0 \rightarrow K^* \gamma$ control sample	99
4.8	Summary of multiplicative systematic uncertainties in the charged mode $B^+ \rightarrow \phi K^+ \gamma$	99
4.9	Summary of multiplicative systematic uncertainties in the neutral mode $B^0 \rightarrow \phi K_S^0 \gamma$	100
4.10	Summary of additive systematic uncertainties from the fit parameters	100
4.11	The likelihood of the fits and signal significances	102
4.12	The signal yields, weighted efficiencies, branching fractions and significances	102
5.1	The re-optimized r -bin dependent LR cuts for the charged as well as the neutral $B \rightarrow \phi K \gamma$ mode	104
5.2	The signal and background events for each PDF in the signal box for $B^+ \rightarrow \phi K^+ \gamma$ mode	105
5.3	The signal and background events for each PDF in the signal box for $B^0 \rightarrow \phi K_S^0 \gamma$ mode	105
5.4	The effective lifetime values obtained from lifetime fits to background MC samples	108
5.5	Lifetime and CP fit results in the $B^0 \rightarrow K^{*0} \gamma$ control sample	113
5.6	Lifetime and CP fit results in the $B^+ \rightarrow \phi K^+ \gamma$ control sample	114
5.7	The CP fit results to four random control samples from $B^+ \rightarrow \phi K^+ \gamma$ mode	117
5.8	Summary of the Systematic Uncertainties for $B^0 \rightarrow \phi K_S^0 \gamma$ mode	123
5.9	Measured signal yields and charge asymmetry in the $B^+ \rightarrow \phi K^+ \gamma$ mode	123
6.1	The expected background events in data from the generic MC in the signal region for the $B^0 \rightarrow \omega K_S^0 \gamma$ mode	130

List of Figures

1.1	The three families of quarks and leptons and the force carriers in the SM	2
1.2	The unitarity triangle of the CKM matrix	6
1.3	The box diagrams showing $B^0\bar{B}^0$ mixing	8
1.4	Standard Model quark level diagrams contributing to $B^0 \rightarrow \psi(2S)K_S^0$ decay	10
1.5	Feynman diagram for the radiative $b \rightarrow s\gamma$ decays	13
1.6	The penguin diagram for $B \rightarrow \phi K\gamma$ decay with $s\bar{s}$ pair creation	14
2.1	The configuration of the KEKB accelerator showing its two rings	18
2.2	The hadronic cross-section for e^+e^- annihilation	19
2.3	Schematic drawing of the crab cavities	20
2.4	Schematic of the Belle Detector	21
2.5	Configuration of the Belle silicon vertex detector	22
2.6	Impact parameter resolutions for the r - φ (left) and z direction (right)	23
2.7	Configuration of SVD2	24
2.8	Schematic view of the CDC structure	25
2.9	Measured dE/dx vs. momentum	26
2.10	Configuration of ACC and TOF system	27
2.11	Pulse-height spectra in units of photoelectrons observed by the ACC for electrons and kaons	28
2.12	Design of an ACC barrel module and end-cap module	28
2.13	Distributions of hadron masses calculated from measured time-of-flight	29
2.14	Configuration of the ECL	30
2.15	Cross section of a KLM superlayer	32
2.16	Configuration of the EFC	33
2.17	Sub-trigger system and the Global Decision Logic (GDL)	34
2.18	Global design of the Belle DAQ system	35
3.1	Invariant mass of $\psi(2S)$ and J/ψ candidates from dileptons	40
3.2	The mass distributions from signal MC for K_S^0 , mass difference ($M_{\psi(2S)} - M_{J/\psi}$) and dipion invariant mass	41
3.3	ΔE , M_{bc} distributions and 2D scatter plot of ΔE versus M_{bc} from signal MC for $B^0 \rightarrow \psi(2S)K_S^0$ decay mode	43
3.4	The experimental dependence of reconstruction efficiency for $B^0 \rightarrow \psi(2S)K_S^0$ mode	44
3.5	Backgrounds in $B^0 \rightarrow \psi(2S)(e^+e^-)K_S^0$ decay	46

3.6	Backgrounds in $B^0 \rightarrow \psi(2S)(J/\psi(e^+e^-)\pi^+\pi^-)K_S^0$ decay	48
3.7	Parameterization of peaking backgrounds in the signal region	49
3.8	Mass difference plot showing six sideband regions	50
3.9	ΔE and M_{bc} projections from the sideband for the $B^0 \rightarrow \psi(2S)K_S^0$ mode .	51
3.10	Schematic diagram of the vertex reconstruction of the two B decay vertices	53
3.11	ΔE and M_{bc} distributions for $B^0 \rightarrow \psi(2S)K_S^0$ mode using the 772×10^6 $B\bar{B}$ pairs data sample	55
3.12	The Δt distributions from the ΔE - M_{bc} 2D sideband for $B^0 \rightarrow \psi(2S)K_S^0$ mode	61
3.13	CP linearity test in $B^0 \rightarrow \psi(2S)K_S^0$ mode	63
3.14	Lifetime fit (simultaneous fit to SVD1 and SVD2) in data for $B^0 \rightarrow \psi(2S)K_S^0$ mode	64
3.15	CP fit (simultaneous fit to SVD1 and SVD2) in data for $B^+ \rightarrow \psi(2S)K^+$ mode	64
3.16	CP fit results in data for $B^0 \rightarrow \psi(2S)K_S^0$ mode using 657 M $B\bar{B}$ pairs . . .	70
4.1	The invariant ϕK_S^0 mass from EvtGen	72
4.2	Invariant mass distributions of the reconstructed ϕ and K_S^0 mesons	73
4.3	The KSFW0 PDF in 7 bins of missing mass	75
4.4	The $\cos \theta_B$ distribution	76
4.5	The LR FOM plots for the final LR cut.	77
4.6	The ΔE and M_{bc} distributions from signal MC and continuum MC after applying the LR cut for the $B^+ \rightarrow \phi K^+\gamma$ mode	77
4.7	The ΔE , M_{bc} and invariant ϕK mass distributions from generic MC	78
4.8	Invariant ϕK_S mass is fitted with a Gaussian function	79
4.9	The ΔE , M_{bc} and invariant ϕK_S^0 distributions after applying the D veto. .	79
4.10	The backgrounds determined from rare MC	81
4.11	The ϕ mass distribution for the background events in the $B^+ \rightarrow \phi K^+\gamma$ mode	82
4.12	Parameterization of the rare backgrounds in the $B^+ \rightarrow \phi K^+\gamma$ mode	83
4.13	Fit to the ΔE - M_{bc} distributions for the ϕ mass sideband in data	84
4.14	$M(K^+K^-)$ distribution in data	85
4.15	Correlation plots in $B^+ \rightarrow \phi K^+\gamma$ mode	86
4.16	Correlation plots in $B^0 \rightarrow \phi K_S^0\gamma$ mode	87
4.17	The results from the toy MC study	88
4.18	The results from the ensemble test study	89
4.19	The ΔE - M_{bc} 2D fit to the $B^0 \rightarrow K^*\gamma$ for exp07 to exp31 sample	90
4.20	The ΔE - M_{bc} 2D fit to the $B^0 \rightarrow K^*\gamma$ for exp33 to exp65 sample	91
4.21	The ΔE and M_{bc} fits in data for $B^+ \rightarrow \phi K^+\gamma$ and $B^0 \rightarrow \phi K_S^0\gamma$ mode . . .	93
4.22	The generated flat $M(X_s)$ mass and reconstructed $M(X_s)$ mass distributions in the fit region	94
4.23	The signal MC efficiency as a function of the $M(X_s)$ mass in the fit region .	95
4.24	The background-subtracted and efficiency-corrected ϕK mass distributions	96
4.25	The likelihood scan of the signal yield	101
5.1	Graphical representation of signal and background fractions in different r - bins for events in signal box	106

5.2	The continuum background Δt PDF parameters determined from ΔE - M_{bc} data sideband	107
5.3	The ΔE - M_{bc} 2D plot showing the signal box and sideband region, lifetime fit to data sideband for $B^0 \rightarrow \phi K_S^0 \gamma$ mode	108
5.4	The lifetime fits to the background MC samples	109
5.5	Toy MC Study for $B^+ \rightarrow \phi K^+ \gamma$ mode	110
5.6	Toy MC Study for $B^0 \rightarrow \phi K_S^0 \gamma$ mode	111
5.7	The residuals of the \mathcal{S} and \mathcal{A} fit results of the linearity check for $B^0 \rightarrow \phi K_S^0 \gamma$ mode	112
5.8	The lifetime fit to the reconstructed Δt distribution	112
5.9	cosine of the angle between the daughter tracks	113
5.10	Lifetime and CP fit results in the $B^0 \rightarrow K^{*0} \gamma$ control sample	114
5.11	Lifetime and CP fit results in the $B^+ \rightarrow \phi K^+ \gamma$ control sample	115
5.12	Lifetime fit in the $B^0 \rightarrow \phi K_S^0 \gamma$ sample	115
5.13	CP fit results to the sideband events	116
5.14	CP fit results to the four random control samples in the 2D \mathcal{A} - \mathcal{S} plane	117
5.15	The Δt distributions and raw asymmetry plot for the $B^0 \rightarrow \phi K_S^0 \gamma$ mode	118
5.16	The Δt distributions and raw asymmetry plot for the good-tagged events in $B^0 \rightarrow \phi K_S^0 \gamma$ mode	118
5.17	The Δt distributions and raw asymmetry plot for the poorly tagged events in $B^0 \rightarrow \phi K_S^0 \gamma$ mode	118
5.18	The toy MC results for $B^0 \rightarrow \phi K_S^0 \gamma$ after box opening	119
5.19	The \mathcal{S} value, error, negative MINOS error and positive MINOS error as a function of sample number	120
5.20	The \mathcal{A} value, error, negative MINOS error and positive MINOS error as a function of sample number	121
5.21	The likelihood curves for \mathcal{S} and \mathcal{A} in $B^0 \rightarrow \phi K_S^0 \gamma$ mode	122
5.22	The residual distributions for \mathcal{S} and \mathcal{A} from toy MC for $B^0 \rightarrow \phi K_S^0 \gamma$ mode	124
5.23	The linearity test in signal MC for $B^0 \rightarrow \phi K_S^0 \gamma$ mode	124
5.24	The linearity test in toy MC for $B^0 \rightarrow \phi K_S^0 \gamma$ mode	124
6.1	Invariant mass of distributions of π^0 and ω	126
6.2	The LR FOM plots for $\omega K_S^0 \gamma$ mode	127
6.3	The ΔE , M_{bc} and ωK distributions showing the backgrounds from generic MC	128
6.4	Invariant $M(K^+ \pi^-)$ and $M(K^+ \pi^- \pi^0)$ distributions for the signal kaon	129
6.5	The ΔE , M_{bc} and invariant ωK_S distributions for the $\omega K^+ \gamma$ decay mode after the D veto	129
6.6	The possible sources of backgrounds from rare MC	130
6.7	The correlation plots for the $B^+ \rightarrow \omega K^+ \gamma$ mode	131
6.8	The correlation plots for the $B^+ \rightarrow \omega K_S^0 \gamma$ mode	131
7.1	Summary of Belle and BaBar measurements of time-dependent CP asymmetries in $b \rightarrow c\bar{c}s$ transitions	133

7.2	Summary of Belle and BaBar measurements of time-dependent CP asymmetries in $b \rightarrow s\gamma$ transitions	135
A.1	Momentum coverage of each detector used for K/π separation	137
A.2	Likelihood ratio $PID(K)$, versus momenta	137
A.3	The distribution of the final unified discriminant used to identify electrons	139
B.1	ΔE and M_{bc} distributions for $B^0 \rightarrow \psi(2S)K_S^0$ using 772×10^6 $B\bar{B}$ pairs data sample	142

List of Acronyms

- ACC** Aerogel threshold Čerenkov Counters
- BCS** Best Candidate Selection
- CDC** Central Drift Chamber
- CKM** Cabibbo-Kobayashi-Maskawa
- CP** Charge-conjugation and Parity
- ECL** Electromagnetic Calorimeter
- FOM** Figure Of Merit
- EFC** Extreme Forward Calorimeter
- HFAG** Heavy Flavor Averaging Group
- HER** High Energy Ring
- IP** Interaction Point
- KEK** High Energy Accelerator Research Organization in Japan
- KEKB** An Asymmetric Electron-Positron Collider for B Physics at KEK
- KLM** K_L^0 and μ detector
- LER** Low Energy Ring
- LR** Likelihood Ratio
- MC** Monte Carlo
- NP** New Physics

PDF Probabilit Density Function

PDG Particle Data Group

PID Particle Identification

SM Standard Model

SVD Silicon Vertex Detector

TOF Time of Flight scintillation counters

TSC Trigger Scintilator Counters

Chapter 1

Introduction

1.1 The Standard Model

The standard model (SM) of particle physics is a theory concerning the strong, electromagnetic and weak interactions that mediate the dynamics of known fundamental particles. In the SM, all known matter particles are composites of three types of fundamental particles: six quarks, six leptons and force carrier particles. In short, the SM describes the universe in terms of Matter (fermions) and Forces (bosons). There are altogether three families of quarks and leptons and their antiparticle counterparts as shown in Fig. 1.1. Their masses and electric charges are listed in Table 1.1 and Table 1.2.

The quarks and leptons are fermions with spin angular momentum equal to $\frac{1}{2}$. Quarks carry fractional charge and are only found inside composite particles known as hadrons. There are only two known types of hadrons: baryons composed of three quarks or antiquarks (for example, protons (uud) and neutrons (udd)), and mesons composed of a quark and antiquark pair (for example, π^+ ($u\bar{d}$), K^+ ($u\bar{s}$)). Therefore, mesons have spin 0 or 1 and hadrons have spin $\frac{1}{2}$ or $\frac{3}{2}$. In contrast to quarks, leptons can be observed as free particles. Finally, every interaction has its own mediator: gluons for the strong force, photons for the electromagnetic force, W^\pm and Z^0 bosons for the weak force. The gravitational force is mediated by gravitons, but is not fully explained by the SM. There is also one additional hypothetical particle predicted by the SM, called the Higgs boson, which has not yet been observed by experiments. It is needed in the model to give mass to the W , Z bosons and all other particles.

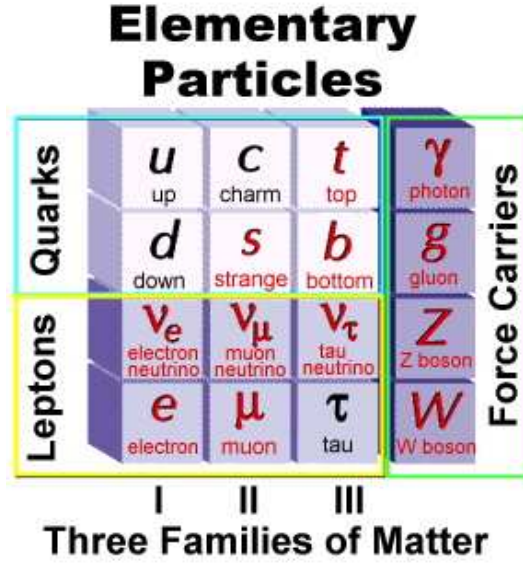


Figure 1.1: The three families of quarks and leptons and the force carriers in the SM.

Table 1.1: The standard model fundamental particles (three generations of quarks and leptons) with their mass and charge. The quarks have spin-parity, $J^P = \frac{1}{2}^+$.

Charge	First Generation		Second Generation		Third Generation	
	Flavor	Mass (GeV/ c^2)	Flavor	Mass (GeV/ c^2)	Flavor	Mass (GeV/ c^2)
$+\frac{2}{3}$	<i>u</i>	0.0015-0.0033	<i>c</i>	$1.27^{+0.07}_{-0.11}$	<i>t</i>	171.2 ± 2.1
$-\frac{1}{3}$	<i>d</i>	0.0035-0.0060	<i>s</i>	$0.104^{+0.026}_{-0.034}$	<i>b</i>	$4.20^{+0.17}_{-0.07}$
-1	e^-	0.000511	μ^-	0.105	τ^-	1.777
0	ν_e	$0(< 7 \times 10^{-9})$	ν_μ	$0(< 0.0003)$	ν_τ	$0(< 0.03)$

Table 1.2: The properties of fundamental forces and their mediators. All mediators have spin 1 except the graviton, which has spin 2.

Interaction	Strength	Range (m)	Gauge boson	Charge	Mass (GeV/ c^2)
Strong	1	10^{-15}	<i>g</i>	0	0
Electromagnetic	1/137	Infinite	γ	0	0
Weak	10^{-6}	10^{-18}	$W^\pm(Z^0)$	$\pm 1(0)$	80.4(91.2)
Gravity	6×10^{-39}	Infinite	gravitons	0	0

1.2 CP Violation

Our universe has a clear dominance of matter over anti-matter. According to the Big Bang theory, the expectation is that early universe had no matter, only energy. As the universe is expanded, this energy was converted into matter and antimatter in equal proportions. However, the world around us today is dominated by matter. The existence of CP violation, violation of the combined operation of C (charge-conjugation) that changes matter to anti-matter and vice-versa and P (parity) that reverses space-coordinates, is one of the three necessary conditions for dominance of matter over antimatter, as described by A. D. Sakharov [1].

A parity transformation (P) is a reflection of all coordinates in the origin so that $\vec{r} \rightarrow -\vec{r}$. P is also called left-right or mirror reflection because a reflection in a plane followed by a rotation of 180° corresponds to the parity transformation. Symmetry under a parity transformation at the subatomic level implies that you cannot tell whether you are examining the real world or its mirror world.

Charge conjugation (C) is particle-antiparticle conjugation. It reverses the sign of the charge of the particle and thus changes a particle into its antiparticle. For example, applying the C transformation to electron, it is transformed to a positron, which has positive charge. In physics, C -symmetry means the symmetry of the physical laws under the charge-conjugation transformation.

CP is the product of the charge conjugation and parity transformations. CP conservation implies no difference between the real world for particles and the mirror world for their antiparticles. Although parity and charge-conjugation are violated separately in the weak interaction, it was thought that their combined operation CP is still conserved. However, the belief was proved to be wrong in 1964 by the discovery of CP violation in neutral kaon system [2].

1.3 The discovery of CP violation in the kaon system

The neutral kaons provide an ideal experimental system to test CP invariance. There are two neutral flavor eigenstates of kaon, namely $|K^0\rangle$ and $|\bar{K}^0\rangle$, which are not CP eigenstates. Under parity and charge conjugation, these flavor eigenstates transform as

follows,

$$P |K^0\rangle = -|K^0\rangle, \quad P |\bar{K}^0\rangle = -|\bar{K}^0\rangle \quad (1.3.1)$$

$$C |K^0\rangle = |\bar{K}^0\rangle, \quad C |\bar{K}^0\rangle = |K^0\rangle \quad (1.3.2)$$

and under combined CP transformation, these states become

$$CP |K^0\rangle = -|\bar{K}^0\rangle, \quad CP |\bar{K}^0\rangle = -|K^0\rangle \quad (1.3.3)$$

Therefore, neither $|K^0\rangle$ nor $|\bar{K}^0\rangle$ are CP eigenstates. The observed particles are a linear combination of K^0 and \bar{K}^0 . The normalized eigenstates of CP are

$$|K_1\rangle = \frac{1}{\sqrt{2}}(|K^0\rangle + |\bar{K}^0\rangle), \quad |K_2\rangle = \frac{1}{\sqrt{2}}(|K^0\rangle - |\bar{K}^0\rangle). \quad (1.3.4)$$

Under CP transformation, these states become

$$CP |K_1\rangle = |K_1\rangle \text{ (CP even)}, \quad CP |K_2\rangle = -|K_2\rangle \text{ (CP odd)}. \quad (1.3.5)$$

The $|K_1\rangle$ is short-lived and decays dominantly to a 2π state that has $CP = +1$. The $|K_2\rangle$ is long lived and decays dominantly to a 3π state that has $CP = -1$. If CP was conserved, the $K_L \rightarrow 2\pi$ decay would be forbidden. In 1964, however, an experiment by Christenson, Cronin, Fitch and Turlay [2] first demonstrated that the K_L meson could also decay to $\pi^+\pi^-$ with a branching fraction of order 10^{-3} .

The mass and lifetime eigenstates $|K_L\rangle$ and $|K_S\rangle$ are admixtures of the CP eigenstates $|K_1\rangle$ and $|K_2\rangle$ and can be expressed as follows

$$|K_L\rangle = \frac{1}{\sqrt{1+|\epsilon|^2}}(|K_2\rangle + \epsilon |K_1\rangle), \quad |K_S\rangle = \frac{1}{\sqrt{1+|\epsilon|^2}}(|K_1\rangle - \epsilon |K_2\rangle) \quad (1.3.6)$$

where ϵ is a small parameter quantifying the CP violation. The degree of CP violation is usually quoted as the ratio of branching fractions :

$$\frac{\mathcal{B}(K_L \rightarrow \pi^+\pi^-)}{\mathcal{B}(K_S \rightarrow \pi^+\pi^-)} = (2.29 \pm 0.02) \times 10^{-3}, \quad \frac{\mathcal{B}(K_L \rightarrow \pi^0\pi^0)}{\mathcal{B}(K_S \rightarrow \pi^0\pi^0)} = (2.28 \pm 0.02) \times 10^{-3} \quad (1.3.7)$$

This small violation of CP symmetry in the neutral-kaon system can be accommodated by the SM. Much larger CP violation is expected in the B meson system.

1.4 CP violation in the Standard Model

The charged current interaction part of the electroweak lagrangian is given by

$$\mathcal{L}_{CC} = -\frac{g}{\sqrt{2}} \begin{pmatrix} \bar{u} & \bar{c} & \bar{t} \end{pmatrix} \gamma^\mu \left(\frac{1-\gamma_5}{2} \right) V_{CKM} \begin{pmatrix} d \\ d \\ b \end{pmatrix} W_\mu^+ + h.c. \quad (1.4.1)$$

where g is the gauge coupling constant, V_{CKM} is the 3×3 Cabibbo-Kobayashi-Maskawa (CKM) matrix [3, 4] or the quark mixing matrix. The matrix describes the relation between the quark mass eigenstates (d, s, b) and their weak interaction eigenstates (d', s', b') :

$$\begin{pmatrix} d' \\ s' \\ b' \end{pmatrix} = \begin{pmatrix} V_{ud} & V_{us} & V_{ub} \\ V_{cd} & V_{cs} & V_{cb} \\ V_{td} & V_{ts} & V_{tb} \end{pmatrix} \begin{pmatrix} d \\ s \\ b \end{pmatrix} = V_{CKM} \begin{pmatrix} d \\ s \\ b \end{pmatrix} \quad (1.4.2)$$

The nine elements of the CKM matrix represent the couplings of the quarks to W bosons. The most useful approximation for the CKM matrix is the Wolfenstein parametrization [5], which expresses the CKM matrix as an expansion in powers of $\lambda \approx \sin \theta_c$.

$$V_{CKM} \approx \begin{pmatrix} 1 - \frac{1}{2}\lambda^2 & \lambda & A\lambda^3(\rho - i\eta) \\ -\lambda & 1 - \frac{1}{2}\lambda^2 & A\lambda^2 \\ A\lambda^3(1 - \rho - i\eta) & -A\lambda^2 & 1 \end{pmatrix} + \mathcal{O}(\lambda^4) \quad (1.4.3)$$

The diagonal elements are of order one. The further off-diagonal one goes, the λ dependence increases and hence the strength of the interaction decreases. The V_{ub} and V_{td} elements contain the complex phase, which is the only source of CP violation in the SM. The unitarity of the CKM matrix leads to the relation,

$$\sum_j V_{ij} V_{jk}^* = 0. \quad (i \neq k) \quad (1.4.4)$$

This provides us the following six relations among its elements. Since each of the six relations requires the sum of three complex quantities to be zero, they can be represented

as six triangles in complex plane. These triangles are called the unitarity triangles.

$$\underbrace{V_{ub}V_{us}^*}_{\lambda} + \underbrace{V_{cd}V_{cs}^*}_{\lambda} + \underbrace{V_{td}V_{ts}^*}_{\lambda^5} = 0, \quad (1.4.5)$$

$$\underbrace{V_{ud}V_{cd}^*}_{\lambda} + \underbrace{V_{us}V_{cs}^*}_{\lambda} + \underbrace{V_{ub}V_{cb}^*}_{\lambda^5} = 0, \quad (1.4.6)$$

$$\underbrace{V_{us}V_{ub}^*}_{\lambda^4} + \underbrace{V_{cs}V_{cb}^*}_{\lambda^2} + \underbrace{V_{ts}V_{tb}^*}_{\lambda^2} = 0, \quad (1.4.7)$$

$$\underbrace{V_{cd}V_{td}^*}_{\lambda^4} + \underbrace{V_{cs}V_{ts}^*}_{\lambda^2} + \underbrace{V_{cb}V_{tb}^*}_{\lambda^2} = 0, \quad (1.4.8)$$

$$\underbrace{V_{ud}V_{td}^*}_{\lambda^3} + \underbrace{V_{us}V_{ts}^*}_{\lambda^3} + \underbrace{V_{ub}V_{tb}^*}_{\lambda^3} = 0, \quad (1.4.9)$$

$$\underbrace{V_{ud}V_{ub}^*}_{\lambda^3} + \underbrace{V_{cd}V_{cb}^*}_{\lambda^3} + \underbrace{V_{td}V_{tb}^*}_{\lambda^3} = 0. \quad (1.4.10)$$

The four unitarity triangles corresponding to Eq. 1.4.5 to 1.4.8 are extremely squashed in shape since the magnitudes of one of the sides of the triangle is much shorter than the other two. In contrast, all the sides in Eq. 1.4.9 and 1.4.10 are of the same order ($\mathcal{O}(\lambda^3)$). Hence, the unitary triangles corresponding to these two relations have larger areas than the first four. Eq. 1.4.5 and 1.4.6 are related to physics in the K meson system. Eq. 1.4.7 and 1.4.8 are related to physics in the B_s meson system. Eqns. 1.4.9 and 1.4.10 are related to physics in the B_d meson system. Since the unitary triangles corresponding to the B_d meson system have larger areas than the other four, the amount of CP violation in B_d meson decay is expected to be larger than in K meson and B_s meson decays. This implies that the B meson sector is the most promising domain to examine the Kobayashi-Maskawa mechanism. In the neutral B_d^0 system we use only Eq. 1.4.10, since it involves mixing, $b \rightarrow c$ and $b \rightarrow u$ transitions while in Eq. 1.4.9 it has transitions that include K meson decays.

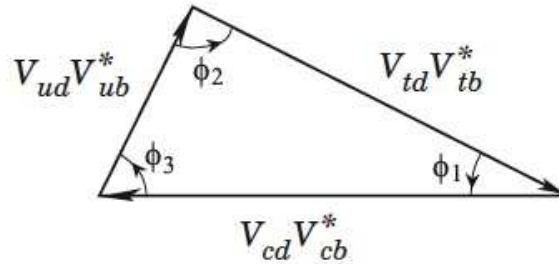


Figure 1.2: The unitarity triangle of the CKM matrix.

The unitarity triangle that controls b quark decays is shown in Fig. 1.2, which corresponds to Eq. 1.4.10. It has six parameters; three angles and three sides. The sides of the triangle can be obtained by measuring specific decay rates, and the angles can be derived from measurements of CP asymmetries. The angles $\phi_1(\beta)$, $\phi_2(\alpha)$, and $\phi_3(\gamma)$ are defined as follows

$$\begin{aligned}\phi_1 &\equiv \pi - \arg\left(\frac{V_{td}V_{tb}^*}{V_{cd}V_{cb}^*}\right), \\ \phi_2 &\equiv \arg\left(\frac{V_{tb}^*V_{td}}{-V_{ub}^*V_{ud}}\right), \\ \phi_3 &\equiv \arg\left(\frac{V_{ub}^*V_{ud}}{-V_{cb}^*V_{cd}}\right).\end{aligned}\tag{1.4.11}$$

Intuitively, the amount of CP violation is directly proportional to the area of the unitary triangle. This implies that the angles should take nonzero values and the sides should be comparable, if CP invariance is violated in B meson system. The measurement of the angles and sides of the unitary triangle is one of the important goals of the B factory.

1.5 Phenomena of B^0 - \bar{B}^0 mixing and CP violation in B decays

The B^0 and \bar{B}^0 can mix through second order weak interaction via the box diagrams shown in Fig. 1.3. Due to this mixing, the neutral B meson in the weak interaction eigenstate (or mass eigenstate) is written as a linear combination of the flavor eigenstates $|B^0\rangle$ and $|\bar{B}^0\rangle$ as

$$|B_L\rangle = p|B^0\rangle + q|\bar{B}^0\rangle, \quad |B_H\rangle = p|B^0\rangle - q|\bar{B}^0\rangle\tag{1.5.1}$$

where p and q are complex parameters and the states $|B_L\rangle$ and $|B_H\rangle$ are the lighter and heavier mass eigenstates. The corresponding eigenvalues are

$$\mu_L = m_L - \frac{i}{2}\Gamma_L, \quad \mu_H = m_H - \frac{i}{2}\Gamma_H\tag{1.5.2}$$

The time evolution of a neutral B meson, which is initially created as a pure flavor eigenstate, B^0 or \bar{B}^0 at time $t = 0$ can be written as

$$|B^0(t)\rangle = f_+(t)|B^0\rangle + \frac{q}{p}f_-(t)|\bar{B}^0\rangle\tag{1.5.3}$$

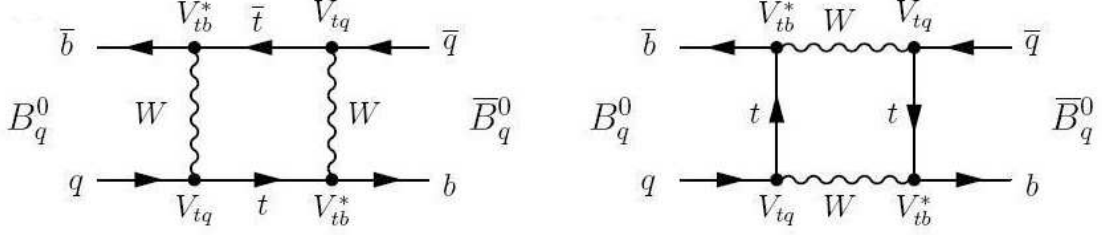


Figure 1.3: The box diagrams showing $B^0\bar{B}^0$ mixing.

$$|\bar{B}^0(t)\rangle = f_+(t) |\bar{B}^0\rangle + \frac{p}{q} f_-(t) |B^0\rangle \quad (1.5.4)$$

where

$$f_{\pm}(t) = \frac{1}{2} (e^{-i\mu_L t} \pm e^{-i\mu_H t}) \quad (1.5.5)$$

We consider the B decays to a CP eigenstate f_{CP} accessible to both B^0 and \bar{B}^0 decay. CP violation occurs if there is an asymmetry in the time-dependent decay rates of $B^0 \rightarrow f_{CP}$ and $\bar{B}^0 \rightarrow f_{CP}$. The time-dependent CP asymmetry, A_{CP} can be expressed as :

$$\begin{aligned} A_{CP}(t) &= \frac{\Gamma[B^0(t) \rightarrow f_{CP}] - \Gamma[\bar{B}^0(t) \rightarrow f_{CP}]}{\Gamma[B^0(t) \rightarrow f_{CP}] + \Gamma[\bar{B}^0(t) \rightarrow f_{CP}]} \\ &= \frac{|\lambda|^2 - 1}{|\lambda|^2 + 1} \cos(\Delta m_d t) + \frac{2 \text{Im}\lambda}{|\lambda|^2 + 1} \sin(\Delta m_d t) \\ &= A_{CP} \cos(\Delta m_d t) + S_{CP} \sin(\Delta m_d t) \end{aligned}$$

where A_{CP} and S_{CP} denote the parameters for direct and mixing-induced CP violation. An alternative notation, $C_{CP} = -A_{CP}$ is used by BaBar, which is another B factory experiment at SLAC. The complex parameter λ is defined as

$$\lambda = \left(\frac{q}{p}\right) \left(\frac{\bar{A}_{f_{CP}}}{A_{f_{CP}}}\right) \quad (1.5.6)$$

where $\bar{A}_{f_{CP}}$ and $A_{f_{CP}}$ represent the decay amplitudes for $\bar{B}^0 \rightarrow f_{CP}$ and $B^0 \rightarrow f_{CP}$, respectively. The first part, $\left(\frac{q}{p}\right)$, describes the mixing, while the $\left(\frac{\bar{A}_{f_{CP}}}{A_{f_{CP}}}\right)$ part describes the decay amplitudes. The parameter λ can be re-written as,

$$\lambda = \left| \frac{\bar{A}_{f_{CP}}}{A_{f_{CP}}} \right| e^{-i(\phi_{\text{mixing}} + \phi_{\text{decay}})} \quad (1.5.7)$$

where ϕ_{mixing} represents the weak phase difference in $B^0\text{-}\bar{B}^0$ mixing and ϕ_{decay} represents the weak phase difference in decay amplitudes.

1.6 Types of CP violation in B decays

The CP violating decays in the B -meson sector can be broadly categorized into the following three types:

- CP violation in decay or direct CP violation ($DCPV$)

This occurs in both charged and neutral decays, where the amplitude for a decay and its CP conjugate process have different magnitudes. B^0 - \bar{B}^0 mixing is not involved in this case. If A_f and $\bar{A}_{\bar{f}}$ are the amplitudes of $B \rightarrow f$ and $\bar{B} \rightarrow \bar{f}$ decays respectively, then the condition for CPV in decay is given by: $\frac{\bar{A}_{\bar{f}}}{A_f} \neq 1$. The amount of CP asymmetry is denoted as A_{CP} and defined as:

$$A_{CP} = \frac{1 - \left| \frac{\bar{A}_{\bar{f}}}{A_f} \right|^2}{1 + \left| \frac{\bar{A}_{\bar{f}}}{A_f} \right|^2} \neq 1 \quad (1.6.1)$$

This type of CP violation has $\Delta B = 1$ or $\Delta S = 1$. Since it occurs directly in the decay, it is called direct CP violation. A non-zero coefficient in front of the cosine mixing term is characteristic of this CP violation. This is only possible source of CP asymmetry in charged B decays.

- CP violation in mixing or indirect CP violation ($ICPV$)

This type of CP violation appears in B^0 - \bar{B}^0 mixing and requires the condition

$$\left| \frac{q}{p} \right| \neq 1 \quad (1.6.2)$$

It is often referred to as indirect CP violation. This type of CP violation has $\Delta B = 2$ or $\Delta S = 2$.

- CP violation in interference between mixing and decay

This type of CP violation arises from the interference between a $B^0 \rightarrow f$ decay and the other decay $\bar{B}^0 \rightarrow B^0 \rightarrow f$. The final state should be a CP eigenstate that is accessible to both B^0 and \bar{B}^0 decays. This requires the condition

$$Im(\lambda) \neq 0 \quad (1.6.3)$$

A non-zero coefficient in front of the sine mixing term is characteristic of this type of CP violation. This type of CP violation has $\Delta B = 2$ or $\Delta S = 2$.

1.7 $B^0 \rightarrow \psi(2S)K_S^0$ decay

The $B^0 \rightarrow \psi(2S)K_S^0$ decay is one of the “golden” modes for measurement of CP -violation due to its clean experimental signature and straightforward theoretical interpretation. The $\psi(2S)$ meson is the second radially excited state (2^3S_1) of charmonium (bound state of a c quark and an anti- c quark), which have parallel spins. It has rest mass of 3686.09 ± 0.04 MeV. In SM, this decay occurs through a color suppressed tree diagram with internal W -emission ($b \rightarrow c$) and a penguin with an intermediate loop diagram ($b \rightarrow s$) as shown in Fig 1.4. The two diagrams have the same weak phase while tree diagram is the dominant contribution. The penguin diagram with an intermediate u quark has a different weak phase, but it is highly suppressed by CKM parameters. From theoretical predictions, the influence of the penguin on the asymmetry is limited to be less than $< 1\%$ [6]. From the experimental point of view the $B^0 \rightarrow \psi(2S)K_S^0$ decay is easy to access because of its relatively large branching fraction with small backgrounds. In this case, both B^0 and \bar{B}^0

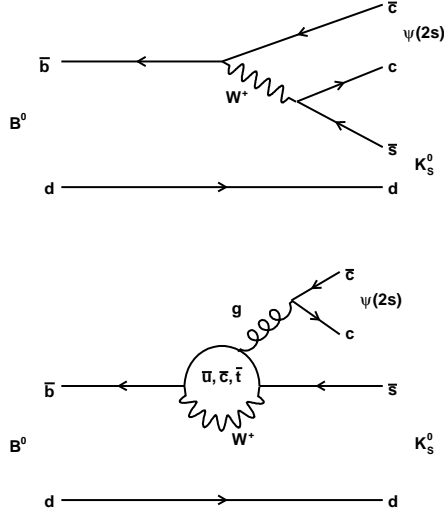


Figure 1.4: Standard Model quark level diagrams contributing to $B^0 \rightarrow \psi(2S)K_S^0$ decay. The color suppressed tree diagram (upper) and the penguin diagram (lower).

decay to the common CP eigenstate $\psi(2S)K_S^0$. The complex parameter $\lambda_{\psi(2S)K_S^0}$ can be

expressed as

$$\lambda_{\psi(2S)K_S^0} = \left(\frac{q}{p}\right) \left(\frac{\bar{A}_{\psi(2S)K_S^0}}{A_{\psi(2S)K_S^0}}\right) \quad (1.7.1)$$

Since there is a K_S^0 in the final state, we have to include K^0 - \bar{K}^0 mixing. The state K_S^0 is a mixture of K^0 and \bar{K}^0 as follows

$$|K_S^0\rangle = p_K |K^0\rangle + q_K |\bar{K}^0\rangle \quad (1.7.2)$$

Now the amplitudes become

$$\bar{A}_{\psi(2S)K_S^0} = \langle \psi(2S)K_S^0 | \bar{B}^0 \rangle = \langle K_S^0 | \bar{K}^0 \rangle = \langle \psi(2S)\bar{K}^0 | \bar{B}^0 \rangle = q_K^* \bar{A}_{\psi(2S)\bar{K}^0} \quad (1.7.3)$$

$$A_{\psi(2S)K_S^0} = \langle \psi(2S)K_S^0 | B^0 \rangle = \langle K_S^0 | K^0 \rangle = \langle \psi(2S)K^0 | B^0 \rangle = p_K^* A_{\psi(2S)K^0} \quad (1.7.4)$$

Inserting Eq. 1.7.3 and 1.7.4 in Eq. 1.7.1, we obtain

$$\begin{aligned} \lambda_{\psi(2S)K_S^0} &= \xi_f \left(\frac{q}{p}\right) \left(\frac{q_K^*}{p_K^*}\right) \left(\frac{\bar{A}_{\psi(2S)K^0}}{A_{\psi(2S)K^0}}\right) \\ &= \xi_f \frac{V_{tb}^* V_{td}}{V_{tb} V_{td}^*} \cdot \frac{V_{cs} V_{cd}^*}{V_{cs}^* V_{cd}} \cdot \frac{V_{cb} V_{cs}^*}{V_{cb}^* V_{cs}} \\ &= \xi_f e^{-2i\phi_1} \end{aligned}$$

where ξ_f is the CP eigenvalue. $\psi(2S)K_S^0$ is a CP -odd state ($\xi_f = -1$). Substituting the values of $\lambda_{\psi(2S)K_S^0}$, the CP -violating parameters :

$$\mathcal{S} = \frac{2 \operatorname{Im}\lambda}{|\lambda|^2 + 1} = -\xi_f \sin 2\phi_1, \quad \mathcal{A} = \frac{|\lambda|^2 - 1}{|\lambda|^2 + 1} = 0, \quad A_{CP}(t) = -\xi_f \sin 2\phi_1 \sin(\Delta m_d t) \quad (1.7.5)$$

New Physics (NP) effects beyond the SM may enter through the tree level diagram. For example flavor changing neutral current (FCNC) is possible through non-standard sZb coupling and subsequent production of the $c\bar{c}$ final state. In the presence of a CP violating phase in the Z -contribution, this could lead to a difference in $\sin 2\beta$ measured among the golden modes. However the NP effects are different depending upon the CP properties of the final $c\bar{c}$ states [7]. In this decay mode, $S_{\psi(2S)K_S^0} = \sin 2\phi_1$.

$$\sin 2\beta_{MK_S} - \sin 2\beta = \sin(2\beta - \arg(MK_S)) - \sin 2\beta \approx -\arg(MK_S) \cos 2\beta \quad (1.7.6)$$

$$|\arg(MK_S)| \leq \begin{cases} 0.11 & \text{for } M = \psi, \psi' \\ 0.25 & \text{for } M = \eta_c, \chi_{c1} \end{cases} \quad (1.7.7)$$

The most recent time-dependent study on $B^0 \rightarrow \psi(2S)K_S^0$ decays has been reported by the BaBar collaboration [8] using a data sample of 465×10^6 $B\bar{B}$ pairs. A total of 861 signal candidates was obtained with purity 87%. The CP violation parameter is measured to be $\mathcal{S}_{\psi(2S)K_S^0} = 0.897 \pm 0.100(\text{stat.})$. Belle’s latest published measurement [9] includes only 152×10^6 $B\bar{B}$ pairs (140 fb^{-1} , the SVDI data set only). The signal yield and purity are

$$\text{N} [\psi(2S)(1^+1^-) K_S^0] = 145 \text{ (purity 93\%)}, \quad \text{N} [\psi(2S)(J/\psi \pi^+ \pi^-) K_S^0] = 163 \text{ (purity 88\%)} \quad (1.7.8)$$

A total of 308 signal candidates are observed with $\mathcal{S}_{\psi(2S)K_S^0} = 0.89 \pm 0.20(\text{stat.})$. Now Belle has an additional data sample with 505×10^6 $B\bar{B}$ pairs (465 fb^{-1} , the SVDII data set), about 3.3 times larger than the previous sample. It is important to measure significant CP violation with a smaller statistical error (~ 0.09) using the higher statistics data accumulated by the Belle detector (657 M $B\bar{B}$ (605 fb^{-1}), about 4.3 times the original SVD1 data sample.

1.8 The $b \rightarrow s\gamma$ decays

Rare radiative B meson decays play an important role in the search for physics beyond the standard model of electroweak interactions. These are flavor changing neutral current (FCNC) decays, forbidden at tree level in the SM, but allowed through electroweak loop processes as in Fig. 1.5. At the leading order, FCNC processes proceed through a loop involving a charged W and a quark. Therefore, these processes are suppressed by at least a factor of the weak coupling constant, relative to other weak interactions with one vertex. The loop can be sensitive to undiscovered particles (for example, a charged Higgs or SUSY particles), that may replace the SM particle in the loop and therefore is sensitive to new physics. The measurements we can make to search for NP include the branching fraction, photon polarization, charge asymmetry and time-dependent CP violation measurement. Here we mainly focus on exclusive search for the two rare radiative decays, $B \rightarrow \phi K\gamma$ and $B \rightarrow \omega K\gamma$ modes.

The current measured inclusive world-average branching fraction for $B \rightarrow X_s\gamma$ is $(3.55 \pm 0.26) \times 10^{-4}$ [10]. The SM prediction at next-to-next-to-leading order (NNLO) is $(3.15 \pm 0.23) \times 10^{-4}$ [11] for a photon energy $E_\gamma > 1.6$ GeV in the B meson rest frame. The experimental value is one standard deviation (σ) higher than the theory prediction and thus allows significant new physics contributions to radiative B decays. Exclusive $b \rightarrow s\gamma$

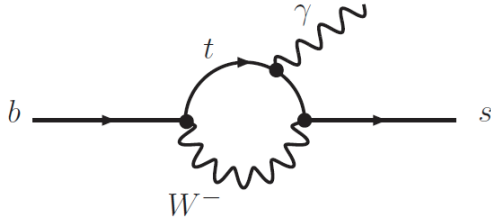


Figure 1.5: Feynman diagram for the radiative $b \rightarrow s\gamma$ decays, showing the SM loop process with the t -quark contribution.

decays have also been extensively measured, but their sum so far accounts only for 44% of the inclusive rate. Therefore, further measurements of branching fractions for exclusive $B \rightarrow \phi(\omega)K\gamma$ modes will improve our understanding of the $b \rightarrow s\gamma$ process.

1.9 Probe for New Physics

Another possible contribution of new physics to the $b \rightarrow s\gamma$ process involves the photon helicity. Since the weak interaction depends on the helicity of the particles involved, the SM predicts a different polarization of the photon depending on whether it comes from a b or \bar{b} quark. The emitted photons are predominantly left-handed (right-handed) in $b \rightarrow s\gamma$ ($\bar{b} \rightarrow \bar{s}\gamma$) decays. Therefore, the photon from \bar{B}^0 or B^- is left-handed and from B^0 or B^+ is right-handed as shown in Fig. 1.6.

The effective Hamiltonian in $b \rightarrow s\gamma$ process has the general structure

$$\mathcal{H}_{\text{rad}} = -\frac{4G_F}{\sqrt{2}}V_{tb}V_{ts}^*(C_{7R}\mathcal{O}_{7R} + C_{7L}\mathcal{O}_{7L}) \quad (1.9.1)$$

where the electromagnetic dipole operators are given by

$$\mathcal{O}_{7L,R} = \frac{e}{16\pi^2}m_b\bar{s}\sigma_{\mu\nu}\frac{1 \pm \gamma_5}{2}bF^{\mu\nu}. \quad (1.9.2)$$

The Wilson coefficients C_{7L} and C_{7R} describe the amplitudes of $b \rightarrow s\gamma$ for left and right-handed photons, respectively. Due to the chiral structure of the W^\pm couplings to quarks in the SM, the amplitude for the emission of a left-handed photon in $b \rightarrow s\gamma$ is enhanced relative to that for a right-handed photon by $C_{7R}/C_{7L} \simeq m_s/m_b$. However, in some extensions of SM such as the left-right symmetric model (LRSM) or the minimal supersymmetric standard model (MSSM), both photon helicities might contribute to the decay. Therefore, measurements of the photon helicity are sensitive to some non-SM theories, which may not give large effects in the measurements of branching fraction or asymmetry.

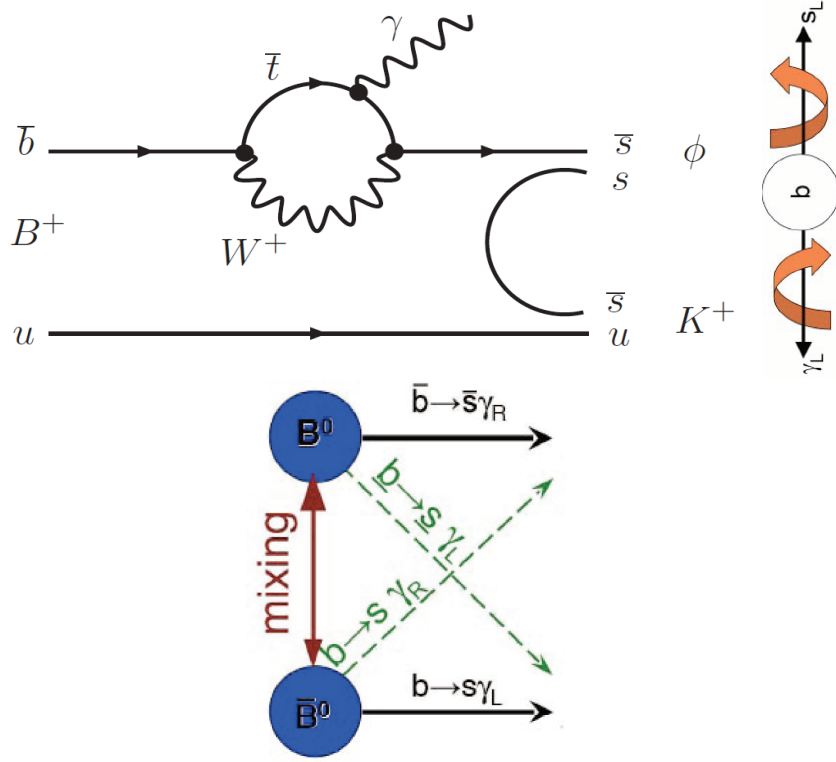


Figure 1.6: The penguin diagram for $B \rightarrow \phi K \gamma$ decay with $s\bar{s}$ pair creation. The lower figure shows the photon polarization in B decays and the possibility of a right-handed current due to mixing.

Atwood, Gronau and Soni proposed to search for the mixing-induced CP asymmetry in radiative B decays [12]. In the B^0 - \bar{B}^0 system, this asymmetry arises when B^0 and \bar{B}^0 decays to a common final state. Since in this case, the polarization of the photon carries information on the original b flavor, the CP asymmetry is suppressed in the SM by the quark mass ratio ($2m_s/m_b$).

$$A(t) \simeq \frac{2m_s}{m_b} \sin(2\phi_1) \sin(\Delta m \Delta t) \quad (1.9.3)$$

The expected asymmetry is nearly 3% for S and 0.6% for A [13] in $B \rightarrow P_1 P_2 \gamma$, where P_1 and P_2 are both eigenstates of charge conjugation.

In the presence of new physics this prediction can be modified, and a significant right-handed photon amplitude can appear in $b \rightarrow s \gamma$ decays. In many extensions of SM, such as the left-right symmetric model (LRSM), the amplitude for right-handed photons grows in proportion to the virtual heavy fermion mass, which can lead to large asymmetries

(even asymmetries larger than 50% are possible). In this thesis, the neutral mode $B^0 \rightarrow \phi K_S^0 \gamma$ [14] is used for the first time to measure the time-dependent CP asymmetry. Due to the narrow width of the ϕ resonance, the decay $B \rightarrow \phi K \gamma$ is well separated from the background and can be effectively used for measurements of photon momenta over a wide interval. In addition, this mode can also be used to search for a possible contribution from kaonic resonances decaying to ϕK . Furthermore, we can probe the photon polarization using the angular distributions of the final state hadrons [15, 16].

The branching fractions of the radiative $B \rightarrow \phi K^+(K^0)\gamma$ decays have already been measured by the Belle Collaboration [17] and BaBar Collaboration [18]. Belle measured $\mathcal{B}(B^- \rightarrow \phi K^- \gamma) = (3.4 \pm 0.9 \pm 0.4) \times 10^{-6}$ and $\mathcal{B}(\bar{B}^0 \rightarrow \phi \bar{K}^0 \gamma) < 8.3 \times 10^{-6}$ at the 90% confidence level using $96 \times 10^6 B\bar{B}$ pairs. BaBar measured $\mathcal{B}(B^- \rightarrow \phi K^- \gamma) = (3.5 \pm 0.6 \pm 0.4) \times 10^{-6}$ and $\mathcal{B}(\bar{B}^0 \rightarrow \phi \bar{K}^0 \gamma) < 2.7 \times 10^{-6}$ at the 90% confidence level using $228 \times 10^6 B\bar{B}$ pairs. BaBar also reported the direct CP asymmetry in $B^- \rightarrow \phi K^- \gamma$, $\mathcal{A}_{CP} = (-26 \pm 14 \pm 5)\%$. Now Belle has accumulated 772 M $B\bar{B}$ pairs, a data sample eight times larger than the previous measurement. In this thesis, we report an updated measurement of branching fractions in $B \rightarrow \phi K^+(K^0)\gamma$ as well as a search for $B \rightarrow \omega K^+(K^0)\gamma$ decays using the higher statistics data accumulated by the Belle detector.

1.10 Experimental Technique

The B factory experiments (KEKB at Japan and PEP-II at SLAC) using an e^+e^- collider provides an ideal environment to measure the CP violation parameters with high accuracy. The collider is designed to operate at the center-of-mass energy of the $\Upsilon(4S)$ resonance. Since the mass of $\Upsilon(4S)$ is just above the $B\bar{B}$ threshold, it decays only to $B^0\bar{B}^0$ or B^+B^- pair. Since the $B\bar{B}$ pairs are produced in a single coherent quantum state (odd C configuration), the only possible neutral B pair combination is $B^0\bar{B}^0$. In the decay chain $\Upsilon(4S) \rightarrow B^0\bar{B}^0 \rightarrow f_{rec}f_{tag}$, where one of the B mesons decays at time t_{rec} to the signal mode f_{rec} and the other decays at time t_{tag} to a final state f_{tag} that distinguishes between B^0 and \bar{B}^0 , the decay rate has a time dependence given by

$$\mathcal{P}(\Delta t) = \frac{e^{-|\Delta t|/\tau_{B^0}}}{4\tau_{B^0}} \left\{ 1 + q \left[\mathcal{S} \sin(\Delta m_d \Delta t) + \mathcal{A} \cos(\Delta m_d \Delta t) \right] \right\}. \quad (1.10.1)$$

Here \mathcal{S} and \mathcal{A} are the CP violation parameters, τ_{B^0} is the neutral B lifetime, Δm_d is the mass difference between the two neutral B mass eigenstates, $\Delta t = t_{rec} - t_{tag}$, and the b -flavor

charge q equals $+1$ (-1) when the tagging B meson is a B^0 (\bar{B}^0). Since the B^0 and \bar{B}^0 are approximately at rest in the $\Upsilon(4S)$ center-of-mass system (cms), Δt can be determined from Δz , the displacement in z between the two decay vertices: $\Delta t \simeq \Delta z/(\beta\gamma c)$.

1.11 Thesis Outline

The outline of the thesis is as follows. The experimental apparatus used to collect data for this work is described in chapter 2. In chapter 3, we precisely measure the time-dependent CP violation parameters in $B^0 \rightarrow \psi(2S)K_S^0$ decays. In chapter 4, we measure the branching fractions for rare radiative $B \rightarrow \phi K\gamma$ modes. The neutral mode $B^0 \rightarrow \phi K_S^0\gamma$ is observed for the first time. In chapter 5, we describe the first time-dependent measurements in $B^0 \rightarrow \phi K_S^0\gamma$ decays. The chapter 6 describes a feasibility study for the rare $B \rightarrow \omega K\gamma$ decay mode. Finally, we summarize the work in chapter 7.

Chapter 2

The Belle Experiment

2.1 Overview of the Belle Experiment

The Belle experiment is a particle physics experiment conducted by the Belle Collaboration, a group of more than 400 physicists from 62 institutes across 15 countries. The main goal of this experiment is to study the origin of CP violation in the B meson system. This experiment operates at the KEKB accelerator, the world's highest luminosity machine. The KEKB accelerator is located at the High Energy Accelerator Research Organisation (KEK) in Tsukuba, Japan. The KEKB [19] is an asymmetric-energy e^+e^- collider, which operates at the $\Upsilon(4S)$ resonance. It accelerates the electron beam to an energy of 8 GeV (E_{e^-}), the positron beam to an energy of 3.5 GeV (E_{e^+}) and collides them with a finite crossing angle of ± 11 mrad to produce the B mesons. The Belle detector surrounds the interaction point (IP) to detect the particles produced from the e^+e^- collisions. The construction of KEKB and Belle was completed in 1998. After half a year of commissioning, the Belle detector was installed in May 1999. In June 1999 the detector started logging data produced from B meson decays.

2.2 The KEKB Accelerator

The configuration of the KEKB storage ring is illustrated in Fig. 2.1. It has two different rings: the ring for 8 GeV electrons is called the High Energy Ring (HER), and that for 3.5 GeV positrons is called the Low Energy Ring (LER). The HER and LER were constructed side by side in the tunnel used for TRISTRAN. Each ring has straight sections in the Fuji, Nikko, Tsukuba and Oho areas. The beams intersect at the IP in the Tsukuba

area, where the Belle detector is located. At the IP, electrons and positrons collide with a finite crossing angle of 22 mrad. The crossing angle itself was one of the novel features of the KEKB design, providing effective beam separation after collision without a high detector background level. The corresponding center-of-mass energy is 10.58 GeV, which coincides with the $\Upsilon(4S)$ resonance, just above $B\bar{B}$ production threshold as shown in Fig. 2.2. The circumference of the ring is 3016 m. In order to make the circumferences of the two rings precisely equal, a cross-over of the two rings was built in the Fuji area (visible on the left side of Fig. 2.1)

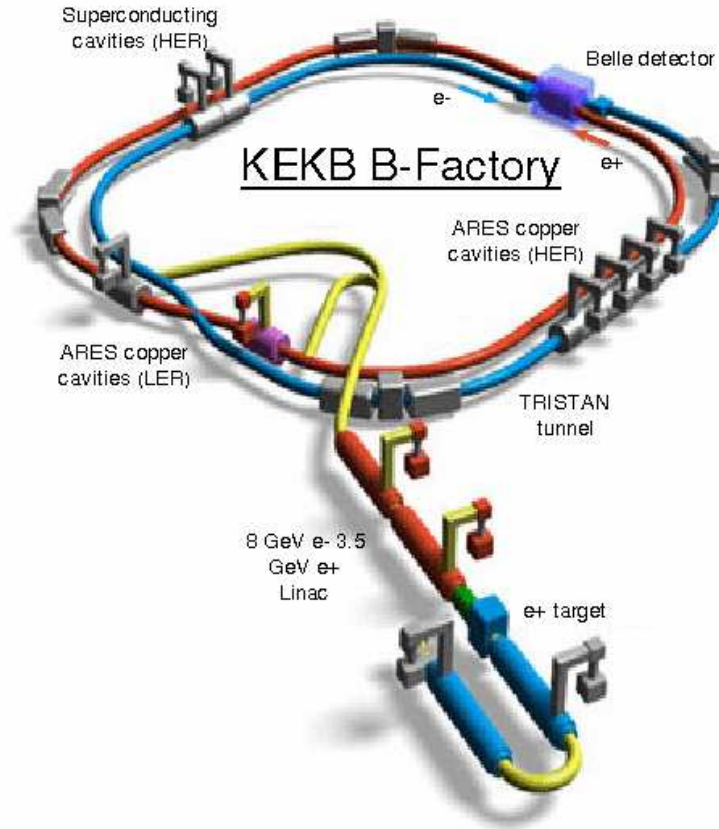


Figure 2.1: The configuration of the KEKB accelerator showing its two rings. The LER is for positrons and HER is for electrons.

The design peak luminosity of KEKB is $1.0 \times 10^{34} \text{cm}^{-2}\text{s}^{-1}$, which corresponds to 10^8 B mesons per year. The most important parameter that determines the capability of an an accelerator is the luminosity \mathcal{L} since it is directly connected to the event rate \dot{N}

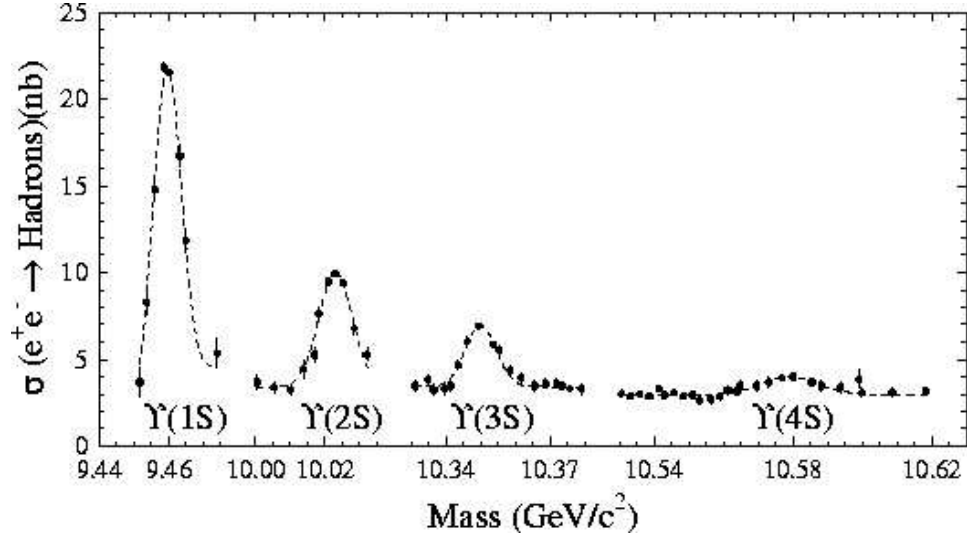


Figure 2.2: The hadronic cross-section for e^+e^- annihilation between 9.4 and 10.7 GeV.

following the relation $\dot{N} = \sigma \mathcal{L}$, where σ is a cross section. The luminosity is given by

$$\mathcal{L} = \frac{N_+ N_- f}{4\pi\sigma_x^* \sigma_y^*} \simeq \left(\frac{1+r}{2er_e} \right) \frac{\gamma_{\pm} \xi_y I_{\pm}}{\beta_y^*}, \quad (2.2.1)$$

where N_{\pm} (number of e^{\pm} particles per bunch), f (collision frequency), $\sigma_{x,y}^*$ (beam size at the IP in the x or y direction), r (aspect ratio of the beam at the IP, σ_y^*/σ_x^*), e (elementary charge), I_{\pm} (current, $eN_{\pm}f$), γ_{\pm} (Lorentz factor), r_e (classical electron radius, $e^2/4\pi\epsilon_0$), $\xi_{x,y}$ (beam-beam parameter in the x or y direction), $\beta_{x,y}^*$ is the β function at IP in x or y direction.

2.2.1 The Crab Cavities

Until 2007, the electron and positron bunches in the KEKB accelerator used to cross at a 22 milliradian angle. To boost the luminosity further, it was necessary to recover an effective head-on collision while retaining the crossing angle. To accomplish this goal, the KEKB researchers built special superconducting radio-frequency (RF) cavities that kick each beam sideways in the horizontal plane so that the bunches collide head-on at the interaction point. These special RF cavities are called "crab cavities" as shown in Fig. 2.3. On June 17, 2009, after the installation of special skew sextupoles that correct chromatic coupling, the KEKB broke the world luminosity record and achieved a peak luminosity of

$2.11 \times 10^{34} \text{cm}^{-2}\text{s}^{-1}$ using these new accelerator devices. This new record is more than a factor of two higher than the original design luminosity of KEKB. While this luminosity was being recorded, the backgrounds were good and the data were recorded smoothly in the Belle experiment. The integrated luminosity, which is proportional to the total number of $B\bar{B}$ events recorded by Belle detector reached 1000fb^{-1} by the end of summer 2010.

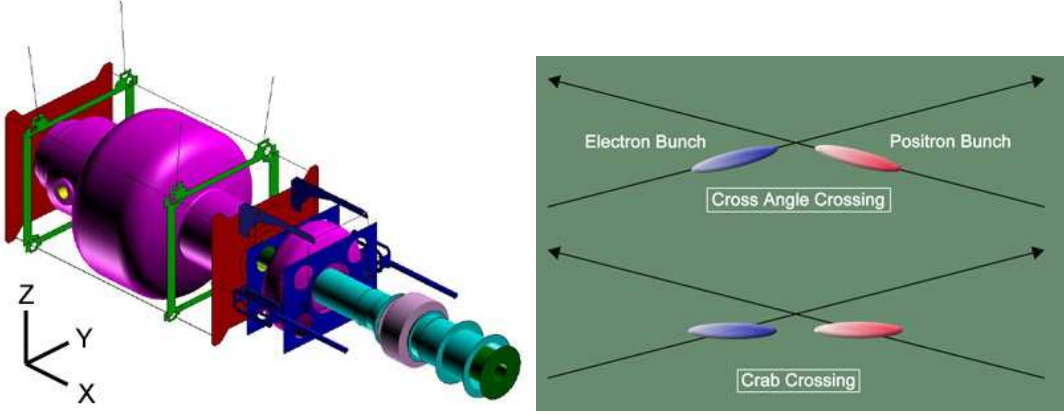


Figure 2.3: Schematic drawing of the crab cavities. (left) Schematic drawing of the crab cavities. (right) Crab cavities tilt the electron and positron bunches so that they collide head-on at the interaction point.

The data sample used for this thesis was collected with the Belle detector. To produce the B mesons the center of mass system (cms) energy is set at 10.58 GeV, which corresponds to the mass of $\Upsilon(4S)$ meson¹. Since we can neglect the e^+ and e^- masses at our energy, the mass of $\Upsilon(4S)$ particle is described in terms of beam energies as

$$M_{\Upsilon(4S)} = \sqrt{(E_{e^-} + E_{e^+})^2 - (\mathbf{p}_{e^-} + \mathbf{p}_{e^+})^2} \simeq \sqrt{4E_{e^-}E_{e^+}}. \quad (2.2.2)$$

Therefore, to produce an $\Upsilon(4S)$ meson alone with e^+e^- collider we can choose any energies of beams if their product is 27.984GeV^2 . The most important studies at a B factory are measurements of CP violation, which require measurement of the decay time distribution. The lifetime of B meson is too short to directly measure the decay time itself. Accordingly, we Lorentz-boost the B mesons and measure their vertex separations. For this purpose KEKB has an asymmetric energy of 8 GeV ($= E^-$) and 3.5 GeV ($= E^+$) for e^- and e^+ , respectively, which provides the Lorentz boost factor of

$$\beta\gamma = \frac{p_{\Upsilon(4S)}}{M_{\Upsilon(4S)}} = \frac{E_{e^-} - E_{e^+}}{\sqrt{s}} = 0.425. \quad (2.2.3)$$

¹ $\mathcal{B}(\Upsilon(4S) \rightarrow B\bar{B}) > 96\%$ [20]

The average decay length of a B^0 meson is

$$l = (\beta\gamma)(c\tau_B) = 0.425 \times 459\mu\text{m} \simeq 200\mu\text{m}, \quad (2.2.4)$$

with a B^0 meson lifetime τ_B . This length is measurable with our solid state vertex detector whose longitudinal vertex resolution is $\sim 100 \mu\text{m}$.

2.3 The Belle Detector

The Belle detector [21] is a large-solid-angle magnetic spectrometer that consists of a silicon vertex detector (SVD), a 50-layer central drift chamber (CDC), an array of aerogel threshold Cherenkov counters (ACC), a barrel-like arrangement of time-of-flight scintillation counters (TOF), and an electromagnetic calorimeter (ECL) comprised of CsI(Tl) crystals located inside a superconducting solenoid coil that provides a 1.5 T magnetic field. An iron flux-return located outside the coil is instrumented to detect K_L^0 mesons and to identify muons (KLM).

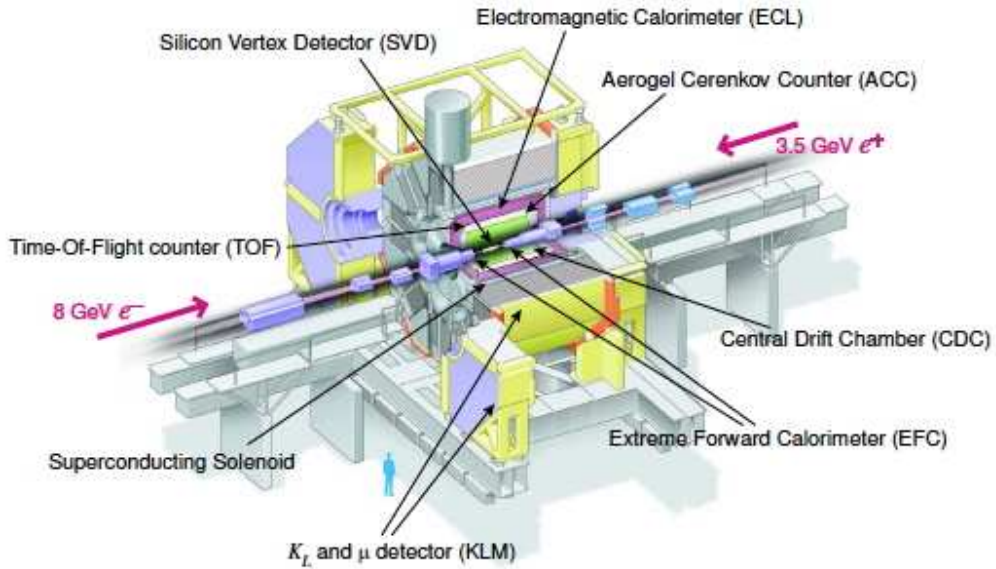


Figure 2.4: Schematic of the Belle Detector.

The conventional definition of the coordinates in Belle and KEKB is

- x horizontal direction, outward to the KEKB ring.
- y vertical direction, upward.
- z opposite of the positron beam direction.
- r $\sqrt{x^2 + y^2}$.
- θ the polar angle with respect to z axis.
- φ the azimuthal angle around z axis.

A schematic view of the Belle detector is shown in Fig. 2.4 and brief description of each sub-detector is given in the following subsections.

2.3.1 Silicon Vertex Detector (SVD)

The silicon vertex detector (SVD) [22] is an essential component of the Belle detector because it provides a precise measurement of the B meson decay vertices, which is essential in the study of time-dependent CP asymmetry. In addition, it is also useful for identifying and measuring the decay vertices of D and τ particles and contributes to the charged particle tracking.

Fig. 2.5 shows the side and end views of the SVD. It consists of three concentric layers of double-sided silicon strip detectors (DSSDs) and covers the polar angle range $23^\circ < \theta < 139^\circ$ where θ is the angle from the beam axis. This corresponds to 86% of the full solid angle.

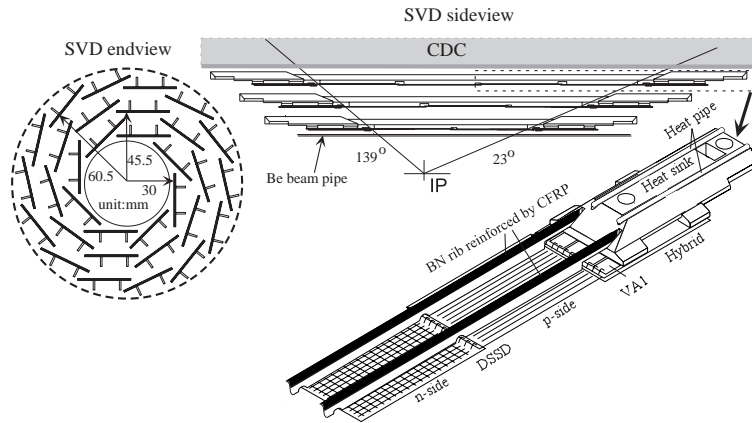


Figure 2.5: Configuration of the Belle silicon vertex detector (SVD1).

The radii of the three layers are 30.0 mm, 45.5 mm, and 60.5 mm. The layers are constructed from 8, 10, and 14 independent ladders from inside to outside, respectively. Each ladder consists of double-sided silicon strip detectors (DSSDs). Each DSSD size is $57.5 \times 33.5 \text{ mm}^2$ and $300 \mu\text{m}$ thick. In total, 102 DSSDs are used and the number of readout channels is 81920. The readout chain for DSSDs is based on the VA1 integrated circuit. The VA1 has excellent noise performance ($200e^- + 8e^-/\text{PF}$) and reasonably good radiation tolerance of 500 kRad. The track-matching efficiency is defined as the probability that a CDC track within the SVD acceptance matches SVD hits in at least two layers, and in at least one layer has both r - φ and r - z information. Tracks from K_S^0 decays are excluded since these tracks do not necessarily pass through the SVD.

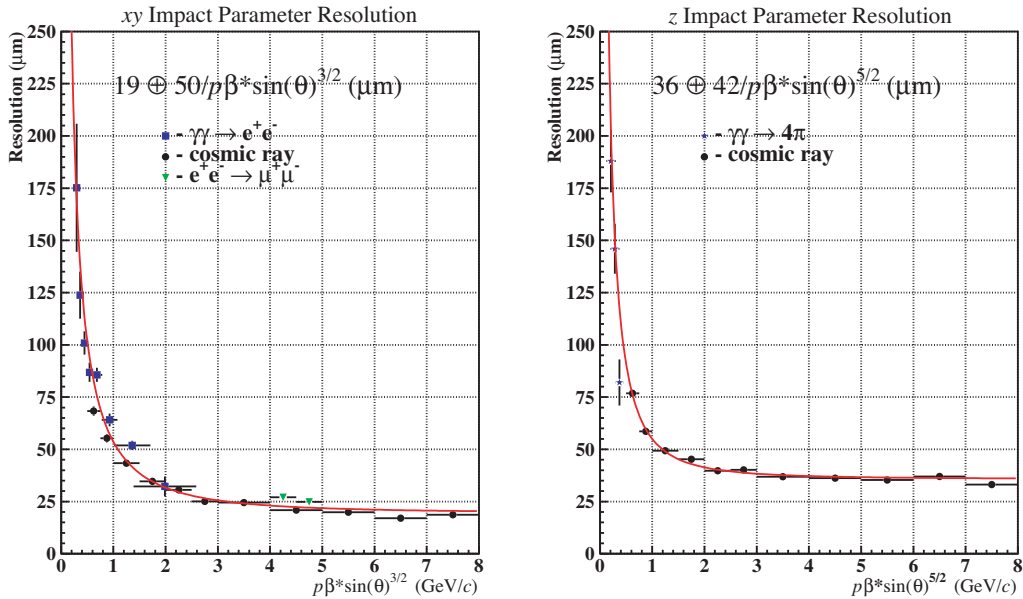


Figure 2.6: Impact parameter resolutions for the r - φ (left) and z direction (right).

When a charged particle passes through the DSSDs, it produces electron-hole pairs along its trajectory. The charges are then collected at the sense strips by the applied electric field. The charge distributions on the orthogonally segmented strips allow one to determine three-dimensional hit positions and, hence, to reconstruct the particle track. The impact parameters of a reconstructed track are defined as the r - φ and z distances of the closest approach of the track to the interaction point.

The momentum and angular dependence of the impact parameter resolution are shown in Fig. 2.6 and well represented by the following formula:

$$\sigma_{r\phi} = 19 \oplus \frac{50}{p\beta \sin^{3/2} \theta} \mu\text{m}, \quad (2.3.1)$$

$$\sigma_z = 36 \oplus \frac{42}{p\beta \sin^{5/2} \theta} \mu\text{m}, \quad (2.3.2)$$

where \oplus indicates a quadratic sum, and the momentum p is given in units of GeV/c . The impact parameter resolution for an $1 \text{ GeV}/c$ normal track is around $55 \mu\text{m}$.

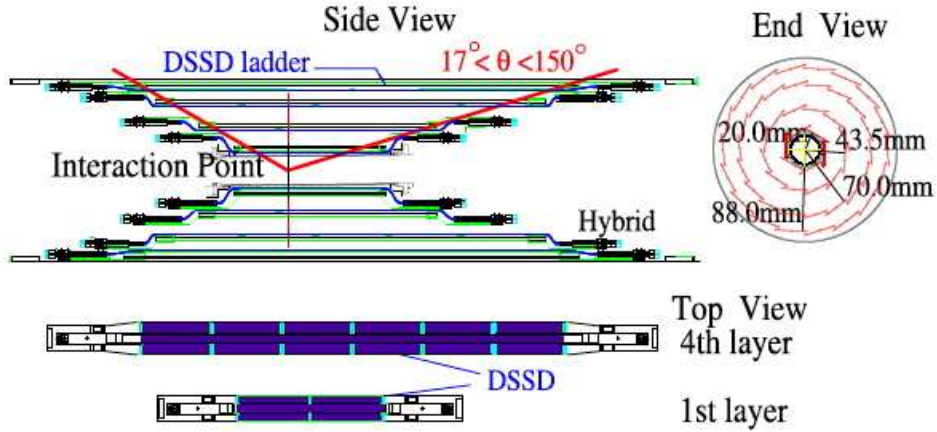


Figure 2.7: Configuration of SVD2.

A new SVD (SVDII) [23] was installed in the summer of 2003. There are many improvements from SVDI. The SVDII consists of four cylindrical layers whose radii are 20.0mm, 43.5mm, 70.0mm and 88.0mm. The angular acceptance extends from 17° to 150° , which is the same as the CDC acceptance. The four layers have 6,12,18 and 18 ladders to cover the entire the ϕ region. Each ladder consists of 2,3,5 and 6 DSSDs, for layers 1 to 4, which are fabricated by Hamamatsu Photonics. There are two kinds of DSSDs. One is used in 1st, 2nd and 3rd layers and has a size of $28.4 \times 79.6 \text{ mm}^2$ with a strip pitch of $75 \mu\text{m}$ on the p-side and $50 \mu\text{m}$ on the n-side. In the 4th layer, the size is $34.9 \times 76.4 \text{ mm}^2$ with a strip pitch of $73 \mu\text{m}$ on the p-side and $65 \mu\text{m}$ on the n-side. The n-side of DSSDs is used for measurement of the $r-\phi$ coordinate and the p-side is used for measurement of the z coordinate. The number of strips are 512 on both the n-side and p-side. The total number of DSSDs is 246. Therefore the total number of readout channels are 110592 ($=216 \times 512$).

2.3.2 Central Drift Chamber (CDC)

The Belle central drift chamber (CDC) [24] has been designed for efficient reconstruction of charged particle tracks and precise determination of their momenta. The path of a charged particle moving in a uniform magnetic field is a helix with its axis parallel to the direction of the magnetic field. The particle momentum can be determined from the curvature of the helix (r) as

$$p_t = 0.3Br \quad (2.3.3)$$

where p_t is in units of GeV/c , B is the magnetic field in Tesla, and r is in meters.

In addition, the CDC is used to measure the energy loss (dE/dx) of charged particles for their particle identification. The CDC is also used to provide important information for the trigger system.

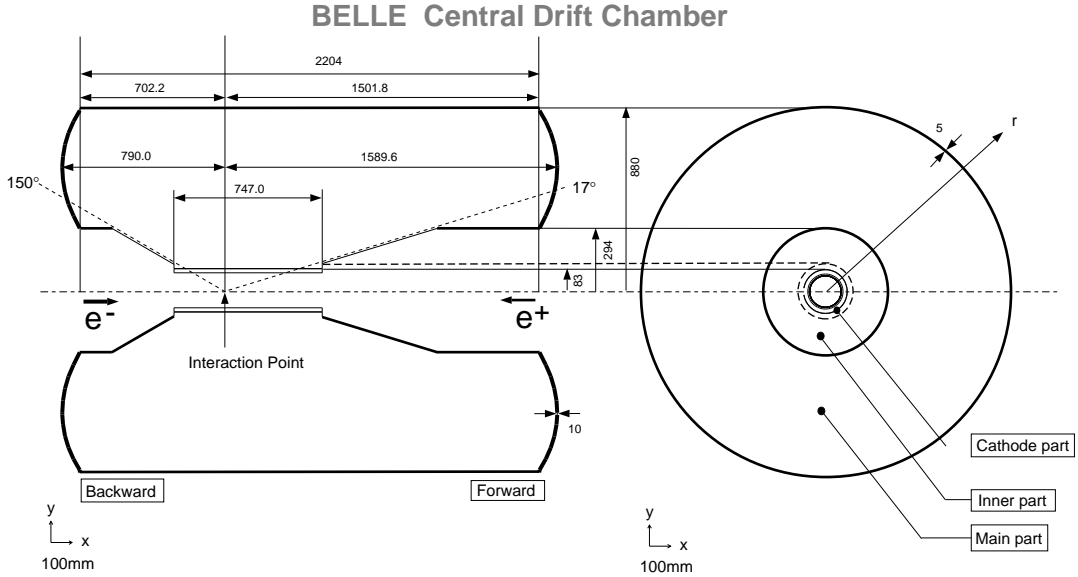


Figure 2.8: Schematic view of the CDC structure. The lengths in the figure are in units of mm's.

The structure of the CDC is shown in Fig. 2.8. It is a cylindrical chamber with inner radius 77 mm, outer radius 880 mm, and length 2400 mm and consists of 50 sense wire layers and three cathode strip layers. The sense wire layers are grouped into 11 super layers, of which six are axial and five are small-angle stereo super layers. Each super-layer consists of between three and six radial layers, all with the same number of drift cells in

the azimuthal direction. The small-angle stereo layers are used in conjunction with the axial layers to provide z coordinate measurements. Stereo layers also provide a highly-efficient fast z -trigger combined with the cathode strips. We optimized the stereo angles in each stereo super layer by maximizing the z -measurement capability while keeping the gain variations along the wire below 10%. The total number of sense wires is 8400, of which 5280 are axial and 3120 are stereo. The cathode strips are divided into eight segments in the φ direction and 64 segments (8.2 mm pitch) in z to provide z -coordinate information used for the fast trigger.

Since the majority of the decay products of a B meson have momenta lower than 1 GeV/ c , the minimization of multiple Coulomb scattering is important for preserving the momentum resolution. Therefore, a low- Z gas (50% helium, 50% ethane) is chosen, which still retains a good dE/dx resolution. The average spatial resolution for the entire drift space is measured to be approximately 130 μm in the r - φ direction.

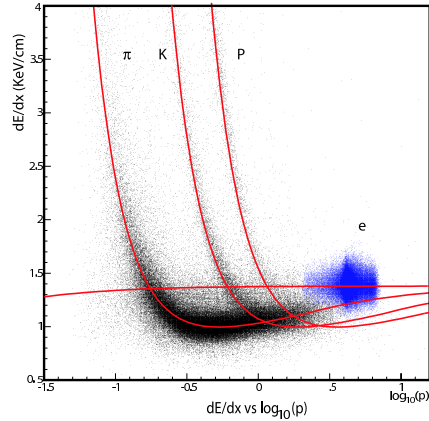


Figure 2.9: Measured dE/dx vs. momentum in collision data. The expected mean energy loss for different particle species are shown.

Fig. 2.9 shows the measured dE/dx as a function of particle momentum, together with the expected mean values for different particle species. Populations of pions, kaons, protons and electrons are clearly seen. The dE/dx resolution is measured to be 7.8% for pions in the momentum range from 0.4 to 0.6 GeV/ c , while the resolution for Bhabha and muon pair events is measured to be about 6%. The dE/dx information provides $\geq 3\sigma$ K/π separation up to 0.8 GeV/ c . The dE/dx bands for kaons and pions cross-over around 1 GeV/ c , however they can provide some discrimination between kaons and pions above

$2 \text{ GeV}/c$. dE/dx also provides more than $3 \sigma e/\pi$ separation for the momentum range from $0.3 \text{ GeV}/c$ to $3 \text{ GeV}/c$.

2.3.3 Aerogel Cerenkov Counter System (ACC)

The Aerogel Cerenkov Counter (ACC) [25] is an important component of the Belle particle identification system. It is capable of identifying high momentum particles (from $1.2 \text{ GeV}/c$ to $3.5 \text{ GeV}/c$), which is beyond the reach of dE/dx measurements by CDC and time-of-flight measurements by TOF (usually below $1 \text{ GeV}/c$).

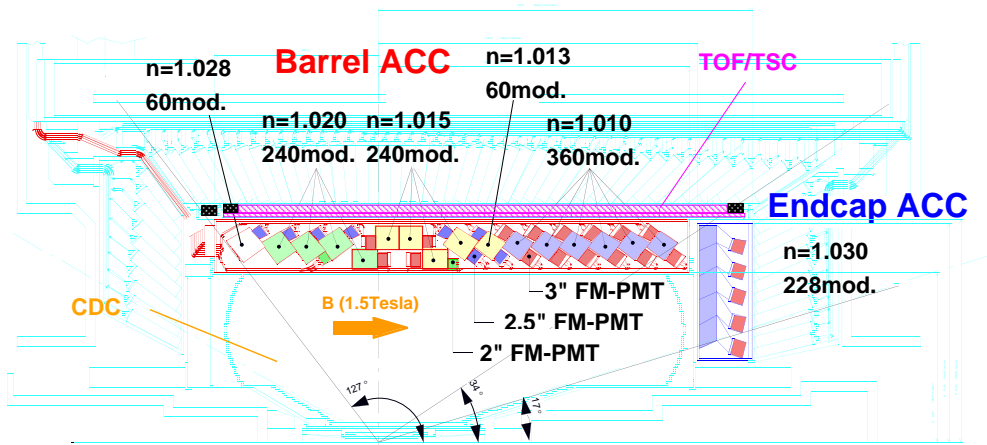


Figure 2.10: Configuration of ACC and TOF system.

The aerogel blocks are read out by either one or two fine mesh PMTs depending on their angular position. A charged particle moving with a velocity $c > c/n$ inside a medium, e.g. silica aerogel, with a refractive index n produces Cerenkov radiation. For a fixed n , the threshold energies for particles to emit Cerenkov photons are proportional to their masses. Therefore, K/π separation in the desired momentum region can be achieved by selection media with appropriate refractive index values.

The configuration of ACC in the central part of the Belle detector is shown in Fig. 2.10. It consists of 960 counter modules segmented into 60 cells in the φ direction for

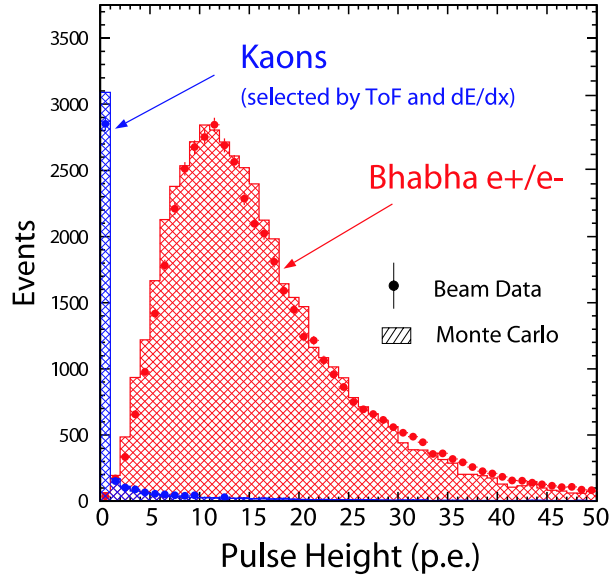


Figure 2.11: Pulse-height spectra in units of photoelectrons observed by the ACC for electrons and kaons. The Monte Carlo expectations are superimposed.

the barrel part and 228 modules arranged in 5 concentric layers for the forward end-cap part of the detector. All the counters are arranged in a semi-tower geometry, pointing to the interaction point, covering a total polar angle range from 17° to 127° . In order to obtain good pion/kaon separation for the whole kinematical range, the refractive indices of aerogels are selected to be between 1.01 and 1.03, depending on their polar angle. A typical single ACC module is shown in Fig. 2.12.

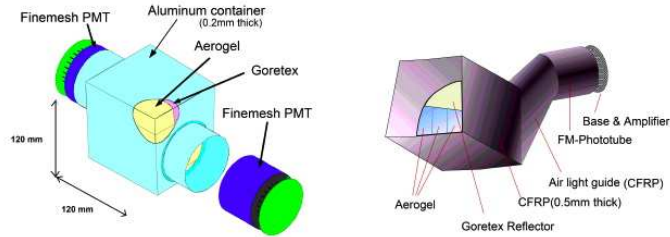


Figure 2.12: Design of an ACC barrel module and end-cap module.

Fig. 2.11 shows the measured pulse height distributions in the barrel ACC for e^\pm tracks in Bhabha events and K^\pm candidates in hadronic events, which are selected by TOF

and dE/dx measurements. The figure demonstrates a clear separation between high energy electrons and below Cerenkov threshold production.

2.3.4 Time-of-Flight Counters (TOF)

A time-of-flight (TOF) detector system [26] provides particle identification information for momenta below $1.2 \text{ GeV}/c$, which encompasses 90% of the particles produced in $\Upsilon(4S)$ decays. It also provides fast timing signals for the trigger system.

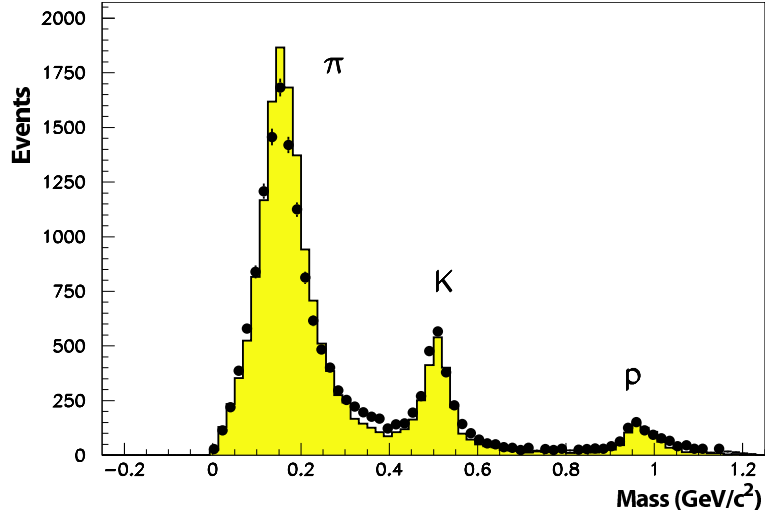


Figure 2.13: Distributions of hadron masses calculated from the measured time-of-flight for particles with momenta less than $1.25 \text{ GeV}/c$. The histogram shows the Monte Carlo prediction obtained by assuming $\sigma_{\text{TOF}} = 100 \text{ ps}$.

The TOF system consists of 128 plastic scintillation counters and 64 thin Trigger Scintillation Counters (TSC). Two trapezoidal shaped TOF counters and one TSC counter form a module. Each TOF (TSC) counter is read out by two (one) fine-mesh photomultipliers. In total, 64 TOF/TSC modules located at a radius of 1.2 m from the interaction point cover a polar angle range from 33° to 121° .

The flight time T of particle in length L is expressed as

$$T = \frac{L}{c} \sqrt{1 + c^2(m/p)^2}. \quad (2.3.4)$$

Given the momentum from the CDC, the time-of-flight can be used for particle identification by calculating the mass of the particle. For the case of particles with momenta of $1.2 \text{ GeV}/c$, $T = 4.0 \text{ ns}$ for pions and $T = 4.3 \text{ ns}$ for kaons with $L = 1.2 \text{ m}$. Thus, a time resolution of

100 ps would provide more than 3 standard deviation separation below 1.2 GeV/c. Fig. 2.13 shows the particle mass distribution calculated from measured time-of-flight for particles with momentum less than 1.25 GeV/c. Clear peaks corresponding to pions, kaons, and protons can be seen.

2.3.5 Electromagnetic Calorimeter (ECL)

The main purpose of Electromagnetic Calorimeter (ECL) [27] is the detection of photons with high efficiency and good resolutions in energy and position. This also plays an important role in the electron identification as it depends on the charged particles momenta and the energy deposit in the calorimeter. At high energy, electrons lose their energy in the calorimeter by bremsstrahlung, and photons lose their energy by electron-positron pair production. These processes repeat over and over again, producing electromagnetic showers that deposit energy in the absorbing material.

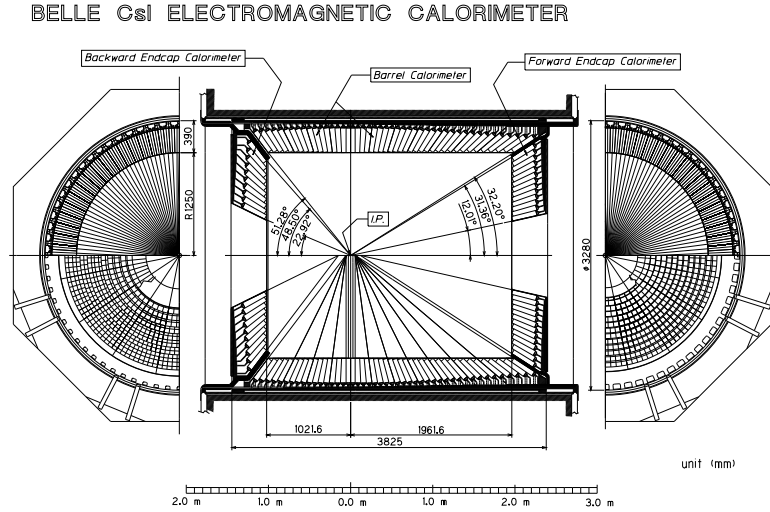


Figure 2.14: Configuration of the ECL.

The overall configuration of the Belle calorimeter, ECL, is shown in Fig. 2.14. The ECL consists of a barrel section of 3.0 m in length with an inner radius of 1.25 m and annular end-caps at $z = +2.0$ m and $z = -1.0$ m from the interaction point. The geometrical parameters of each section are given in Table 2.1. The ECL consists of 8736

CsI(Tl) crystals covering the polar angle region of $17^\circ < \theta < 150^\circ$, corresponding to a total solid-angle coverage of 91% of 4π .

Table 2.1: Geometrical parameters of the ECL.

Item	θ coverage	θ segment	φ segment	No.of crystals
Forward end-cap	$12.4^\circ - 31.4^\circ$	13	48-144	1152
Barrel	$32.2^\circ - 128.7^\circ$	46	144	6624
Backward end-cap	$130.7^\circ - 155.1^\circ$	10	64-144	960

The photon energy resolution is measured to be

$$\frac{\sigma_E}{E} = 1.34 \oplus \frac{0.066}{E} \oplus \frac{0.81}{E^{1/4}}\% \quad (2.3.5)$$

Electrons and charged pions can be separated in the ECL because electrons deposit most of their energies while charged pions deposit only a fraction of their energies. Measurements from the ECL combined those from the CDC, ACC and TOF provide an electron identification efficiency of about 80% and a π fake rate of less than 1% in the momentum range from 500 MeV/ c to 2 GeV/ c .

2.3.6 Superconducting Solenoid Magnet

The superconducting solenoid magnet [28] provides a magnetic field of 1.5 T parallel to the beam pipe. The magnetic field is used to measure the momentum of charged particles from the radii of curvature of their trajectories. The superconducting coil consists of a single layer of a niobium-titanium-copper alloy embedded in a high purity aluminum stabilizer. It is wound around the inner surface of an aluminium support cylinder with a diameter between 3.4 m and 4.4 m. Indirect cooling is provided by liquid helium circulating through a tube on the inner surface of the cylinder.

2.3.7 K_L^0 and Muon Detection System (KLM)

The KLM system [29] is designed to identify K_L^0 's and muons with high efficiency over a broad momentum range greater than 600 MeV/ c . The KLM consists of an alternating sandwich of 4.7 cm thick iron plates and glass resistive plate counters (RPCs) located outside the superconducting magnet. The barrel-shaped region around the interaction point covers the angular range $45^\circ < \theta < 125^\circ$ and endcaps in forward and backward directions extend

this to $20^\circ < \theta < 125^\circ$. There are 15 detector layers and 14 iron layers in the octagonal barrel region and 14 detector layers and 14 iron layers in each of forward and backward endcaps.

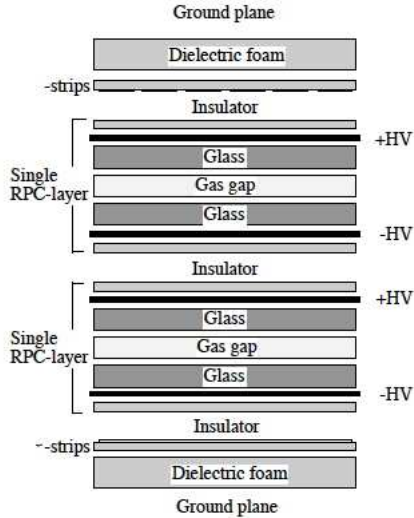


Figure 2.15: Cross section of a KLM superlayer.

Fig. 2.15 shows the cross section of a superlayer for the barrel region, in which two RPCs are sandwiched between orthogonal θ and φ pickup-strips with the ground planes for signal reference and proper impedance. A K_L^0 that interacts in the iron or in the ECL produces a cascade shower of ionizing particles. The location of this shower determines the direction of K_L^0 , however fluctuations in the size of the hadronic shower limit a useful measurement of the K_L^0 energy. The multiple layers of charged particle detectors and iron allow discrimination between muons and charged hadrons based upon their range and transverse scattering. Muons travel much farther with smaller deflections than strongly interacting hadrons. The detection of charged particles is provided by glass-electrode-resistive plate counters (RPCs) [30]. RPCs have two parallel plate electrodes with high bulk resistivity ($> 10^{10}\Omega - \text{cm}$) separated by a gas-filled gap.

2.3.8 Extreme Forward Calorimeter (EFC)

The EFC [31] is a calorimeter that further extends the polar angle coverage by the ECL to 6.4° to 11.5° in the forward direction and 163.3° to 171.2° in the backward direction (Fig. 2.16).

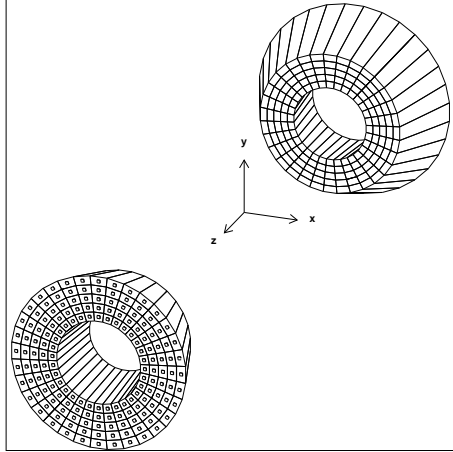


Figure 2.16: Configuration of the EFC.

It is mainly used as supplementary luminosity monitor for Belle and is also to tag two photon $e^+e^- \rightarrow \gamma\gamma$ decays. The EFC is not used in Belle reconstruction. It is also required to function as a beam mask to reduce background to the CDC. Since the EFC is placed in a very high radiation level area around the beam pipe near the IP, a radiation-hard BGO (Bismuth Germanate, $\text{Bi}_4\text{Ge}_3\text{O}_{12}$) crystal is used. The detector is segmented into 32 sectors in φ and 5 in θ for both the forward and backward detectors. The radiation lengths of the forward and backward crystals are 12 and 11, respectively.

2.4 Trigger System (TRG)

The Belle trigger system consists of a Level-1 hardware trigger and a Level-3 software trigger. It is used to select good events and reject background events as efficiently as possible. Fig. 2.17 shows the signal flow in the Level-1 trigger system.

The trigger consists of the sub detector trigger systems and the central trigger system called the Global Decision Logic (GDL). The trigger system provides a trigger signal at a fixed time $2.2 \mu\text{s}$ after the e^+e^- collision. The trigger efficiency for hadronic events is

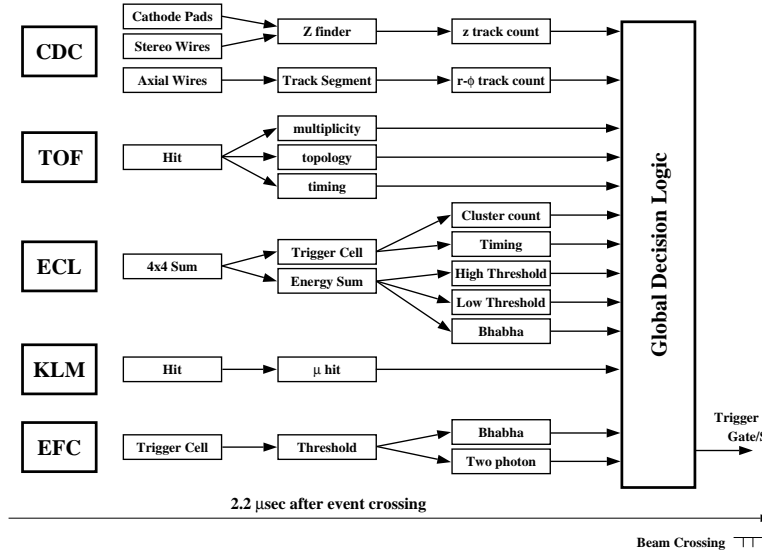


Figure 2.17: Sub-trigger system and the Global Decision Logic (GDL).

more than 99%. The event rates for physics processes and backgrounds are 200 Hz and 600 Hz respectively, at a luminosity of $2 \times 10^{34} \text{cm}^{-2} \text{s}^{-1}$.

2.5 Data Acquisition System (DAQ)

The Belle Data Acquisition (DAQ) system deals with the data flow from the analog signals acquired by the individual sub-detectors to their digitized form, which is saved in mass storage for online data processing as shown in Fig. 2.18.

The Belle DAQ system consists of three parts: a front-end readout part, an event building part and a mass storage part. For the front-end readout part, each sub-detector uses the FASTBUS TDC system or Common Pipelined Platform for Electronic Readout (COPPER) TDC, except for the SVD. The data from the SVD is digitized by a FADC and processed by a PC-based readout system and is then sent to the event building farm directly via the network. For the event building part, data flow is divided into two parallel streams in order to prevent saturation by the network limit. After partial event building, the event is sent to storage for online data processing. In online data processing, events must have at least one track originating from the IP, $dr < 1.0 \text{ cm}$ and $dz < 4.0 \text{ cm}$, with $p_t > 300 \text{ MeV}/c$. Events passing this requirement undergo full event reconstruction. Tracks

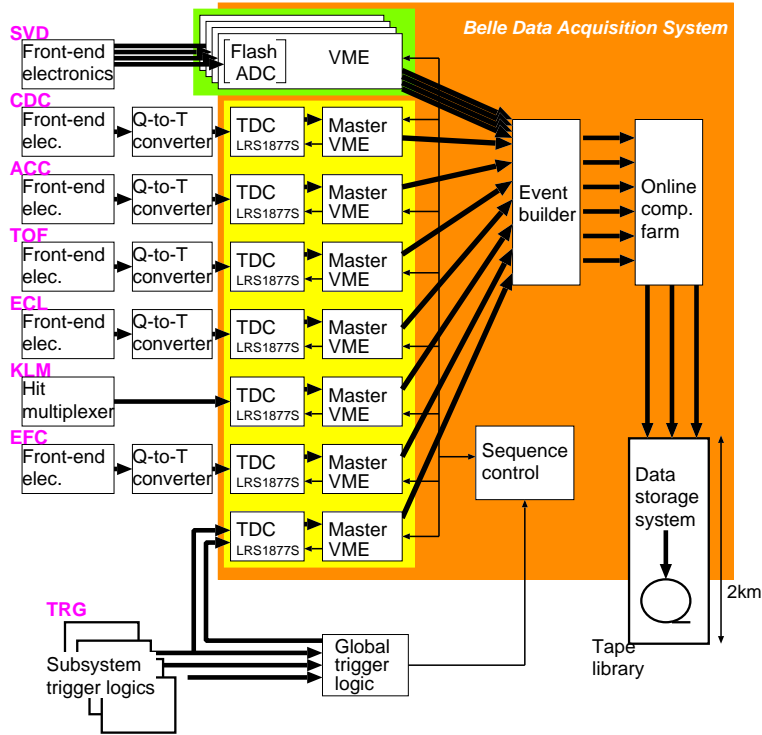


Figure 2.18: Global design of the Belle DAQ system.

are reconstructed with hits in the CDC, then these tracks are extrapolated towards the IP to search for associated SVD hits. They are also extrapolated outwards to search for hits in the outer detectors.

2.6 Offline Software and Computing

The data obtained from each of the sub-detectors are in the form of hits and times (Raw Data). They are converted into physics objects, for example, 4-vectors of position (x_μ), momentum (p_μ) and associated particle identification information [32]. The events are then classified into several categories based upon certain selection criteria according to physics interest and are stored as skimmed data. Based on those data, detector calibrations are carried out in detail and the offline luminosity is computed. The analysis described in this thesis uses the HadronB sample [33], a data skim optimized for B meson physics studies. In physics analyses, one does not need require the complete information stored in DST. Since collaborators need to process a large amount of data, easy access to experimental

data is highly desirable. For this purpose, data are stored in MDST (Minimal sets of Data Summary Tape) format, which is compact and sufficient to study physics events.

The event processing framework, called the Belle Analysis Framework (BASF) [34], takes users' reconstruction and analysis codes as modules, which are dynamically linked at run time. A module is written as an object on a class of C++. The class, inherited from the module class of BASF that has virtual functions for events, also includes begin and end run processing and other utility functions such as initialization, termination, and histogram definitions.

Monte Carlo (MC) simulations play an important role in physics analysis. We use the EvtGen program [35] to generate events for specific decay channels. The response of the Belle detector is modeled by a GEANT3-based full-simulation program [35]. The simulated events are then reconstructed and analyzed with the same procedure as is used for the real data. The standard reconstruction module for subdetectors, global reconstruction of four momenta and likelihoods for specific particle hypothesis such as electrons, muons, pions, kaons, are prepared. Using this information, reconstruction codes are written to identify specific decay channels and to produce physics results such as those described in this thesis.

Chapter 3

Measurements of time-dependent CP violation in $B^0 \rightarrow \psi(2S)K_S^0$

3.1 Introduction

In this chapter, we describe the measurements of time-dependent CP violation parameters for $B^0(\bar{B}^0)$ decays to the CP -eigenstate $\psi(2S)K_S^0$. The $\psi(2S)$ candidates are reconstructed via the decay modes: $\psi(2S) \rightarrow l^+l^-$ and $\psi(2S) \rightarrow J/\psi(l^+l^-)\pi^+\pi^-$, where l is either an electron or a muon. The methods for background rejection and signal extraction are described in detail. One neutral B meson is reconstructed in the $\psi(2S)K_S^0$ decay channel, and the flavor of the accompanying B meson is identified from its decay products. We then reconstruct the decay vertex positions of both the B mesons and determine the CP violation parameters from the asymmetries in the distributions of the proper-time intervals.

3.2 Hadronic Event Selection

This analysis is based on a 605 fb^{-1} data sample, which contains $657 \times 10^6 B\bar{B}$ pairs collected with the Belle detector at the $\Upsilon(4S)$ resonance [36]. This corresponds to experimental datasets 07 to 55, collected from January 2000 to December 2006. We apply the following selection criteria [33] to select hadronic events and to suppress contamination from τ pair production, two photon processes, QED processes including Bhabha and radiative Bhabha processes as well as beam gas processes. The selected data sample after all these cuts is known as the HadronB sample. We define charged tracks as good tracks that satisfy the requirements $|dr| < 2.0 \text{ cm}$, $|dz| < 4.0 \text{ cm}$ and $P_t > 0.1 \text{ GeV}/c$, where dr , dz , and P_t

represent the impact parameters to the nominal interaction point in the x - y plane, along the z -axis and the transverse momentum, respectively. Good clusters are defined as clusters in the ECL with energies greater than 100 MeV. Good photons are defined as good clusters that cannot be associated with tracks in the CDC acceptance ($17^\circ < \theta < 150^\circ$). In addition, we apply the following hadronic event selection requirements.

- The number of good charged tracks is required to be greater than two, $N_{\text{track}} \geq 3$.
- The number of good clusters in the barrel region of the ECL is required to be greater than one, $N_{\text{ECL}} > 1$.
- The visible energy, E_{vis} , which is the sum of good track momenta and good photon energies is required to satisfy $E_{\text{vis}} \geq 0.2\sqrt{s}$, where \sqrt{s} represents the center-of-mass (cms) energy.
- The energy sum of the good ECL clusters in the central barrel section of the ECL, E_{sum} is required to satisfy $0.1 < E_{\text{sum}}/\sqrt{s} < 0.8$.
- The vector sum of the z momenta of all good tracks and good photons is required to be $|P_z| < 0.5\sqrt{s}$.
- The distance between the primary event vertex and the beam spot is required to be smaller than 1.5 cm in the x - y plane, and smaller than 3.5 cm in the z direction.
- Either the energy sum of all ECL clusters is required to be greater than $0.18\sqrt{s}$, or the heavy jet mass is required to be greater than 1.8 GeV.
- The heavy jet mass is required to be greater than either $0.25 E_{\text{vis}}$ or 1.8 GeV.
- The average cluster energy is required to be smaller than 1.0 GeV.

These selection criteria retain more than 99% of $B\bar{B}$ events while reducing the contamination from non-hadronic processes to less than 5%.

3.3 Signal Reconstruction

The signal is reconstructed in the decay $B^0 \rightarrow \psi(2S)K_S^0$, where the $\psi(2S)$ meson decays in the l^+l^- ($l = e$ or μ) and $J/\psi\pi^+\pi^-$ decay channel. Intermediate states are

reconstructed in the following modes: $J/\psi \rightarrow l^+l^-$ and $K_S^0 \rightarrow \pi^+\pi^-$. We use the decay mode $B^\pm \rightarrow \psi(2S)K^\pm$ as a control sample to calibrate the signal shape and for the CP study. All the charged tracks used in the reconstruction (except for charged pions from K_S^0 's) are required to satisfy a requirement on the distance of closest approach to the interaction point (IP) along the beam direction $|dz| < 5$ cm and in the transverse direction $dr < 1.5$ cm. This eliminates poorly reconstructed tracks or tracks that do not come from the interaction region.

3.3.1 Reconstruction of J/ψ and $\psi(2S)$ from di-leptons

The candidate J/ψ and $\psi(2S)$ mesons are reconstructed using their decays to lepton pairs (where the lepton pairs are either e^+e^- or $\mu^+\mu^-$ pairs).

- Dielectron Reconstruction

We identify the electron candidates using the likelihood ratio $\mathcal{L}_{\text{eid}} > 0.01$, which is an electron likelihood probability calculated from the light yield in the ACC, the time of flight (TOF) and the ionization loss (dE/dx) in drift chamber (CDC). In order to increase the reconstruction efficiency, we also use less restrictive requirements for one of the two tracks. One of the tracks is identified using $\mathcal{L}_{\text{eid}} > 0.01$ and the other with $E/p > 0.5$ or $dE/dx > 0.5$, but with no \mathcal{L}_{eid} requirement. Here E/p is the ratio of energy measured by the calorimeter and momentum measured by drift chamber. To take into account final state radiation, we include the bremsstrahlung photons that are within 50 mrad of the e^+e^- tracks having energy less than 3.5 GeV. Due to the radiative tail we use an asymmetric invariant mass window $-0.150 \text{ GeV}/c^2 < M_{e^+e^-(\gamma)} - m_{J/\psi(\psi(2S))} < +0.036 \text{ GeV}/c^2$ to select the J/ψ and $\psi(2S)$ candidates (Fig. 3.1), where $m_{J/\psi(\psi(2S))}$ is the world-average mass [20].

- Dimuon Reconstruction

We identify the dimuons as follows. Either both the tracks satisfy the requirement $\mathcal{L}_{\text{muid}} > 0.1$ or one track satisfies this requirement and the other one should have energy measured by ECL between 0.1 to 0.3 GeV. Since the $\mu^+\mu^-$ radiative tail is smaller, we select $-0.060 \text{ GeV}/c^2 < M_{\mu^+\mu^-(\gamma)} - m_{J/\psi(\psi(2S))} < +0.036 \text{ GeV}/c^2$ (Fig. 3.1).

Using these loose selection criteria, we have nearly a 6% gain in efficiency for modes with electrons and 12% for modes with muons relative to tight selection criteria (when both the daughters are positively identified as leptons).

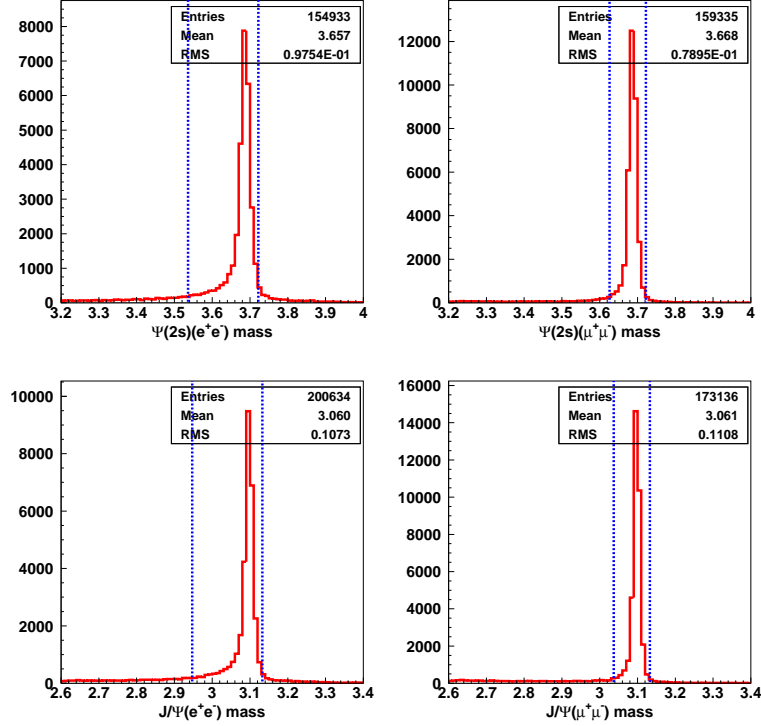


Figure 3.1: Invariant mass of $\psi(2S)$ and J/ψ candidates from dileptons. The corresponding mass cuts are shown by vertical blue lines.

3.3.2 K_S^0 Reconstruction

Neutral kaon (K_S^0) candidates are formed from $\pi^+\pi^-$ combinations with the invariant mass of the pion pair required to lie in the range $0.482 \text{ GeV}/c^2 < M_{\pi^+\pi^-} < 0.514 \text{ GeV}/c^2$ (Fig. 3.2). The selected candidates must pass a set of momentum-dependent requirements [37] on impact parameter, vertex displacement, mismatch in the z direction, and the direction of the pion pair momentum as described below (and given in Table 3.1).

- dr : This is the smaller of dr_1 and dr_2 , which are the distances of closest approach to the IP from the two tracks in the x - y plane.

Table 3.1: The K_S^0 selection criteria in three momentum ranges.

Momentum (GeV)	dr (cm)	$d\phi$ (rad)	z dist (cm)	f_l (cm)
< 0.5	> 0.05	< 0.3	< 0.8	-
0.5-1.5	> 0.03	< 0.1	< 1.8	> 0.08
> 1.5	> 0.02	< 0.03	< 2.4	> 0.22

- $d\phi$: This is the azimuthal angle between the momentum vector and the decay vertex vector of the K_S^0 candidate.
- z dist: This is the distance between the two daughter tracks at their intersection point.
- f_l : This is the flight length of the K_S^0 candidate in x - y plane.

3.3.3 Reconstruction of $\psi(2S)$ from $J/\psi\pi^+\pi^-$

The $\psi(2S)$ meson is also reconstructed via its $J/\psi\pi^+\pi^-$ decay. For this submode the selection is based upon the mass difference cut $0.58 \leq M_{l+l-\pi^+\pi^-} - M_{l+l-} \leq 0.60$ GeV/ c^2 . We select $\pi^+\pi^-$ pairs with an invariant mass greater than 400 MeV/ c^2 (Fig. 3.2).

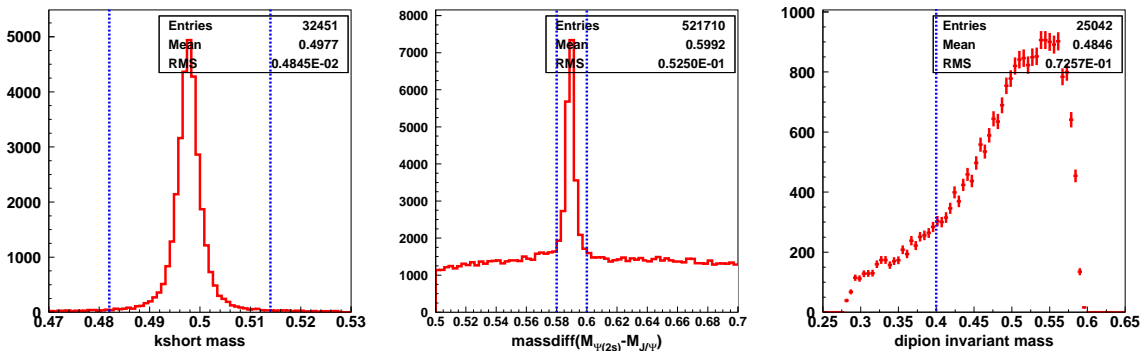


Figure 3.2: The mass distributions from signal MC for K_S^0 , mass difference ($M_{\psi(2S)} - M_{J/\psi}$) (middle) and dipion invariant mass (right). The corresponding mass cuts are shown by vertical blue lines.

3.3.4 B Candidate Selection

We combine the $\psi(2S)$ and K_S^0 to form a neutral B meson. The B candidates are identified using two kinematic variables: the energy difference (ΔE) and beam-energy-constrained mass (M_{bc}), defined as

$$\Delta E \equiv E_B^{\text{cms}} - E_{\text{beam}}^{\text{cms}}, \quad M_{bc} \equiv \sqrt{(E_{\text{beam}}^{\text{cms}})^2 - (p_B^{\text{cms}})^2} \quad (3.3.1)$$

where $E_{\text{beam}}^{\text{cms}}$ is the beam energy in the cms (half of the energy of the $\Upsilon(4S)$), and E_B^{cms} and p_B^{cms} are the cms energy and momentum, respectively, of the reconstructed B candidate. For a correctly reconstructed B candidate, ΔE will peak at zero and M_{bc} will peak at the nominal B mass. The M_{bc} resolution is dominated by E_{beam} and is about 3 MeV. The ΔE resolution is highly sensitive to the momentum of the final state particles. In order to improve the ΔE resolution, the masses of the selected J/ψ and $\psi(2S)$ candidates are constrained to their nominal masses using mass-constrained kinematic fits. From signal MC study, it is found that $\sim 1\%$ of events have more than one B candidate. For those events having multiple candidates, we select the best candidate with smallest mass $\chi^2 (= \chi_\psi^2 + \chi_{K_S}^2 + \chi_{\Delta M}^2)$ given by

$$\chi_\psi^2 = \left(\frac{M_{l+l^-} - M_{\psi(\text{nominal})}}{\sigma} \right)^2 \quad (3.3.2)$$

where σ is the resolution of the corresponding mass distribution as listed in Table 3.2. The candidates that satisfy the requirements $M_{bc} > 5.2 \text{ GeV}/c^2$ and $|\Delta E| < 0.1 \text{ GeV}$ (defined as the fit region) are selected for further analysis. For the CP asymmetry fit, we select the candidates in the ΔE - M_{bc} signal region defined as $|\Delta E| < 0.03 \text{ GeV}$ and $5.27 \text{ GeV}/c^2 < M_{bc} < 5.29 \text{ GeV}/c^2$.

Table 3.2: Typical resolutions in the mass distributions, ΔE and M_{bc} from signal MC for the $B^0 \rightarrow \psi(2S)K_S^0$ decay mode.

Decay Modes	Resolution (MeV)					
	J/ψ mass	$\psi(2S)$ mass	K_S^0 mass	ΔM	ΔE	M_{bc}
$\psi(2S) \rightarrow e^+e^-$	-	13.2	2.8	-	8.8	2.8
$\psi(2S) \rightarrow \mu^+\mu^-$	-	17.4	2.7	-	7.1	2.8
$\psi(2S) \rightarrow J/\psi(\rightarrow e^+e^-)\pi^+\pi^-$	10.8	-	2.9	2.9	9.6	2.9
$\psi(2S) \rightarrow J/\psi(\rightarrow \mu^+\mu^-)\pi^+\pi^-$	13.1	-	2.9	2.5	8.3	2.7

3.3.5 Reconstruction Efficiency

We generate events for signal MC using the EvtGen program. A GEANT-based simulation [35] of the Belle detector is used to produce signal Monte Carlo (MC) event samples. The reconstruction efficiency (ϵ) is defined as

$$\epsilon = \frac{\text{MC signal yield}}{\text{Number of generated events}} \quad (3.3.3)$$

The signal yield is determined by fitting the ΔE and M_{bc} distributions. We fit the ΔE distribution with a sum of double Gaussian and a first order Chebyshev polynomial. For the M_{bc} distribution, we use a sum of Gaussian and ARGUS functions [38]. The scatter plot of ΔE and M_{bc} together with their projections onto each axis is shown in Fig. 3.3. Since the self cross-feed (SCF) background (random combinations of final state tracks from the other B with part of the signal) is small ($\sim 1\%$), it is included in the signal while fitting.

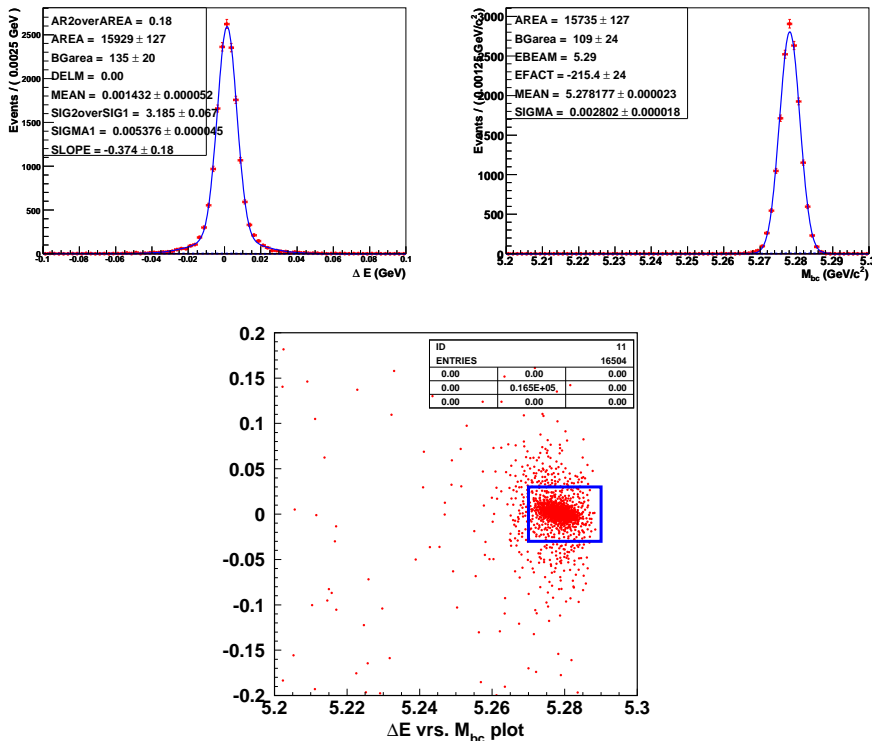


Figure 3.3: ΔE , M_{bc} distributions and 2D scatter plot of ΔE versus M_{bc} from signal MC for $B^0 \rightarrow \psi(2S)K_S^0$ decay mode. The signal box is shown in blue rectangle.

After December 2006, Belle recorded additional datasets exp61-65 [36] at the $\Upsilon(4S)$ resonance. Furthermore, the tracking algorithm has been significantly improved

for the SVD2 dataset (exp31-65). The experimental dependence of reconstruction efficiency for $B^0 \rightarrow \psi(2S)K_S^0$ mode is shown in Fig. 3.4. It is clear that we have a nearly 16% gain in efficiency for $\psi(2S)(ll)K_S^0$ modes and 27% for $\psi(2S)(J/\psi\pi\pi)K_S^0$ modes. The larger gain in efficiency for $J/\psi\pi\pi$ modes is due to low momentum tracks in the final state. In the control sample, we have nearly a 5% gain in efficiency for $\psi(2S)(ll)K^+$ modes and 15% for $\psi(2S)(J/\psi\pi\pi)K^+$ modes. The selection efficiencies for each sub-decay mode are listed in Table 3.3 for the $B^0 \rightarrow \psi(2S)K_S^0$ mode and in Table 3.4 for the $B^+ \rightarrow \psi(2S)K^+$ mode. We determine the efficiencies separately for three different datasets: SVD1 (exp07-27), SVD2a (exp31-55) and SVD2b (exp61-65). We also checked that the efficiency from ΔE fits is comparable with that from M_{bc} fits and for muons it is 1.2 times higher than electrons.

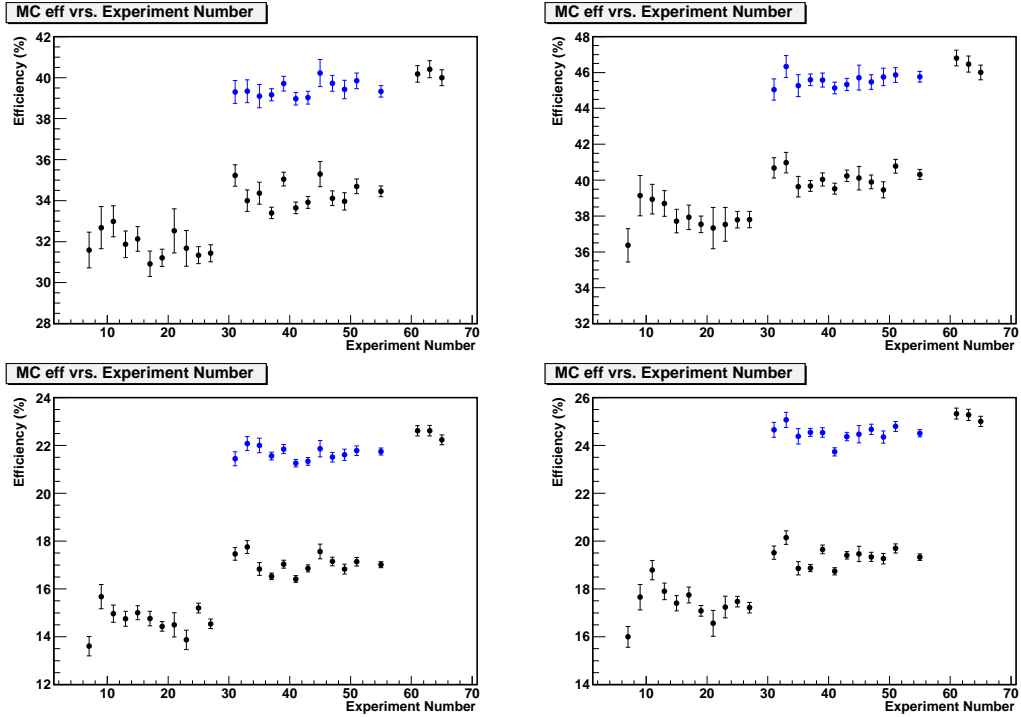


Figure 3.4: The experimental dependence of reconstruction efficiency for $B^0 \rightarrow \psi(2S)K_S^0$ mode. The blue points correspond to the SVD2 dataset (exp31-55) with new tracking. Upper left for e^+e^- , upper right for $\mu^+\mu^-$, lower left for $J/\psi(e^+e^-)\pi^+\pi^-$, lower right for $J/\psi(\mu^+\mu^-)\pi^+\pi^-$.

Table 3.3: Reconstruction efficiency from signal MC for the $B^0 \rightarrow \psi(2S)K_S^0$ mode.

Decay Mode	Reconstruction Efficiency (%)		
	SVD1	SVD2a	SVD2b
$\psi(2S) \rightarrow e^+e^-$	31.9 ± 0.2	34.3 ± 0.1	40.0 ± 0.2
$\psi(2S) \rightarrow \mu^+\mu^-$	38.1 ± 0.2	40.1 ± 0.1	46.1 ± 0.2
$\psi(2S) \rightarrow J/\psi(\rightarrow e^+e^-)\pi^+\pi^-$	14.7 ± 0.1	16.9 ± 0.1	22.5 ± 0.1
$\psi(2S) \rightarrow J/\psi(\rightarrow \mu^+\mu^-)\pi^+\pi^-$	17.4 ± 0.1	19.3 ± 0.1	25.2 ± 0.1

Table 3.4: Reconstruction efficiency from signal MC for the control sample ($B^+ \rightarrow \psi(2S)K^+$).

Decay Mode	Reconstruction Efficiency (%)		
	SVD1	SVD2a	SVD2b
$\psi(2S) \rightarrow e^+e^-$	41.0 ± 0.2	42.0 ± 0.1	45.2 ± 0.2
$\psi(2S) \rightarrow \mu^+\mu^-$	48.6 ± 0.2	49.1 ± 0.1	52.3 ± 0.1
$\psi(2S) \rightarrow J/\psi(\rightarrow e^+e^-)\pi^+\pi^-$	19.7 ± 0.1	21.7 ± 0.1	25.7 ± 0.1
$\psi(2S) \rightarrow J/\psi(\rightarrow \mu^+\mu^-)\pi^+\pi^-$	23.0 ± 0.1	24.6 ± 0.1	28.9 ± 0.1

3.4 Background Suppression

The background sources are classified according to the physical processes involved. There are backgrounds from $e^+e^- \rightarrow q\bar{q}$ ($q = u, d, s$ or c) continuum events. These events are jet-like in contrast to the spherical $B\bar{B}$ signal. We suppress them by using the event-shape variable, $R_2 < 0.5$, where R_2 is the ratio of second to zeroth Fox-Wolfram moments [39]. The backgrounds from B decays are analysed using inclusive J/ψ and $\psi(2S)$ MC samples, which are equivalent to 100 times exp07-41 (100 times 388×10^6 $B\bar{B}$ pairs, or equivalently 59 times the exp07-55 data sample) [40]. We identified the main background modes by using the MC truth information. The backgrounds having the same final state as the signal, peak in the ΔE - M_{bc} signal box, hence are known as peaking backgrounds. The other backgrounds, which have more (less) tracks than the signal mode shift towards lower (higher) ΔE . The type of backgrounds that involve random or wrongly reconstructed combinations of the final state particles are known as combinatorial backgrounds.

- $B^0 \rightarrow \psi(2S)K_S^0, \psi(2S) \rightarrow l^+l^-$

In this case the background is mainly dominated by the decay mode $B \rightarrow \psi(2S)K^*(892)$ where $\psi(2S) \rightarrow l^+l^-$. In the neutral B case, $K^{*0} \rightarrow K_S^0\pi^0$ (upper plot in Fig. 3.5) and the charged B case, $K^{*+} \rightarrow K_S^0\pi^+$ (lower plot in Fig. 3.5). These events are reconstructed as $B \rightarrow \psi(2S)K$ signal when the additional pion is not detected. This background peaks around -0.18 GeV, which is quite well separated from the lower range of the ΔE signal region while in M_{bc} there are no peaking backgrounds.

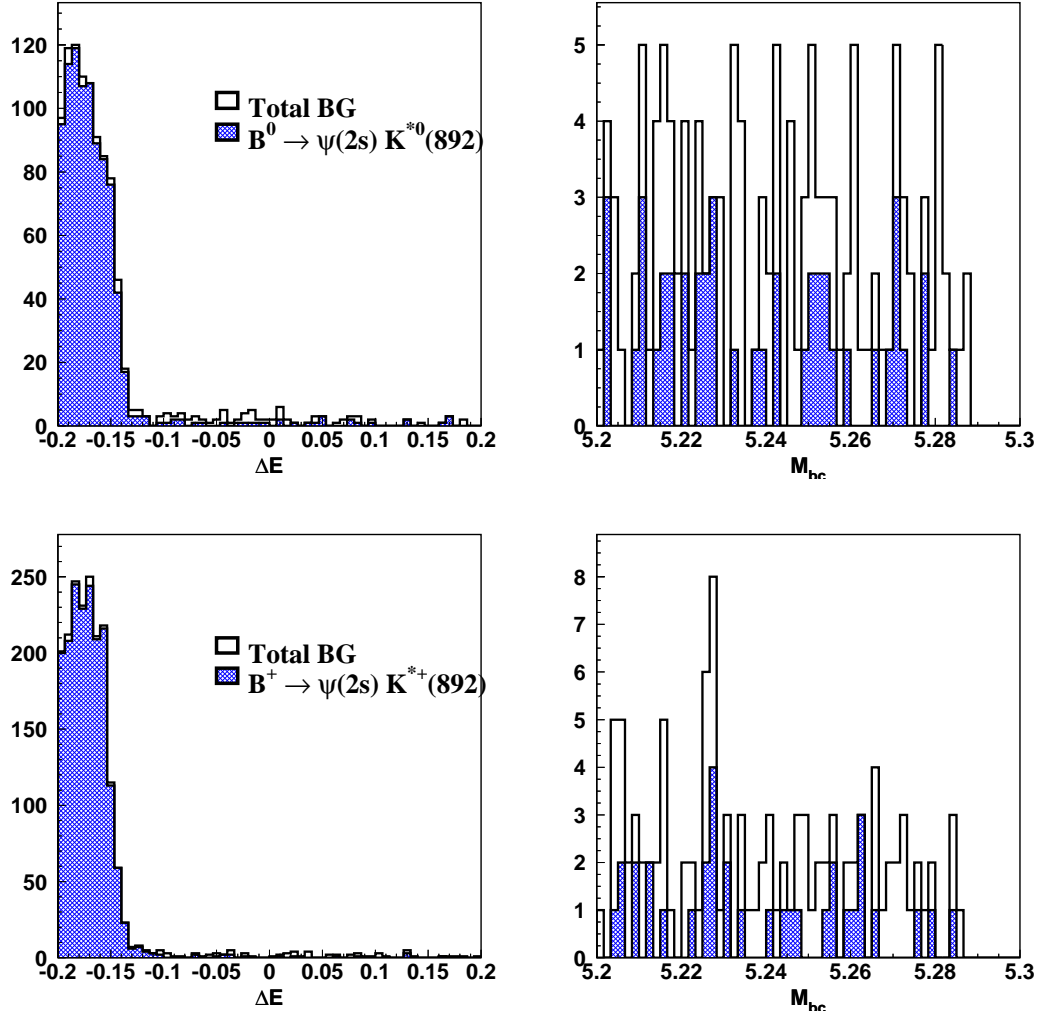


Figure 3.5: Background from neutral B (upper) and charged B mesons (lower) for $B^0 \rightarrow \psi(2S)(e^+e^-)K_S^0$ decay.

- $B^0 \rightarrow \psi(2S)K_S^0$, $\psi(2S) \rightarrow J/\psi\pi^+\pi^-$, $J/\psi \rightarrow l^+l^-$

In this decay chain, the background is from decays having the same final state and peaks in ΔE and M_{bc} . The peaking background is mainly due to $B^0 \rightarrow J/\psi K_1^0(1270)$, $B^0 \rightarrow J/\psi K^{*-}(892)\pi^+$ and $B^0 \rightarrow J/\psi K^0\pi^+\pi^-$ (as shown in Fig. 3.6). All these backgrounds peak in the ΔE - M_{bc} signal region. It should be noted that even if all these modes have same final state, they do not peak at the $\psi(2S)$ mass, hence we can determine them from the sidebands of the mass difference plot. The number of events found in the signal box (counting) in inclusive MC sample are listed in Table 3.5. The shape of the peaking background in ΔE is well described by the sum of a single Gaussian and a first order Chebyshev polynomial while that in M_{bc} can be parameterized by a single Gaussian and an ARGUS shape as shown in Fig. 3.7. From MC study, this background is very small compared to the signal yield ($\sim 3\%$). Furthermore, as described in section 3.5.1, the peaking background is overestimated as compared to data. In the charged B case, the main background comes from $B^+ \rightarrow \psi(2S)K^{*+}(892)$ decay, which peaks in a lower range, -0.18 GeV, in the ΔE distribution while in M_{bc} there is no peaking background.

Table 3.5: Individual background modes in the signal region for $B^0 \rightarrow \psi(2S)K_S^0$ mode determined from mixed $\psi(2S)$ MC.

Decay Modes	Events in data within the signal box (counting)	
	$J/\psi(\rightarrow e^+e^-)\pi^+\pi^-$	$J/\psi(\rightarrow \mu^+\mu^-)\pi^+\pi^-$
$B^0 \rightarrow J/\psi K^0 \pi^+ \pi^-$	5.24	5.24
$B^0 \rightarrow J/\psi K_1^0(1270)$	4.02	4.12
$B^0 \rightarrow \psi(2S)(J/\psi \pi^0\pi^0) K_S^0$	3.76	4.08
$B^0 \rightarrow J/\psi K^{*-}(892) \pi^+$	3.29	3.97
$B^0 \rightarrow \psi(2S)(J/\psi \eta) K_S^0$	1.12	1.25
$B^0 \rightarrow J/\psi K^0 \rho^0(770)$	0.73	0.95
$B^0 \rightarrow J/\psi K^{*0}(892)$	0.58	0.59
$B^0 \rightarrow J/\psi K_2^{*0}(1430)$	0.41	0.41
$B^0 \rightarrow J/\psi K^0 \pi^0 \pi^0$	0.36	0.24
$B^0 \rightarrow \psi(2S) K^{*0}(892)$	0.2	0.12
TOTAL Events	19.69	21.15

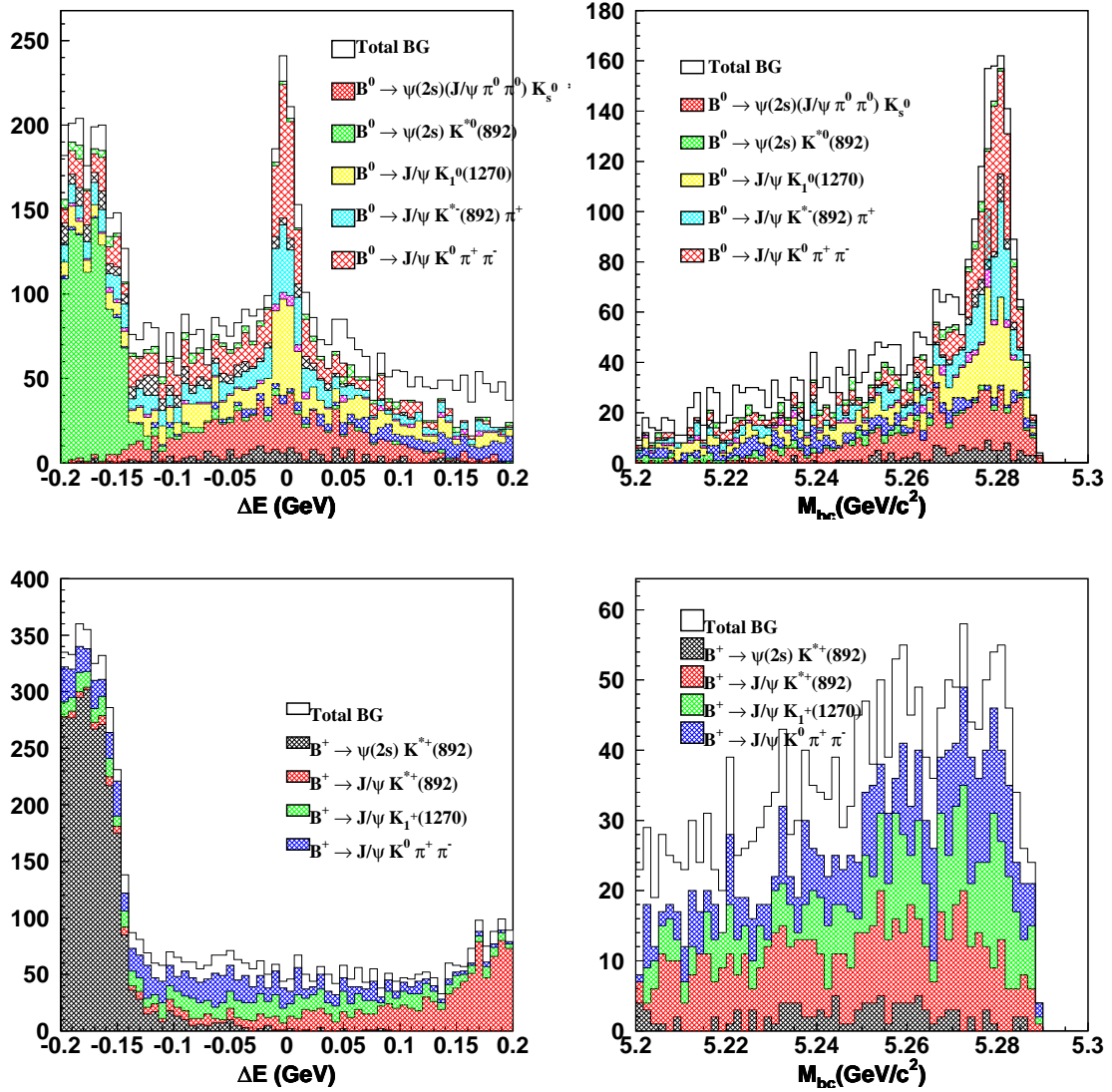


Figure 3.6: Backgrounds from neutral B (upper) and charged B mesons (lower) for $B^0 \rightarrow \psi(2S)(J/\psi(e^+e^-)\pi^+\pi^-)K_S^0$ decay.

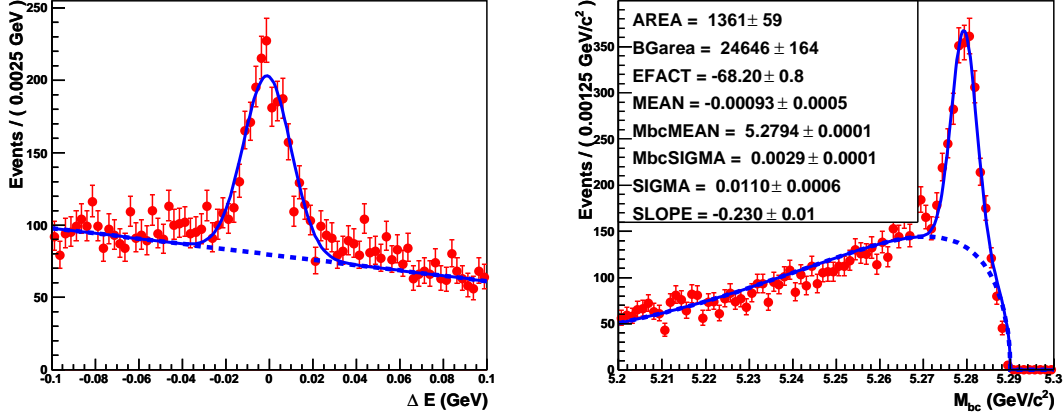


Figure 3.7: Parameterization of peaking backgrounds in the signal region.

3.5 Mass Difference Sideband Study

To check the MC prediction of peaking backgrounds, we look at the ΔE and M_{bc} distributions from mass difference ($M_{\psi(2S)-J/\psi}$) sidebands. We consider six sideband regions (as shown in Fig. 3.8 with the corresponding values in Table 3.6), each having the same width as the signal region (0.02 GeV). A mass-constrained fit is applied separately to each sideband by constraining to the center of the region considered. This is done in order to treat the backgrounds from sidebands in a similar way as in the signal region. While fitting the data sideband, we fixed the mean, sigma of the Gaussian from the inclusive MC sideband, while the slope of the polynomial and the shape parameter of the ARGUS function were floated. Table 3.7 summarizes the backgrounds from the MC signal region, MC sideband and data sideband (determined from 2D fit as shown in Fig. 3.9). MC (no signal) is scaled 59 times, MC (sideband) is scaled 59×6 times for comparison with data and the data sideband is scaled 6 times.

Table 3.6: The six sideband regions in the mass difference plot. The units are in GeV.

Left sideband			Signal region	Right sideband		
0.51-0.53	0.53-0.55	0.55-0.57	0.58-0.60	0.61-0.63	0.63-0.65	0.65-0.67

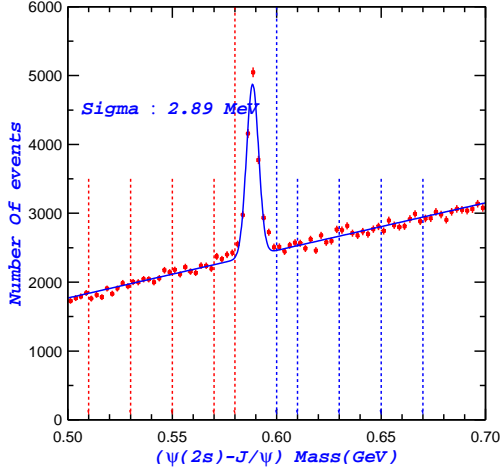


Figure 3.8: Mass difference plot showing six sideband regions.

Decay Mode	Background events		
	Inclusive MC (no signal)	Inclusive MC (sideband)	data (sideband)
$B^\pm \rightarrow \psi(2S)K^\pm$	66 ± 2	48 ± 0.6	24 ± 4
$B^0 \rightarrow \psi(2S)K_S^0$	23 ± 1	17 ± 0.3	7 ± 2

Table 3.7: Background estimated from mass difference sidebands.

3.5.1 Discrepancy between MC and data sidebands

There is a discrepancy between MC (sideband) and data (sideband). We have nearly two times higher yield from MC sidebands as compared to data sidebands as shown in Table 3.7. The value $\mathcal{B}(J/\psi K^0 \pi^+ \pi^-) = (10 \pm 0.4) \times 10^{-4}$ [41] was measured by CDF and includes contributions from other decay modes, such as $J/\psi K_1(1270)$, $J/\psi K^* \pi$, $J/\psi K^0 \rho^0$ and $J/\psi K^0 \pi^+ \pi^- (\text{NR})$. We assumed in the Belle MC simulation that $\mathcal{B}(J/\psi K^0 \pi^+ \pi^-)_{CDF} = \mathcal{B}(J/\psi K^0 \rho^0) + \mathcal{B}(J/\psi K^0 \pi^+ \pi^-) (\text{NR})$. In addition, there is one typographical error in the decay table: $\mathcal{B}(J/\psi K^0 \pi^+ \pi^-)$ appears twice ($0.00046 + 0.00066$) whereas $\mathcal{B}(J/\psi \bar{K}^0 \pi^+ \pi^-)$ appears only once (0.00046). Taking all these factors into account the MC is overestimated by a factor of two compared to data, which is verified by examining the sidebands in MC and data (Table 3.7).

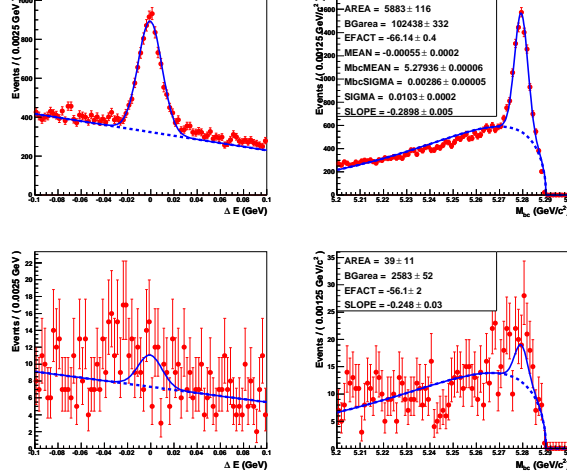


Figure 3.9: ΔE and M_{bc} projections from the sideband for the $B^0 \rightarrow \psi(2S)K_S^0$ mode. The upper plot is from the MC sideband and the lower one is from data.

3.6 Branching Fraction Checks

For a cross-check, we calculated the branching fractions for each of the sub-decay modes using the yield from inclusive $B \rightarrow J/\psi X$ MC. The values obtained were consistent with the values used in the decay table ($\mathcal{B}(B^0 \rightarrow \psi(2S)K^0) = 6.2 \times 10^{-4}$ and $\mathcal{B}(B^\pm \rightarrow \psi(2S)K^\pm) = 6.8 \times 10^{-4}$). Tables 3.8 and 3.9 summarizes the efficiency, yield (from the M_{bc} fit) and branching fraction using a data sample containing 535×10^6 $B\bar{B}$ pairs. Note that the results in the Tables 3.8 and 3.9 do not include corrections for differences between data and MC in PID efficiencies.

Table 3.8: Efficiency, Yield and Branching fractions (\mathcal{B}) calculated for $B^+ \rightarrow \psi(2S)K^+$ mode using a data sample containing 535×10^6 $B\bar{B}$ pairs.

Decay Mode	Efficiency (%)	Yield	\mathcal{B} (10^{-4})
$\psi(2S) \rightarrow e^+e^-$	41.8 ± 0.1	1065.0 ± 34.4	6.33 ± 0.21
$\psi(2S) \rightarrow \mu^+\mu^-$	49.0 ± 0.1	1278.9 ± 38.0	6.51 ± 0.19
$\psi(2S) \rightarrow J/\psi(\rightarrow e^+e^-)\pi^+\pi^-$	21.2 ± 0.1	1331.6 ± 38.6	6.06 ± 0.18
$\psi(2S) \rightarrow J/\psi(\rightarrow \mu^+\mu^-)\pi^+\pi^-$	24.2 ± 0.1	1496.3 ± 40.9	5.98 ± 0.16

Table 3.9: Efficiency, Yield and Branching fractions (\mathcal{B}) calculated for $B^0 \rightarrow \psi(2S)K^0$ mode using a data sample containing $535 \times 10^6 B\bar{B}$ pairs.

Decay Mode	Efficiency (%)	Yield	\mathcal{B} (10^{-4})
$\psi(2S) \rightarrow e^+e^-$	33.7 ± 0.1	240.5 ± 16.0	5.13 ± 0.34
$\psi(2S) \rightarrow \mu^+\mu^-$	39.6 ± 0.1	299.3 ± 18.3	5.44 ± 0.33
$\psi(2S) \rightarrow J/\psi(\rightarrow e^+e^-)\pi^+\pi^-$	16.4 ± 0.1	243.6 ± 16.5	4.14 ± 0.28
$\psi(2S) \rightarrow J/\psi(\rightarrow \mu^+\mu^-)\pi^+\pi^-$	18.9 ± 0.1	281.9 ± 18.2	4.16 ± 0.27

3.7 $B^0 \rightarrow \psi(2S)K_S^0$ Signal Extraction

The signal yield is obtained from an extended unbinned maximum-likelihood fit to the two dimensional ΔE - M_{bc} distribution ($-0.1 < \Delta E < 0.1$ and $5.2 < M_{bc}$). We use the events that remain after successful vertex reconstruction and flavor tagging as described below.

3.7.1 Vertex Reconstruction

We use the decay chain $\Upsilon(4S) \rightarrow B^0\bar{B}^0 \rightarrow f_{CP}f_{\text{tag}}$, where one of the neutral B meson decays at time t_{CP} to a CP eigenstate f_{CP} (which is $\psi(2S)K_S^0$) and the other decays at time t_{tag} to a flavor specific decay f_{tag} , that distinguishes between B^0 and \bar{B}^0 . Figure 3.10 shows a schematic drawing of the vertex reconstruction of the two B decay vertices.

The vertex position for the f_{CP} decay is reconstructed using two lepton tracks from the $\psi(2S)$ in the decay $\psi(2S) \rightarrow l^+l^-$ and four tracks (the two lepton tracks from J/ψ and the two pions tracks from $\psi(2S)$) in the decay $\psi(2S) \rightarrow J/\psi\pi^+\pi^-$. The pions from K_S^0 decays are not used for vertexing. Each track used in vertex fit is required to have at least one SVD hit [42] in r - ϕ and two hits in the z plane. A constraint on the IP is also used with the selected tracks; the IP profile is convolved with the finite B -flight length in the plane perpendicular to the z axis. This allows us to determine the vertex of the B decay in which only one track satisfies the requirement on SVD hits.

The vertex position of the f_{tag} is reconstructed from all the tracks remaining after the $\psi(2S)K_S^0$ reconstruction. The quantity Δt can be determined from the displacement in z between the two decay vertices: $\Delta t \simeq \Delta z/(\beta\gamma c)$. Since the mass of $\Upsilon(4S)$ is close to

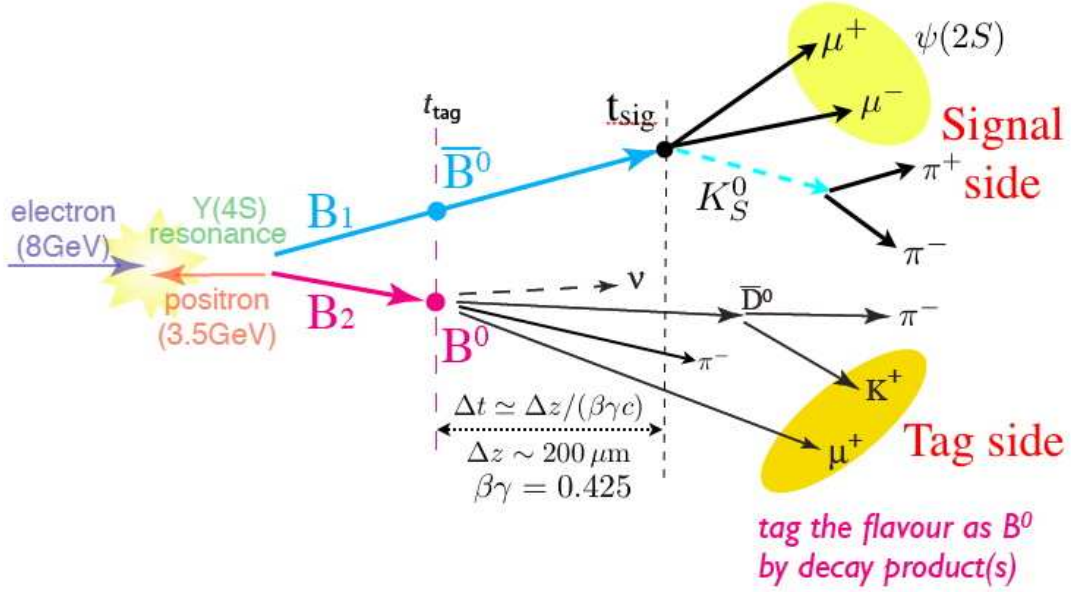


Figure 3.10: Schematic diagram of the vertex reconstruction of the two B decay vertices in the event topology $\Upsilon(4S) \rightarrow B^0\bar{B}^0 \rightarrow f_{CP}f_{\text{tag}}$.

the sum of the two B^0 masses, the produced B mesons are almost at rest in the $\Upsilon(4S)$ cms system. In order to make the Δz displacement measurable, we boost the B mesons using asymmetric e^+e^- beams (3.5 on 8.0 GeV) in the KEKB collider. This produces a Lorentz boost of 0.425 along the z axis, which leads to an average decay length of $\sim 200\mu\text{m}$ of the B mesons in the laboratory frame. This can be measured by a solid state vertex detector with enough resolution. For the CP side, the typical vertex reconstruction efficiency and z resolution are 95% and $78 \mu\text{m}$, respectively [43]. For the tag side, the typical vertex reconstruction efficiency and z resolution are 93% and $140 \mu\text{m}$, respectively [43]. Here the secondary decays of charm have a large effect in the resolution.

3.7.2 Flavor Tagging

After the exclusive reconstruction of a neutral B meson into $\psi(2S)K_S^0$ final state, all the remaining particles should belong to the final state, f_{tag} , the decay of the other B meson. To measure time-dependent CP violation, we need to ascertain whether that decay is $B^0 \rightarrow f_{\text{tag}}$ or $\bar{B}^0 \rightarrow f_{\text{tag}}$. This determination is known as “flavor tagging”. The b -flavor of

the accompanying B meson is identified by a tagging algorithm [44] that categorizes charged leptons, kaons and Λ baryons found in the event. All these inputs are combined, taking their correlations into account, in a way that maximizes the flavor tagging performance. The performance is characterised by two parameters ϵ (raw-tagging efficiency) and w (wrong tag fraction). Here w is the probability that the flavor tagging is wrong and hence a non-zero value of w results in a dilution of the true asymmetry. We use two parameters, q and r , to represent the flavor tagging information. q corresponds to the sign of the b quark charge, where $q = +1$ for B^0 and $q = -1$ for \bar{B}^0 . The parameter r is the event-by-event flavor-tagging dilution factor that ranges from $r = 0$ for no flavor discrimination to $r = 1$ for unambiguous flavor assignment. If $r < 0.1$, the accompanying B meson provides negligible tagging information and we set the wrong tag probability to 0.5. Events with $r > 0.1$ are divided into six r intervals. The seven r -bins are defined as: $0.0 \leq r \leq 0.1$, $0.1 < r \leq 0.25$, $0.25 < r \leq 0.5$, $0.5 < r \leq 0.625$, $0.625 < r \leq 0.75$, $0.75 < r \leq 0.875$, $0.875 < r \leq 1.0$.

3.7.3 Fitting Procedure

We model the shape for the signal component using the product of a double Gaussian for ΔE and a single Gaussian for M_{bc} whereas the combinatorial background is described by the product of a first-order Chebyshev polynomial for ΔE and an ARGUS function for M_{bc} . In the $\psi(2S) \rightarrow l^+l^-$ mode, since the background is displaced from the signal region, it does not affect the signal yield extraction. In the $\psi(2S) \rightarrow J/\psi\pi^+\pi^-$ mode, the peaking background shape and yield is fixed from data sidebands in the $\psi(2S)$ - J/ψ mass difference. We fit the ΔE and M_{bc} distributions from the sidebands and then scale the yield by the corresponding luminosity to determine the peaking background yield. To take into account the different shapes of MC and data, we calculate fudge factors (separately for SVD1 and SVD2) for ΔE parameters (mean, σ and σ_2/σ_1) and M_{bc} parameters (mean, σ) from a data control sample ($B^+ \rightarrow \psi(2S)K^+$). These fudge factor corrections are applied while fitting the $B^0 \rightarrow \psi(2S)K_S^0$ signal. The PDFs used to model the the final fit is shown in the Table 3.10 and ΔE - M_{bc} 2D fit is shown in Fig. 3.11.

1. Signal: Shape parameters are fixed from signal MC with fudge factor corrections applied from $\psi(2S)K^+$.
2. Combinatorial : Floated.

Table 3.10: The PDFs used to model each component in the 2D fit for $B^0 \rightarrow \psi(2S)K_S^0$ mode. The peaking component is only for $J/\psi\pi\pi$ modes.

Component	ΔE	M_{bc}
Signal	double Gaussian	single Gauss
Combinatorial	1st Order Chebyshev	ARGUS
Peaking	single Gauss	single Gauss

3. Peaking: This is only for $J/\psi\pi\pi$ modes. The shape and yield are fixed from mass difference sideband.

Table 3.11 summarizes the signal yield from $\psi(2S)K^\pm$ and $\psi(2S)K_S^0$. In the neutral mode, after all selection criteria are applied, we obtain 1618 and 1202 events for the l^+l^- and $J/\psi\pi^+\pi^-$ modes in the ΔE - M_{bc} fit region defined as $5.2 \text{ GeV}/c^2 < M_{bc} < 5.3 \text{ GeV}/c^2$ and $-0.1 \text{ GeV} < \Delta E < 0.1 \text{ GeV}$, of which 680 and 712, respectively, are in the signal region.

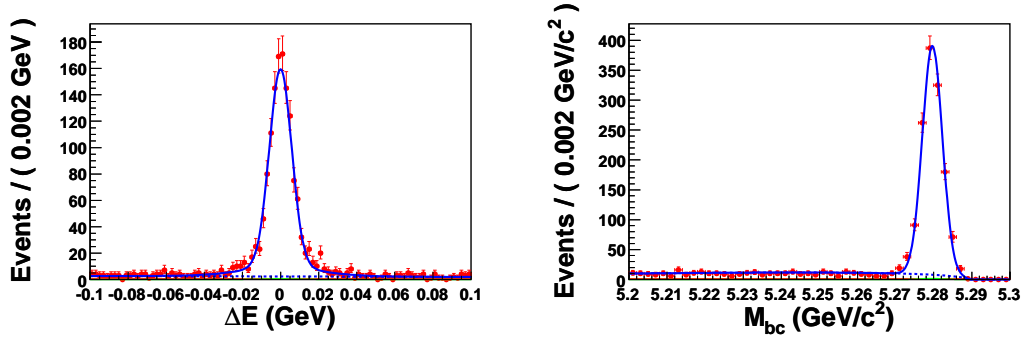


Figure 3.11: ΔE distribution within the M_{bc} signal region, and M_{bc} distribution within the ΔE signal region for $B^0 \rightarrow \psi(2S)K_S^0$ using the $772 \times 10^6 B\bar{B}$ pairs data sample. The solid curves show the fits to the sum of signal and background distributions, while the dashed curves show the background contributions. The purity of the signal is 0.92 ± 0.01 .

3.8 Determination of CP Asymmetries

We determine $\mathcal{S}_{f_{CP}}$ and $\mathcal{A}_{f_{CP}}$ by performing an unbinned maximum-likelihood fit to the observed Δt distribution for the candidate events in the signal region. We maximize

Table 3.11: Signal yield in data for each subsample.

Decay Mode	$\psi(2S) \rightarrow l^+l^-$		$\psi(2S) \rightarrow J/\psi(l^+l^-)\pi^+\pi^-$	
	SVD1	SVD2	SVD1	SVD2
$B^\pm \rightarrow \psi(2S)K^\pm$	592±26	2191±52	756±29	2579±53
$B^0 \rightarrow \psi(2S)K_S^0$	136±12	515±23	146±12	517±23

the log likelihood function ($-2 \log \mathcal{L}$) given by

$$\mathcal{L}(\mathcal{S}_{f_{CP}}, \mathcal{A}_{f_{CP}}) = \prod_i \mathcal{P}_i(\mathcal{S}_{f_{CP}}, \mathcal{A}_{f_{CP}}; \Delta t_i), \quad (3.8.1)$$

where the product is over all events in the signal region. We only use events with vertices that satisfy $|\Delta t| < 70$ ps and $\xi < 250$, where ξ is the χ^2 of the vertex fit calculated only in the z direction. For the time-dependent fit, we use events after successful vertex reconstruction and flavor tagging. Table 3.12 summarizes the number of events found in the signal box ($|\Delta E| < 0.03$ and $5.27 < M_{bc}$) before and after vertexing, flavor tagging and the number of events used for time-dependent fit in data.

Table 3.12: Events in the signal box in data (before and after tagging and vertexing, and for time-dependent fit).

Decay Mode ($B^0 \rightarrow \psi(2S)K_S^0$)	Before V/T	After V/T	TCPV fit
		SVD1	
$\psi(2S) \rightarrow l^+l^-$	160	142	134
$\psi(2S) \rightarrow J/\psi(l^+l^-)\pi^+\pi^-$	165	156	148
	SVD2		
$\psi(2S) \rightarrow l^+l^-$	560	538	523
$\psi(2S) \rightarrow J/\psi(l^+l^-)\pi^+\pi^-$	583	556	495

The time-dependent probability density function (PDF) for the proper-time difference is given by

$$\mathcal{P}(\Delta t) = (1 - f_{ol}) [f_{\text{sig}} \mathcal{P}_{\text{sig}}(\Delta t) + (1 - f_{\text{sig}}) \mathcal{P}_{\text{bkg}}(\Delta t)] + f_{ol} \mathcal{P}_{ol}(\Delta t) \quad (3.8.2)$$

where $\mathcal{P}_{\text{sig}}(\Delta t)$ is the signal PDF and $\mathcal{P}_{\text{bkg}}(\Delta t)$ is the background PDF (consists of two components: combinatorial and peaking). Each of the PDF's is the convolution of a true

PDF with resolution functions to take into account detector effects. Here f_{sig} is the signal fraction, which depends on the r region and is calculated on an event-by-event basis as a function of ΔE and M_{bc} . $\mathcal{P}_{\text{ol}}(\Delta t)$ is the outlier component, which is represented by a single Gaussian with zero mean and event-independent width.

3.8.1 Signal Fraction Estimation

The signal fraction, f_{sig} is calculated in the signal region as a function of ΔE and M_{bc} for each of the reconstructed events. It is described as

$$f_{\text{sig}}(\Delta E, M_{\text{bc}}) = \frac{F_{\text{SIG}}(\Delta E, M_{\text{bc}})}{F_{\text{SIG}}(\Delta E, M_{\text{bc}}) + F_{\text{BG}}(\Delta E, M_{\text{bc}})} \quad (3.8.3)$$

where $F_{\text{SIG}}(\Delta E, M_{\text{bc}})$ is the signal function and $F_{\text{BG}}(\Delta E, M_{\text{bc}})$ is the background function. The signal function F_{SIG} is the product of a double Gaussian in ΔE and a Gaussian in M_{bc} whereas the background function F_{BG} is the product of a linear function in ΔE and an ARGUS function in M_{bc} .

$$F_{\text{SIG}}(\Delta E, M_{\text{bc}}) = P(r) \text{DoubleGauss}(\Delta E; \mu_{\Delta E}, \sigma_{1\Delta E}, R, \sigma_{2\Delta E}) \times \text{Gauss}(M_{\text{bc}}; \mu_{M_{\text{bc}}}, \sigma_{M_{\text{bc}}}) \quad (3.8.4)$$

$$F_{\text{BG}}(\Delta E, M_{\text{bc}}) = (1 - P(r)) \text{Linear}(\Delta E) \times \text{Argus}(M_{\text{bc}}) \quad (3.8.5)$$

where R is the ratio of events in the 2nd Gaussian to total events in the double Gaussian (fixed to 0.15) (both Gaussians have the same mean). $P(r)$ is the r -bin dependent purity obtained from an unbinned maximum likelihood fit. We determine the signal and background events in each r bin by performing a simultaneous fit to all r bins.

3.8.2 Signal PDF

The true signal probability density function for CP fitting is given by

$$\mathcal{P}_{\text{sig}}(\Delta t) = \frac{e^{-|\Delta t|/\tau_B}}{4\tau_B} \left[1 - q\Delta w + q(1 - 2w) \left(\mathcal{S} \sin(\Delta m_d \Delta t) + \mathcal{A} \cos(\Delta m_d \Delta t) \right) \right] \quad (3.8.6)$$

where q is the flavor of B meson. The PDF has been modified from the theoretical distribution in order to incorporate the effect of incorrect flavor assignment. We use b -flavor dependent wrong-tag fraction to accommodate possible differences between B^0 and \overline{B}^0 decays. We determine the average wrong-tag probabilities $w_l \equiv (w_l^+ + w_l^-)/2$ ($l = 1, 2, \dots, 7$) and differences between B^0 and \overline{B}^0 decays, $\Delta w_l \equiv w_l^+ - w_l^-$, where $w_l^{+(-)}$ is the wrong tag probability for $B^0(\overline{B}^0)$ decay in each r interval. The values are listed in Tables 3.14 and

Table 3.13: Signal fractions in individual r -bins for $B^0 \rightarrow \psi(2S)K_S^0$ mode.

$B^0 \rightarrow \psi(2S)K_S^0$	$\psi(2S) \rightarrow l^+l^-$		$\psi(2S) \rightarrow J/\psi(l^+l^-)\pi^+\pi^-$	
	r-bin	SVD1	SVD2	SVD1
1	0.92268	0.92002	0.948252	0.940641
2	0.92817	0.93273	0.918004	0.916089
3	0.93493	0.94100	0.951505	0.951035
4	0.93655	0.93996	0.93647	0.933605
5	0.93165	0.93160	0.944266	0.93855
6	0.94325	0.94226	0.951865	0.946709
7	0.98893	0.98921	0.970893	0.969424

3.15. We use PDG 2006 values for the B^0 lifetime ($\tau_{B^0} = 1.53$ ps) and mixing parameter ($\Delta m_d = 0.507$ ps $^{-1}$).

The signal probability density function for the lifetime fit is given by

$$\mathcal{P}(\Delta t; \tau_B) = \frac{1}{2 \tau_{B^0}} \exp\left(-\frac{|\Delta t|}{\tau_{B^0}}\right) \quad (3.8.7)$$

where τ_{B^0} is a free parameter in the fit.

In order to take into account the effect of Δt smearing due to experimental resolution, \mathcal{P}_{sig} is convoluted with a resolution function (R_{sig}),

$$P_{\text{sig}}(\Delta t) = \int_{-\infty}^{+\infty} d(\Delta t') \mathcal{P}_{\text{sig}}(\Delta t') R_{\text{sig}}(\Delta t - \Delta t') \quad (3.8.8)$$

The event by event resolution function for signal events consists of three components:

- detector resolution due to tracking uncertainty for the reconstructed B_{CP} and B_{tag} vertices.
- smearing on B_{tag} vertices due to non-primary tracks.
- smearing due to the kinematic approximation.

3.8.3 Peaking Background PDF

We also consider the 1% peaking background in $J/\psi\pi^+\pi^-$ modes. The PDF is same as that of signal with \mathcal{S} and \mathcal{A} parameters set to zero.

Table 3.14: Wrong tag fractions, w_l and wrong tag fraction differences, Δw_l in MC for each r -interval.

l	r -interval	SVD1		SVD2	
		w_l	Δw_l	w_l	Δw_l
0	0.000 - 0.100	0.5	0.0	0.5	0.0
1	0.100 - 0.250	0.413653	0.0456694	0.412019	-0.0322979
2	0.250 - 0.500	0.310305	-0.00811093	0.304503	-0.0255096
3	0.500 - 0.625	0.215106	-0.0234073	0.208394	0.0190514
4	0.625 - 0.750	0.151385	-0.00217406	0.149832	0.00594418
5	0.750 - 0.875	0.0934167	-0.00573868	0.0865786	-0.0171155
6	0.875 - 1.000	0.0212698	-0.00115232	0.0243203	0.00400088

Table 3.15: Wrong tag fractions, w_l and wrong tag fraction differences, Δw_l in data for each r -interval.

l	r -interval	SVD1		SVD2	
		w_l	Δw_l	w_l	Δw_l
0	0.000 - 0.100	0.5	0.0	0.5	0.0
1	0.100 - 0.250	0.422837	0.0577827	0.429423	-0.039313
2	0.250 - 0.500	0.336574	0.0124391	0.327273	-0.035766
3	0.500 - 0.625	0.235379	-0.0122602	0.22304	0.0175526
4	0.625 - 0.750	0.166249	-0.0108194	0.160854	0.00232484
5	0.750 - 0.875	0.104922	0.00818429	0.105316	-0.0270618
6	0.875 - 1.000	0.0262446	0.0034784	0.0192838	-0.000737663

3.8.4 Combinatorial Background PDF

The proper-time difference distribution for the background events is obtained from data using the events in the ΔE - M_{bc} background dominated region. We use the sideband ($-0.03 \leq \Delta E \leq 0.2$ GeV) and ($M_{bc} \leq 5.26$ GeV), assuming that the combinatorial background Δt distribution in this region is same as that in the signal box. The region ($-0.2 \leq \Delta E \leq -0.03$) is excluded due to the background from $B \rightarrow \psi(2S)K^*$. The background PDF is modeled as a sum of prompt and exponential components convoluted with a sum of two Gaussians.

$$P_{\text{bkg}}(\Delta t) = (1 - f_{\text{ol}}^{\text{bkg}}) \int_{-\infty}^{\infty} d(\Delta t') \mathcal{P}_{\text{bkg}}(\Delta t') R_{\text{bkg}}(\Delta t - \Delta t') + f_{\text{ol}}^{\text{bkg}} P_{\text{ol}}^{\text{bkg}}(\Delta t) \quad (3.8.9)$$

where

$$\mathcal{P}_{\text{bkg}}(\Delta t) = f_{\delta}^{\text{bkg}} \delta(\Delta t - \mu_{\delta}^{\text{bkg}}) + (1 - f_{\delta}^{\text{bkg}}) \frac{1}{2\tau_{\text{bkg}}} \exp\left(-\frac{|\Delta t - \mu_{\tau}^{\text{bkg}}|}{\tau_{\text{bkg}}}\right) \quad (3.8.10)$$

$$R_{\text{bkg}}(t) = (1 - f_{\text{tail}}^{\text{bkg}}) G\left(t; s_{\text{main}}^{\text{bkg}} \sqrt{\sigma_{\text{rec}}^2 + \sigma_{\text{asc}}^2}\right) + f_{\text{tail}}^{\text{bkg}} G\left(t; s_{\text{tail}}^{\text{bkg}} \sqrt{\sigma_{\text{rec}}^2 + \sigma_{\text{asc}}^2}\right) \quad (3.8.11)$$

$$P_{\text{ol}}^{\text{bkg}}(\Delta t) = G(\Delta t; \sigma_{\text{ol}}^{\text{bkg}}) \quad (3.8.12)$$

We use common background parameters S_{main} , S_{tail} , f_{tail} , f_{δ} , τ_{bg} and $\mu_{\delta}(= \mu_{\tau})$ for multiple and single tracks (since the statistics of the single track sample are small). In the $B^0 \rightarrow J/\psi\pi^+\pi^+$ mode background parameters are common to SVD1 and SVD2. The background parameters obtained from the data sideband are summarized in Table 3.16 and the fit result is shown in Fig. 3.12.

3.8.5 Final PDF for CP fitting

Combining the signal, peaking and combinatorial PDFs, the final PDF is given by

$$\begin{aligned} \mathcal{P}_i &= (1 - f_{\text{ol}}) \int \left[f_{\text{sig}} \mathcal{P}_{\text{sig}}(\Delta t') R_{\text{sig}}(\Delta t_i - \Delta t') \right. \\ &+ f_{\text{peak}} \mathcal{P}_{\text{peak}}(\Delta t') R_{\text{sig}}(\Delta t_i - \Delta t') \\ &+ (1 - f_{\text{sig}} - f_{\text{peak}}) \mathcal{P}_{\text{bkg}}(\Delta t') R_{\text{bkg}}(\Delta t_i - \Delta t') \left. \right] d(\Delta t') \\ &+ f_{\text{ol}} P_{\text{ol}}(\Delta t_i). \end{aligned} \quad (3.8.13)$$

Table 3.16: The background shape parameters from data sideband for the $B^0 \rightarrow \psi(2S)K_S^0$ mode.

Parameter	$\psi(2S) \rightarrow l^+l^-$ (SVD1)	$\psi(2S) \rightarrow l^+l^-$ (SVD2)	$\psi(2S) \rightarrow J/\psi(l^+l^-)\pi^+\pi^-$
S_{main}	2.14 ± 0.42	5.69 ± 1.38	1.71 ± 0.41
S_{tail}	0.44 ± 0.14	0.22 ± 0.05	0.37 ± 0.14
f_{tail}	0.41 ± 0.28	0.89 ± 0.05	0.38 ± 0.25
f_{δ}	0.91 ± 0.10	0.35 ± 0.20	0.31 ± 0.15
τ_{bg}	2.46 ± 1.48	0.72 ± 0.22	1.25 ± 0.19
μ_l	-0.18 ± 0.11	0.02 ± 0.04	-0.03 ± 0.08

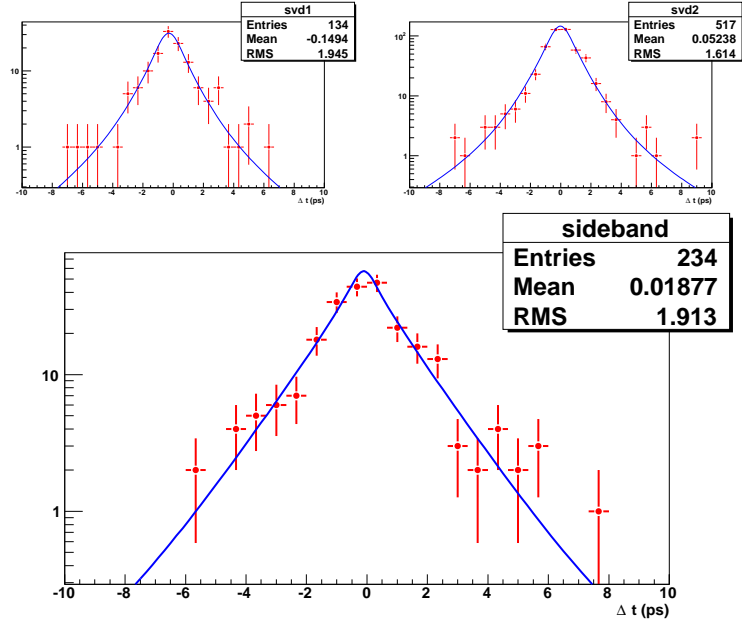


Figure 3.12: The Δt distributions from the ΔE - M_{bc} 2D sideband for $B^0 \rightarrow \psi(2S)K_S^0$ mode. The upper two are for $\psi(2S) \rightarrow l^+l^-$ and the lower one is for $\psi(2S) \rightarrow J/\psi\pi^+\pi^-$.

3.9 Validation Checks

Before proceeding to the CP fit in the final data sample, we did various cross-checks to ensure the reliability of the results.

3.9.1 Cross-check with $J/\psi K_S^0$ fitter

To test our CP fitter, we cross-check with the official $J/\psi K_S^0$ fitter. We obtain $\tau_{B^0} = 1.56 \pm 0.02$ ps from the lifetime fit and $\mathcal{S} = (0.644 \pm 0.038)$, $\mathcal{A} = (-0.001 \pm 0.028)$ for the CP fit using $J/\psi K_S^0$ data. This is based upon the exp07-49 data sample and agrees with the official result.

3.9.2 CP Linearity Test

In order to check for any possible fit biases, we generated GEANT signal MC samples with the input \mathcal{S} value varied in steps of 0.2 from -1 to 1 (while the \mathcal{A} value was fixed to zero). This was done for exp27 with each sample having 50,000 events for the $B^0 \rightarrow \psi(2S)K_S^0$ decay mode. The Fig. 5.7 shows the residuals of the fit results (fitter value - input value). Although there are small statistical fluctuations, no significant bias is observed.

3.9.3 Fit Bias

To check for bias in \mathcal{S} and \mathcal{A} , we generated 500,000 GEANT MC events for $\psi(2S) \rightarrow l^+l^-$ and $\psi(2S) \rightarrow J/\psi(l^+l^-)\pi^+\pi^-$, both in exp27 (SVD1) and exp37 (SVD2). The results of the CP fit are summarized in Table 3.17. In summary, no significant bias is observed even with large statistics (the statistical error is 10 times smaller than that expected in data). The generated value of \mathcal{S} is 0.69.

Table 3.17: Checks for fit bias in \mathcal{S} and \mathcal{A} in signal MC for $B^0 \rightarrow \psi(2S)K_S^0$ mode.

Data Sample	$\psi(2s) \rightarrow l^+l^-$		$\psi(2s) \rightarrow J/\psi(l^+l^-)\pi^+\pi^-$	
	\mathcal{S}	\mathcal{A}	\mathcal{S}	\mathcal{A}
SVD1 (exp27)	0.681 ± 0.008	0.004 ± 0.006	0.694 ± 0.012	-0.002 ± 0.009
SVD2 (exp37)	0.692 ± 0.007	0.003 ± 0.006	0.708 ± 0.012	0.012 ± 0.008

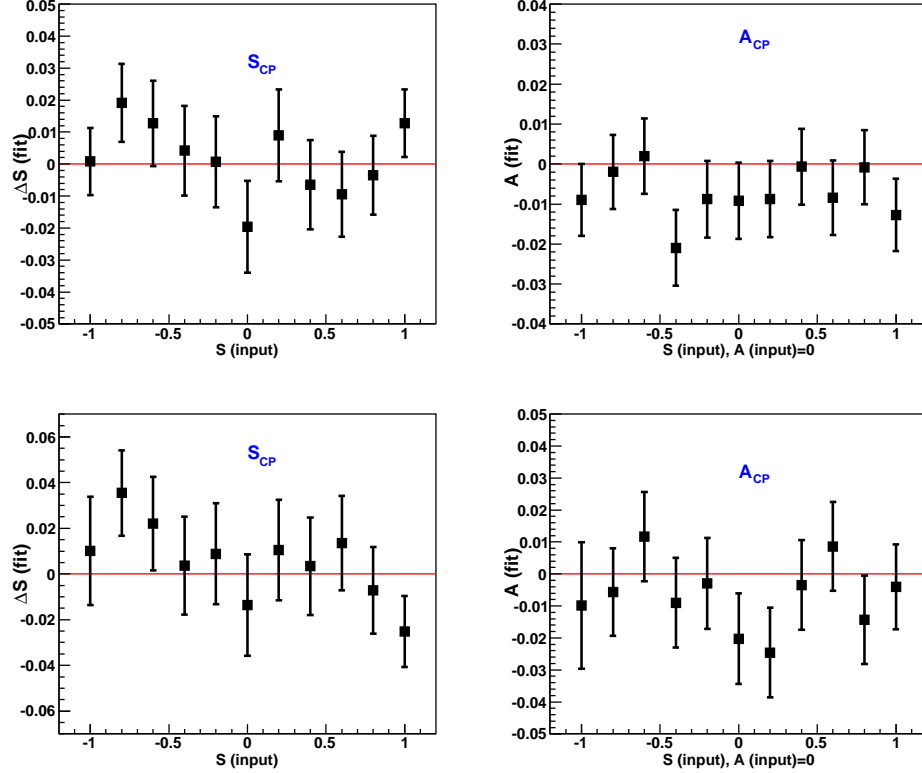


Figure 3.13: CP linearity plot for $\psi(2S) \rightarrow l^+l^-$ (upper) and for $\psi(2S) \rightarrow J/\psi\pi^+\pi^-$ (lower).

3.9.4 Lifetime Fit

We also performed a lifetime fit in data to check the understanding of the time distribution and background parameterization. The results of the lifetime fit for both $\psi(2S)K^+$ and $\psi(2S)K_S^0$ are listed in Tables 3.18 and 3.19. The results agree with the respective world-average values. Fig. 3.14 shows the lifetime fits along with the background component and outlier components.

3.9.5 CP Fit in Control Sample

We also performed a CP fit to control sample data. The value of τ_{B^+} is fixed to the PDG 2006 value (1.64 ps). The background parameters are fixed by fitting the data in ΔE - M_{bc} sideband. The results are summarized in Table 3.20 along with the results of a simultaneous fit to the SVD1 and SVD2 data samples.

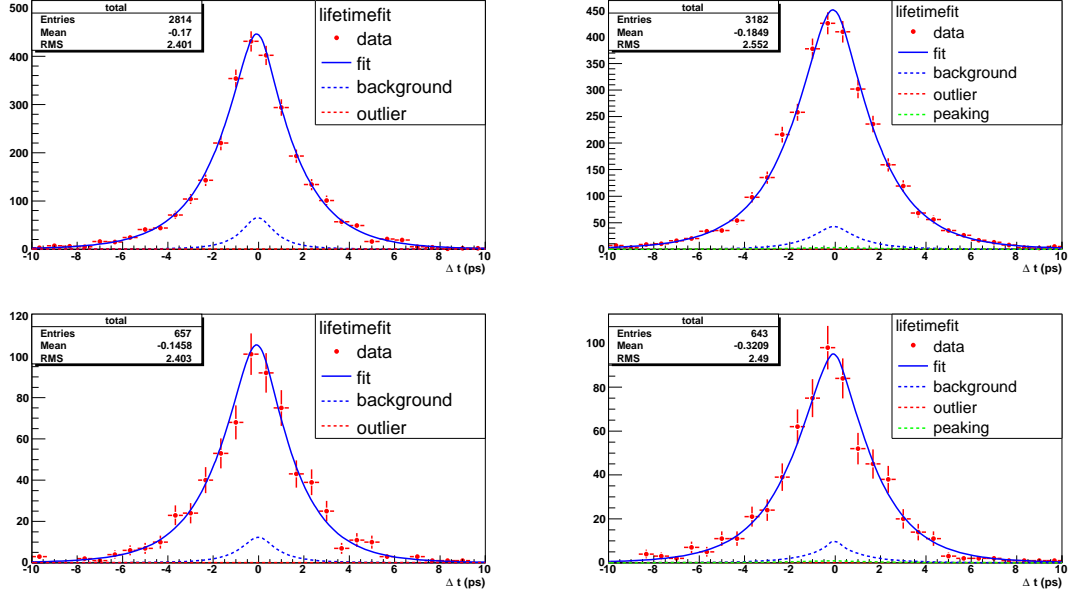


Figure 3.14: Lifetime fit (simultaneous fit to SVD1 and SVD2) in data for $B^\pm \rightarrow \psi(2S)(l^+l^-)K^\pm$ (upper left), $B^\pm \rightarrow \psi(2S)(J/\psi(l^+l^-)\pi^+\pi^-)K^\pm$ (upper right), $B^0 \rightarrow \psi(2S)(l^+l^-)K_S^0$ (lower left) and $B^0 \rightarrow \psi(2S)(J/\psi(l^+l^-)\pi^+\pi^-)K_S^0$ (lower right).

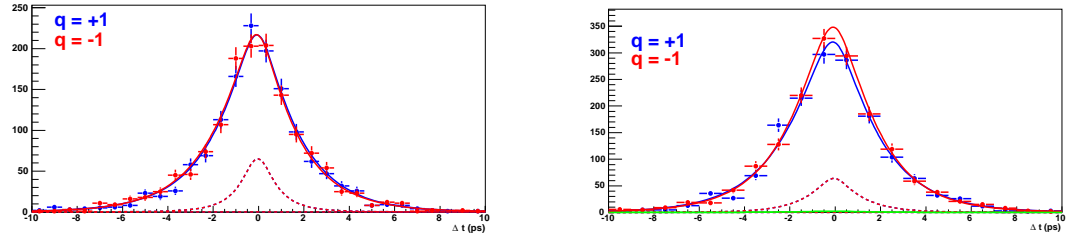


Figure 3.15: CP fit (simultaneous fit to SVD1 and SVD2) in data for $B^\pm \rightarrow \psi(2S)K^\pm$. Left is for $\psi(2S) \rightarrow l^+l^-$ and right is for $\psi(2S) \rightarrow J/\psi(l^+l^-)\pi^+\pi^-$ mode. The peaking background is shown in green for the $J/\psi\pi^+\pi^-$ mode.

Table 3.18: Lifetime fit in data for $B^\pm \rightarrow \psi(2S)K^\pm$ (units are in ps).

Data Sample	$\psi(2S) \rightarrow l^+l^-$	$\psi(2S) \rightarrow J/\psi(l^+l^-)\pi^+\pi^-$	Total
SVD1	1.65 ± 0.08	1.74 ± 0.08	1.70 ± 0.06
SVD2	1.58 ± 0.04	1.61 ± 0.04	1.60 ± 0.03
Total	1.60 ± 0.04	1.64 ± 0.04	1.62 ± 0.03
τ_{B^+} (PDG2006)	1.64 ± 0.01		

Table 3.19: Lifetime fit in data for $B^0 \rightarrow \psi(2S)K_S^0$ (units are in ps).

Data Sample	$\psi(2S) \rightarrow l^+l^-$	$\psi(2S) \rightarrow J/\psi(l^+l^-)\pi^+\pi^-$	Total
SVD1	1.53 ± 0.16	1.21 ± 0.14	1.38 ± 0.11
SVD2	1.47 ± 0.08	1.63 ± 0.09	1.55 ± 0.06
Total	1.49 ± 0.07	1.54 ± 0.08	1.51 ± 0.05
τ_{B^0} (PDG2006)	1.53 ± 0.01		

3.10 Systematic Uncertainty

The systematic uncertainties are evaluated by varying the fixed parameters used in the CP fit. We vary the parameters from their nominal values by $\pm 1\sigma$ for real data and $\pm 2\sigma$ for MC by their statistical error (asymmetric MINOS errors are used wherever available). We then add the differences in \mathcal{S} and \mathcal{A} quadratically and assign the largest value as a systematic error. Each category of uncertainty is described below and the results are shown in Table 3.21.

Vertexing This category includes seven different types systematics as shown in Table 3.22:

Table 3.20: CP fit in data ($B^\pm \rightarrow \psi(2S)K^\pm$).

Data Sample	$\psi(2S) \rightarrow l^+l^-$		$\psi(2S) \rightarrow J/\psi(l^+l^-)\pi^+\pi^-$		Total	
	\mathcal{S}	\mathcal{A}	\mathcal{S}	\mathcal{A}	\mathcal{S}	\mathcal{A}
SVD1	0.34 ± 0.14	0.16 ± 0.10	-0.12 ± 0.13	-0.25 ± 0.10	0.1 ± 0.1	-0.06 ± 0.07
SVD2	0.001 ± 0.080	-0.01 ± 0.05	-0.001 ± 0.074	-0.04 ± 0.05	0.0003 ± 0.05	-0.03 ± 0.04
Total	0.08 ± 0.07	0.02 ± 0.05	-0.03 ± 0.07	-0.08 ± 0.05	0.02 ± 0.05	-0.03 ± 0.03

1. IP Profile: The reconstructed and tag side vertices were constructed with an IP constraint smeared in the xy plane by $21\ \mu\text{m}$ to account for the finite flight length of the B meson. We estimate the systematic by varying the smearing by $\pm 10\ \mu\text{m}$.
2. TagV (dr and σ_z): For the track selection criteria of the tag side, we require $\sigma_z \leq 0.05\ \text{cm}$ and $dr \leq 0.05\ \text{cm}$. These conditions are varied by $\pm 10\%$ to assign a systematic error.
3. Scale Error: We turn off the scale error function and the differences in \mathcal{S} and \mathcal{A} are assigned as systematics.
4. Δt : We vary the Δt cut by $\pm 30\ \text{ps}$ (the nominal value is $70\ \text{ps}$).
5. ξ : The vertex quality cut is set to 150 and 500 (nominal value is 250).
6. Δz Bias: This systematic is 0.005 for \mathcal{S} and 0.0195 for \mathcal{A} (obtained from a $J/\psi K_S^0$ study).
7. Misalignment: This systematic is for imperfect SVD alignment. The value is 0.0056 for \mathcal{S} and 0.004 for \mathcal{A} (obtained from $J/\psi K_S^0$ study).

Physics Parameters We vary the physics parameters τ_{B^0} and Δm_d with their errors according to the results in PDG 2006.

$$\begin{aligned}\tau_{B^0} &= 1.530 \pm 0.009\ \text{ps}, \\ \Delta m_d &= 0.507 \pm 0.005\ \text{ps}^{-1}\end{aligned}$$

Wrong tag fraction We vary ω_l and $\Delta\omega_l$ by their errors for each r region [45].

Background ΔE Shape We obtain the parameters for combinatorial background from the ΔE - M_{bc} sidebands. These parameters are varied to calculate systematics.

Resolution Function We estimate the uncertainty due to the resolution function by varying the signal resolution parameters by $\pm 1\sigma$ (the parameters for non-primary (R_{np}) are varied by $\pm 2\sigma$).

ΔE - M_{bc} PDF Shape We vary the ΔE and M_{bc} shape factors (signal and background) with their errors from the final fit. For the signal shape, we also considered the fudge factor errors. The CP fit is repeated to obtain the uncertainty due to these parameters.

Signal and Background Fraction In the nominal fit, we used the different signal and background fractions for each r -bin. The signal and background fractions are varied with their errors according to binomial statistics.

Fit Bias This is determined from the CP fit with a large statistics signal MC sample as mentioned in Table 3.17.

Peaking Background To determine the effect of peaking background on the CP asymmetry, we set the \mathcal{S} and \mathcal{A} parameters to $+1(-1)$ for the peaking backgrounds. The peaking background fraction is also fixed to a value 0% and 2% for the systematic calculation. The mean and width are also varied with their statistical errors obtained from the fit in the MC sideband.

Tag Side Interference (TSI) We also include the effects of interference between CKM-favored and CKM-suppressed $B \rightarrow D$ transitions in the f_{tag} final state [46]. This systematic is obtained by using Belle’s official program with the $B \rightarrow D^*l\nu$ decay mode.

Table 3.21: Summary of the Systematic Uncertainties for $B^0 \rightarrow \psi(2S)K_S^0$ mode.

Parameter	$\Delta\mathcal{S}_{\psi(2S)K_S^0}$	$\Delta\mathcal{A}_{\psi(2S)K_S^0}$
Vertexing	0.026	0.020
Wrong tag fraction	0.006	0.023
Resolution function	0.007	0.005
Fit bias	0.012	0.011
Physics parameters	0.001	0.001
Peaking background	0.006	0.005
PDF shape and fraction	0.001	0.003
Background Δt shape	0.003	0.003
Tag side interference	0.001	0.036
Total	0.031	0.049

Table 3.22: Systematic Uncertainties in Vertexing for $B^0 \rightarrow \psi(2S)K_S^0$ mode.

Parameter	$\Delta\mathcal{S}_{\psi(2S)K_S^0}$	$\Delta\mathcal{A}_{\psi(2S)K_S^0}$
IP Profile	0.013	0.005
dr (track)	0.002	0.002
σ_z (track)	0.002	0.005
Scale Error	0.018	0.016
Δt	0.000	0.000
Vertex ξ	0.012	0.009
Δz Bias	0.005	0.002
Misalignment	0.006	0.004
Total	0.026	0.020

3.11 CP Fit Results in $B^0 \rightarrow \psi(2S)K_S^0$

The unbinned maximum likelihood fit to the 1300 events in the signal region results in the CP violation parameters,

$$\begin{aligned}\mathcal{S}_{\psi(2S)K_S^0} &= +0.72 \pm 0.09(\text{stat}) \pm 0.03(\text{syst}), \\ \mathcal{A}_{\psi(2S)K_S^0} &= +0.04 \pm 0.07(\text{stat}) \pm 0.05(\text{syst}).\end{aligned}\tag{3.11.1}$$

This is based on a data sample containing 657×10^6 $B\bar{B}$ pairs. The CP fit results in different subsamples are summarized in Table 3.23.

Table 3.23: CP fit results in data with different subsamples for the $B^0 \rightarrow \psi(2S)K_S^0$ decay mode.

Data Sample	$\psi(2S) \rightarrow l^+l^-$		$\psi(2S) \rightarrow J/\psi(l^+l^-)\pi^+\pi^-$		Total	
	\mathcal{S}	\mathcal{A}	\mathcal{S}	\mathcal{A}	\mathcal{S}	\mathcal{A}
SVD1	0.90±0.23	0.09±0.20	1.07±0.32	-0.1±0.2	0.97±0.18	-0.02±0.13
SVD2	0.82±0.15	0.16±0.10	0.53±0.14	-0.08±0.12	0.66±0.10	0.05±0.08
Total	0.84±0.13	0.14±0.09	0.61±0.13	-0.09±0.10	0.72±0.09	0.04±0.07

We define the raw asymmetry in each Δt bin by $(N_+ - N_-)/(N_+ + N_-)$, where N_+ (N_-) is the number of observed candidates with $q = +1$ (-1). Figure 3.16 shows the observed Δt distributions for $q = +1$ and $q = -1$ with no requirement on the tagging

quality (top), and the raw asymmetry for events with good tagging quality ($r > 0.5$) (middle) and poor tagging quality ($r < 0.5$) (bottom). These measurements supersede our previous result [9] and is statistically consistent with Belle's measurement using the $B^0 \rightarrow J/\psi K^0$ mode, which gives $\sin 2\phi_1 = 0.642 \pm 0.031 \pm 0.017$ [47]. Combining the results from $B^0 \rightarrow J/\psi K^0$ and $B^0 \rightarrow \psi(2S)K_S^0$ decays, we obtain a new Belle average $\sin 2\phi_1 = 0.650 \pm 0.029 \pm 0.018$.

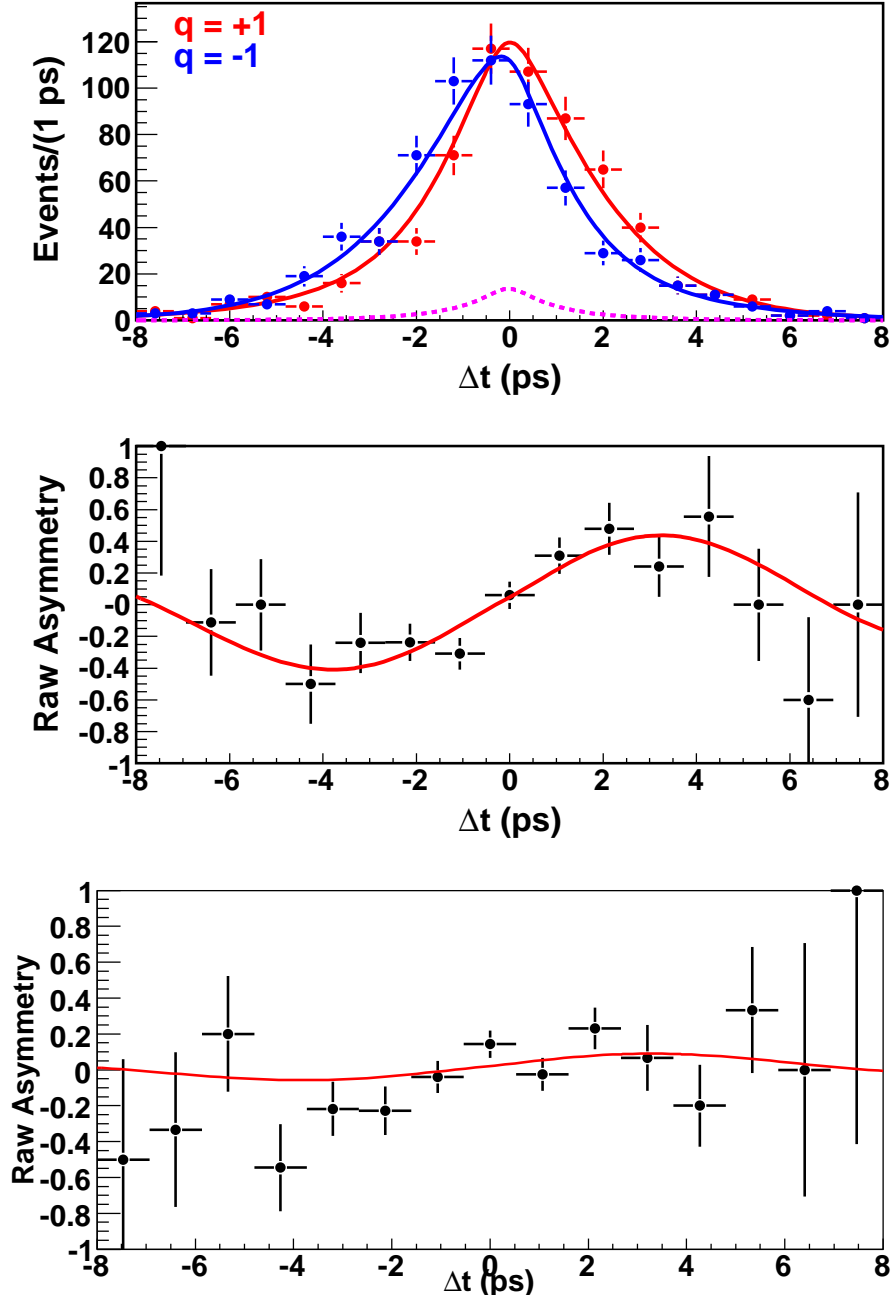


Figure 3.16: CP fit results in data for $B^0 \rightarrow \psi(2S)K_S^0$ mode using 657 M $B\bar{B}$ pairs. The top plot shows the Δt distributions for $q = +1$ and $q = -1$ with no requirement on r . The dashed curve is the sum of backgrounds while the solid curves are the sum of signal and backgrounds. The middle plot shows the raw asymmetry for well-tagged events ($r > 0.5$, 45% of the total) and the bottom plot is for poorly-tagged events ($r < 0.5$). The solid curve shows the result of the unbinned maximum-likelihood fit.

Chapter 4

Observation of $B^0 \rightarrow \phi K_S^0 \gamma$

4.1 Introduction

In this chapter, we describe the selection procedure for identifying $B \rightarrow \phi K \gamma$ radiative decays. These modes proceed mainly through $b \rightarrow s$ penguin diagrams. Different sources of backgrounds are mentioned and the methods to suppress them are discussed. We then fit the two dimensional ΔE - M_{bc} distribution to establish the existence of a signal and determine its branching fractions.

4.2 Event Selection

This analysis is based on the full dataset (700 fb^{-1}) collected by the Belle detector, which contains 772 million $B\bar{B}$ pairs. The data are required to pass the hadronic event selection cuts described in chapter 3. The signal is reconstructed in the decays $B^+ \rightarrow \phi K^+ \gamma$ and $B^0 \rightarrow \phi K_S^0 \gamma$, with $\phi \rightarrow K^+ K^-$ and $K_S^0 \rightarrow \pi^+ \pi^-$. For the event generation, we assume that the B meson decays to an intermediate heavy kaon resonance and a photon. The resonance then decays to a ϕ and K_S^0 or K^\pm . In the EvtGen MC simulation, an artificial resonance with a mass of $1800 \text{ MeV}/c^2$, width of $500 \text{ MeV}/c^2$ and spin one is used. We then reweight the mass distribution so that it is flat from the kinematic limit to $2.8 \text{ GeV}/c^2$ [48].

All the charged tracks used in the reconstruction (except for charged pions from K_S^0 's) are required to satisfy a requirement on the distance of closest approach to the IP along the beam direction $|dz| < 5 \text{ cm}$ and in the transverse direction $|dr| < 2 \text{ cm}$. This eliminates poorly reconstructed tracks or tracks that do not come from the interaction region. Charged kaons are identified using a likelihood ratio $\mathcal{L}(K/\pi) > 0.6$, based on the

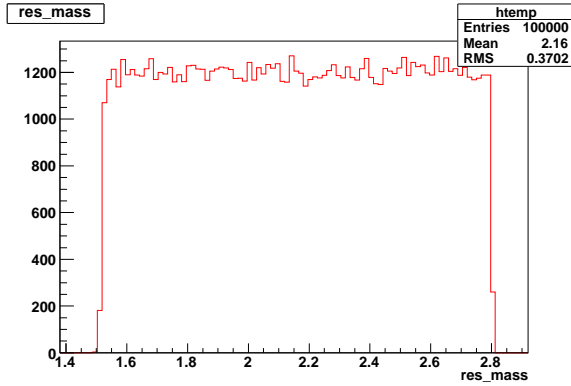


Figure 4.1: The invariant ϕK_S^0 mass from EvtGen. The decay is generated assuming flat mass distribution with upper limit fixed to 2.8 GeV/c^2 . The lower limit on the mass spectrum is the ϕK threshold (1.52 GeV/c^2).

information from the ACC, TOF and CDC (dE/dx) detectors. This requirement has an efficiency of 90% for kaons and a 8% pion fake rate. The K_S^0 selection criteria are same as those described in chapter 3.

4.2.1 $\phi(1020)$ meson reconstruction

We reconstruct the ϕ meson in the K^+K^- decay channel ($\mathcal{B} = (49.1 \pm 0.6)\%$). A less restrictive likelihood ratio requirement $\mathcal{L}(K/\pi) > 0.4$ is applied to the kaon candidates, which are used to reconstruct the ϕ meson. The invariant mass of the ϕ candidates is required to be within the range $-0.01 < M_{K^+K^-} - m_\phi < +0.01 \text{ GeV}/c^2$, where m_ϕ denotes the world-average ϕ mass [20]. This corresponds to $\sim \pm 2.3\Gamma$ (where Γ is the natural width of the ϕ meson).

4.2.2 Radiative γ reconstruction

The primary signature of this decay is a high energy prompt photon. These are selected from isolated ECL clusters within the acceptance of the barrel region ($32^\circ < \theta_\gamma < 129^\circ$, where θ_γ is the polar angle of the photon in the laboratory frame) and cms energy (E_γ^{cms}) in the range 1.4 to 3.4 GeV. The selected photon candidates are required to be consistent with isolated electromagnetic showers, i.e., 95% of the energy in an array of 5×5 CsI(Tl) crystals should be concentrated in an array of 3×3 crystals and should have no charged tracks associated with it. We also remove the photons from $\pi^0(\eta) \rightarrow \gamma\gamma$ using

a likelihood $\mathcal{L}_{\pi^0}(\mathcal{L}_\eta) < 0.25$, calculated for each photon pair consisting of the candidate photon and any other photon in the event [49].

4.2.3 B meson reconstruction

We combine the ϕ , a charged or neutral kaon candidate and the radiative photon to form a B meson. The B candidates are identified using two kinematic variables: the energy difference $\Delta E \equiv E_B^{\text{cms}} - E_{\text{beam}}^{\text{cms}}$ and the beam-energy-constrained mass $M_{\text{bc}} \equiv \sqrt{(E_{\text{beam}}^{\text{cms}})^2 - (p_B^{\text{cms}})^2}$, where $E_{\text{beam}}^{\text{cms}}$ is the beam energy in the cms, and E_B^{cms} and p_B^{cms} are the cms energy and momentum, respectively, of the reconstructed B candidate. In the M_{bc} calculation, the photon momentum is rescaled by $(E_{\text{beam}}^{\text{cms}} - E_{\phi K}^{\text{cms}})$ to improve resolution. In particular, we rescale the p_B^{cms} using the following equation so that $\Delta E = 0$.

$$\mathbf{p}_B^{\text{cms}} = \mathbf{p}_\phi^{\text{cms}} + \mathbf{p}_K^{\text{cms}} + \frac{\mathbf{p}_\gamma^{\text{cms}}}{E_\gamma^{\text{cms}}} (E_{\text{beam}}^{\text{cms}} - E_{\phi K}^{\text{cms}} - E_K^{\text{cms}}) \quad (4.2.1)$$

The events that satisfy the requirements $M_{\text{bc}} > 5.2 \text{ GeV}/c^2$ and $|\Delta E| < 0.3 \text{ GeV}$ (defined as the fit region) are selected for further analysis. We define the signal region as $5.27 \text{ GeV}/c^2 < M_{\text{bc}} < 5.29 \text{ GeV}/c^2$ and $-0.08 \text{ GeV} < \Delta E < 0.05 \text{ GeV}$. The ΔE signal region is asymmetric in order to include the tail in the lower region due to photon energy leakage in the ECL.

Figure 4.2 shows the ϕ and K_S^0 mass distributions. The ϕ mass is fitted with a Breit-Wigner function and a linear polynomial. The K_S^0 mass distribution is fitted with a double Gaussian function and a polynomial of order one.

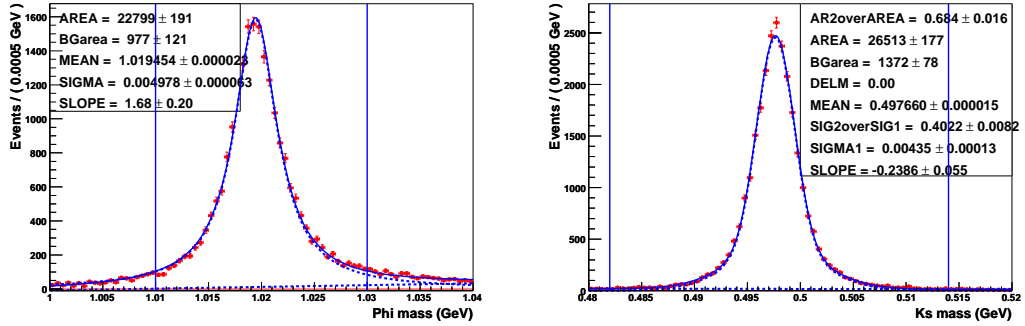


Figure 4.2: Invariant mass distributions of ϕ (left) and K_S^0 (right).

4.2.4 Best Candidate Selection (BCS)

After applying all selection criteria, there are still multiple candidates per event. Using MC simulations, we find that the average multiplicity (total B candidates/total events with at least one B candidate) and fraction of events with more than one B candidate in the fit region. The multiplicity is ~ 1.04 (3%) for $\phi K_S \gamma$ and ~ 1.18 (12%) for $\phi K^+ \gamma$. In case of multiple candidates, we choose the best candidate based on a series of selection criteria, which depend on a χ^2 variable formed using the candidate's ϕ mass (and K_S^0 mass in the neutral mode) as well as the highest E_γ^{cms} and the highest $\mathcal{L}(K/\pi)$ in the charged mode. For events with multiple candidates, this selection method chooses the correct B candidate for the $B^+ \rightarrow \phi K^+ \gamma$ ($B^0 \rightarrow \phi K^0 \gamma$) mode 57% (69%) of the time. If we find candidates in both $\phi K^+ \gamma$ and $\phi K_S^0 \gamma$, we consider both of them as signal events (the fraction of such events is $< 1\%$). The χ^2 definition used in the selection is defined below:

$$\chi^2 = \left(\frac{M_{KK} - m_\phi}{\sigma_{KK}} \right)^2 + \left(\frac{M_{\pi\pi} - m_{K_S}}{\sigma_{\pi\pi}} \right)^2 \text{ for } B^0 \rightarrow \phi K_S^0 \gamma \quad (4.2.2)$$

$$\chi^2 = \left(\frac{M_{KK} - m_\phi}{\sigma_{KK}} \right)^2 + \text{highest KID for } B^\pm \rightarrow \phi K^\pm \gamma \quad (4.2.3)$$

4.3 Continuum Suppression

The dominant background comes from $e^+e^- \rightarrow q\bar{q}$ ($q = u, d, s, \text{ or } c$) continuum events. These backgrounds can be separated from $B\bar{B}$ events using event topology, which is spherical for $B\bar{B}$ events in the cms and jet-like for continuum events. We also use another event-shape variable, the cosine value of the angle between B flight direction and the beam axis in the cms ($\cos\theta_B$) to separate the signal and continuum events. The event-shape variables are trained using a continuum MC, which is 2.6 times the size of the experimental data.

4.3.1 ROOKSFW

We use Belle's official ROOKSFW package, the ROOT version of KSFW (Kakuno san's modified Super Fox Wolfram moments). The Super Fox-Wolfram (SFW) variables combine the Fox-Wolfram momenta [39, 50] of B candidate's and non- B candidate's daughter tracks with a Linear Fisher Discriminant [51]. In KSFW, the missing momentum is treated as one additional particle when calculating the Fox-Wolfram moments of each event.

The KSFW variable is defined as

$$KSFW = \sum_{l=0,4} R_l^{so} + \sum_{l=0,4} R_l^{oo} + \gamma \sum_{n=1}^{N_t} |(P_t)_n| \quad (4.3.1)$$

There are a total of 17 parameters in the KSFW, which are determined using the continuum MC. The KSFW coefficients are trained in both signal and continuum MC. For signal MC, we use correctly reconstructed events in the signal region. For continuum MC, to increase the statistics for an accurate determination of the PDF'S, we use all events in the fit region. The ROOKSFW package directly gives the variable LRKSFW depending upon whether the final state particles are used in the KSFW moments calculation (LRKSFW1) or not used (LRKSFW0). The latter one uses the daughters of B directly. However, the optimal one to be used for the final LR cut is determined from the figure of merit (FOM) value and after study with a control sample.

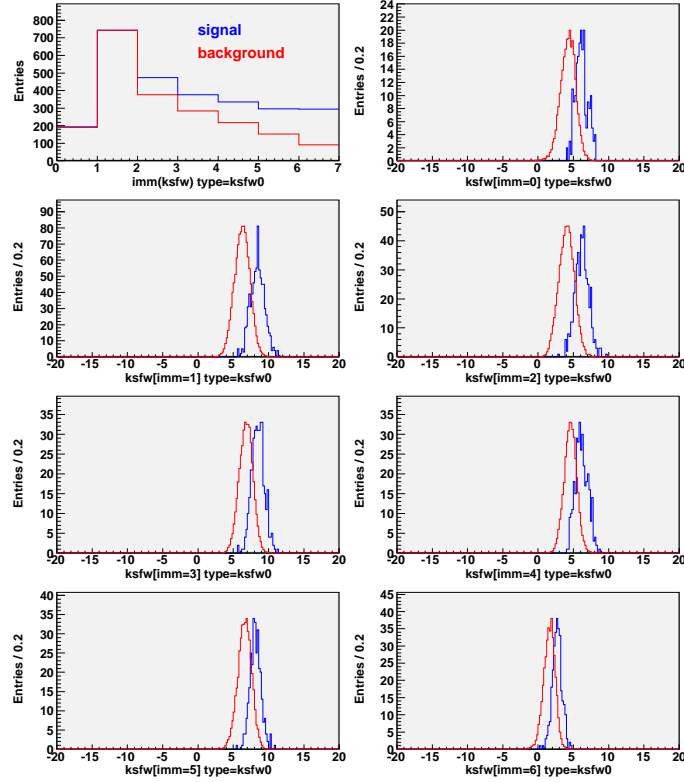


Figure 4.3: The KSFW0 PDF in 7 bins of missing mass.

4.3.2 $\cos \theta_B$

The decay of $\Upsilon(4S) \rightarrow B\bar{B}$ is a $V \rightarrow SS$ decay. Therefore, the polar angular distribution of the B candidate in the cms follows a $1-\cos^2 \theta$ distribution. Figure 4.4 shows the $\cos \theta_B$ distributions for signal and continuum, each fitted with a second order polynomial. The $\cos \theta_B$ LR variable is constructed by using the corresponding PDF for signal (for correctly reconstructed events in the signal region) and continuum background (from fit region).

$$\mathcal{LR}(\cos \theta_B) = \frac{\mathcal{P}_S(\cos \theta_B)}{\mathcal{P}_S(\cos \theta_B) + \mathcal{P}_B(\cos \theta_B)} \quad (4.3.2)$$

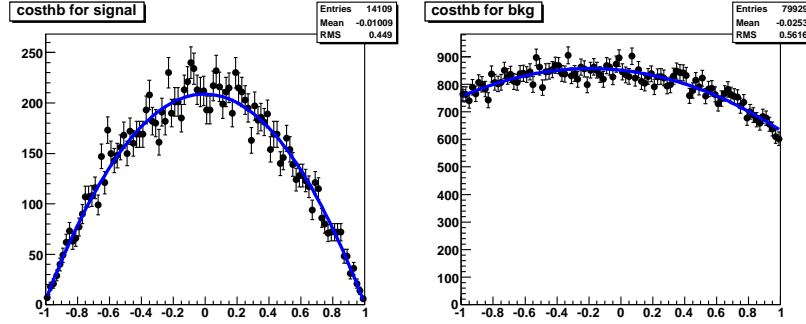


Figure 4.4: The $\cos \theta_B$ distributions fitted with second order polynomial for the $\phi K^+ \gamma$ decay mode. The left is for signal and right is for continuum.

4.3.3 Likelihood Ratio (LR)

We use the Likelihood Ratio (LR) approach to discriminate between the signal and the continuum background. The likelihood ratio is constructed from the LRKSF0 and LR $\cos \theta_B$ variables as follows:

$$\mathcal{LR}(KSF0, \cos \theta_B) = \frac{\mathcal{LR}(KSF0)\mathcal{LR}(\cos \theta_B)}{\mathcal{LR}(KSF0)\mathcal{LR}(\cos \theta_B) + (1 - \mathcal{LR}(KSF0))(1 - \mathcal{LR}(\cos \theta_B))}$$

The \mathcal{LR} cut is optimized using the FOM, $N_S/\sqrt{N_S + N_B}$, where N_S (N_B) is the expected number of signal (continuum) events in the ΔE - M_{bc} signal region. We used the branching fractions measured by C. Jacoby [52] to scale the MC to the data sample.

Figure 4.5 shows the FOM plots for both modes, each trained and optimized separately. The red curve is the FOM constructed from LRKSF0 and blue curve from LRKSF1. It is clear that the FOM for LRKSF0 is higher than LRKSF1. We use

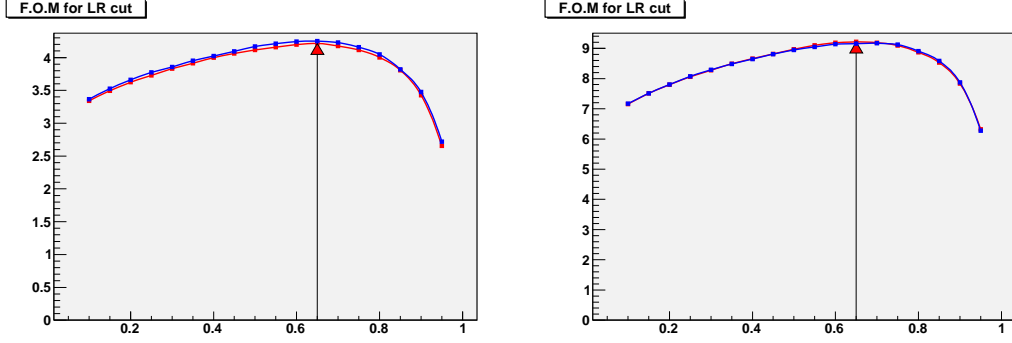


Figure 4.5: The LR FOM plots for the $\phi K_S^0 \gamma$ (left) and $\phi K^+ \gamma$ (right) modes. We use the final LR cut calculated from LRKSF0 and LR $\cos \theta_B$.

the LR cut 0.65 for the ϕ channel, which corresponds to the FOM value of 4.22 for $\phi K_S \gamma$ and 9.21 for $\phi K^+ \gamma$. This selection criteria removes 91% of the continuum while retaining 76% of the signal.

Figure 4.6 shows the ΔE and M_{bc} distributions from signal MC (upper) and continuum MC (lower), after applying the continuum suppression cut. For signal MC, the ΔE shape is described by the sum of a Crystal Ball line shape [53] and a first order Chebyshev polynomial while the M_{bc} shape is the sum of a single Gaussian and an ARGUS function. For continuum MC, the ΔE shape is described by 1st order Chebyshev polynomial and the M_{bc} shape is parameterized by an ARGUS function.

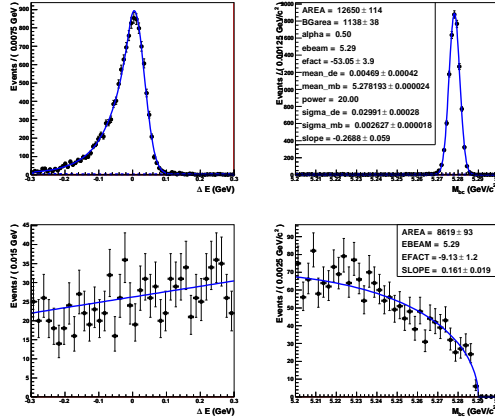


Figure 4.6: The ΔE and M_{bc} distributions from signal MC (upper) and continuum MC (lower) for the $B^+ \rightarrow \phi K^+ \gamma$ mode after applying the LR cut.

4.4 Generic B Backgrounds

Using a sample of five times $B\bar{B}$ MC events with a model of all $b \rightarrow c$ decays, we investigate the backgrounds from other B decay modes. Figure 4.7 shows the ΔE fit (with a projection in M_{bc}) and an M_{bc} fit (with a projection in ΔE) and ϕK distribution in the fit region for the backgrounds from the generic MC. These distributions are shown after applying the LR cut, which removes 50% of generic backgrounds in addition to suppressing the continuum. The ΔE distributions are modelled by a second order Chebyshev polynomial. The backgrounds peak in the M_{bc} distributions. We estimate the expected peaking events in data by fitting the MC with the sum of an ARGUS and a Gaussian function (the yield of the Gaussian is scaled by a factor of 5 to compare with data). The mean and sigma of the Gaussian is fixed to the corresponding value from the signal MC.

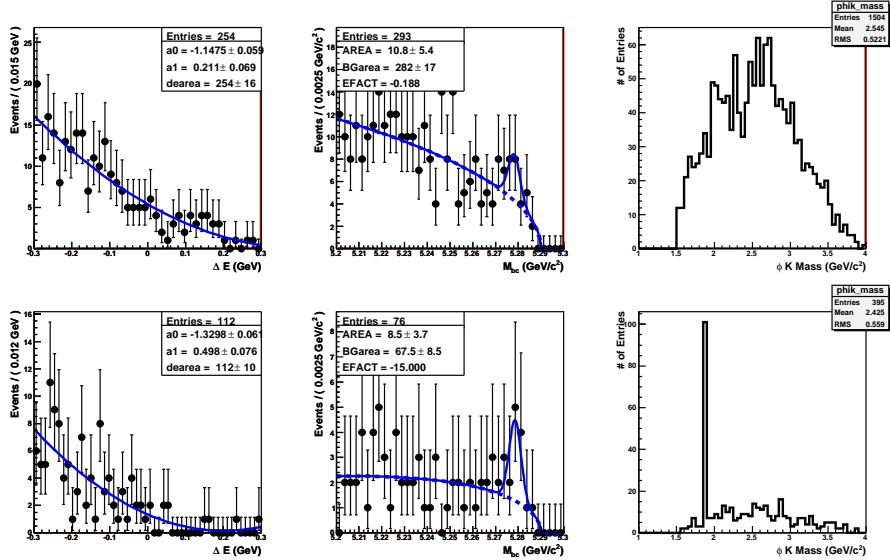


Figure 4.7: The ΔE , M_{bc} and invariant ϕK distributions from generic MC for the $\phi K^+\gamma$ (first row), $\phi K_S^0\gamma$ (second row) decay mode before the D veto, which will be applied only in $\phi K_S^0\gamma$ mode.

For the $B^+ \rightarrow \phi K^+\gamma$ mode, the expected peaking background in M_{bc} is 2.2 ± 1.1 ($\sim 1.3\%$ of the expected signal yield in data). It is difficult to identify a single source of these events. Since the peaking component is very small (first row in Fig. 4.7) compared to the yield in data, we vary this component in the systematic calculation.

For the $B^0 \rightarrow \phi K_S^0 \gamma$ mode, the expected peaking events in M_{bc} is 1.7 ± 0.7 ($\sim 5\%$ of the expected yield in data). These events are from $D^0(D^\pm)$ decays (such as $D^0\pi^0$, $D^0\eta$, $D^-\rho^+$), which peak around 1.87 GeV in the ϕK_S^0 invariant mass. We apply a D veto in the invariant ϕK_S^0 mass to reduce these backgrounds. The size of the veto window is determined by fitting the ϕK_S^0 mass distribution (Fig. 4.8) (the LR cut is removed to increase the statistics). We choose a 4σ cut around the peak, where σ is the width of the Gaussian.

In summary, we apply the D veto only in $B^0 \rightarrow \phi K_S \gamma$ mode. The efficiency loss due to this veto is 2% and the peaking background after veto is estimated to be 0.3 ± 0.5 (which is consistent with zero) (Fig. 4.9). This small peaking background will be taken account of in the systematic calculation.

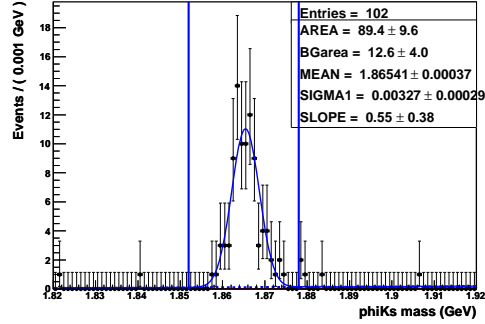


Figure 4.8: Invariant ϕK_S mass is fitted with a Gaussian function. We apply a 4σ veto window $1.852 < M(\phi K_S^0) < 1.878$ GeV/ c^2

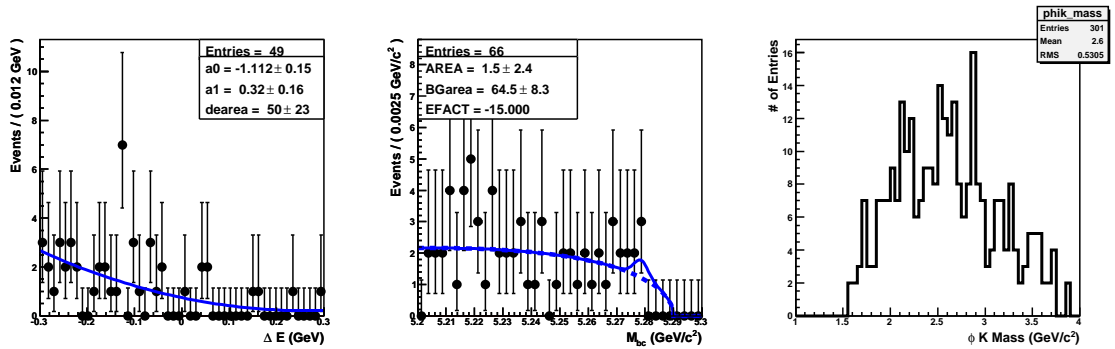


Figure 4.9: The ΔE , M_{bc} and invariant ϕK_S^0 distributions for the $B^0 \rightarrow \phi K_S^0 \gamma$ decay mode after applying the D veto.

4.5 Reconstruction Efficiency

We calculate the signal reconstruction efficiency by fitting the M_{bc} and ΔE distributions after applying all selection criteria and background reduction cuts (LR cut and D veto). In order to take into account different experimental conditions, we generated 500,000 signal MC events (exp07-65) weighted to the data luminosity.

The M_{bc} distribution is well described by a Gaussian function for signal and the ARGUS function for background. The ΔE distribution is modeled by a Crystal Ball line shape function and a first order Chebyshev polynomial. The Crystal Ball parameters α and n seems to be very unstable and correlated with μ and σ . We follow a different procedure in MC to fix these two parameters. The ALPHA (α) parameter determines where the function starts to diverge from a normal Gaussian in terms of SIGMA (σ) and the POWER (n) parameter controls the length of the tail to lower energies. We do one dimensional fits in each mode in an extended region of ΔE to fix the long tail and obtain a stable value of n . We then repeat the fit with a fixed n value to determine a stable value of α . In the final fits, we find values of n (20) and α (0.5).

The signal reconstruction efficiency is determined from a ΔE - M_{bc} 2D fit. The efficiency in the $B^+ \rightarrow \phi K^+ \gamma$ mode is $(13.4 \pm 0.1)\%$ and in the charged mode $(10.0 \pm 0.1)\%$. There is significant improvement of the efficiency due to the new tracking algorithm (22% for $B^0 \rightarrow \phi K_S^0 \gamma$ and 11% for $B^+ \rightarrow \phi K^+ \gamma$), as there are low-momentum tracks in the final state. We also checked the efficiency dependence on $M(\phi K)$ mass in a large signal MC sample. We divided the $M(\phi K)$ mass in 10 bins and the efficiency is calculated for each bin in the ΔE - M_{bc} signal region. We do not see any strong dependence on the mass and will correct the efficiency for the actual distribution of ϕK mass in data (as described in the section 4.9).

4.6 Rare B Backgrounds

We identify the possible sources of charmless backgrounds using a sample of rare $B\bar{B}$ MC events, which is 50 times the size of the experimental data. This MC sample includes decays that have very low branching fractions such as charmless, Cabibbo-suppressed and color suppressed decays. It contains two-body non-resonant $B \rightarrow X_s \gamma$ decays, where the X_s decays into hadrons is controlled by PYTHIA fragmentation. This uses the JETSET

program, which decays the X_s via phase-space production from the available quarks. We remove the events from the rare MC in which the X_s decays to the signal mode ($\phi K_S^0(K^+)$) for further study.

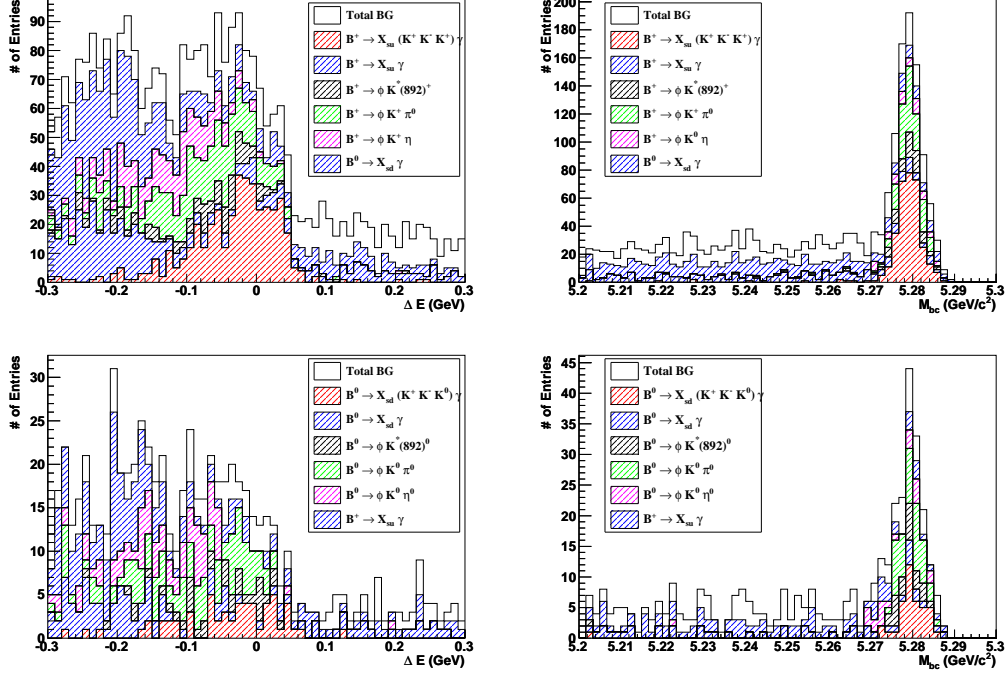


Figure 4.10: The rare backgrounds (charged and mixed) in the ΔE and M_{bc} distributions for the $B^+ \rightarrow \phi K^+ \gamma$ (upper) and $B^0 \rightarrow \phi K_S^0 \gamma$ (lower) mode. The ΔE plots have projections in M_{bc} and the M_{bc} plots have projection in ΔE .

The identified background sources for $B^+ \rightarrow \phi K^+ \gamma$ mode are shown in Fig. 4.10. The dominant peaking background is the non-resonant $B^+ \rightarrow K^+ K^- K^+ \gamma$ decay, which peaks in the ΔE - M_{bc} signal region ($\sim 4\%$ of the expected signal yield in data). The other peaking backgrounds are $B^+ \rightarrow \phi K^*(892)^+$, $B^+ \rightarrow \phi K^+ \pi^0$ and $B^+ \rightarrow \phi K^+ \eta$. In these charmless modes, one of the photons from a π^0 or η may not be detected in the calorimeter while the other is reconstructed as a signal high-energy photon. Therefore, these backgrounds shift towards lower in ΔE but peak in M_{bc} . Since the non-resonant component is flat in the ϕ mass signal region, we can estimate it from the ϕ mass sideband. As the other peaking component is small, we plan to fix it in the final fit to the expected value from MC.

Similarly in the $B^0 \rightarrow \phi K_S^0 \gamma$ mode, the largest contribution is from the non-resonant decay $B^0 \rightarrow K^+ K^- K^0 \gamma$, which will be estimated from the ϕ mass sideband.

The other peaking backgrounds are $B^0 \rightarrow \phi K^*(892)^0$, $B^0 \rightarrow \phi K^0 \pi^0$ and $B^0 \rightarrow \phi K^0 \eta$. Like the control mode, for these backgrounds one γ is not detected and hence the decay is reconstructed at lower ΔE , but all peak in the M_{bc} . Therefore, in this mode, we will follow the same procedure for the rare background parameterization as in the control mode.

4.6.1 ϕ mass sideband study in MC

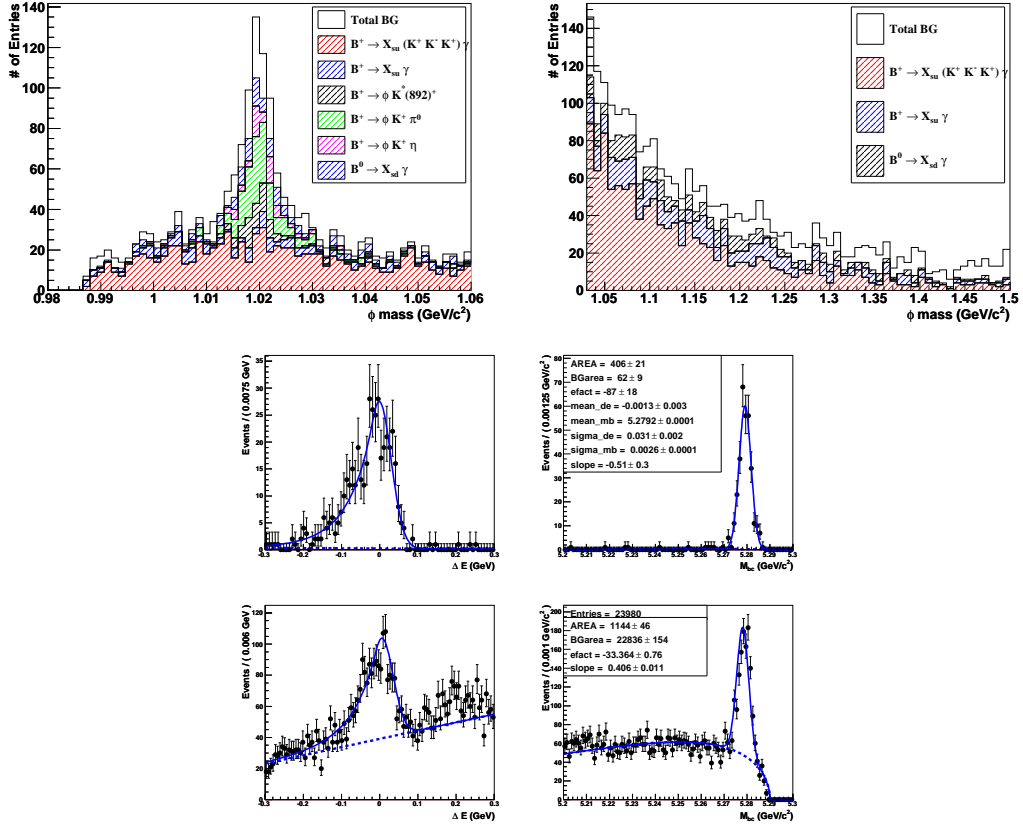


Figure 4.11: The ϕ mass distribution for the background events in the $B^+ \rightarrow \phi K^+ \gamma$ mode. The non-resonant component is shown in red. The ϕ signal region is [1.01-1.03] GeV and sideband region is [1.05-1.3] GeV (which will be used to estimate the non-resonant component). Lower left is the 2D fit to the non-resonant component in the signal region and lower right is the fit to all events in the sideband.

The dominant background is from non-resonant $B \rightarrow K^+ K^- K \gamma$ decays, which peak in the ΔE - M_{bc} signal region, but are flat in the ϕ signal region (the red component in the upper left plot of Fig. 4.11). Therefore, we can estimate this contamination from

the ϕ mass sideband. The lower ϕ mass sideband is limited by the K^+K^- phase space (0.988 GeV). Therefore, we choose the region from 1.05 to 1.3 GeV in the upper sideband. We noticed that the $K^+K^-K\gamma$ mass distribution is not perfectly flat, but has some shape (as shown in the upper right plot of Fig. 4.11). There is also a small contribution from $B \rightarrow \phi K\gamma$ signal leaking into the sideband.

Therefore, before interpolating the yield from the sideband to the signal region, we make two corrections.

1. We correct the yield from the sideband for the shape of the non-resonant background. This we call the “shape factor”, defined as the ratio of the non-resonant yield from the ϕ signal region to the sideband region.

For example : in the $\phi K^+\gamma$ mode, the non-resonant component from ϕ signal region is (8.1 ± 0.4) and from ϕ sideband region (21.7 ± 0.7) . The shape factor is the ratio of these two, which is (0.37 ± 0.02) . Similarly, for the $\phi K_S\gamma$ mode, the factor is (0.3 ± 0.05) .

2. We also determine the small contribution from the signal leakage in the sideband from signal MC.

4.6.2 Parameterization of the Rare Background

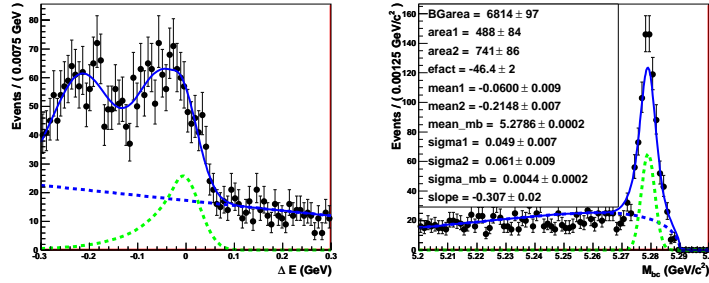


Figure 4.12: Parameterization of the rare backgrounds in the $B^+ \rightarrow \phi K^+\gamma$ mode. The ΔE distribution is fitted with two Gaussians, a first order Chebyshev polynomial and a Crystal Ball (for the nonresonant component, fixed from ϕ mass sideband). The M_{bc} distribution is fitted with a Gaussian for the non-resonant component and another Gaussian for other peaking backgrounds. The green dotted PDF is for the non-resonant component.

We fix the yield of the non-resonant component to the events from the ϕ mass sideband (after the two corrections mentioned previously). This component is well described by a Crystal Ball in ΔE and Gaussian in M_{bc} . We parameterize the remaining backgrounds in ΔE by two Gaussians (with different means and widths) and a first order Chebyshev polynomial, while the remaining background in M_{bc} is parameterized by a single Gaussian. The results of 2D fit are shown in the Fig. 4.12.

4.6.3 ϕ mass sideband study in Data

We apply the same procedure as in MC to determine the non-resonant component from data sideband. First, we do a ΔE - M_{bc} 2D fit to the events from ϕ mass sideband in data, with the mean and sigma of the peaking background component fixed to the MC sideband. The fitted distributions are shown in Fig. 4.13 and the invariant K^+K^- mass distributions are shown in Fig. 4.14.

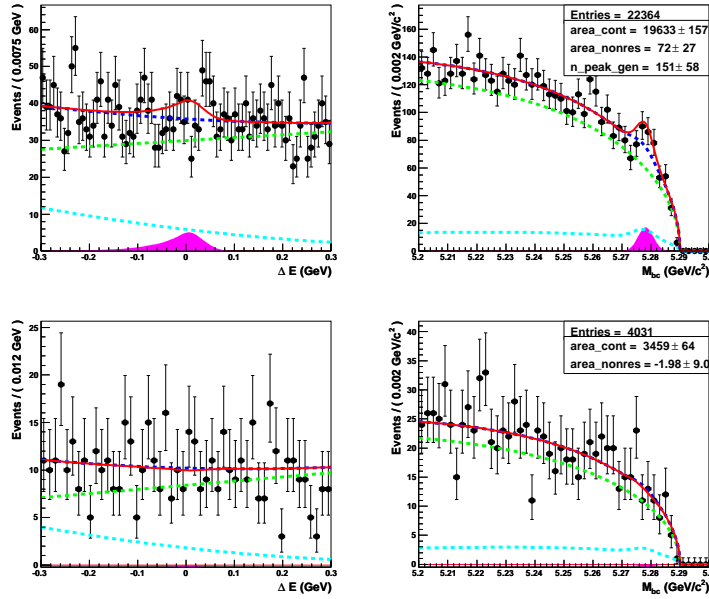


Figure 4.13: Fit to the ΔE - M_{bc} distributions for the ϕ mass sideband in data.

From data sideband, we obtain 72 ± 27 events. This is scaled by the shape factor mentioned and a correction of 6 events for signal leakage $((72 \pm 27) \cdot 0.37 - 6 = 20.6 \pm 10)$. The systematic error of 4.3 is obtained by varying all fixed parameters in the fit by their $\pm 1\sigma$

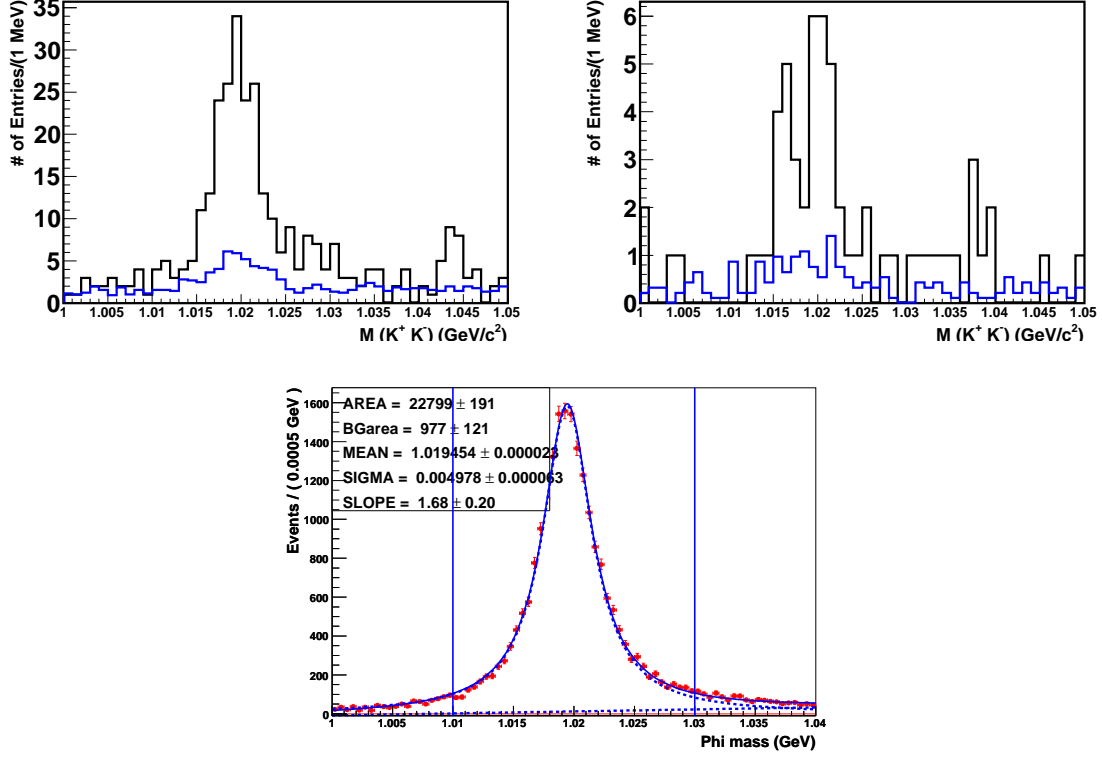


Figure 4.14: $M(K^+K^-)$ distribution in data for the events in the ΔE - M_{bc} signal window. Upper left is for the charged mode and upper right one is for the neutral mode. The blue histogram is the background from M_{bc} sideband region ($5.20 < M_{bc} < 5.26$ GeV/c^2). The events inside the window $1.01 < M(K^+K^-) < 1.03$ GeV are used for the signal extraction. The lower plot is the $M(K^+K^-)$ distribution from the signal MC.

statistical errors. The ratio of non-resonant component to the signal yield in $B^+ \rightarrow \phi K^+ \gamma$ mode can be used fix the non-resonant component in the $B^0 \rightarrow \phi K_S \gamma$ mode.

4.7 Signal Extraction Procedure

4.7.1 Correlation between ΔE and M_{bc}

The signal yield is obtained from an extended unbinned maximum-likelihood fit to the two-dimensional ΔE - M_{bc} distribution in the fit region. Before moving to the final fit, a one dimensional fit has been done in ΔE and M_{bc} and the two variables are checked for any possible correlations.

Table 4.1: Non-resonant component from rare MC (signal region), rare MC (sideband) and data sideband. All numbers are scaled to the signal region in data.

Decay Mode	Rare MC (signal region)	Rare MC (sideband)	Data
$B^+ \rightarrow \phi K^+ \gamma$	8.1 ± 0.4	8.5 ± 0.3	$20.6 \pm 10.0 \pm 4.3$
$B^0 \rightarrow \phi K_S \gamma$	1.2	1.3 ± 0.1	-2.0 ± 9.0

Figure 4.15 shows the correlation plots ($\Delta E: M_{bc}$) for the $B^+ \rightarrow \phi K^+ \gamma$ mode. The mean of ΔE is shown in bins of M_{bc} (red points with error bars) on a 2D scatter plot. There is no correlation in signal, continuum and generic MC, but the rare MC shows modest correlations: the mean of ΔE starts decreasing when M_{bc} is greater than 5.27 GeV. Since the correlation is small, we can assume that the 2D PDF is the product of ΔE and M_{bc} 1D PDFs and will correct for any possible bias introduced in the signal yield. The PDFs used to model the the final fit are shown in Table 4.2.

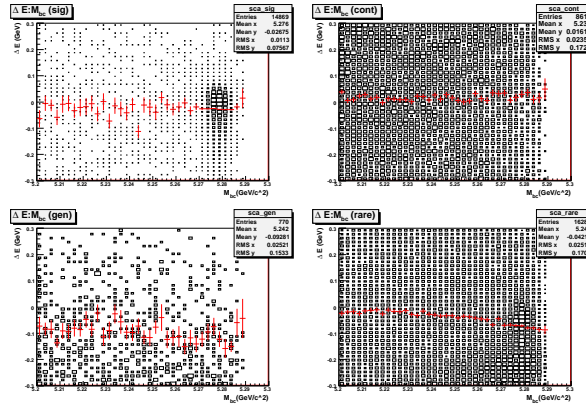


Figure 4.15: The mean of ΔE is shown in bins of M_{bc} (red points) on a scatter plot for the $\phi K^+ \gamma$ mode.

1. Signal: Shape parameters are fixed from signal MC with fudge factor corrections.
2. Continuum: Floated.
3. Generic: Both shape and yield are fixed from Generic MC. The shape of the peaking component is fixed to the signal shape.

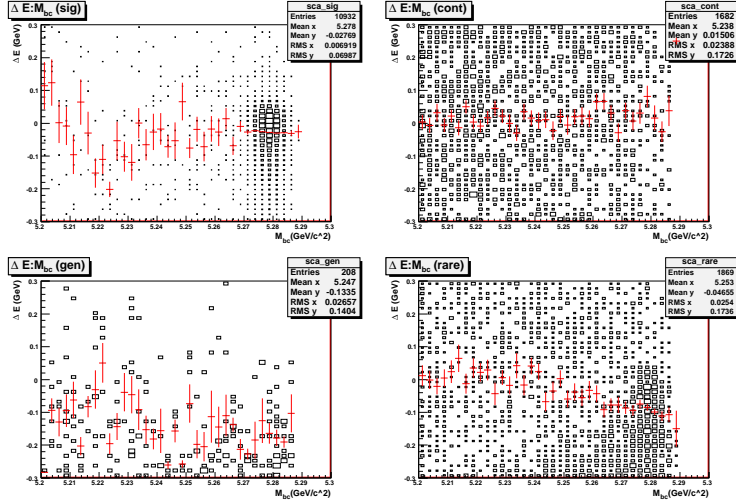


Figure 4.16: The mean of ΔE is shown in bins of M_{bc} (red points) on a scatter plot for the $B^0 \rightarrow \phi K_S^0 \gamma$ mode.

Table 4.2: The PDFs used to model each component in the 2D fit for $B \rightarrow \phi K \gamma$ mode.

MC Type	ΔE	M_{bc}
Signal	Crystal Ball	Gauss
Continuum	1st Order Chebyshev	ARGUS
Generic	2nd Order Chebyshev	ARGUS (+peaking)
Rare	two Gauss + Crystal Ball (nonres)	Gauss + Gauss (nonres)

- Rare: The non-resonant yield is fixed from ϕ -mass sideband and shape is fixed to the signal. The shape and yield of other components are fixed from rare MC.

All the fixed parameters are taken from 2D fits in the individual MC simulation. Since the signal resolution is dominated by the radiative γ , we use the same signal shape parameters for the $B^0 \rightarrow \phi K_S^0 \gamma$ mode as in the control mode.

4.7.2 Fitter Tests

In order to determine the stability and to correct for any possible bias in the fitter, we generate many samples of MC and fit with the same technique. We use two different

MC generation methods, toy MC and full simulation (EvtGen and GSiM). In toy MC, we generate 10,000 statistically independent samples using the shape parameters of the fit PDF determined from the full simulation. The actual number of events generated are sampled from a Poisson distribution around the expected event yield in data for each component. The toy MC is a good test of fit biases introduced by incorrect assumptions about the background PDFs. The accuracy of each fitter is determined by calculating the pull of the yield, defined as

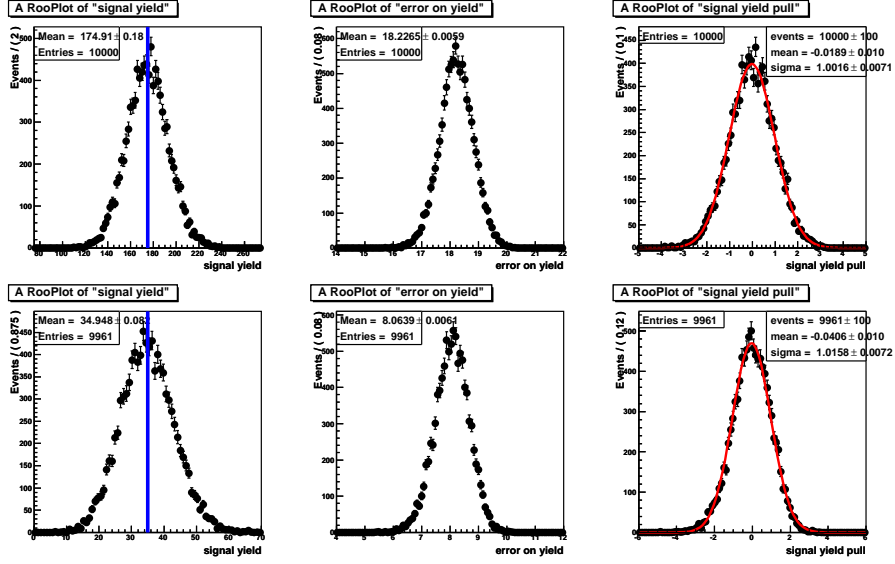


Figure 4.17: The signal yield, error on the yield and pull of the yield from toy MC study (10,000 samples). Upper plot is for the $B^+ \rightarrow \phi K^+ \gamma$ mode and lower plot is for the $B^0 \rightarrow \phi K_S^0 \gamma$ mode.

$$\text{Pull} = \frac{N_i^{\text{fit}} - N_i^{\text{exp}}}{\sigma_i^{\text{fit}}} \quad (4.7.1)$$

where N_i^{fit} is the returned signal yield, σ_i^{fit} is the error on the yield from the fit of each sample and N_i^{exp} is the expected yield in data. The yield, error and the pull of signal yield from pure toy MC are shown in Fig. 4.17. The pull distributions are fitted with a Gaussian function to determine the mean and sigma. We carefully checked that the fit converged successfully for all the points used in the pull study.

We also did an ensemble test in fully simulated MC to avoid any possible bias introduced due to correlations between fitting variables. A large amount of signal MC

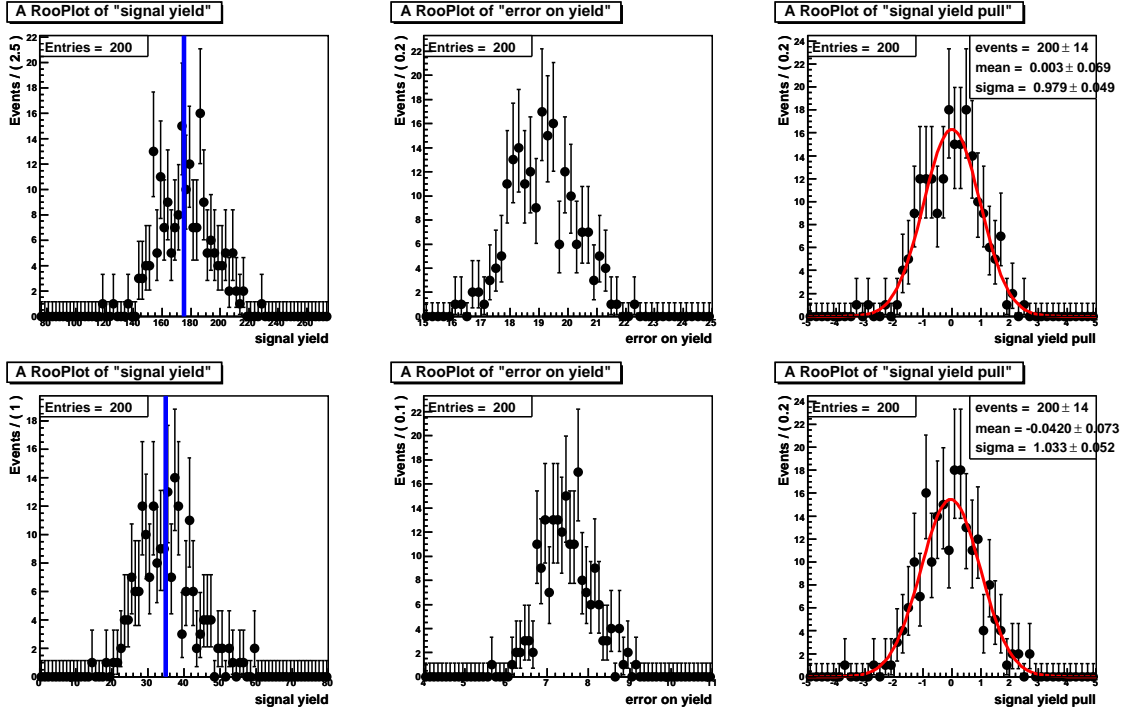


Figure 4.18: The yield, error on the yield and pull of the yield from Ensemble study (200 samples). Upper plot is for $B^+ \rightarrow \phi K^+ \gamma$ mode and lower plot is for $B^0 \rightarrow \phi K_S^0 \gamma$ mode.

is generated (~ 200 times) and independent samples are prepared by randomly selecting events expected in data. Since generic (5 times) and continuum MC (3 times) are limited in statistics, we generate these background samples using the shape parameters determined from full simulation. From Rare MC (50 times), we prepared 200 samples by randomly selecting events expected in data. Once prepared, we fit each ensemble to calculate the pull of the yield, which is shown in the Figure 4.18. The expected yields in data (175 for $B^+ \rightarrow \phi K^+ \gamma$ and 35 for $B^0 \rightarrow \phi K_S^0 \gamma$) are shown as vertical lines on the yield distribution.

In both the studies, no significant bias is found. However, the pull distribution from toy MC study shows a systematic shift on the negative side. This is nearly 2%(4%) of the expected statistical error 18(8) in $\phi K^+ \gamma$ ($\phi K_S^0 \gamma$) mode. These small bias of 0.36 and 0.32 events, will be included as additional sources of systematic error.

4.7.3 Signal PDF Calibration

In order to take into account any possible differences of the signal shape parameters between MC and real data, we calibrate the ΔE and M_{bc} signal shapes using a high statistics $B^0 \rightarrow K^*(892)^0(\rightarrow K^+\pi^-)\gamma$ control sample. This decay mode has a branching fraction, $\mathcal{B} = 4.01(2/3) \times 10^{-5} = 2.7 \times 10^{-5}$, one order of magnitude higher than the signal mode. Though it is different from the signal mode with a charged track, the resolutions in ΔE and M_{bc} are nearly same (since they are dominated by the radiative γ). In order to check the resolutions and for any possible experimental dependence, we generated 500,000 events for $B^0 \rightarrow K^{*0}(\rightarrow K^+\pi^-)\gamma$ signal MC (from exp07 to exp65), weighted according to luminosity of the data subsamples. It was reported that the measured photon energy is significantly shifted after exp31, causing a shift in the ΔE distribution. Therefore, we divide the sample into two parts, dataset1 (exp07 to exp31) and dataset2 (exp33 to exp65) to study the experimental dependence of the photon energy shift.

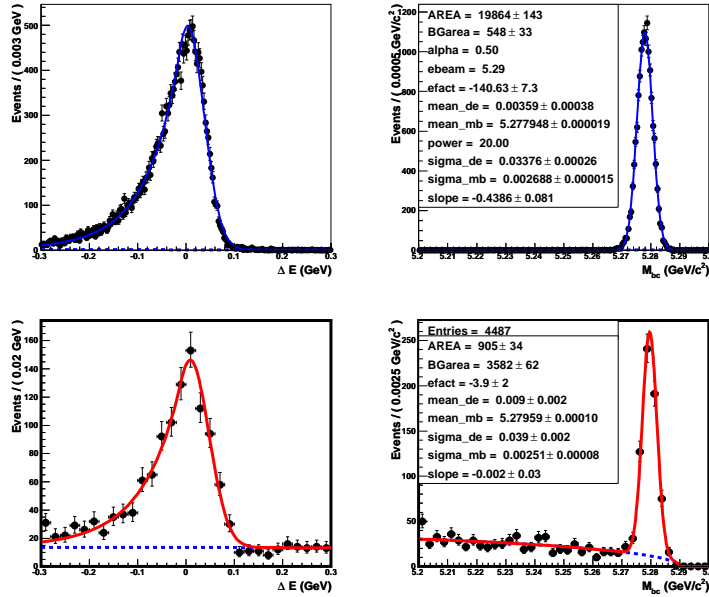


Figure 4.19: The ΔE - M_{bc} 2D fit to the $B^0 \rightarrow K^*\gamma$ sample for dataset1 (exp07 to exp31). The upper plot is from MC and the lower one is from data.

For the event selection in $B^0 \rightarrow K^*\gamma$, we use identical cuts for all particles common to $B^+ \rightarrow \phi K^+\gamma$. The $K^*(\rightarrow K^+\pi^-)$ candidates are selected with a mass cut $0.82 < M_{k\pi} < 0.97 \text{ GeV}/c^2$. We perform an extended unbinned maximum likelihood fit to the

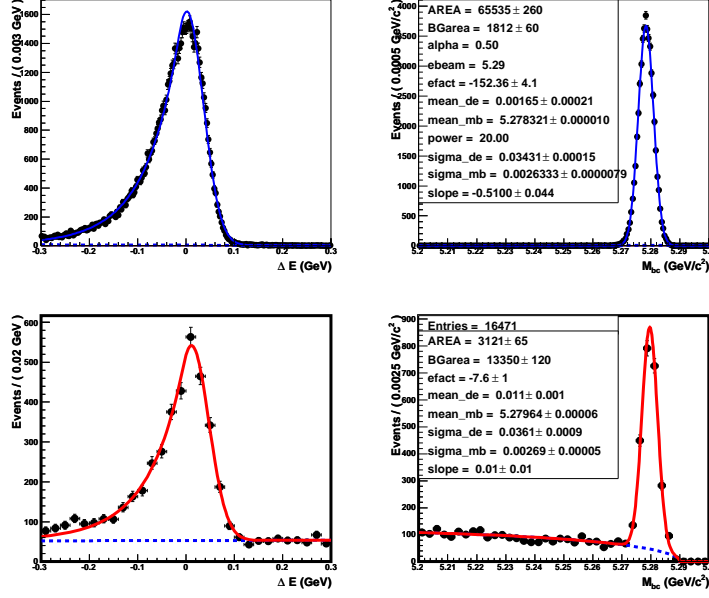


Figure 4.20: The ΔE - M_{bc} 2D fit to the $B^0 \rightarrow K^*\gamma$ sample for the dataset2 (exp33 to exp65). The upper plot is from MC and the lower one is from data.

Table 4.3: The fudge factor corrections from the $B^0 \rightarrow K^*\gamma$ sample, for dataset1 (exp07 to exp31). The units are in MeV.

$B^0 \rightarrow K^*\gamma$	Data	MC	Fudge Factor
ΔE (μ)	8.85 ± 2.27	3.59 ± 0.38	5.26 ± 2.31
ΔE (σ)	38.74 ± 1.71	33.76 ± 0.26	1.15 ± 0.05
M_{bc} (μ)	5729.56 ± 0.10	5277.95 ± 0.02	1.64 ± 0.10
M_{bc} (σ)	2.51 ± 0.08	2.69 ± 0.01	0.93 ± 0.03

Table 4.4: The fudge factor corrections from the $B^0 \rightarrow K^*\gamma$ sample, for dataset2 (exp33 to exp65). The units are in MeV.

$B^0 \rightarrow K^*\gamma$	Data	MC	Fudge Factor
ΔE (μ)	11.43 ± 1.15	1.65 ± 0.21	9.79 ± 1.17
ΔE (σ)	36.11 ± 0.89	34.31 ± 0.15	1.05 ± 0.03
M_{bc} (μ)	5729.64 ± 0.06	5278.32 ± 0.01	1.32 ± 0.06
M_{bc} (σ)	2.69 ± 0.05	2.63 ± 0.01	1.02 ± 0.02

two-dimensional ΔE - M_{bc} distribution. The ΔE distribution is modelled with a Crystal Ball line shape for signal (same α and N as in $B^+ \rightarrow \phi K^+ \gamma$) and a first order Chebyshev polynomial for the background. The M_{bc} distribution is modelled with a Gaussian for signal and ARGUS function [38] for background. The ΔE and M_{bc} fits to the $K^* \gamma$ sample are shown in Figs. 4.19 and 4.20. The corresponding fudge factors are listed in the Tables 4.3 and 4.4. We observed a shift of nearly 3.0 MeV in the mean of ΔE for the dataset2. The significant corrections are for ΔE mean by 5.26 (9.79) MeV for dataset1 (dataset2). The data is 15% (5%) wider in ΔE for dataset1 (dataset2). We apply these corrections when fitting the full data sample as described in the next section. We also checked that the resolutions in the neutral mode are nearly same as those for the charged mode, as shown in Table 4.6. Therefore, we apply same fudge factor corrections in both the modes.

Table 4.5: Signal shape parameters from the weighted MC sample for two different datasets ($B^+ \rightarrow \phi K^+ \gamma$). The units are in MeV.

data set	M_{bc}		ΔE	
	μ (MeV/ c^2)	σ (MeV/ c^2)	μ (MeV)	σ (MeV)
exp07-31	5277.47 ± 0.02	2.68 ± 0.02	3.11 ± 0.38	30.08 ± 0.26
exp33-65	5277.82 ± 0.01	2.65 ± 0.01	2.05 ± 0.21	30.29 ± 0.14

Table 4.6: Signal shape parameters from the weighted MC sample (exp07-65). The units are in MeV.

Decay Mode	M_{bc}		ΔE	
	μ (MeV/ c^2)	σ (MeV/ c^2)	μ (MeV)	σ (MeV)
$B^+ \rightarrow \phi K^+ \gamma$	5277.74 ± 0.01	2.66 ± 0.01	2.30 ± 0.18	30.2 ± 0.1
$B^0 \rightarrow \phi K_S \gamma$	5278.12 ± 0.01	2.65 ± 0.01	1.59 ± 0.21	30.1 ± 0.1

4.8 $B \rightarrow \phi K \gamma$ Signal

The signal yield is obtained from an extended unbinned maximum-likelihood fit to the two-dimensional ΔE - M_{bc} distribution. We model the shape for the signal component using the product of a Crystal Ball line shape for ΔE and a single Gaussian for M_{bc} . The

continuum background is modelled with the product of a first order Chebyshev polynomial for ΔE and an ARGUS function for M_{bc} . The $b \rightarrow c$ background is modelled with a product of a second order Chebyshev polynomial for ΔE and an ARGUS (ARGUS plus Gaussian) function for M_{bc} in the charged (neutral) mode. The small rare backgrounds (except the non-resonant component) are modelled with a product of two different Gaussians for ΔE and a single Gaussian for M_{bc} . In the final fit, the continuum parameters are floated while all other background parameters are fixed to the values from MC. The shape of the peaking backgrounds are fixed to that of signal. In the $B^+ \rightarrow \phi K^+ \gamma$ mode, the non-resonant background yield is fixed to the value from the ϕ sideband and using isospin symmetry, the same signal to background fraction is assumed in the neutral mode.

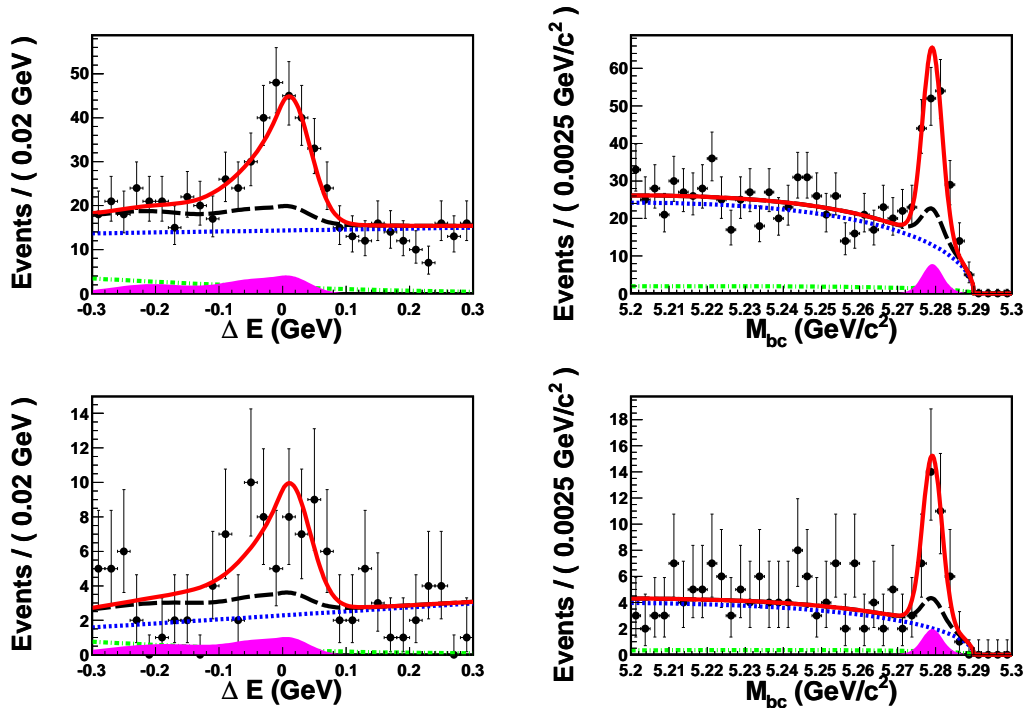


Figure 4.21: The ΔE and M_{bc} projections for $B^+ \rightarrow \phi K^+ \gamma$ (upper) and $B^0 \rightarrow \phi K_S^0 \gamma$ (lower). The points with error bars are the data. The different curves show the total fit function (solid, red), total background function (long-dashed, black), continuum component (dotted, blue), the $b \rightarrow c$ component (dashed-dotted, green), the sum of the non-resonant component and other charmless backgrounds (filled histogram, magenta).

We do a simultaneous fit to dataset1 and dataset2 while fixing the signal shape using the fudge factors obtained from the $B^0 \rightarrow K^* \gamma$ sample. The fit yields a signal of

$(144 \pm 17) B^+ \rightarrow \phi K^+ \gamma$ and $(37 \pm 8) B^0 \rightarrow \phi K_S^0 \gamma$ candidates. The projections of the fit results onto ΔE and M_{bc} are shown in Fig. 4.21.

4.9 $M(X_s)$ Efficiency Calibration

4.9.1 $M(X_s)$ mass dependence of the efficiency

In the signal MC generation, we modelled the X_s pseudo-resonance with a flat mass distribution from the kinematic limit $1.52 \text{ GeV}/c^2$ to $2.8 \text{ GeV}/c^2$. However, the reconstructed mass is no longer flat as shown in Fig. 4.22. In addition, the MC efficiency has a dependence on $M(X_s)$ mass. We divide the spectrum into seven bins and calculate the efficiency in each bin (number of events reconstructed divided by number of events generated in each bin). The results are shown in Fig. 4.23. The error on each point is the Poisson error of the reconstructed events divided by the number of generated events. We find a relative change in MC efficiency of 20% (15%) across the full spectrum in the $B^+ \rightarrow \phi K^+ \gamma$ ($B^0 \rightarrow \phi K_S^0 \gamma$) mode. The dip in the right plot in Fig. 4.22 corresponds to the D veto region ($1.852 < M(\phi K_S^0) < 1.878 \text{ GeV}/c^2$) in the neutral mode. This also results in the efficiency drop for the third bin in the right plot of Fig. 4.23. All these plots are from the ΔE - M_{bc} fit region.

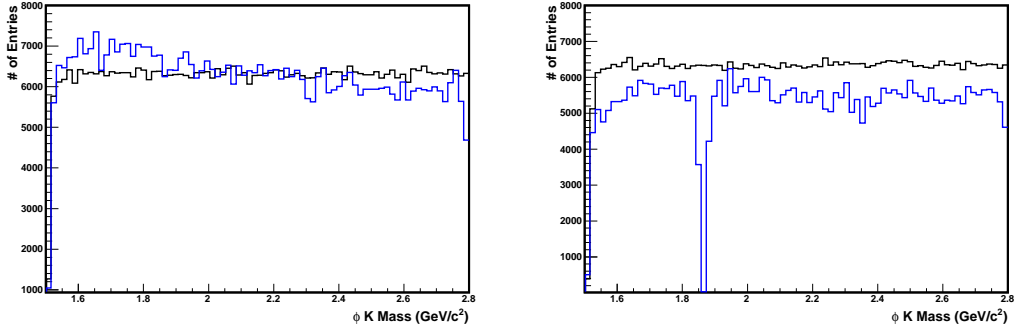


Figure 4.22: The generated flat $M(X_s)$ mass (black) and reconstructed $M(X_s)$ mass (blue) distributions in the fit region for the $B^+ \rightarrow \phi K^+ \gamma$ (left) and $B^0 \rightarrow \phi K_S^0 \gamma$ (right) decay modes. Clearly, the reconstructed mass differs from the generated distribution. The dip in the right plot is due to the D veto. The blue histogram is normalized to the total number of events in the black histogram.

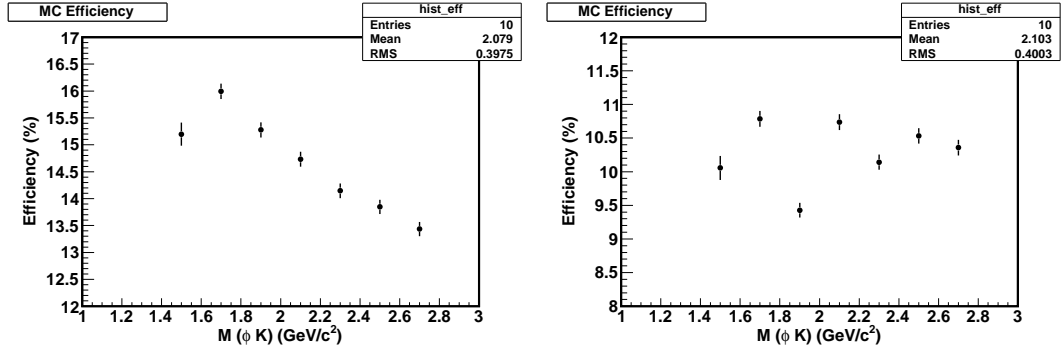


Figure 4.23: The signal MC efficiency as a function of the $M(X_s)$ mass in the fit region for the $B^+ \rightarrow \phi K^+ \gamma$ (left) and $B^0 \rightarrow \phi K_S^0 \gamma$ (right) mode. The efficiency drop in the third bin is due to the D veto.

4.9.2 $M(X_s)$ mass distribution in data

We search for a possible contribution from kaonic resonances decaying to ϕK . To unfold the $M_{\phi K}$ distribution, we subtract all possible backgrounds and correct the ϕK invariant mass for the efficiency. The background-subtracted and efficiency-corrected $M_{\phi K}$ distributions are shown in Fig. 4.24. The yield in each bin is obtained by the fitting procedure described in the previous section. The signal and background shapes are fixed to the values from the fit of total events. The fixed background yields are scaled by the ratio of events in each bin to that of total events. The three-body phase-space model from the MC simulation is shown by circles and is normalized to the efficiency-corrected signal yield. Nearly 72% of the signal events are concentrated in the low-mass region ($1.5 < M_{\phi K} < 2.0$ GeV/ c^2). It is clear that the observed ϕK mass spectrum differs significantly from that expected in a three-body phase-space decay.

The MC determined reconstruction efficiencies are corrected for this $M_{\phi K}$ dependence. We calculate a weighted average of the efficiency with the yield from the background subtracted and efficiency corrected $M(X_s)$ plot using the the following formula:

$$\epsilon_{avg} = \frac{\sum_i \epsilon_i N_i}{N} \quad (4.9.1)$$

where i runs over all bins. ϵ_i is MC efficiency and N_i is the number of events in i -th bin of the background subtracted and efficiency corrected plot. N is the total number of events, summed over all bins. The MC efficiency is analyzed upto 2.8 GeV while data are examined up to 4.0 GeV. For all bins after 2.8 GeV, the efficiency of the closest bin is assigned. The

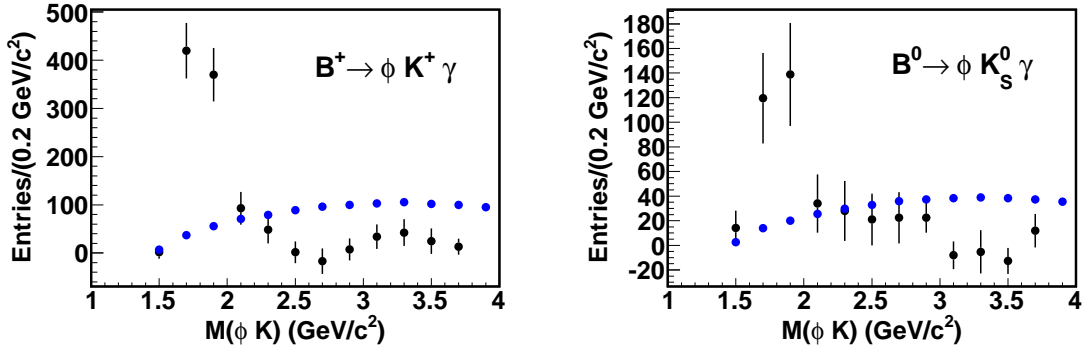


Figure 4.24: The background-subtracted and efficiency-corrected ϕK mass distributions for $B^+ \rightarrow \phi K^+ \gamma$ (left) and $B^0 \rightarrow \phi K_S^0 \gamma$ (right). The points with error bars represent the data. The three-body phase-space model from the MC simulation is shown by the circles (blue).

error on ϵ_{avg} is calculated using the error propagation formula:

$$(\Delta\epsilon)^2 = \sum_i \left[\frac{(\epsilon_i - \epsilon_{avg})}{N} * \Delta N_i \right]^2 + \sum_i \left[\left(\frac{N_i}{N} \right) * \Delta\epsilon_i \right]^2 \quad (4.9.2)$$

In the $B^+ \rightarrow \phi K^+ \gamma$ mode, the fitted efficiency from MC is $(13.4 \pm 0.1)\%$ and the re-weighted efficiency is $(15.3 \pm 0.1)\%$. In the $B^0 \rightarrow \phi K_S^0 \gamma$ mode, the fitted efficiency from MC is $(10.0 \pm 0.1)\%$ and re-weighted efficiency is $(10.2 \pm 0.1)\%$.

4.10 Systematic Errors

Various sources of systematic errors are considered for the branching fraction measurement. Each category of systematic is described in detail below. The multiplicative systematics are listed in Table 4.8 and Table 4.9. The additive systematics, which affect the signal yield are listed in Table 4.10. We add each contribution in quadrature to obtain the total systematic error.

1. Fit parameter

We calculate this systematic error by varying all the fixed parameters in the final fit by $\pm 1\sigma$ of their statistical error. This includes varying the fixed signal, background shapes and the background yields. We also include the uncertainty due to the calibration by varying the fudge factors by their errors. The resulting percentage changes in the returned signal yield are listed in Table 4.10. The total uncertainty on the signal

yield from the fit parameters is 8.17% in the $\phi K^+\gamma$ mode and 8.57% in the $\phi K_S^0\gamma$ mode. The dominant contribution is from the non-resonant $K^+K^-K\gamma$ yield (8.0%).

2. Charged track reconstruction Efficiency

The reconstruction efficiency of charged tracks is calculated using the tracking efficiency error function provided by the tracking group [32]. This is based from a study of partially versus fully reconstructed D^* decays, which calculates the tracking efficiency error based on the particle type and momentum. The program is run over the signal MC (generated for each experiment proportional to the luminosity) and the mean error is calculated for each reconstructed track in the final state. The results are then linearly summed to obtain the final tracking uncertainty, which is 3.27% (4.62%) for $B^+ \rightarrow \phi K^+\gamma$ ($B^0 \rightarrow \phi K_S^0\gamma$).

3. Particle identification efficiency

The charged kaon identification efficiency is calculated using a program provided by the PID group [54], determined from D^{*+} decays in the channel, $D^{*+} \rightarrow D^0(K^-\pi^+)\pi^+$. It gives the efficiency ratio ϵ (data/MC). We run the program for each kaon track separately for SVDI and SVDII datasets and weight them according to the integrated luminosity. The final efficiency ratio is the product of the efficiency ratios for all kaon tracks and the error is obtained by adding the fractional uncertainties in quadrature. The error is included as an additional source of systematics, which is 1.36% (1.41%) for $B^+ \rightarrow \phi K^+\gamma$ ($B^0 \rightarrow \phi K_S^0\gamma$).

4. Photon detection efficiency

An error of 2.0% on the reconstruction efficiency of the signal photon is taken from a study of the radiative Bhabha sample [55].

5. $N_{B\bar{B}}$

In this analysis, we use the Belle data collected through experiments 07 to 65, which contains $(771.581 \pm 10.566) \times 10^6$ $B\bar{B}$ events [36]. This accounts for an error of 1.37% in the final result.

6. K_S^0 reconstruction efficiency

The error on the reconstruction of the K_S^0 candidates is taken to be 4.6% from a study of D^+ decays into $K_S^0\pi^+$ and $K^-\pi^+\pi^+$ [56].

7. MC efficiency

We reweight the MC efficiency with the yield from the background subtracted and efficiency corrected $M(X_s)$ plot. The fractional errors are included in systematics, which is 0.95% (1.21%) for $B^+ \rightarrow \phi K^+ \gamma$ ($B^0 \rightarrow \phi K_S^0 \gamma$).

8. Daughter branching fractions

We use the daughter branching fractions $\mathcal{B}(\phi \rightarrow K^+ K^-) = (49.2 \pm 0.6) \times 10^{-2}$ and $\mathcal{B}(K_S^0 \rightarrow \pi^+ \pi^-) = (69.20 \pm 0.05) \times 10^{-2}$ from PDG 2008 [20]. This accounts for a total uncertainty of 1.22%.

9. Fit bias

The small bias found in the 2D fitter using the Toy MC pull test and the ensemble test are used as an additional source of systematics.

10. LR cut efficiency

We use the $B \rightarrow K^* \gamma$ control sample to calculate the LR cut efficiency. We vary the LR cut by 10% of its nominal value (0.65). For each cut, we estimate the MC efficiency, fit the data to determine the signal yield and calculate the ratio (yield/efficiency). (the values are summarized in Table 5.1). The percentage change in the ratio from the nominal value is used as the systematic error, which is 0.33% for the positive variation and 0.28% for the negative variation. The same values of systematic uncertainty are used for both the charged and neutral mode.

11. D^0 veto

The D veto (1.852 to 1.878 GeV) is applied in the neutral mode. The veto window corresponds to $\sim \pm 4\sigma$, where σ is the width of the Gaussian (3.27 GeV) obtained by fitting the peak near the D mass. The number of events rejected in data by this veto is 49 (4) in the ΔE - M_{bc} fit (signal) region.

Table 4.7: The signal yields, efficiencies, ratio and systematics using the $B^0 \rightarrow K^*\gamma$ control sample.

LR Cut	Yield	Efficiency (%)	ratio (10^4)	systematics (%)
0.715	3802 ± 69	16.1 ± 0.1	2.3615	0.327
0.650	4025 ± 73	17.1 ± 0.1	2.3538	-
0.585	4225 ± 76	17.9 ± 0.1	2.3603	0.276

Table 4.8: Summary of multiplicative systematic uncertainties in the charged mode $B^+ \rightarrow \phi K^+\gamma$.

Systematic error sources	Uncertainty (%)	
	$+\sigma$	$-\sigma$
Charged track efficiency	3.27	-3.27
Particle identification efficiency	1.36	-1.36
Photon detection efficiency	2.40	-2.40
$N_{B\bar{B}}$	1.37	-1.37
MC efficiency	0.95	-0.95
Daughter branching fractions	1.22	-1.22
Fit bias	0.2	-0.2
LR cut efficiency	0.33	0.0
Total	4.76	-4.75

Table 4.9: Summary of multiplicative systematic uncertainties in the neutral mode $B^0 \rightarrow \phi K_S^0 \gamma$.

Systematic error sources	Uncertainty (%)	
	$+\sigma$	$-\sigma$
Charged track efficiency	4.62	-4.62
Particle identification efficiency	1.41	-1.41
Photon detection efficiency	2.40	-2.40
K_S^0 reconstruction efficiency	4.60	-4.60
$N_{B\bar{B}}$	1.37	-1.37
MC efficiency	1.21	-1.21
Daughter branching fractions	1.22	-1.22
LR cut efficiency	0.33	0.0
Total	7.43	-7.42

Table 4.10: Summary of additive systematic uncertainties from the fit parameters. The values in the right two columns are the percentage changes in the yield.

Systematic error sources	Uncertainties (%)	
	$B^+ \rightarrow \phi K^+ \gamma$	$B^0 \rightarrow \phi K_S^0 \gamma$
Signal PDF shape	0.2	0.2
Generic PDF shape	0.2	0.4
Rare PDF shape	0.5	1.0
Generic yield	0.6	1.0
Rare yield	0.7	1.6
Fudge factor	1.3	1.1
Non-resonant yield	8.0	8.0
Fit bias	0.2	2.7
Total	8.19	9.00

4.11 Branching Fraction and Significance

The branching fraction (\mathcal{B}) of the $B \rightarrow \phi K \gamma$ decay is defined as

$$\mathcal{B} = \frac{N_{\text{sig}}}{\epsilon \times N_{B\bar{B}} \times \mathcal{B}_{\text{sec}}} \quad (4.11.1)$$

where N_{sig} is the signal yield, ϵ is the weighted efficiency, $N_{B\bar{B}}$ is the number of $B\bar{B}$ pairs in the data sample and \mathcal{B}_{sec} is the product of daughter branching fractions [20]. The results are summarized in Table 4.12. The total systematic error is 9.47% (11.67%) in $B^+ \rightarrow \phi K^+ \gamma$ ($B^0 \rightarrow \phi K_S^0 \gamma$) mode after adding multiplicative and additive systematics in quadrature.

The signal in the charged mode has a significance of 9.6σ , whereas that for the neutral mode is 5.4σ , including systematic uncertainties described above. The significance is defined as $\sqrt{-2\ln(\mathcal{L}_0/\mathcal{L}_{\text{max}})}$, where \mathcal{L}_{max} (\mathcal{L}_0) denote the maximum likelihood for the best fit (with signal yield fixed to zero). The additive sources of systematic uncertainty described below are included in the significance by varying each by its error and taking the lowest significance. The likelihood scan of the signal yield is shown in Fig. 4.25. The Y-axis is the square of the significance and the X-axis is the signal yield.

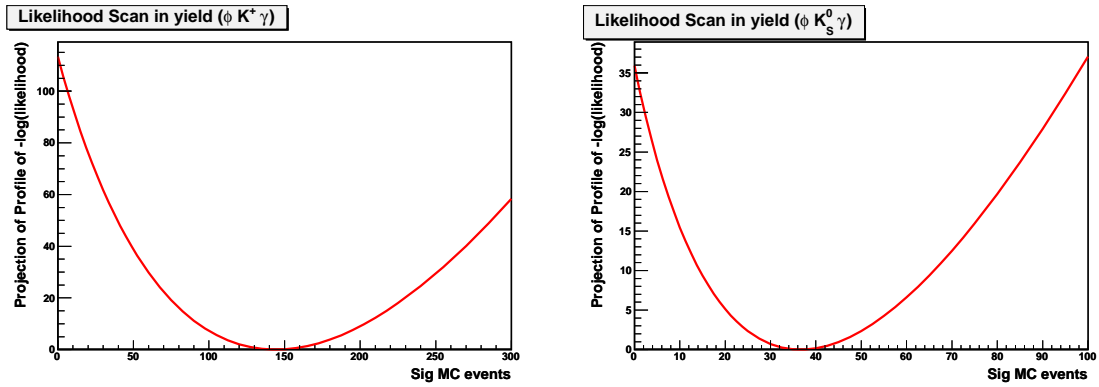


Figure 4.25: The likelihood scan of the signal yield for $B^+ \rightarrow \phi K^+ \gamma$ (left) and $B^0 \rightarrow \phi K_S^0 \gamma$ (right) decay mode (statistical only).

Table 4.11: The likelihood of the fits and signal significances (\mathcal{S}) for the $B^+ \rightarrow \phi K^+ \gamma$ and $B^0 \rightarrow \phi K_S^0 \gamma$ decay modes (Errors are statistical only).

Mode	$-\ln(\mathcal{L}_0)$	$-\ln(\mathcal{L}_{\max})$	$-2 \ln(\mathcal{L}_0/\mathcal{L}_{\max})$	$\mathcal{S} (\sigma)$
$B^+ \rightarrow \phi K^+ \gamma$	-34000.5	-34057.1	113.3	10.6
$B^0 \rightarrow \phi K_S^0 \gamma$	-4682.2	-4700.1	35.9	6.0

Table 4.12: The signal yields (Y), weighted efficiencies (ϵ), branching fractions (\mathcal{B}) and significances (\mathcal{S}) for the $B^+ \rightarrow \phi K^+ \gamma$ and $B^0 \rightarrow \phi K^0 \gamma$ decay modes (the systematic uncertainty is included in the significance).

Decay Mode	Y	ϵ (%)	$\mathcal{B} (10^{-6})$	$\mathcal{S} (\sigma)$
$B^+ \rightarrow \phi K^+ \gamma$	144 ± 17	15.3 ± 0.1	$2.48 \pm 0.30 \pm 0.24$	9.6
$B^0 \rightarrow \phi K^0 \gamma$	37 ± 8	10.2 ± 0.1	$2.74 \pm 0.60 \pm 0.32$	5.4

Chapter 5

Measurements of time-dependent CP violation in $B^0 \rightarrow \phi K_S^0 \gamma$

5.1 Introduction

In this chapter, we describe the first measurements of time-dependent CP violation parameters in a $b \rightarrow s\gamma$ transition decay, $B^0 \rightarrow \phi K_S^0 \gamma$ using the full data sample (772×10^6 $B\bar{B}$ pairs) collected by the Belle detector. This decay is sensitive to NP from right-handed currents rather than a NP phase. Since the CP asymmetry is suppressed in the SM, any significantly larger value will be a clear hint of NP. For the time-dependent measurement, we follow similar procedures for vertex reconstruction, flavor-tagging and CP fit as described in chapter 3 for the $B^0 \rightarrow \psi(2S)K_S^0$ mode. The vertex position for the f_{rec} decay is reconstructed using the two charged kaon tracks from the ϕ meson. In order to increase the signal yield for CP-fitting, we loosen some of the selection criteria that were used for the branching fraction measurement.

5.2 Selection Criteria

Using the event selection described for the branching fraction measurements in $B \rightarrow \phi K \gamma$ decays, we have a signal yield of 144 ± 17 events for the charged mode and 37 ± 8 events for the neutral mode (determined from an ΔE - M_{bc} 2D fit). In order to increase the signal event yield for the time-dependent analysis, we use r -bin dependent LR cuts and include the photons from the endcap region of the calorimeter. This increases the efficiency by 17% compared to the branching fraction analysis.

5.2.1 r -bin dependent LR cut

For the branching fraction measurement, we used a common LR cut ($LR > 0.65$) for all the seven flavor tagging r -bins. This is used to suppress the continuum background. For the time-dependent measurement, we re-optimize this separately for each r -bin ($r = 1 - 2w_{\text{tag}}$, w_{tag} is the wrong tag fraction). The selection criteria is determined by maximizing the FOM, $S_i/\sqrt{S_i + B_i}$ ($i = 0, 1, \dots, 6$), where S_i (B_i) are the expected number of signal (continuum) events in the ΔE - M_{bc} signal region. We use the branching fractions measured in section 4 to scale the MC to the data sample.

In summary, we apply a common set of LR cuts for both modes : $LR > 0.65$ for bins 0 to 4, $LR > 0.5$ for bin 5 and $LR > 0.2$ for bin 6 (as summarized in the Table 5.1). Significant improvement comes from the higher two bins (5% gain in signal efficiency) since signal purity is high in those bins.

Table 5.1: The re-optimized r -bin dependent LR cuts for the charged as well as the neutral $B \rightarrow \phi K \gamma$ mode.

r -bin	0	1	2	3	4	5	6
Range	$0 \leq r \leq 0.1$	$0.1 < r \leq 0.25$	$0.25 < r \leq 0.5$	$0.5 < r \leq 0.625$	$0.625 < r \leq 0.75$	$0.75 < r \leq 0.875$	$0.875 < r \leq 1.0$
LR cut	0.65	0.65	0.65	0.65	0.65	0.5	0.2

5.2.2 Endcap photons and Signal box

Using the branching fraction cuts, we have nearly 108 (27) signal events for $B^+ \rightarrow \phi K^+ \gamma$ ($B^0 \rightarrow \phi K_S^0 \gamma$) mode in the signal box defined as $-0.08 \text{ GeV} < \Delta E < 0.05 \text{ GeV}$ and $5.27 \text{ GeV}/c^2 < M_{\text{bc}} < 5.29 \text{ GeV}/c^2$. In order to increase the signal yield events for the CP fit, we also apply the following cuts in addition to the r -bin dependent LR cut. We select events inside the box defined as $-0.2 \text{ GeV} < \Delta E < 0.1 \text{ GeV}$ and $5.27 \text{ GeV}/c^2 < M_{\text{bc}} < 5.29 \text{ GeV}/c^2$. The ΔE window is enlarged to include the tail of the signal (a gain of $\sim 24\%$ in signal efficiency). In the branching fraction measurement, only ECL barrel region photons were used. We extend the photon coverage to both endcap regions while keeping the same energy cut ($1.4 < E_\gamma^* < 3.4 \text{ GeV}$). We have nearly a $\sim 12\%$ gain in efficiency due to the addition of endcap photons.

The ΔE - M_{bc} 2D fit is repeated including these new cuts. The fixed backgrounds are re-estimated from a fit to the corresponding MC samples. The signal gain is consistent with the increase in efficiency with a small increase in background. Since the non-resonant

($B \rightarrow K^+K^-K\gamma$) component has the same new physics effects as the signal $B \rightarrow \phi K\gamma$, we treat this as signal for the time-dependent study [13]. Using the new cuts, we have 168 (40) signal events (non-resonant is included) in the $B^+ \rightarrow \phi K^+\gamma$ ($B^0 \rightarrow \phi K_S^0\gamma$) mode for CP fitting. The events for each component are summarized in Table 5.2 and 5.3.

We also studied the efficiency of $M(\phi)$ cut (increasing the cut range from 10 MeV to 20 MeV). This results in 8% increase in signal with 40% additional continuum background. However, from a toy-MC study (described in next section) there is only a slight improvement in the statistical error of S from 0.34 to 0.32. Therefore, to keep the background treatment simple and to avoid additional background systematics, we retain the 10 MeV $M(\phi)$ cut used for the branching fraction measurement.

Table 5.2: The signal and background components in the TCPV signal box for the $B^+ \rightarrow \phi K^+\gamma$ mode (vertexing is applied, $\sim 94\%$ efficiency). The background components are categorized according to the different PDFs used in the fit.

	BF cuts	New Cuts	$M(\phi) < 20$ MeV
Sig	139	148	160
Continuum	209	252	352
Gen_peak	4	5	5
Gen_bg	22	26	40
Rare1	9	9	11
Rare2	7	9	10
Non-res	20	20	37

Table 5.3: The signal and background components in the TCPV signal box for the $B^0 \rightarrow \phi K_S^0\gamma$ mode (vertexing is applied, $\sim 94\%$ efficiency). The background components are categorized according to the different PDFs used in the fit.

	BF cuts	New Cuts
Sig	32.8	35.5
Continuum	33.6	37.3
Gen_peak	0.5	0.6
Gen_bg	4.8	5.5
Rare1	1.4	1.7
Rare2	3.2	3.5
Non-res	5.1	4.7

5.3 Parameters for time-dependent Study

5.3.1 Signal and background fractions

For the CP fit, we use r -bin dependent signal and background fractions. The partition of the signal and fixed backgrounds (generic, rare) into r -bins are determined from separate fits to the appropriate MC samples. We multiply these MC determined r -bin ratios with the yield from data to obtain event yields in each r -bin (For the non-resonant $B \rightarrow K^+K^-K^+\gamma$ contribution, we use signal MC r -bin ratios). Similarly the partition of continuum into r -bins is obtained from data fits for each r -bin. Here, we fix the shape and yield of all other PDFs obtained from fit to entire data sample. Since the $B\bar{B}$ background MC samples in the neutral mode are limited in statistics, we use the same background r -bin ratios as in the control mode. A graphical representation of signal and background fractions in different r -bins is shown in Fig. 5.1.

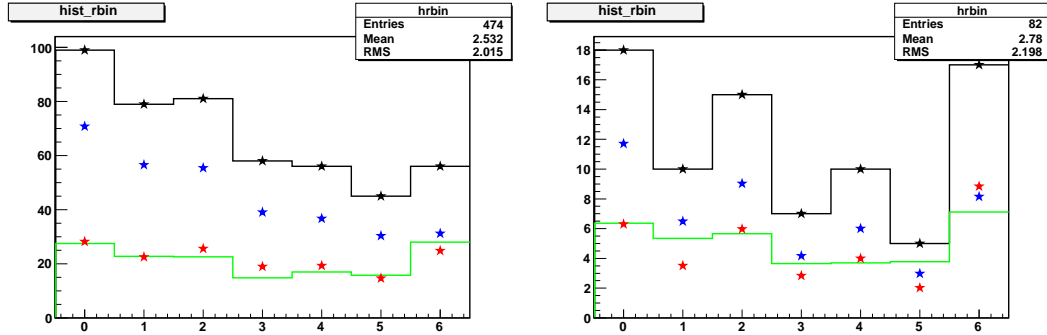


Figure 5.1: Graphical representation of signal and background fractions in different r -bins for events in signal box. $B^+ \rightarrow \phi K^+\gamma$ (left) and $B^0 \rightarrow \phi K_S^0\gamma$ (right). The points are data (solid black histogram), signal MC (solid green histogram), red point (assumed signal distribution in data), blue points (assumed background distribution in data) and black points (sum of signal and background in data).

5.3.2 Continuum parameters from data sideband

We use the data sideband ($0.1 \text{ GeV} < \Delta E < 0.3 \text{ GeV}$ and $M_{bc} < 5.26 \text{ GeV}/c^2$) to determine the continuum parameters. The sideband contains nearly 97% of continuum with a 3% contamination from generic background. We include an additional lifetime PDF while fitting the sideband (the effective lifetime is determined from generic MC sideband). A total

of 11 parameters are obtained from the sideband. These include the global parameters (τ_{bg} , μ_l , μ_d) and s_{main} , s_{tail} , f_{tail} , f_δ parameters for single and multiple tracks. In the SVD1 dataset for the charged mode and in the neutral mode, where statistics are limited, we obtain common parameters for single and multiple tracks. The fit results are shown in figures 5.2 and 5.3.

FCN=	686.6274	FROM MINOS	STATUS=SUCCESSFUL	772 CALLS	1015 TOTAL
		EDM= 0.38E-09	STRATEGY= 1	ERROR MATRIX	ACCURATE
EXT PARAMETER			PARABOLIC	MINOS ERRORS	
NO.	NAME	VALUE	ERROR	NEGATIVE	POSITIVE
1	MU_L	-0.74280E-02	0.84320E-01	-0.84442E-01	0.84653E-01
2	TAU_BG	0.35418	0.14910	-0.16913	0.14661
3	S_MAIN	0.55988	0.17810	-0.18651	0.18348
4	S_TAIL	3.2893	0.85794	-0.72260	1.2755
5	F_TAIL	0.39823	0.18074	-0.16469	0.19843
FCN=	2960.424	FROM MINOS	STATUS=SUCCESSFUL	4304 CALLS	4886 TOTAL
		EDM= 0.19E-07	STRATEGY= 1	ERROR MATRIX	ACCURATE
EXT PARAMETER			PARABOLIC	MINOS ERRORS	
NO.	NAME	VALUE	ERROR	NEGATIVE	POSITIVE
1	MU_L	-0.10911	0.20785	-0.53069	0.18413
2	MU_D	0.95669E-01	0.96124E-01	-0.97696E-01	0.10174
3	TAU_BG	0.55638	0.18880	-0.18393	0.20908
4	S_MAIN1	1.1989	0.12125	-0.11853	0.12350
5	S_TAIL1	11.195	3.7186	-2.8998	5.4669
6	F_TAIL1	0.43830E-01	0.22959E-01	-0.19443E-01	0.26831E-01
7	S_MAIN2	1.1697	0.90401E-01	-0.90215E-01	0.91899E-01
8	S_TAIL2	2.8796	0.34769	-0.31120	0.40795
9	F_TAIL2	0.18179	0.72157E-01	-0.66570E-01	0.78224E-01
10	F_DELTA	0.59344	0.20919	-0.25007	0.24410
FCN=	789.0687	FROM MINOS	STATUS=SUCCESSFUL	901 CALLS	1234 TOTAL
		EDM= 0.24E-08	STRATEGY= 1	ERROR MATRIX	ACCURATE
EXT PARAMETER			PARABOLIC	MINOS ERRORS	
NO.	NAME	VALUE	ERROR	NEGATIVE	POSITIVE
1	MU_L	-0.18090	0.68952E-01	-0.69522E-01	0.68536E-01
2	TAU_BG	0.35972	0.12393	-0.13401	0.12123
3	S_MAIN	0.53212	0.17636	-0.15757	0.23396
4	S_TAIL	2.8022	0.88457	-0.83027	1.0634
5	F_TAIL	0.66197	0.17566	-0.21405	0.16346

Figure 5.2: The continuum background Δt PDF parameters determined from ΔE - M_{bc} data sideband. The fit results for the charged mode (upper for the SVD1 dataset, middle for the SVD2 dataset) and for the neutral mode (lower).

5.3.3 Effective lifetime of $B\bar{B}$ backgrounds

The time-dependent PDF for the non-resonant component is modeled in the same way as signal. Other $B\bar{B}$ backgrounds such as generic and rare decays are also treated like signal, but with different effective lifetimes obtained from fits to the appropriate MC

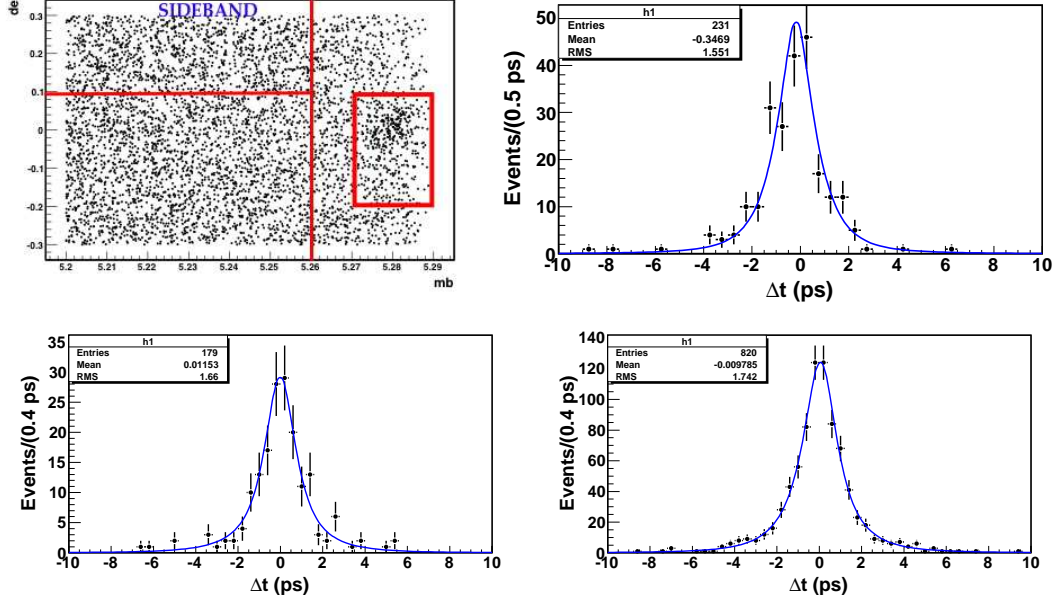


Figure 5.3: The ΔE - M_{bc} 2D plot showing the signal box and sideband region (upper left), lifetime fit to data sideband for $B^0 \rightarrow \phi K_S^0 \gamma$ (upper right) and $B^+ \rightarrow \phi K^+ \gamma$ (lower left for SVD1, lower right for SVD2).

sample. For the rare component, we remove the non-resonant background to determine the effective lifetime. We assume no CP in the $B\bar{B}$ background components. Possible CP violation will be considered in systematics. Figure 5.4 shows the proper time distribution of the generic and rare backgrounds. The fit results are summarized in Table 5.4.

Table 5.4: The effective lifetime values obtained from lifetime fits to background MC samples. These values are fixed in the final CP fit.

Background	$B^+ \rightarrow \phi K^+ \gamma$	$B^0 \rightarrow \phi K_S^0 \gamma$
Rare (w/o non-res)	1.49 ± 0.05 ps	1.45 ± 0.10 ps
Generic (box)	1.23 ± 0.16 ps	1.94 ± 0.48 ps
Generic (sideband)	0.52 ± 0.11 ps	1.86 ± 0.40 ps

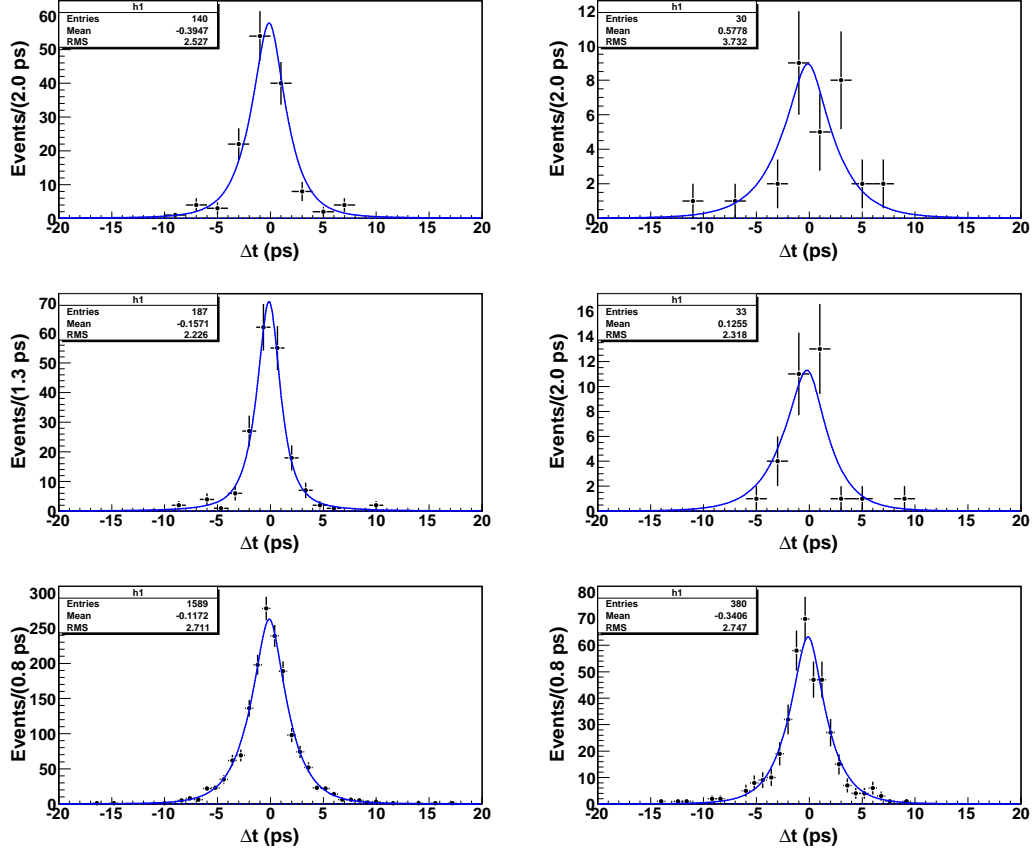


Figure 5.4: The lifetime fits to the background MC samples. The left column for $B^+ \rightarrow \phi K^+ \gamma$ and right column for $B^0 \rightarrow \phi K_S^0 \gamma$. The fit plots from upper to lower are for generic MC (signal box), generic MC (sideband), rare MC (signal box).

5.4 Ensemble Test

In order to check for any possible fit bias and to estimate the expected error on \mathcal{S} and \mathcal{A} in the final data, we generate a large number of pseudo-experiments with toy MC. Each toy sample is generated with central values $(\mathcal{S}, \mathcal{A}) = (0, 0)$ and having the same number of events as in the data signal box. The CP fit is then performed for each pseudo-experiment with the same PDF as used in the generation. The accuracy of each fit is determined by calculating the pull defined as

$$\text{Pull} = \frac{S_i^{\text{fit}} - S_i^{\text{gen}}}{\sigma_i^{\text{fit}}} \quad (5.4.1)$$

where $\mathcal{S}_i^{\text{fit}}$ and σ_i^{fit} are the fitted \mathcal{S} value and error on it for each sample (the same definition is also used for the pull of \mathcal{A}). We use the asymmetric MINOS errors opposite to the sign of the residual. The fit result, error and the pull distribution are shown in figures 5.5 and 5.6. The pull distributions are fitted with a Gaussian function to determine the mean and sigma. We only use the samples where the fit converged successfully.

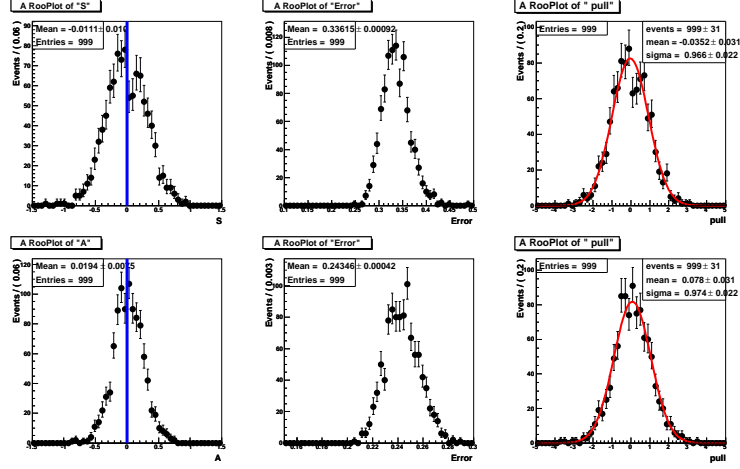


Figure 5.5: (Toy MC Study for $B^+ \rightarrow \phi K^+ \gamma$) The central value, error and pull distributions for \mathcal{S} (upper) and \mathcal{A} (lower).

The expected errors for $\phi K^+ \gamma$ are 0.34 for \mathcal{S} and 0.24 for \mathcal{A} . We also perform a similar toy MC study for the 20 MeV $M(\phi)$ cut. The error on \mathcal{S} is slightly improved to 0.32. The expected errors for $B^0 \rightarrow \phi K_S^0 \gamma$ are 0.78 for \mathcal{S} and 0.50 for \mathcal{A} . In the neutral mode, nearly 33% of the samples have CP parameters outside of the physical boundary ($\sqrt{\mathcal{S}^2 + \mathcal{A}^2} > 1$). The error distribution for these low statistics also departs from a normal Gaussian distribution and has a long tail.

5.5 Validation Checks

Before proceeding to the CP fit in the final data sample, we did various cross-checks to ensure the reliability of the results.

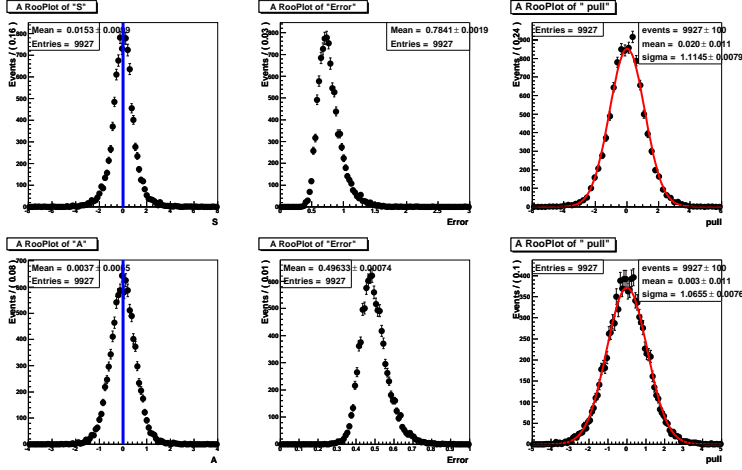


Figure 5.6: (Toy MC Study for $B^0 \rightarrow \phi K_S^0 \gamma$) The central value, error and pull distributions for S (upper) and A (lower).

5.5.1 CP fit in Signal MC

We perform a CP fit to signal MC. The S and A fit results are consistent with zero in the control sample ($S = 0.002 \pm 0.03$, $A = 0.003 \pm 0.02$). In the neutral mode, we use the EVTGEN MC model SVP_CP to generate CP -violating effects. The generated value of S is 0.69 and the fit results are consistent ($S = 0.71 \pm 0.03$ and $A = 0.01 \pm 0.02$).

5.5.2 CP Linearity Check

For the neutral mode, in order to check for any fit biases, we generate GEANT Signal MC samples with the input S value varied in steps of 0.2 from -1 to 1 (with A fixed to zero). The residuals of the fit results (fitter value–input value) are shown in figure 5.7. Although there is a small statistical fluctuations, no significant bias is observed.

5.5.3 Lifetime fit in Signal MC

We did a lifetime fit to the generator Δt in signal MC. The fit results $\tau(B^+) = (1.640 \pm 0.008)$ ps and $\tau(B^0) = (1.526 \pm 0.007)$ ps are consistent with the generator level input. We then perform a lifetime fit to the reconstructed Δt distribution in high statistics MC samples as shown in figure 5.8. The fit results are $\tau(B^+) = (1.60 \pm 0.01)$ ps and $\tau(B^0) = (1.51 \pm 0.01)$ ps. These lifetimes are shorter than the input value by 5σ and 2σ .

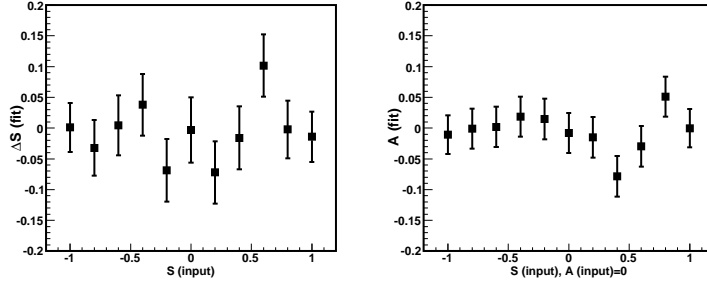


Figure 5.7: The residuals of the \mathcal{S} and \mathcal{A} fit results of the linearity check for $B^0 \rightarrow \phi K_S^0 \gamma$ mode.

Since the CP violation parameters are unbiased, we will include this small lifetime bias in the systematics.

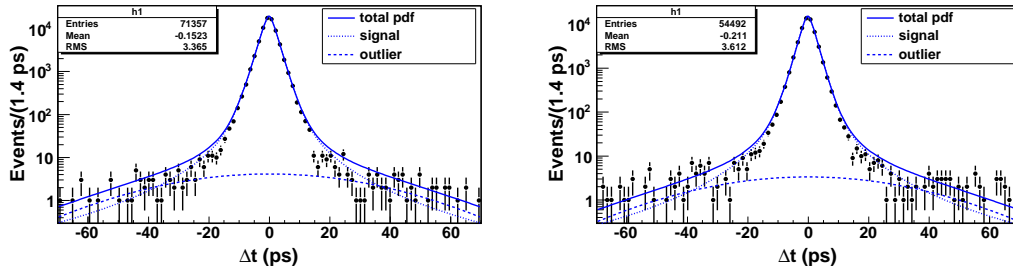


Figure 5.8: The lifetime fit to the reconstructed Δt in signal MC for $B^+ \rightarrow \phi K^+ \gamma$ (left) and $B^0 \rightarrow \phi K_S^0 \gamma$ (right).

5.5.4 Vertex Resolution

We check the vertex resolution for the rec side and the tag side by plotting the difference between reconstructed and generated z position. The rec side resolution ($115 \mu m$) is worse than the tag side ($104 \mu m$) (similar values are also found for the neutral mode). We compared the resolution with other modes like $B^+ \rightarrow \phi K^+$ ($100 \mu m$ rec, $102 \mu m$ tag) and $B^+ \rightarrow \psi(2S)K^+$ ($60 \mu m$ rec, $104 \mu m$ tag). The poor resolution is caused by the narrow $\phi \rightarrow K^+ K^-$ opening angle and low momentum tracks (multiple scattering in the three body decay).

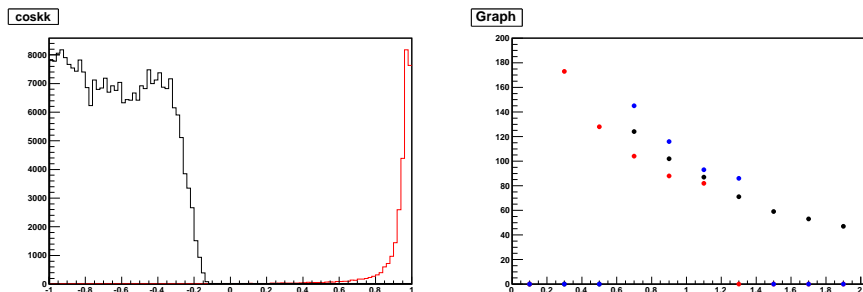


Figure 5.9: The left plot shows the cosine of the angle between the K^+ and K^- (red) or e^+ and e^- (black). The right plot shows the z resolution in bins of average transverse momentum ($\langle P_T \rangle$) of the daughter tracks. Red points are for $\phi K^+ \gamma$, blue points for ϕK^+ and black points are for $\psi(2S) K^+$.

5.5.5 Lifetime and CP fit in $B^0 \rightarrow K^{*0} \gamma$

We cross-checked the CP fitter in a high statistics flavor-specific control sample ($B^0 \rightarrow K^{*0} \gamma$). The B^0 decay vertex is reconstructed from K^+ and π^- tracks from the K^{*0} decay. We follow exactly the same procedure as in $B \rightarrow \phi K \gamma$. The shape parameters are determined from the $\Delta E - M_{bc}$ 2D fit (with a cut on K^{*0} mass : $0.82 < M(K^*) < 0.97$ GeV). Different shape parameters, signal and background fractions as well as continuum Δt parameters are determined separately for SVD1 and SVD2. We obtain 4903 events in the signal box with a signal fraction of 80% and background fraction of 20%. The lifetime and CP fit results are summarized in the Table 5.5 and are shown in Figure 5.10. The results are all consistent with the PDG value.

Table 5.5: Lifetime and CP fit results in the $B^0 \rightarrow K^{*0} \gamma$ control sample.

Data Sample	Lifetime fit (ps)	CP fit	
		S	A
SVD1	1.56 ± 0.08	0.15 ± 0.15	0.12 ± 0.10
SVD2	1.56 ± 0.03	-0.01 ± 0.06	-0.09 ± 0.04
TOTAL	1.56 ± 0.03	0.02 ± 0.06	-0.06 ± 0.04

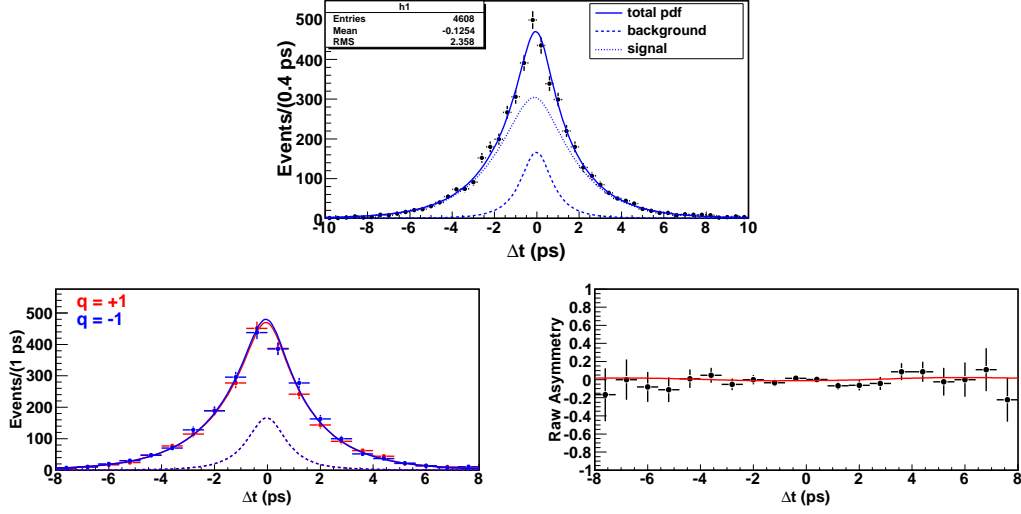


Figure 5.10: Lifetime and CP fit results in the $B^0 \rightarrow K^{*0}\gamma$ control sample.

5.5.6 Lifetime and CP fit in $B^+ \rightarrow \phi K^+\gamma$

From the fit shown in previous section, we obtained 474 events in the tcpv signal box with a signal fraction of 37% and background fraction of 63%. The lifetime and CP fit results to 772 M $B\bar{B}$ data sample are summarized in the Table 5.6 and are shown in figure 5.11. The lifetime result is consistent with PDG value. In addition, no CP asymmetry is found as expected. The errors on S and A are consistent with the expectation from toy MC pseudo-experiments.

Table 5.6: Lifetime and CP fit results in the $B^+ \rightarrow \phi K^+\gamma$ control sample.

Data Sample	Lifetime fit (ps)	CP fit	
		S	A
$B^+ \rightarrow \phi K^+\gamma$	1.70 ± 0.20	0.25 ± 0.33	0.18 ± 0.26

5.5.7 Lifetime fit in $B^0 \rightarrow \phi K_S^0\gamma$

From the fit shown in previous section, we obtained 82 events in the tcpv signal box with a signal fraction of 45% and background fraction of 55%. We have 40 signal events for CP fitting (including the non-resonant $K^+K^-K_S^0\gamma$ component). A lifetime fit to the

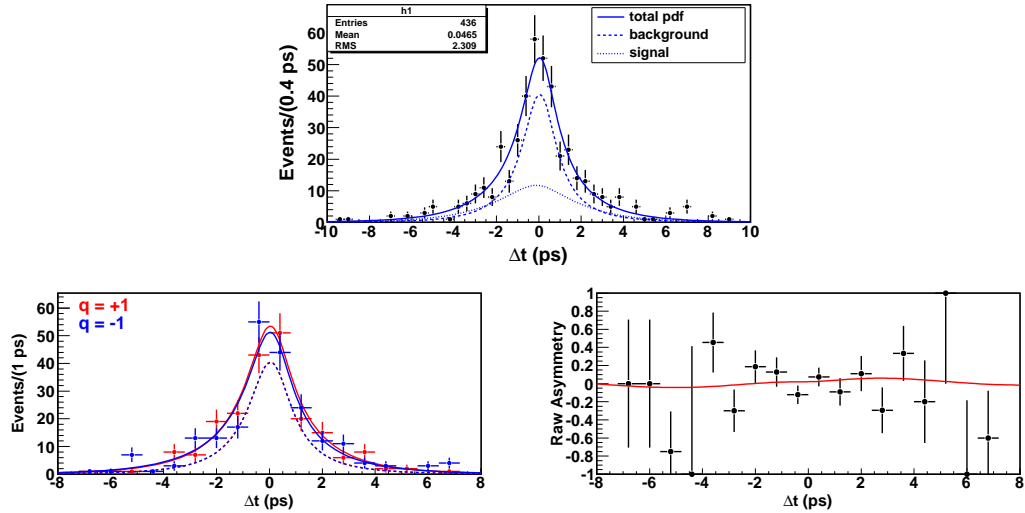


Figure 5.11: Lifetime and CP fit results in the $B^+ \rightarrow \phi K^+ \gamma$ control sample.

full data sample gives $\tau = 2.09 \pm 0.45$ ps, which is consistent with the PDG value. The fit result is shown in figure 5.12.

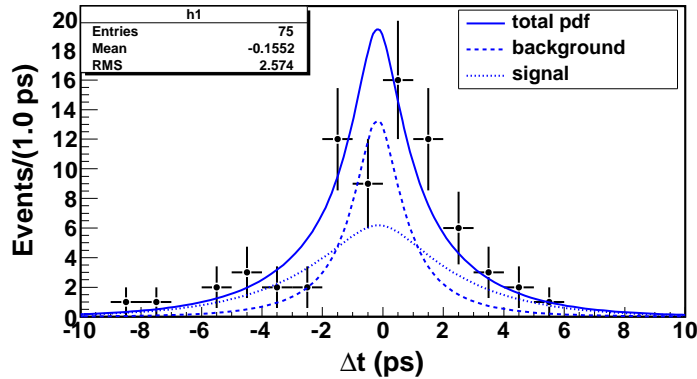


Figure 5.12: Lifetime fit in the $B^0 \rightarrow \phi K_S^0 \gamma$ sample.

5.5.8 CP fit to Sideband events

We perform a CP fit to the data sideband. The sideband contains nearly 97% continuum with a 3% contamination of generic background. In order to carry out the CP

fit, we treat the continuum as signal with lifetime fixed to the continuum lifetime. We observe no asymmetry in sideband events. The fit results are shown in figure 5.13.

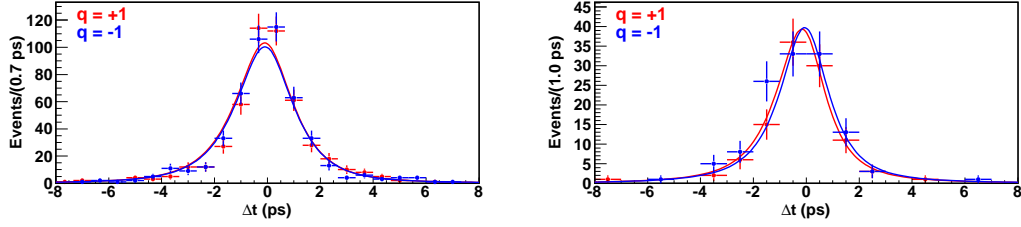


Figure 5.13: CP fit results to the sideband events in $B^+\phi K^+\gamma$ (left) and $B^0 \rightarrow \phi K_S^0\gamma$ (right).

5.5.9 Random Flavor Tagging

As one of the validity checks, we perform a random flavor tagging test. We assign the flavor charge ($q = +1$ or -1) randomly to the tag side. The input seed is also varied randomly and a CP fit is performed. The results are consistent with zero. We do not quote the central values as they have no physical meaning. The errors on \mathcal{S} is 0.32 and on \mathcal{A} is 0.26 for the $B^+ \rightarrow \phi K^+\gamma$ mode. This is consistent with the measured value. However in the $B^0 \rightarrow \phi K_S^0\gamma$ mode, the typical errors on \mathcal{S} are 0.55 and those on \mathcal{A} are 0.45. These are much smaller than the expected toy MC mean error because the central value is always close to zero.

5.5.10 CP fit to four Random Control Samples

We have 40 signal events for CP fitting in the neutral mode. The charged control sample has nearly four times more signal events (168). For a crosscheck of the errors on \mathcal{S} and \mathcal{A} , we select four statistically independent samples from the control mode and perform CP fits. The results are summarized in the Table 5.7 and shown in figure 5.14. The errors are typically somewhat larger when the central value is close to the physical boundary.

Table 5.7: The CP fit results to four random control samples from $B^+ \rightarrow \phi K^+ \gamma$ mode.

Data Sample	S	A
sample1	0.13 ± 0.77	1.42 ± 0.68
sample2	1.96 ± 0.88	0.09 ± 0.58
sample3	-1.09 ± 0.73	0.01 ± 0.43
sample4	0.46 ± 0.56	-0.09 ± 0.55

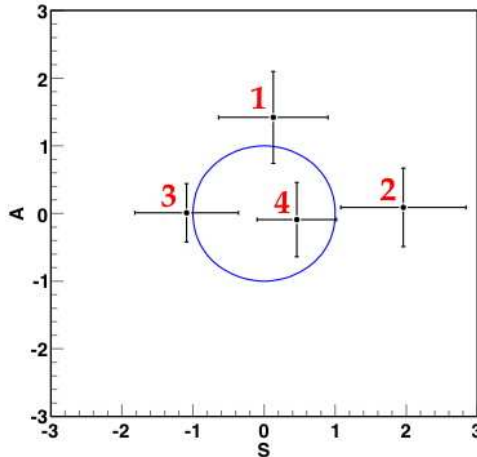


Figure 5.14: Plot of the CP fit results to the four random control samples in the 2D \mathcal{A} - \mathcal{S} plane.

5.6 CP Fit Results in $B^0 \rightarrow \phi K_S^0 \gamma$

The unbinned maximum likelihood fit to the 75 events in the signal region results in the CP violation parameters,

$$\begin{aligned} \mathcal{S}_{\phi K_S^0 \gamma} &= 0.74 \pm 0.39(\text{stat}), \\ \mathcal{A}_{\phi K_S^0 \gamma} &= 0.35 \pm 0.45(\text{stat}). \end{aligned} \tag{5.6.1}$$

This is based on a data sample containing $772 \times 10^6 B\bar{B}$ pairs. The central value is within the physical boundary ($r = 0.81$) and 1.9σ away from the SM expectation ($\mathcal{S} \sim 3\%$). The asymmetric MINOS errors on \mathcal{S} are $(-0.45, 0.32)$, on \mathcal{A} are $(-0.45, 0.42)$ and correlation is small (0.9%). We define the raw-asymmetry in each Δt bin by $(N_+ - N_-)/(N_+ + N_-)$, where N_+ (N_-) is the number of observed candidates with $q = +1(-1)$.

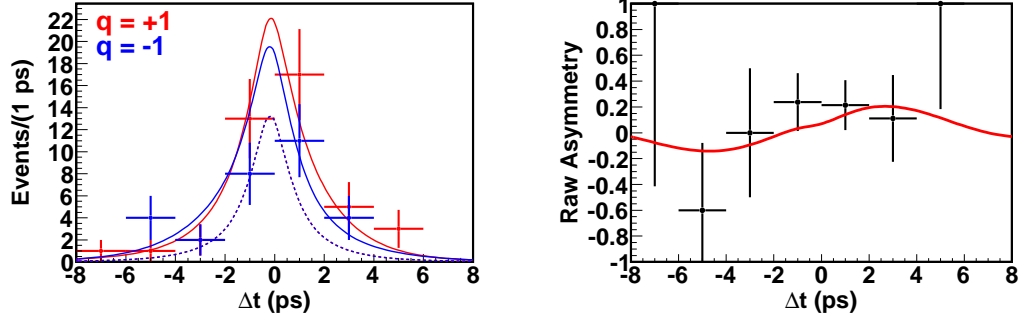


Figure 5.15: The Δt distributions and raw asymmetry plot for the $B^0 \rightarrow \phi K_S^0 \gamma$ mode (all events).

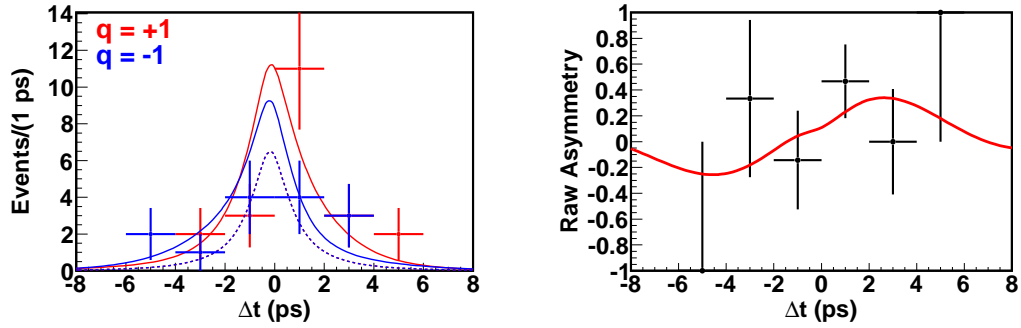


Figure 5.16: The Δt distributions and raw asymmetry plot for the $B^0 \rightarrow \phi K_S^0 \gamma$ mode (well-tagged events, $r > 0.5$, 48% of total).

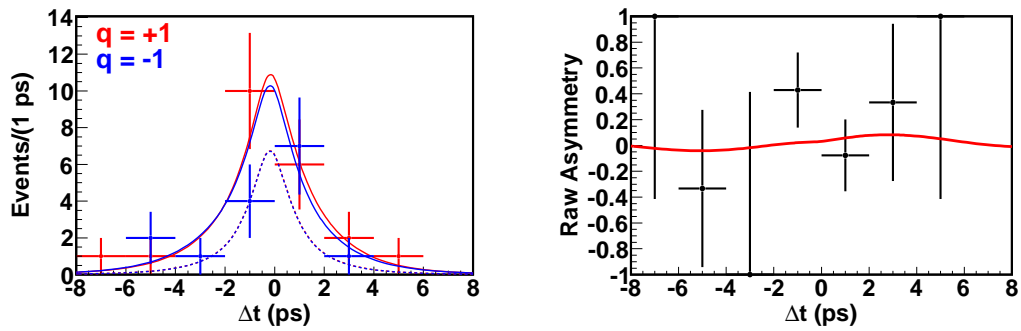


Figure 5.17: The Δt distributions and raw asymmetry plot for the $B^0 \rightarrow \phi K_S^0 \gamma$ mode (poorly-tagged events, $r < 0.5$).

5.7 Checks after box opening

5.7.1 Toy MC with Measured parameters

The toy MC test is repeated by using the measured parameters: \mathcal{S} (0.73659), \mathcal{A} (0.34532) and τ_{B^0} (2.0891 ps). The mean of the error distribution is 0.74 for \mathcal{S} and 0.51 for \mathcal{A} . The toy MC shows that the error from the nominal MINUIT minimization has a probability of only 0.6%.

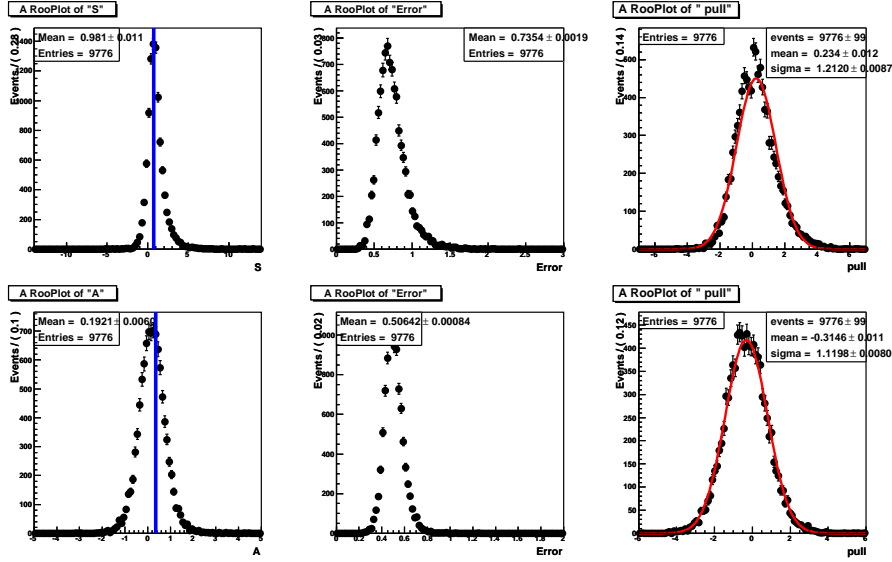


Figure 5.18: The toy MC results for $B^0 \rightarrow \phi K_S^0 \gamma$ after box opening. The central value, error and pull distributions for \mathcal{S} (upper) and \mathcal{A} (lower).

5.7.2 Katayama Scan

We have a total of 82 events in the signal box. We remove the first event from the sample and perform the CP fit. We then put back the event and do the fit by removing the second event. The same procedure is repeated for all events in the signal box. The values of \mathcal{S} , \mathcal{A} , the parabolic error, the negative and positive MINOS errors as a function of sample number are shown below. The presence of a single special event ($\Delta t = -3.64$ ps and $r = 0.96$) is partly responsible for the small error. Excluding this events, the fit results are (sample 44 from the scan figure):

$$\mathcal{S} = 1.40 \pm 0.49(\text{stat.}), \quad \mathcal{A} = 0.31 \pm 0.38(\text{stat.})$$

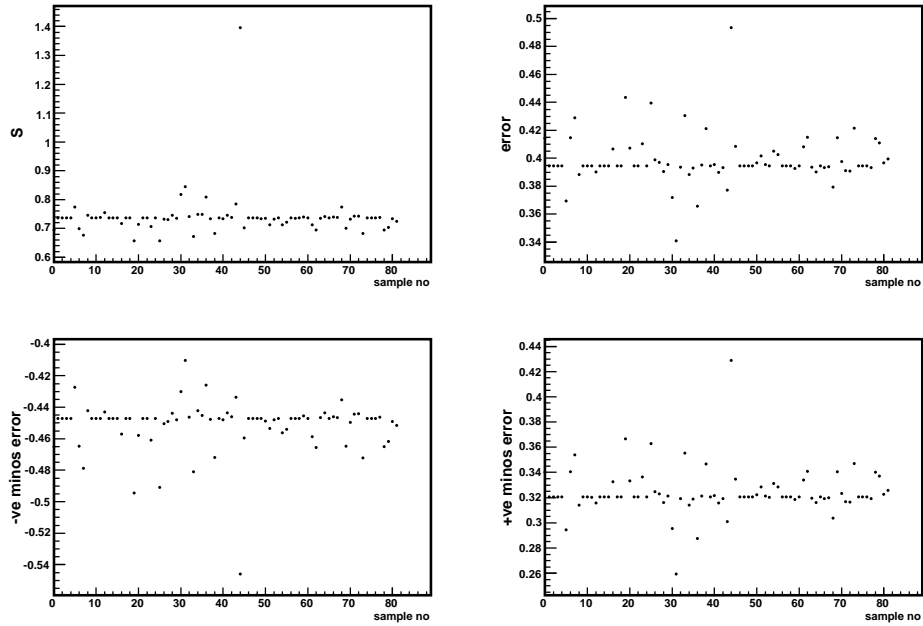


Figure 5.19: The \mathcal{S} value, error, negative MINOS error and positive MINOS error as a function of sample number from the Katayama scan.

5.7.3 Likelihood Scan

We do a scan of likelihood versus \mathcal{S} and \mathcal{A} in $B^0 \rightarrow \phi K_S^0 \gamma$ mode. The plot of $-\ln(L_0/L_{\max})$ versus \mathcal{S} and \mathcal{A} is shown below. The vertical line corresponds to asymmetric minos error limits. This shows that difference in $\log(\text{likelihood})$ is exactly one at the limits.

5.8 Systematic Uncertainty

We follow the same procedures for time-dependent systematic uncertainty evaluation as described in chapter 3 for the $B^0 \rightarrow \psi(2S)K_S^0$ mode. The small changes from the procedure are described below and the results are summarized in Table 5.8.

Vertexing The vertex related cut variations are exactly same as those of $B^0 \rightarrow \psi(2S)K_S^0$ except the vertex quality cut (ξ) is varied by ± 100 (nominal value is 250) and the $\pm 1\sigma$ error is used in systematics. Due to statistical fluctuation, the vertexing systematic

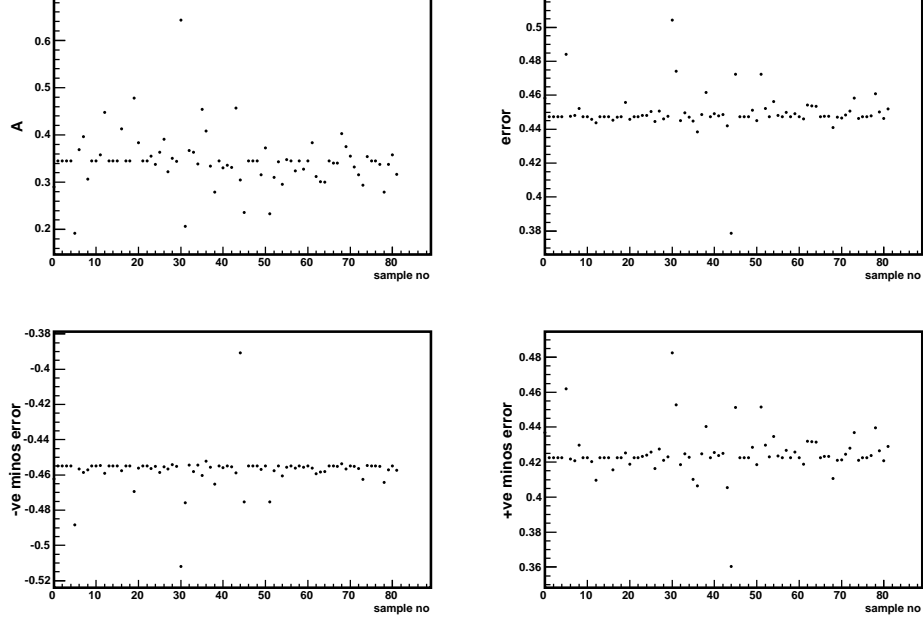


Figure 5.20: The \mathcal{A} value, error, negative MINOS error and positive MINOS error as a function of sample number from the Katayama scan.

for the neutral mode is large: 0.05 for \mathcal{S} and 0.27 for \mathcal{A} . Therefore, we use the corresponding value from the charged mode as mentioned in the Table 5.8.

Physics Parameters We vary the physics parameters (τ_{B^0} and Δm_d) by their errors in PDG 2008. We also vary all background (generic, rare) lifetimes with their errors obtained from MC. For the nominal fit, we assumed no CP for the rare background. As a conservative estimate, we vary the CP violation parameters within the physical limit and the difference is assigned to the systematic error.

Signal and background Fraction In the nominal fit, we used different signal and background fractions for each bin. The signal and continuum fractions are varied within their errors (binomial), while other fractions are varied by $\pm 100\%$.

Fit bias We fit a large GSIM sample with \mathcal{S} fixed to the measured data value and the difference is assigned as a systematic error.

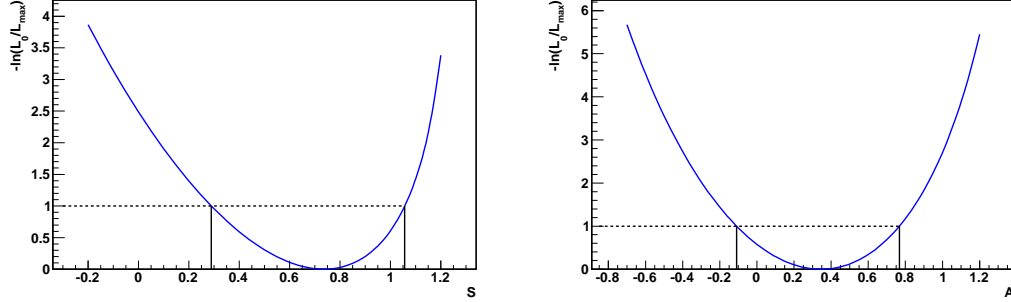


Figure 5.21: The likelihood curves for \mathcal{S} and \mathcal{A} in $B^0 \rightarrow \phi K_S^0 \gamma$ mode.

5.9 Statistics Issues in $B^0 \rightarrow \phi K_S^0 \gamma$

The asymmetric statistical errors on \mathcal{S} in data from MINUIT minimization are $+0.32$ and -0.45 . These are much smaller than the expectation from MC simulation (0.78) and have a probability of only 0.6%. This is due to low statistics and the presence of a single special event.

Instead of using the fit error, we use the residual distribution ($S_{\text{fit}} - S_{\text{gen}}$) from pseudo-experiments to obtain new MC-based asymmetric uncertainties (this approach is similar to that used in $B^0 \rightarrow \pi^+ \pi^-$ analysis [57]). We determine one sigma error band limits ($\pm 68\%$ CL in MC) and correct for the mean shift. The new asymmetric errors are $+0.72$ and -1.05 . We also change the statistical errors on \mathcal{A} to those obtained from fitting the toy MC residual distribution.

We also observe a bias due to low statistics (35 signal events) and high central value (checked in toy MC). The shift is $+0.22$ for \mathcal{S} and is included in the negative systematic uncertainty. The shift is -0.21 for \mathcal{A} and is included in the positive systematic uncertainty. This is checked carefully for different values of \mathcal{S} and \mathcal{A} as shown in Fig. 5.23 for signal MC and in Fig. 5.24 for toy MC. The toy MC simulations also show that this bias significantly reduces with an increase in statistics (with twice the signal, the bias decreases to 0.04)

Considering all these issues related to the statistical error, the final result is:

$$\mathcal{S}_{\phi K_S^0 \gamma} = 0.74^{+0.72}_{-1.05}(\text{stat})^{+0.10}_{-0.24}(\text{syst}), \quad \mathcal{A}_{\phi K_S^0 \gamma} = 0.35 \pm 0.58(\text{stat})^{+0.23}_{-0.10}(\text{syst})$$

With the present statistics, these measurements are consistent with the SM predictions ($\mathcal{S} \sim 3\%$) and there is no indication yet of new physics from right-handed currents.

Table 5.8: Summary of the Systematic Uncertainties for $B^0 \rightarrow \phi K_S^0 \gamma$ mode. For each category the errors on \mathcal{S} and \mathcal{A} are symmetrized.

Parameter	$\Delta\mathcal{S}_{\phi K_S^0 \gamma}$	$\Delta\mathcal{A}_{\phi K_S^0 \gamma}$
Vertexing	0.08	0.04
Resolution Function	0.02	0.03
Wrong Tag Fraction	0.01	0.01
Physics Parameter	0.05	0.03
PDF Shape	0.01	0.01
Signal Fraction	0.03	0.07
Background Δt Shape	0.01	0.02
Fit Bias	0.00/−0.22	+0.21/0.00
TSI	0.00	0.03
Total	+0.10/−0.24	+0.23/−0.10

5.10 Charge Asymmetry in $B^+ \rightarrow \phi K^+ \gamma$

We also measure the charge asymmetry in $B^+ \rightarrow \phi K^+ \gamma$, which is defined as

$$A_{CP} = \frac{N(B^- \rightarrow \phi K^- \gamma) - N(B^+ \rightarrow \phi K^+ \gamma)}{N(B^- \rightarrow \phi K^- \gamma) + N(B^+ \rightarrow \phi K^+ \gamma)} \quad (5.10.1)$$

where N is the signal yield. The fitter is written to directly output the A_{CP} as a free parameter. The results are obtained from a simultaneous 2D fit to the ΔE - M_{bc} distributions. The PDF shapes are the same for both B^+ and B^- decays. The asymmetry of the backgrounds are fixed to zero in the nominal fit. For systematic calculations, we vary the asymmetry of the rare backgrounds by $\pm 58\%$ (RMS value of a flat distribution between -1 to 1). The fixed shapes and normalizations are varied by their $\pm 1\sigma$ errors and are included in the systematics. The measured signal yield and the charge asymmetry are shown in Fig. 5.9.

Table 5.9: Measured signal yields and charge asymmetry in the $B^+ \rightarrow \phi K^+ \gamma$ mode.

$N(B^- \rightarrow \phi K^- \gamma)$	$N(B^+ \rightarrow \phi K^+ \gamma)$	A_{CP}
74 ± 13	79 ± 13	$-0.03 \pm 0.11 \pm 0.08$

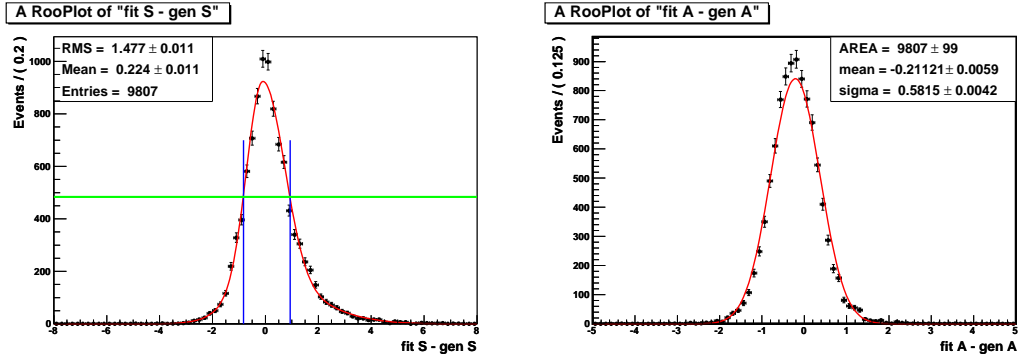


Figure 5.22: The residual distributions (output-generated) for \mathcal{S} and \mathcal{A} from toy MC for $B^0 \rightarrow \phi K_S^0 \gamma$ mode. The vertical lines at -0.83 and 0.94 correspond to $\pm 68\%$ confidence intervals. The new values after correcting the mean shift (0.224) are -1.05 and 0.72 .

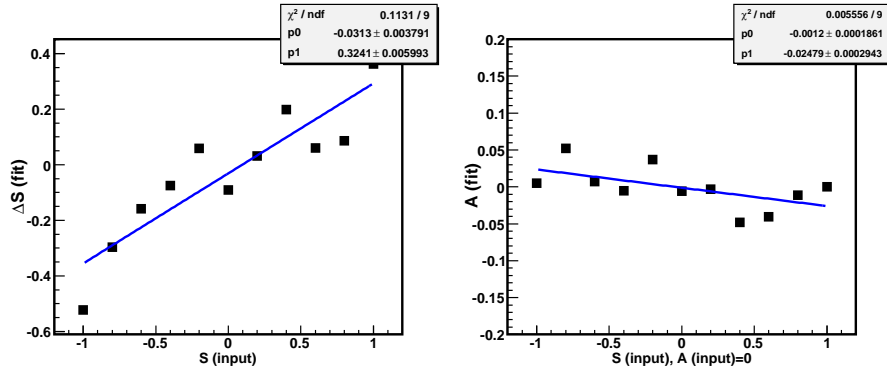


Figure 5.23: The linearity test in signal MC for $B^0 \rightarrow \phi K_S^0 \gamma$ mode.

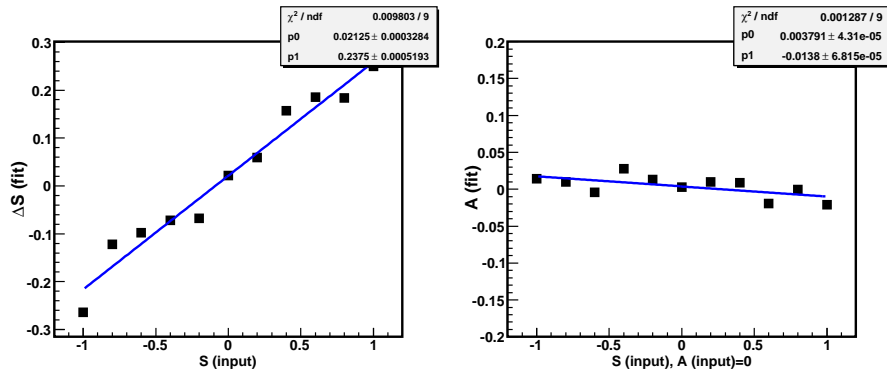


Figure 5.24: The linearity test in toy MC for $B^0 \rightarrow \phi K_S^0 \gamma$ mode.

Chapter 6

Search for $B \rightarrow \omega K \gamma$ decays

6.1 Introduction

In this chapter, we describe a feasibility study for the radiative decay $B \rightarrow \omega K \gamma$. This is also a $b \rightarrow s$ penguin decay similar to $B \rightarrow \phi K \gamma$. The ω meson is reconstructed via its decay to $\pi^+ \pi^- \pi^0$. The selection criteria and a background study are described.

6.2 Event Selection

Similar to the $B \rightarrow \phi K \gamma$ mode, the data are required to pass hadronic event selection cuts. The signal is reconstructed in the decays $B^+ \rightarrow \omega K^+ \gamma$ and $B^0 \rightarrow \omega K_S^0 \gamma$, with $\omega \rightarrow \pi^+ \pi^- \pi^0$ and $K_S^0 \rightarrow \pi^+ \pi^-$. For the event generation, we assume that the B meson decays to an intermediate heavy kaon resonance and a photon. The resonance then decays to ω and K_S^0 or K^\pm . In the EvtGen MC simulation, the $K_1(1400)$ resonance with a width of $174 \text{ MeV}/c^2$ and spin one is used. We then reweight the mass distribution so that it is flat from the kinematic limit to $2.8 \text{ GeV}/c^2$ [48].

6.2.1 π^0 meson reconstruction

Neutral pions (π^0) are reconstructed from photon pairs. The energy of each photon in laboratory frame is required to be greater than 100 MeV for the ECL end-cap regions ($12^\circ < \theta < 32^\circ$ or $129^\circ < \theta < 156^\circ$) and 50 MeV for the barrel region ($32^\circ < \theta < 129^\circ$). Further for each photon, we require $E_9/E_{25} > 0.9$, where E_9/E_{25} is the ratio of sum of energies deposited in 3×3 and 5×5 ECL cells. For the π^0 selection, we require the invariant mass of the photon pairs to satisfy $0.12 < M_{\gamma\gamma} < 0.15 \text{ GeV}/c^2$. This corresponds

to $\sim \pm 2.5\sigma$ in the π^0 mass resolution. We require the cms momentum of π^0 candidates to be greater than 0.3 GeV/c. The photon momenta are then recalculated by applying π^0 mass-constrained kinematic fits.

6.2.2 $\omega(782)$ meson reconstruction

The ω meson is reconstructed from its decay to $\pi^+\pi^-\pi^0$. This is the dominant decay mode of ω ($\mathcal{B} = (89.1 \pm 0.7)\%$). The invariant mass of the ω candidates is required to be within $-0.03 < M_{\pi^+\pi^-\pi^0} - m_\omega < +0.03$ GeV/ c^2 where m_ω denotes the world-average ω mass. This corresponds to $\sim 3.5\Gamma$ (where Γ is the ω natural width).

Figure 6.1 shows the π^0 and ω mass distributions. The π^0 mass is fitted with a Crystal Ball function and a linear background. The ω mass distribution is fitted with a Breit-Wigner function and a linear background.

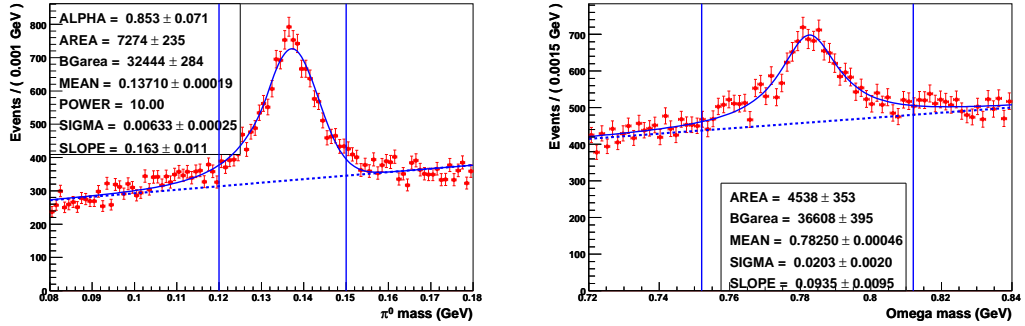


Figure 6.1: Invariant mass of distributions of π^0 (left) and ω (right).

6.2.3 B meson reconstruction

We combine the ω , a charged or neutral kaon candidate and a radiative photon to form a B meson. As in the $B \rightarrow \phi K \gamma$ mode, the B candidates are identified using the ΔE and M_{bc} variables. In the M_{bc} calculation, the photon momentum is rescaled by $(E_{\text{beam}}^{\text{cms}} - E_{\omega K}^{\text{cms}})$ to improve resolution. The ΔE - M_{bc} fit region and signal box definitions are same as those in the $B \rightarrow \phi K \gamma$ mode. Using MC simulations, we find a multiplicity of ~ 1.34 (24%) for $\omega K_S \gamma$ and ~ 1.48 (32%) for $\omega K^+ \gamma$. A mode dependent BCS cut is applied to select the best B candidate, which is based upon the lowest ω mass χ^2 , highest KID and

highest cms γ energy. The best candidate selection is about 75% efficient in ω channels for selecting the correct B candidate. The χ^2 definition used in the selection is defined below:

$$\chi^2 = \left(\frac{M_{\pi^+\pi^-\pi^0} - m_\omega}{\sigma_{\pi^+\pi^-\pi^0}} \right)^2 + \left(\frac{M_{\pi\pi} - m_{K_S}}{\sigma_{\pi\pi}} \right)^2 \text{ for } B^0 \rightarrow \omega K_S^0 \gamma$$

$$\chi^2 = \left(\frac{M_{\pi^+\pi^-\pi^0} - m_\omega}{\sigma_{\pi^+\pi^-\pi^0}} \right)^2 + \text{highest KID for } B^\pm \rightarrow \omega K^\pm \gamma$$

6.3 Continuum Suppression

We follow the same continuum suppression methods as described for $B \rightarrow \phi K \gamma$ in chapter 4. We use a Fisher discriminant formed from modified Fox-Wolfram moments and the $\cos \theta$ to distinguish the signal from continuum. Figure 6.2 shows the FOM plots for both the modes. We use the LR cut 0.85 for the ω channel, which corresponds to the FOM value 3.90 for $\omega K_S^0 \gamma$ and 7.36 for $\omega K^\pm \gamma$. This selection criterion removes 98% of the continuum while retaining 52% of the signal.

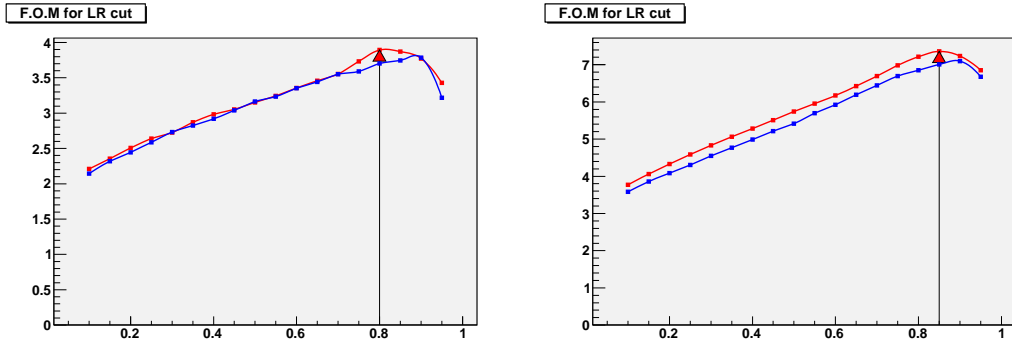


Figure 6.2: The LR FOM plots for $\omega K_S^0 \gamma$ mode (left) and $\omega K^\pm \gamma$ (right). We use the final LR cut calculated from LRKSF0 and LR $\cos \theta_B$.

6.4 Generic B Backgrounds

We use the same sample of $B\bar{B}$ MC events as in $B \rightarrow \phi K \gamma$ to investigate the backgrounds from other B decay modes. Figure 6.3 shows the ΔE fit (with a projection in the M_{bc} signal region) and the M_{bc} fit (with a projection in the ΔE signal region) and the ωK distribution in the fit region for the backgrounds from the generic MC. These distributions are shown after applying LR cut, which removes 70% of generic backgrounds.

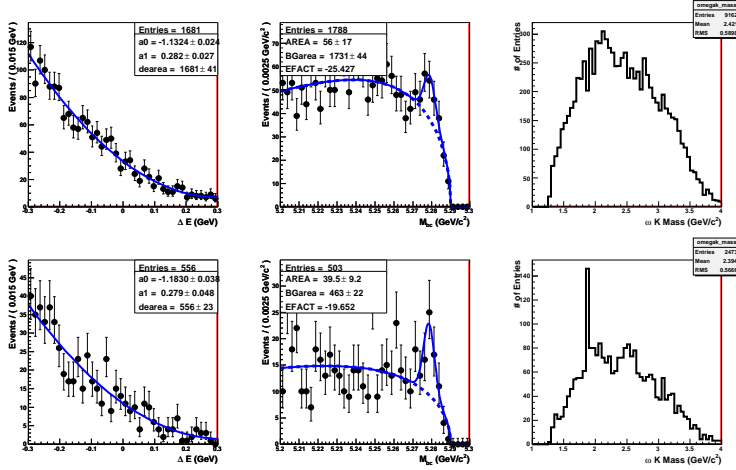


Figure 6.3: The ΔE , M_{bc} and ωK distributions for the $\omega K^+\gamma$ (first row) and $\omega K_S^0\gamma$ (second row) decay mode before the D veto. The D veto will be applied only for $\omega K^+\gamma$ mode.

The expected peaking events in M_{bc} is 11.2 ± 3.4 ($\sim 7\%$ of the expected yield in data). The dominant backgrounds are $B^- \rightarrow D^0\rho^-$ and $B^- \rightarrow D^{*0}\rho^-$. We calculated the invariant masses of the signal kaon with any other particle in the events and found that the $K\pi$ and $K^+\pi^-\pi^0$ mass distributions show strong peaking from generic MC (shown in Fig. 6.4, signal MC [black], generic MC [red]). We then fit these invariant mass distributions and apply a 4σ veto window. This removes 60% of the peaking while the signal efficiency loss is 9%. There are 4.8 ± 2.6 peaking events after the veto. We plan to use this in the estimation of systematics.

The expected peaking in M_{bc} is 8 ± 2 ($\sim 23\%$ of the expected yield in data). The source of this peaking is from several decay modes such as $D^-\rho^+$, $D^0\rho^+$, $D^{*0}\rho^+$, $D^0\pi^0$ (the background events found in each mode in the signal region are listed in Table 6.1). Many final states are possible in which the candidate signal K_S^0 can combine with all other particles in the event (π^+ , π^- , π^0) to form a D meson. We found only the $K_S\pi^\pm\pi^0$ and $K_S\pi^+\pi^-\pi^0$ invariant mass distributions have peaking in the generic MC. A veto on these masses removes only the specific background mode, but significantly decreases the signal efficiency. Therefore, it is not effective to apply a veto in this mode. Since these modes are well measured, we plan to fix the peaking components in data.

After applying all these selection criteria, we have a signal reconstruction efficiency of $(1.55 \pm 0.04)\%$ for $B^0 \rightarrow \omega K_S^0\gamma$ and $(2.11 \pm 0.05)\%$ for $B^+ \rightarrow \omega K^+\gamma$ mode (determined

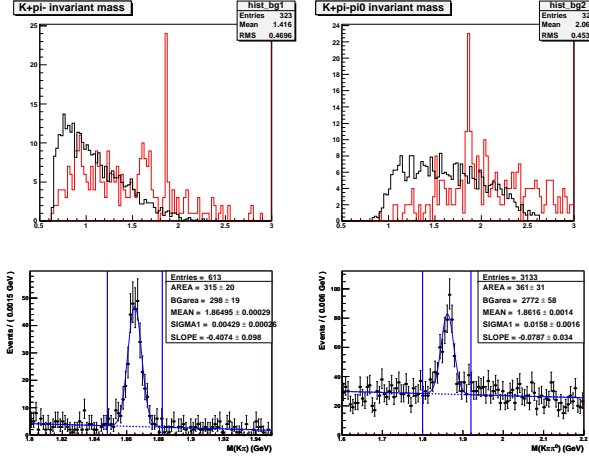


Figure 6.4: Invariant $M(K^+\pi^-)$ and $M(K^+\pi^-\pi^0)$ distributions for the signal kaon. Black is from signal MC and red is from generic MC. The second row are the corresponding fits to the invariant mass distributions.

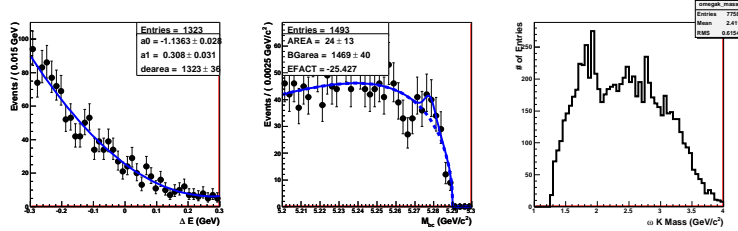


Figure 6.5: The ΔE , M_{bc} and invariant ωK_S distributions for the $\omega K^+\gamma$ decay mode after the D veto.

by fitting M_{bc} distribution). The geometrical efficiency (after charged track selection and BCS cut) in ϕ channel is 12% and in ω channel is 3%. We loose a factor of four in efficiency due to the extra π^0 selection. The efficiency loss due to other cuts are: ϕ (11%), K_S (1%), BCS (2%), $LR(> 0.65)$ cut (24%). The low efficiency in ω modes is due to other cuts: $p_{\pi^0}^*$ cut (16%), E_9/E_{25} (15%), π^0 mass cut (1%), ω mass cut (6%), BCS cut (11%) and finally the $LR > 0.85$ cut (48%). We also checked that there is significant improvement of the efficiency due to the new tracking algorithm (32% for $B^0 \rightarrow \omega K_S^0 \gamma$ and 23% for $B^+ \rightarrow \omega K^+ \gamma$) as there are low-momentum tracks in the final state.

Table 6.1: The expected background events in data from the generic MC in the signal region for the $B^0 \rightarrow \omega K_S^0 \gamma$ mode.

Decay Mode	Events in the signal region
$B^0 \rightarrow D^- \rho^+$	4.8
$B^+ \rightarrow D^0 \rho^+$	2.6
$B^+ \rightarrow D^{*0} \rho^+$	2.6
$B^0 \rightarrow D^0 \pi^0$	1.4
$B^0 \rightarrow D^0 \eta$	0.6
$B^0 \rightarrow D^{*0} \eta$	0.2

6.5 Rare B backgrounds

In ω modes, the dominant background is from $B \rightarrow X_S \gamma$ decays, where the decay of X_S is modelled by the Pythia MC. This contribution is $\sim 70\%$ of the total peaking background. We determine it from an ω mass sideband study, as MC is not reliable to fix this.

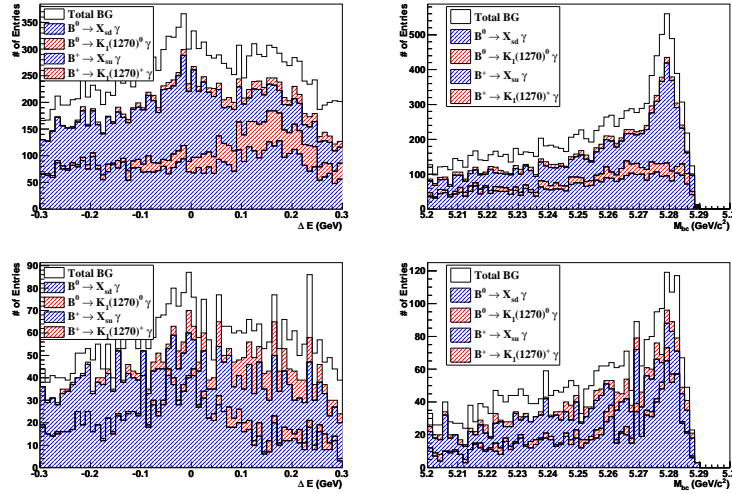


Figure 6.6: The possible sources of backgrounds from rare MC (charged and mixed) in ΔE and M_{bc} distributions for the $B^+ \rightarrow \omega K^+ \gamma$ (upper) and $B^0 \rightarrow \omega K_S \gamma$ (lower) mode. The ΔE plots require M_{bc} to lie in the signal window while the M_{bc} plots require ΔE in the signal region.

6.6 Correlation between ΔE and M_{bc}

The correlation between ΔE and M_{bc} is very small as shown in Fig. 6.7.

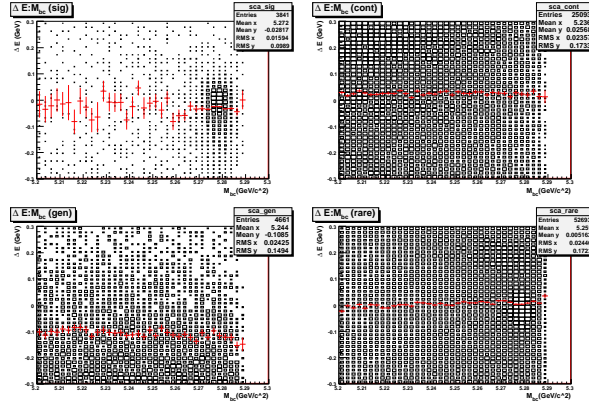


Figure 6.7: The mean of ΔE is shown in bins of M_{bc} (red points) on a scatter plot for the $B^+ \rightarrow \omega K^+ \gamma$ mode.

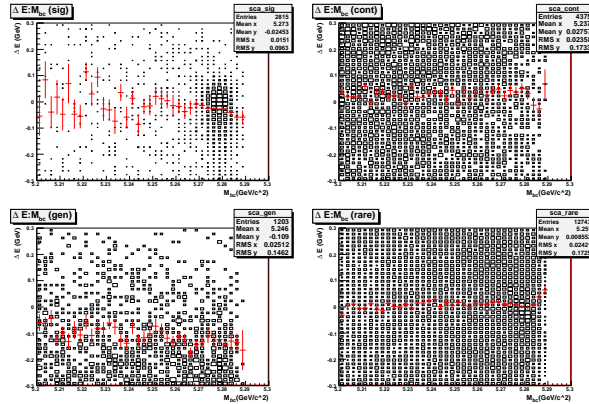


Figure 6.8: The mean of ΔE is shown in bins of M_{bc} (red points) on a scatter plot for the $B^0 \rightarrow \omega K_s^0 \gamma$ mode.

Chapter 7

Conclusions

7.1 Measurements of time-dependent CP violation in $B^0 \rightarrow \psi(2S)K_S^0$

We have measured the time-dependent CP asymmetry in one of the golden charmonium mode, where the neutral B meson decays to a $\psi(2S)$ meson and a K_S^0 meson. This analysis is based on a data sample of 657×10^6 $B\bar{B}$ pairs collected with the Belle detector. This decay mode is a CP eigenstate dominated by a $b \rightarrow c\bar{c}s$ generated transition. From an unbinned maximum likelihood fit to the 1300 events in the signal region, we obtain the CP violation parameters,

$$\begin{aligned}\mathcal{S}_{\psi(2S)K_S^0} &= +0.72 \pm 0.09(\text{stat}) \pm 0.03(\text{syst}), \\ \mathcal{A}_{\psi(2S)K_S^0} &= +0.04 \pm 0.07(\text{stat}) \pm 0.05(\text{syst}).\end{aligned}$$

This is one of the most precise measurements of CP asymmetries in $B^0 \rightarrow \psi(2S)K_S^0$ mode and supersedes Belle's previous result [9]. Compared to our previous publication, we used improved analysis techniques in addition to the increase in statistics. The peaking backgrounds are estimated directly from the data sidebands. The signal and peaking fractions in the time-dependent PDF are determined for each r -bin. In addition to the lepton tracks from the J/ψ , we also use the prompt $\pi^+\pi^-$ tracks in the vertex reconstruction for the $\psi(2S)(J/\psi\pi^+\pi^-)K_S^0$ decay mode. Only lepton tracks from the J/ψ were used in the previous analysis.

This result is also statistically consistent with Belle's measurement using $B^0 \rightarrow J/\psi K^0$ mode [47]. By combining our results with $B^0 \rightarrow J/\psi K^0$, we obtain a new Belle

average $\sin 2\phi_1 = 0.650 \pm 0.029 \pm 0.018$. This result has been published in Physical Review D [58]. The Heavy Flavor Averaging Group (HFAG) summary [59] of the comparison between our result with the other measurements of time-dependent CP asymmetries in $b \rightarrow c\bar{c}s$ transitions is shown in Fig. 7.1.

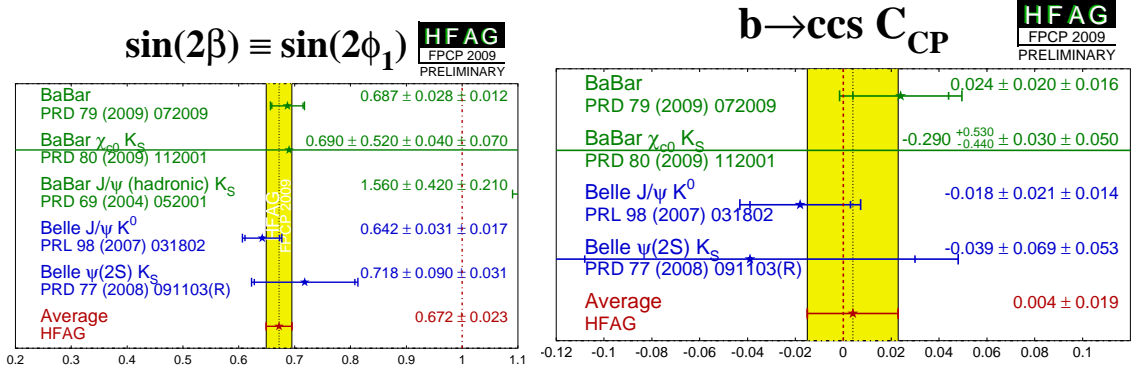


Figure 7.1: Summary of Belle and BaBar measurements of time-dependent CP asymmetries in $b \rightarrow c\bar{c}s$ transitions.

This work can be extended to other $b \rightarrow c\bar{c}s$ modes (for example, $B^0 \rightarrow \chi_{c1} K_S^0$ and $B^0 \rightarrow \eta_c K_S^0$) to determine whether the effective value of $\sin 2\phi_1$ is same for all modes. Some new physics scenarios [7] predict small differences in the $\sin 2\phi_1$ values between different charmonium modes. This possibility can be probed by precise measurements with more statistics. An ongoing analysis using Belle's full data sample is described in Appendix B.

7.2 Observation of $B^0 \rightarrow \phi K_S^0 \gamma$ and Measurements of time-dependent CP violation

We have observed for the first time the rare radiative decay $B^0 \rightarrow \phi K_S^0 \gamma$ using the full data sample ($772 \times 10^6 B\bar{B}$ pairs) collected by the Belle detector. We observed a signal of 37 ± 8 events with a significance of 5.4 standard deviations. The measured branching fraction is

$$\mathcal{B}(B^0 \rightarrow \phi K^0 \gamma) = (2.74 \pm 0.60 \pm 0.32) \times 10^{-6}. \quad (7.2.1)$$

We also precisely measured the branching fraction for the charged mode using 144 ± 17 signal events

$$\mathcal{B}(B^+ \rightarrow \phi K^+ \gamma) = (2.48 \pm 0.30 \pm 0.24) \times 10^{-6}. \quad (7.2.2)$$

The observed $M_{\phi K}$ mass spectrum shows that the signal events are mostly concentrated at low ϕK mass, which differs significantly from the expectation in a three-body phase-space decay. We have also presented a measurement of the rate asymmetry between B^+ and B^- decays to $\phi K^\pm \gamma$ final state,

$$A_{CP} = -0.03 \pm 0.11 \pm 0.08. \quad (7.2.3)$$

This is consistent with the SM expectation.

This decay mode is sensitive to new physics from right-handed currents, which could affect the CP asymmetry. Since in SM, the emitted photon is polarized, the CP violation due to interference between B mixing and decay is suppressed (3% for \mathcal{S}). We used the neutral mode $B^0 \rightarrow \phi K_S^0 \gamma$ for the first time to measure time-dependent CP asymmetries. Using Belle's full dataset, we found

$$\begin{aligned} \mathcal{S}_{\phi K_S^0 \gamma} &= +0.74_{-1.05}^{+0.72}(\text{stat})_{-0.24}^{+0.10}(\text{syst}), \\ \mathcal{A}_{\phi K_S^0 \gamma} &= +0.35 \pm 0.58(\text{stat})_{-0.10}^{+0.23}(\text{syst}) \end{aligned} \quad (7.2.4)$$

These results are being prepared for publication in Physical Reviews Letters. The Heavy Flavor Averaging Group (HFAG) summary [59] of the comparison between our result with the other measurements of time-dependent CP asymmetries in $b \rightarrow s \gamma$ transitions is shown in Fig. 7.2.

With the present statistics, these measurements are consistent with the SM predictions ($\mathcal{S} \sim 3\%$) and there is no indication of NP from right-handed currents. A Super B factory [60] would make precise measurement of this decay mode. A factor of two more signal events would reduce the systematic uncertainty to 0.04. With more statistics, these modes can be used in a study of angular distributions of the decay products, which provides another window to probe photon polarization [15, 16].

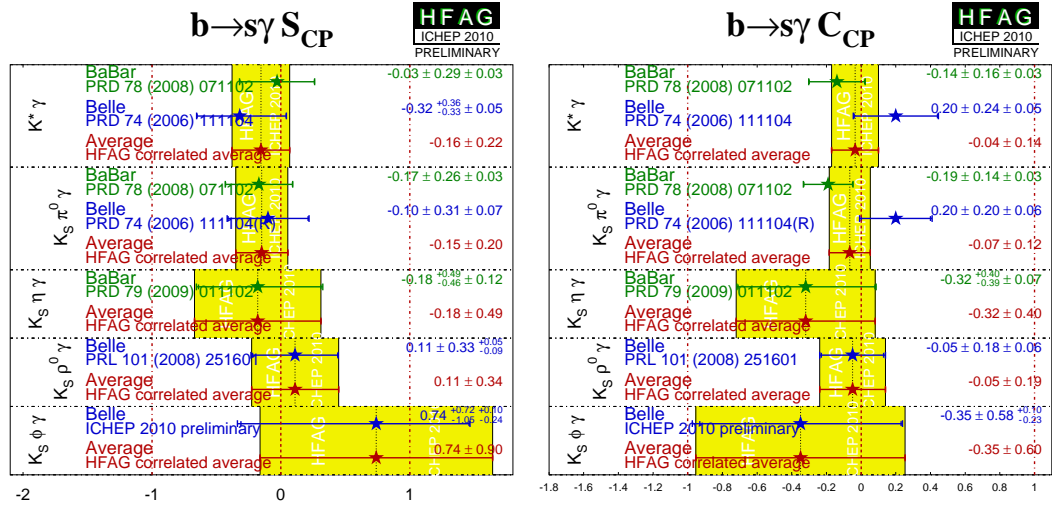


Figure 7.2: Summary of Belle and BaBar measurements of time-dependent CP asymmetries in $b \rightarrow s \gamma$ transitions.

Appendix A

Particle Identification

In this appendix, we describe the particle identification in Belle. First, the K/π identification is described, then the electron and finally, the muon identification is mentioned.

A.1 K/π Identification

The K/π identification is carried out by combining information from three nearly independent measurements:

- dE/dx measurement by CDC,
- TOF measurement, and
- measurement of the number of photoelectrons in the ACC.

The momentum coverage of each detector for K/π separation is shown in Fig. A.1. For each charged track, we calculate three likelihood functions using subdetector information with either the kaon or pion hypothesis, L_h^{ACC} , L_h^{TOF} and L_h^{CDC} , where h denotes the assumed particle species. A combined likelihood is then calculated from the product of these likelihood functions for a specific hadron species,

$$L_h = L_h^{\text{ACC}} \times L_h^{\text{TOF}} \times L_h^{\text{CDC}}. \quad (\text{A.1.1})$$

A particle is then identified as a kaon or a pion by the selection based on the likelihood ratio \mathcal{P} :

$$\mathcal{P}(K/\pi) = \frac{L_K}{L_K + L_\pi}, \quad \mathcal{P}(\pi/K) = 1 - \mathcal{P}(K/\pi). \quad (\text{A.1.2})$$

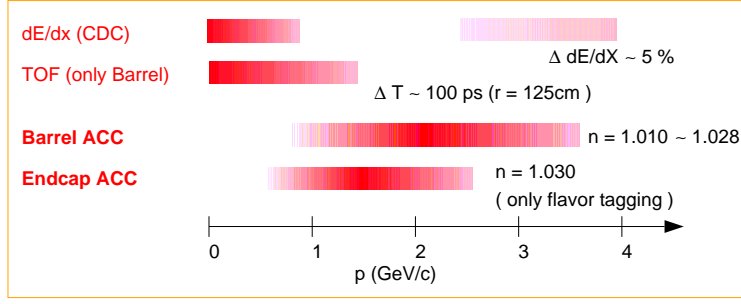


Figure A.1: Momentum coverage of each detector used for K/π separation.

This gives a value close to one for a kaon-like particle and a value close to zero for a pion-like particle.

The validity of the K/π identification has been demonstrated using the charm decay, $D^{*+} \rightarrow D^0\pi^+$, followed by $D^0 \rightarrow K^-\pi^+$. The characteristic slow π^+ from the D^{*+} decay allows these decays to be selected with a good S/N ratio (better than 30), without relying on particle identification. Therefore, the detector performance can be directly probed with the daughter K and π mesons from the D decay, which can be tagged by their relative charge with respect to the slow pion. Figure A.2 (left) shows two-dimensional plots

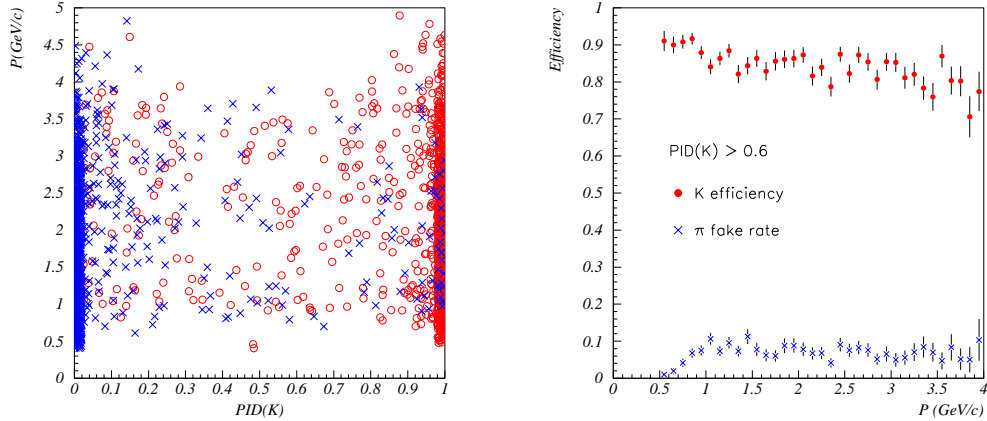


Figure A.2: (left) Likelihood ratio $PID(K)$, versus momenta for daughter tracks from $D^0 \rightarrow K^-\pi^+$ decays, tagged by the charge of the slow π^+ 's. The open circles correspond to kaons and the cross points to pions. (right) K efficiency and π fake rate, measured with $D^{*+} \rightarrow D^0(K\pi) + \pi^+$ decays, for the barrel region. The likelihood ratio cut $PID(K) \geq 0.6$ is applied.

of the likelihood ratio $\mathcal{P}(K/\pi)$ and measured momenta for the kaon and pion tracks. The figure demonstrates the clear separation of kaons and pions up to around 4 GeV/ c . The measured K efficiency and π fake rate in the barrel region are plotted as functions of the track momentum from 0.5 to 4.0 GeV/ c in Fig. A.2 (right). The likelihood ratio selection, $\mathcal{P}(K/\pi) > 0.6$, is applied in this figure. For most of the region, the measured K efficiency exceeds 80%, while the π fake rate is kept below 10%.

A.2 Electron Identification

Electrons are identified by using the following discriminants [61]:

- ratio of energy deposited in the ECL and charged track momentum measured by the CDC,
- transverse shower shape at the ECL,
- the matching between a cluster at ECL and charged track position extrapolated to the ECL,
- dE/dx measured by the CDC,
- light yield in the ACC, and
- time-of-flight measured by the TOF.

As in the case of K/π identification, the PDFs for the discriminants are made beforehand. Based on each PDF, likelihood probabilities are calculated on a track-by-track basis, and unified into a final likelihood output. This likelihood calculation is carried out taking into account the momentum and angular dependence. Figure A.3 (left) shows the output from the above procedure. Closer to unity a particle is more likely to be an electron. The solid (dashed) histogram shows the distribution for e^\pm in $e^+e^- \rightarrow e^+e^-e^+e^-$ data (π^\pm in $K_S^0 \rightarrow \pi^+\pi^-$ decays in data). A clear π/e separation can be seen.

The efficiency and fake rate are displayed in Fig. A.3 (right) using electrons in real $e^+e^- \rightarrow e^+e^-e^+e^-$ events for the efficiency measurement, and $K_S^0 \rightarrow \pi^+\pi^-$ decays in real data for the fake rate evaluation. For momenta greater than 1 GeV/ c , the electron identification efficiency is above 90% while the fake rate is in the range 0.2 to 0.3%.

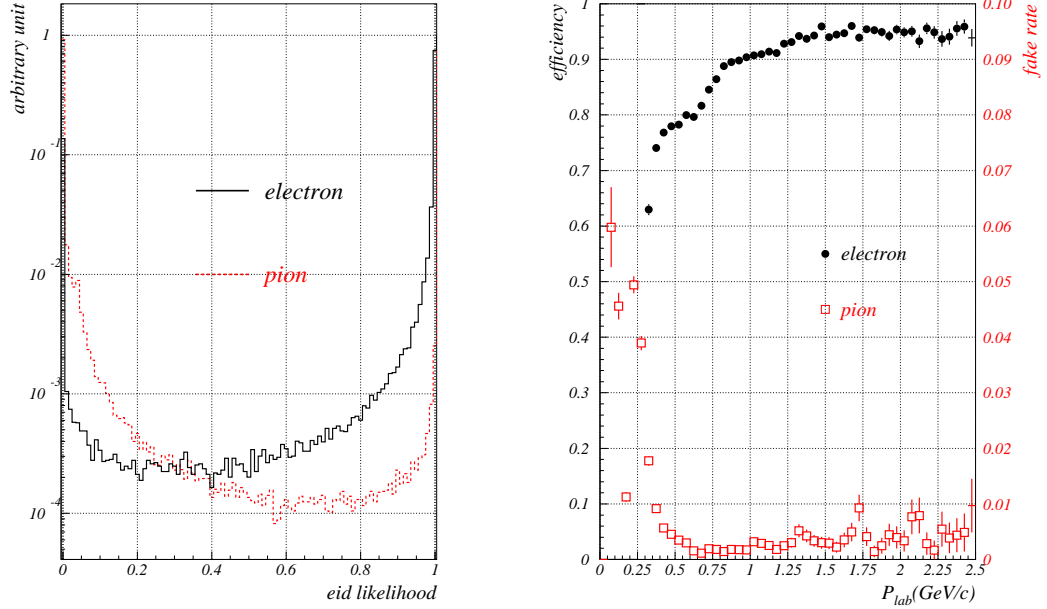


Figure A.3: (left) The distribution of the final unified discriminant used to identify electrons. The solid histogram is for electrons in $e^+e^- \rightarrow e^+e^-e^+e^-$ events and the dashed one for charged pions. (right) Electron identification efficiency (circles) and fake rate for charged pions (squares). Note the different scales for the efficiency and fake rate.

A.3 Muon Identification

Muon identification begins with the extrapolation of the track reconstructed in the CDC, through the outer detectors. A track is considered to be within the KLM acceptance if it crosses at least one RPC layer: This requires at least $0.6 \text{ GeV}/c$ of momentum. Associated RPC hits in KLM are then examined. The outermost layer crossed by the extrapolated track defines the predicted range of the track assuming the track has no hadronic interaction with the intervening material. The actual range of the track is measured by the outermost layer with an associated RPC hit.

For muon identification, two quantities are used to test the hypothesis that a track is a muon rather than a hadron [62]. These are

- ΔR : the difference between the measured and expected range of the track.
- χ_r^2 : the normalized transverse deviations of the recorded KLM hits from the extrapolated track.

Probability density distributions of two discriminant variables are constructed beforehand using simulated single track events containing a muon, pion, or kaon with measured chamber efficiencies. The probability densities \mathcal{P}_μ , \mathcal{P}_π , and \mathcal{P}_K for muons, pions, and kaons, respectively, are then obtained from the distributions, defined as $P(\Delta R, \chi_r^2) = P(\Delta R) \times P(\chi_r^2)$. We use the normalized muon likelihood

$$\mathcal{L}_\mu = \frac{\mathcal{P}_\mu}{\mathcal{P}_\mu + \mathcal{P}_\pi + \mathcal{P}_K}, \quad (\text{A.3.1})$$

for muon identification. The muon identification efficiency and pion fake rate are estimated using the two-photon control, $e^+e^- \rightarrow e^+e^-\mu^+\mu^-$ and $K_S^0 \rightarrow \pi^+\pi^-$ sample. For charged tracks with momenta between 1.0 GeV/ c and 3.0 GeV/ c , the muon identification efficiency is measured to be $\sim 90\%$ and the pion fake rate is $\sim 2\%$.

Appendix B

$B^0 \rightarrow \psi(2S)K_S^0$ Signal using $772 \times 10^6 B\bar{B}$ pairs

B.1 $B^0 \rightarrow \psi(2S)K_S^0$ Signal Extraction using Belle's Full data sample

We update the $B^0 \rightarrow \psi(2S)K_S^0$ analysis by adding Belle's latest recorded data sets (exp61-65) and replacing the SVD2 data sample with the corresponding sample reprocessed with the new improved tracking algorithm. The integrated luminosity of the full data sample is 700 fb^{-1} and contains $772 \times 10^6 B\bar{B}$ pairs. We follow the same signal extraction procedure described in the section 3.7. The peaking background is updated using the corrected inclusive MC samples. The ΔE and M_{bc} distributions from the final fit are shown in Fig. B.1.

The signal yield is 1981 ± 46 , purity is 0.95 ± 0.01 and vertexing efficiency 95.4%. We have nearly a 50% gain in signal yield due to the new tracking and the addition of more data. A time-dependent study is in progress. We expect an error of ~ 0.07 on $\sin 2\phi_1$ using the full data sample.

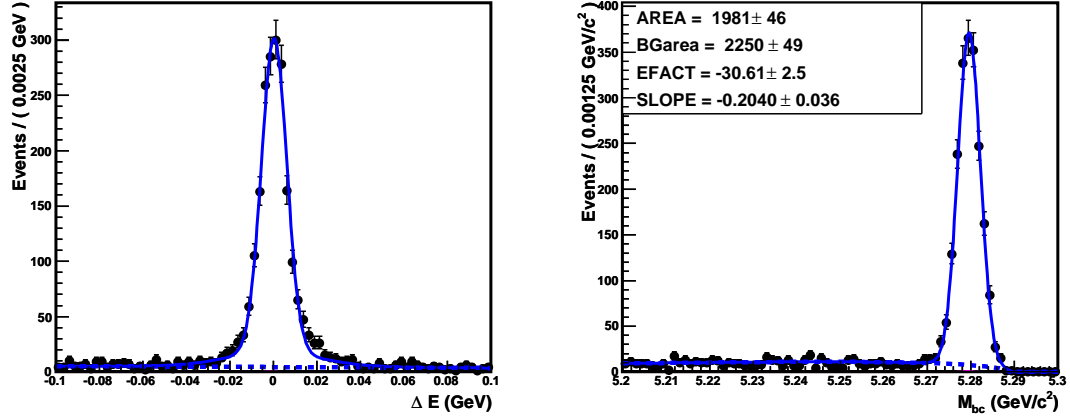


Figure B.1: ΔE distribution within the M_{bc} signal region, and M_{bc} distribution within the ΔE signal region for $B^0 \rightarrow \psi(2S)K_S^0$ using 772×10^6 $B\bar{B}$ pairs data sample. The solid curves show the fits to the signal plus background distributions, while the dashed curves show the background contributions. Purity of the signal is 0.95 ± 0.01 .

Appendix C

Publications

Measurements of time-dependent CP violation in $B^0 \rightarrow \psi(2S)K_S^0$ decays

H. Sahoo,⁶ T. E. Browder,⁶ K. Trabelsi,⁷ I. Adachi,⁷ H. Aihara,⁴⁰ K. Arinstein,¹ T. Aushev,^{11,16} S. Bahinipati,² A. M. Bakich,³⁵ V. Balagura,¹¹ E. Barberio,¹⁹ A. Bay,¹⁶ I. Bedny,¹ K. Belous,¹⁰ U. Bitenc,¹² A. Bondar,¹ A. Bozek,²⁵ M. Bračko,^{12,18} M.-C. Chang,³ Y. Chao,²⁴ A. Chen,²² W. T. Chen,²² B. G. Cheon,⁵ R. Chistov,¹¹ I.-S. Cho,⁴⁵ Y. Choi,³⁴ J. Dalseno,¹⁹ M. Dash,⁴⁴ A. Drutskoy,² S. Eidelman,¹ B. Golob,^{12,17} H. Ha,¹⁴ J. Haba,⁷ K. Hara,²⁰ T. Hara,³⁰ K. Hayasaka,²⁰ H. Hayashii,²¹ M. Hazumi,⁷ D. Heffernan,³⁰ Y. Hoshi,³⁸ W.-S. Hou,²⁴ Y. B. Hsiung,²⁴ H. J. Hyun,¹⁵ K. Inami,²⁰ A. Ishikawa,³¹ H. Ishino,⁴¹ R. Itoh,⁷ M. Iwasaki,⁴⁰ N. J. Joshi,³⁶ D. H. Kah,¹⁵ J. H. Kang,⁴⁵ P. Kapusta,²⁵ N. Katayama,⁷ H. Kichimi,⁷ H. J. Kim,¹⁵ Y. J. Kim,⁴ K. Kinoshita,² S. Korpar,^{12,18} Y. Kozakai,²⁰ P. Križan,^{12,17} P. Krokovny,⁷ R. Kumar,⁴⁶ C. C. Kuo,²² Y. Kuroki,³⁰ Y.-J. Kwon,⁴⁵ J. S. Lee,³⁴ M. J. Lee,³³ S. E. Lee,³³ T. Lesiak,²⁵ J. Li,⁶ A. Limosani,¹⁹ D. Liventsev,¹¹ F. Mandl,⁹ A. Matyja,²⁵ S. McOnie,³⁵ T. Medvedeva,¹¹ W. Mitaroff,⁹ K. Miyabayashi,²¹ H. Miyake,³⁰ H. Miyata,²⁷ Y. Miyazaki,²⁰ R. Mizuk,¹¹ G. R. Moloney,¹⁹ E. Nakano,²⁹ M. Nakao,⁷ Z. Natkaniec,²⁵ S. Nishida,⁷ O. Nitoh,⁴³ S. Noguchi,²¹ S. Ogawa,³⁷ T. Ohshima,²⁰ S. Okuno,¹³ S. L. Olsen,^{6,8} P. Pakhlov,¹¹ G. Pakhlova,¹¹ H. Palka,²⁵ C. W. Park,³⁴ H. Park,¹⁵ L. S. Peak,³⁵ R. Pestotnik,¹² L. E. Piilonen,⁴⁴ Y. Sakai,⁷ O. Schneider,¹⁶ C. Schwanda,⁹ A. J. Schwartz,² K. Senyo,²⁰ M. E. Sevior,¹⁹ M. Shapkin,¹⁰ C. P. Shen,⁸ H. Shibuya,³⁷ J.-G. Shiu,²⁴ B. Shwartz,¹ A. Somov,² S. Stanič,²⁸ M. Starič,¹² K. Sumisawa,⁷ T. Sumiyoshi,⁴² F. Takasaki,⁷ M. Tanaka,⁷ G. N. Taylor,¹⁹ Y. Teramoto,²⁹ I. Tikhomirov,¹¹ S. Uehara,⁷ K. Ueno,²⁴ Y. Uno,⁵ S. Uno,⁷ P. Urquijo,¹⁹ Y. Usov,¹ G. Varner,⁶ K. E. Varvell,³⁵ K. Vervink,¹⁶ S. Villa,¹⁶ C. H. Wang,²³ P. Wang,⁸ X. L. Wang,⁸ Y. Watanabe,¹³ R. Wedd,¹⁹ E. Won,¹⁴ H. Yamamoto,³⁹ Y. Yamashita,²⁶ C. C. Zhang,⁸ Z. P. Zhang,³² V. Zhulanov,¹ and A. Zupanc¹²

(Belle Collaboration)

¹*Budker Institute of Nuclear Physics, Novosibirsk*²*University of Cincinnati, Cincinnati, Ohio 45221*³*Department of Physics, Fu Jen Catholic University, Taipei*⁴*The Graduate University for Advanced Studies, Hayama*⁵*Hanyang University, Seoul*⁶*University of Hawaii, Honolulu, Hawaii 96822*⁷*High Energy Accelerator Research Organization (KEK), Tsukuba*⁸*Institute of High Energy Physics, Chinese Academy of Sciences, Beijing*⁹*Institute of High Energy Physics, Vienna*¹⁰*Institute of High Energy Physics, Protvino*¹¹*Institute for Theoretical and Experimental Physics, Moscow*¹²*J. Stefan Institute, Ljubljana*¹³*Kanagawa University, Yokohama*¹⁴*Korea University, Seoul*¹⁵*Kyungpook National University, Taegu*¹⁶*École Polytechnique Fédérale de Lausanne (EPFL), Lausanne*¹⁷*Faculty of Mathematics and Physics, University of Ljubljana, Ljubljana*¹⁸*University of Maribor, Maribor*¹⁹*University of Melbourne, School of Physics, Victoria 3010*²⁰*Nagoya University, Nagoya*²¹*Nara Women's University, Nara*²²*National Central University, Chung-li*²³*National United University, Miao Li*²⁴*Department of Physics, National Taiwan University, Taipei*²⁵*H. Niewodniczanski Institute of Nuclear Physics, Krakow*²⁶*Nippon Dental University, Niigata*²⁷*Niigata University, Niigata*²⁸*University of Nova Gorica, Nova Gorica*²⁹*Osaka City University, Osaka*³⁰*Osaka University, Osaka*³¹*Saga University, Saga*³²*University of Science and Technology of China, Hefei*³³*Seoul National University, Seoul*³⁴*Sungkyunkwan University, Suwon*

³⁵University of Sydney, Sydney, New South Wales³⁶Tata Institute of Fundamental Research, Mumbai³⁷Toho University, Funabashi³⁸Tohoku Gakuin University, Tagajo³⁹Tohoku University, Sendai⁴⁰Department of Physics, University of Tokyo, Tokyo⁴¹Tokyo Institute of Technology, Tokyo⁴²Tokyo Metropolitan University, Tokyo⁴³Tokyo University of Agriculture and Technology, Tokyo⁴⁴Virginia Polytechnic Institute and State University, Blacksburg, Virginia 24061⁴⁵Yonsei University, Seoul⁴⁶Panjab University, Chandigarh

(Received 4 February 2008; published 13 May 2008)

We report improved measurements of time-dependent CP violation parameters for $B^0(\bar{B}^0) \rightarrow \psi(2S)K_S^0$. This analysis is based on a data sample of $657 \times 10^6 B\bar{B}$ pairs collected at the $\Upsilon(4S)$ resonance with the Belle detector at the KEKB energy-asymmetric e^+e^- collider. We fully reconstruct one neutral B meson in the $\psi(2S)K_S^0$ CP -eigenstate decay channel, and the flavor of the accompanying B meson is identified to be either B^0 or \bar{B}^0 from its decay products. CP violation parameters are obtained from the asymmetries in the distributions of the proper-time intervals between the two B decays: $\mathcal{S}_{\psi(2S)K_S^0} = +0.72 \pm 0.09(\text{stat}) \pm 0.03(\text{syst})$, $\mathcal{A}_{\psi(2S)K_S^0} = +0.04 \pm 0.07(\text{stat}) \pm 0.05(\text{syst})$. These results are in agreement with results from measurements of $B^0 \rightarrow J/\psi K^0$.

DOI: 10.1103/PhysRevD.77.091103

PACS numbers: 11.30.Er, 12.15.Hh, 13.25.Hw

In the standard model, CP violation in B^0 meson decays originates from an irreducible complex phase in the 3×3 Cabibbo-Kobayashi-Maskawa (CKM) mixing matrix [1]. In the decay chain $\Upsilon(4S) \rightarrow B^0\bar{B}^0 \rightarrow f_{CP}f_{\text{tag}}$, where one of the B mesons decays at time t_{CP} to a CP eigenstate f_{CP} and the other decays at time t_{tag} to a final state f_{tag} that distinguishes between B^0 and \bar{B}^0 , the decay rate has a time dependence [2] given by

$$\mathcal{P}(\Delta t) = \frac{e^{-|\Delta t|/\tau_{B^0}}}{4\tau_{B^0}} \{1 + q \cdot [\mathcal{S}_{f_{CP}} \sin(\Delta m_d \Delta t) + \mathcal{A}_{f_{CP}} \cos(\Delta m_d \Delta t)]\}. \quad (1)$$

Here $\mathcal{S}_{f_{CP}}$ and $\mathcal{A}_{f_{CP}}$ are the CP violation parameters, τ_{B^0} is the neutral B lifetime, Δm_d is the mass difference between the two neutral B mass eigenstates, $\Delta t = t_{CP} - t_{\text{tag}}$, and the b -flavor charge q equals $+1$ (-1) when the tagging B meson is a B^0 (\bar{B}^0). For f_{CP} final states resulting from a $b \rightarrow c\bar{c}s$ transition, the standard model predicts $\mathcal{S}_{f_{CP}} = -\xi_f \sin 2\phi_1$ [3] and $\mathcal{A}_{f_{CP}} \simeq 0$, where $\xi_f = +1$ (-1) for CP -even (CP -odd) final states and ϕ_1 is one of the three interior angles of the CKM unitarity triangle, defined as $\phi_1 \equiv \pi - \arg(V_{tb}^* V_{td} / V_{cb}^* V_{cd})$. Measurements of CP asymmetries in $b \rightarrow c\bar{c}s$ transitions have been reported by Belle [4,5] and BABAR [6]. Results from our previously published $B^0 \rightarrow \psi(2S)K_S^0$ analysis were based on a 140 fb^{-1} data sample corresponding to $152 \times 10^6 B\bar{B}$ pairs [4]. Here we report new measurements with an improved analysis [7] incorporating an additional 465 fb^{-1} data sample for a total of 605 fb^{-1} ($657 \times 10^6 B\bar{B}$ pairs).

At the KEKB energy-asymmetric e^+e^- (3.5 on 8.0 GeV) collider [8], the $\Upsilon(4S)$ is produced with a Lorentz boost of

$\beta\gamma = 0.425$ nearly along the z axis, which is defined as opposite to the positron beam direction. Since the B^0 and \bar{B}^0 are approximately at rest in the $\Upsilon(4S)$ center-of-mass system (cms), Δt can be determined from the displacement in z between the two decay vertices: $\Delta t \simeq \Delta z / (\beta\gamma c)$, where c is the speed of light.

The Belle detector is a large-solid-angle magnetic spectrometer that consists of a silicon vertex detector (SVD), a 50-layer central drift chamber (CDC), an array of aerogel threshold Cherenkov counters (ACC), a barrel-like arrangement of time-of-flight scintillation counters (TOF), and an electromagnetic calorimeter (ECL) comprised of CsI(Tl) crystals located inside a superconducting solenoid coil that provides a 1.5 T magnetic field. An iron flux-return located outside the coil is instrumented to detect K_L^0 mesons and to identify muons (KLM). The detector is described in detail elsewhere [9]. Two different inner detector configurations were used. For the first sample of $152 \times 10^6 B\bar{B}$ pairs, a 2.0 cm radius beampipe and a 3-layer silicon vertex detector (SVD-I) were used; for the latter $505 \times 10^6 B\bar{B}$ pairs, a 1.5 cm radius beampipe, a 4-layer silicon detector (SVD-II), and a small-cell inner drift chamber were used [10].

We reconstruct $\psi(2S)$ mesons in the l^+l^- decay channel ($l = e$ or μ) and $J/\psi\pi^+\pi^-$ decay channel. J/ψ mesons are reconstructed in the l^+l^- decay channel and include the bremsstrahlung photons that are within 50 mrad of each of the e^+ and e^- tracks [denoted as $e^+e^-(\gamma)$]. The invariant mass of the J/ψ candidates is required to be within $-0.150 \text{ GeV}/c^2 < M_{e^+e^-(\gamma)} - m_{J/\psi} < +0.036 \text{ GeV}/c^2$ and $-0.060 \text{ GeV}/c^2 < M_{\mu^+\mu^-} - m_{J/\psi} < +0.036 \text{ GeV}/c^2$, where $m_{J/\psi}$ denotes the world-average J/ψ mass [11],

and $M_{e^+e^-(\gamma)}$ and $M_{\mu^+\mu^-}$ are the reconstructed invariant masses of the $e^+e^-(\gamma)$ and $\mu^+\mu^-$ candidates, respectively. For the $\psi(2S) \rightarrow l^+l^-$ candidates, the same procedure is used. In this case, the invariant mass is required to be within $-0.150 \text{ GeV}/c^2 < M_{e^+e^-(\gamma)} - m_{\psi(2S)} < +0.036 \text{ GeV}/c^2$ and $-0.060 \text{ GeV}/c^2 < M_{\mu^+\mu^-} - m_{\psi(2S)} < +0.036 \text{ GeV}/c^2$, where $m_{\psi(2S)}$ denotes the world-average $\psi(2S)$ mass [11]. For the $\psi(2S) \rightarrow J/\psi\pi^+\pi^-$ candidates, $\Delta M \equiv M_{l^+\pi^+\pi^-} - M_{l^+l^-}$ is required to be within $0.580 \text{ GeV}/c^2 < \Delta M < 0.600 \text{ GeV}/c^2$. To reduce the fraction of incorrectly reconstructed $\psi(2S)$ signal candidates, we select $\pi^+\pi^-$ pairs with an invariant mass greater than $400 \text{ MeV}/c^2$. The K_S^0 selection criteria are the same as those described in Ref. [12]; the invariant mass of the pion pairs is required to satisfy $0.482 \text{ GeV}/c^2 < M_{\pi^+\pi^-} < 0.514 \text{ GeV}/c^2$.

We combine the $\psi(2S)$ and K_S^0 to form a neutral B meson. The B candidates are identified using two kinematic variables: the energy difference $\Delta E \equiv E_B^{\text{cms}} - E_{\text{beam}}^{\text{cms}}$ and the beam-energy-constrained mass $M_{\text{bc}} \equiv \sqrt{(E_{\text{beam}}^{\text{cms}})^2 - (p_B^{\text{cms}})^2}$, where $E_{\text{beam}}^{\text{cms}}$ is the beam energy in the cms, and E_B^{cms} and p_B^{cms} are the cms energy and momentum, respectively, of the reconstructed B candidate. In order to improve the ΔE resolution, the masses of the selected J/ψ and $\psi(2S)$ candidates are constrained to their nominal masses using mass-constrained kinematic fits. For the CP asymmetry fit, we select the candidates in the ΔE - M_{bc} signal region defined as $|\Delta E| < 0.03 \text{ GeV}$ and $5.27 \text{ GeV}/c^2 < M_{\text{bc}} < 5.29 \text{ GeV}/c^2$. To suppress background from $e^+e^- \rightarrow q\bar{q}$ ($q = u, d, s,$ or c) continuum events, we require that the event-shape variable R_2 be less than 0.5, where R_2 is the ratio of second to zeroth Fox-Wolfgram moments [13].

The b flavor of the accompanying B meson is identified by a tagging algorithm [14] that categorizes charged leptons, kaons, and Λ baryons found in the event. The algorithm returns two parameters: the b -flavor charge q , and r , which measures the tag quality and varies from $r = 0$ for no flavor discrimination to $r = 1$ for unambiguous flavor assignment. If $r < 0.1$, the accompanying B meson provides negligible tagging information and we set the wrong tag probability to 0.5. Events with $r > 0.1$ are divided into six r intervals.

The vertex position for the f_{CP} decay is reconstructed using charged tracks that have a minimum number of SVD hits [15]. A constraint on the interaction point is also used with the selected tracks; the interaction point profile is convolved with the finite B -flight length in the plane perpendicular to the z axis. The pions from K_S^0 decays are not used for vertexing. The typical vertex reconstruction efficiency and z resolution are 95% and $78 \mu\text{m}$, respectively [12]. The f_{tag} vertex determination is obtained with well-reconstructed tracks that are not assigned to f_{CP} . The typical vertex reconstruction efficiency and z resolu-

tion are 93% and $140 \mu\text{m}$, respectively [12]. After all selection criteria are applied, we obtain 1618 and 1202 events for the l^+l^- and $J/\psi\pi^+\pi^-$ modes in the ΔE - M_{bc} fit region defined as $5.2 \text{ GeV}/c^2 < M_{\text{bc}} < 5.3 \text{ GeV}/c^2$ and $-0.1 \text{ GeV} < \Delta E < 0.1 \text{ GeV}$, of which 680 and 712, respectively, are in the signal region.

Figure 1 shows the reconstructed variables ΔE and M_{bc} after flavor tagging and vertex reconstruction. The signal yield is obtained from an extended unbinned maximum-likelihood fit to the ΔE - M_{bc} distribution. We model the shape for the signal component using the product of a double Gaussian for ΔE and a single Gaussian for M_{bc} , whereas the combinatorial background is described by the product of a first-order polynomial for ΔE and an ARGUS [16] function for M_{bc} . For the $\psi(2S) \rightarrow J/\psi\pi^+\pi^-$ mode, there is a background component that peaks like the signal (peaking background) in the ΔE - M_{bc} signal region. This peaking background is mainly due to the $J/\psi K_1(1270)^0$, $J/\psi K^*(892)^-\pi^+$, and $J/\psi K_S^0\pi^+\pi^-$ modes, with no real

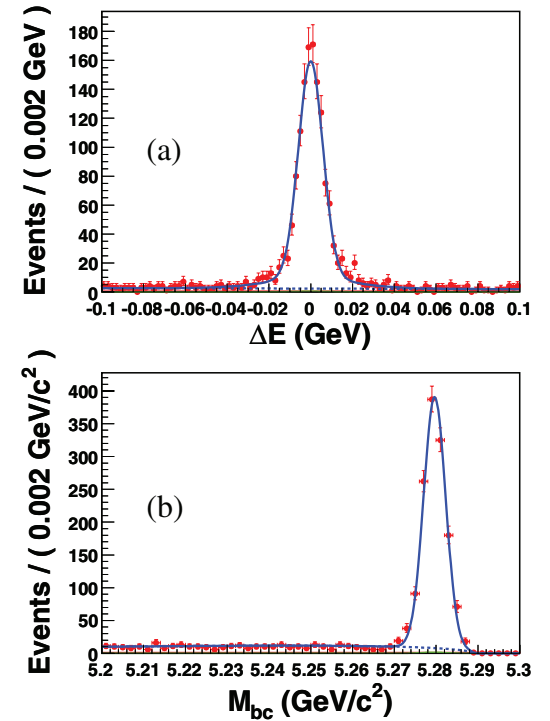


FIG. 1 (color online). (a) ΔE distribution within the M_{bc} signal region, (b) M_{bc} distribution within the ΔE signal region for $B^0 \rightarrow \psi(2S)K_S^0$. The solid curves show the fits to the signal plus background distributions, while the dashed curves show the background contributions. The small contribution from peaking backgrounds is discussed in the text.

H. SAHOO *et al.*TABLE I. Number of signal B candidates (N_{sig}) and estimated purity (p) in the signal region after flavor tagging and vertex reconstruction.

Mode	N_{sig}	p
$\psi(2S)(l^+l^-)K_S^0$	628 ± 26	0.92 ± 0.01
$\psi(2S)(J/\psi\pi^+\pi^-)K_S^0$	656 ± 26	0.92 ± 0.01

$\psi(2S) \rightarrow J/\psi\pi^+\pi^-$ in the final state. The fraction of such peaking events is estimated to be 1% from the ΔM sidebands in data. The signal and background shapes for each decay mode are determined from Monte Carlo (MC) events; these shapes are adjusted for small differences between MC and data using a control sample of $B^+ \rightarrow \psi(2S)K^+$ [17] events, which have a final state similar to the signal but with higher statistics. This sample, where no CP asymmetry is expected, is also used to check the potential bias in the measurements of CP violation parameters. The signal yields and purity in the ΔE - M_{bc} signal region after flavor tagging and vertex reconstruction are listed in Table I. We define the purity as the ratio of the signal yield to the total number of candidate events in the signal region.

We determine $S_{f_{CP}}$ and $\mathcal{A}_{f_{CP}}$ by performing an unbinned maximum-likelihood fit to the observed Δt distribution for the candidate events in the signal region. The likelihood function is

$$\mathcal{L}(S_{f_{CP}}, \mathcal{A}_{f_{CP}}) = \prod_i \mathcal{P}_i(S_{f_{CP}}, \mathcal{A}_{f_{CP}}; \Delta t_i), \quad (2)$$

where the product includes events in the signal region. We only use events with vertices that satisfy $|\Delta t| < 70$ ps and $\xi < 250$, where ξ is the χ^2 of the vertex fit calculated only in the z direction. The probability density function (PDF) is given by

$$\begin{aligned} \mathcal{P}_i = & (1 - f_{\text{ol}}) \int [f_{\text{sig}} \mathcal{P}_{\text{sig}}(\Delta t') R_{\text{sig}}(\Delta t_i - \Delta t') \\ & + f_{\text{peak}} \mathcal{P}_{\text{peak}}(\Delta t') R_{\text{sig}}(\Delta t_i - \Delta t') \\ & + (1 - f_{\text{sig}} - f_{\text{peak}}) \mathcal{P}_{\text{bkg}}(\Delta t') R_{\text{bkg}}(\Delta t_i - \Delta t')] d(\Delta t') \\ & + f_{\text{ol}} P_{\text{ol}}(\Delta t_i). \end{aligned} \quad (3)$$

The signal fraction f_{sig} and the peaking fraction f_{peak} depend on the r region and are calculated on an event-by-event basis as a function of ΔE and M_{bc} . The PDF for signal events, $\mathcal{P}_{\text{sig}}(\Delta t)$, is given by Eq. (1) and modified to incorporate the effect of incorrect flavor assignment; the parameters τ_{B^0} and Δm_d are fixed to their world-average values [11]. The distribution is then convolved with a resolution function $R_{\text{sig}}(\Delta t)$ to take into account the finite vertex resolution. The resolution function parameters, along with the wrong tag fractions for the six r intervals, w_l ($l = 1, 6$), and possible differences in w_l between B^0 and \bar{B}^0 decays (Δw_l) are determined using a high-statistics control sample of semileptonic and hadronic $b \rightarrow c$ decays [4,12]. The PDF for non-peaking background events,

$\mathcal{P}_{\text{bkg}}(\Delta t)$, is modeled as a sum of exponential and prompt components and is convolved with a sum of two Gaussians, which parameterizes the resolution function $R_{\text{bkg}}(\Delta t)$. Parameters in $\mathcal{P}_{\text{bkg}}(\Delta t)$ and $R_{\text{bkg}}(\Delta t)$ are determined from a fit to the Δt distribution of events in the ΔE - M_{bc} data sideband ($M_{bc} < 5.26$ GeV/ c^2 , -0.03 GeV $< \Delta E < 0.20$ GeV). The PDF for peaking background events, $\mathcal{P}_{\text{peak}}(\Delta t)$, is the same as $\mathcal{P}_{\text{sig}}(\Delta t)$ with CP parameters fixed to zero. The term $P_{\text{ol}}(\Delta t)$ is a broad Gaussian function that represents an outlier component with a small fraction f_{ol} . The only free parameters in the final fit are $S_{f_{CP}}$ and $\mathcal{A}_{f_{CP}}$; these are determined by maximizing the likelihood function given by Eq. (2).

The unbinned maximum-likelihood fit to the 1300 events in the signal region results in the CP violation parameters,

$$S_{\psi(2S)K_S^0} = +0.72 \pm 0.09(\text{stat}) \pm 0.03(\text{syst}),$$

$$\mathcal{A}_{\psi(2S)K_S^0} = +0.04 \pm 0.07(\text{stat}) \pm 0.05(\text{syst}),$$

where the systematic uncertainties listed are described below. We define the raw asymmetry in each Δt bin by $(N_+ - N_-)/(N_+ + N_-)$, where N_+ (N_-) is the number of observed candidates with $q = +1$ (-1). Figure 2 shows the observed Δt distributions for $q = +1$ and $q = -1$ with no requirement on the tagging quality (top), and the raw asymmetry for events with good tagging quality ($r > 0.5$) (bottom).

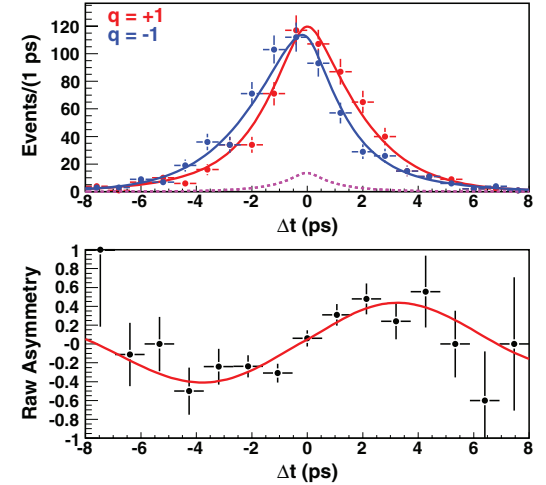


FIG. 2 (color online). The top plot shows the Δt distributions for $q = +1$ and $q = -1$ with no requirement on r . The dashed curve is the sum of backgrounds, while the solid curves are the sum of signal and backgrounds. The bottom plot is the raw asymmetry of well-tagged events ($r > 0.5$, 45% of the total). The solid curve shows the result of the unbinned maximum-likelihood fit.

The systematic errors on $S_{f_{CP}}$ and $\mathcal{A}_{f_{CP}}$, summarized in Table II, are evaluated by fitting the data with each fixed parameter varied by its 1 standard deviation (σ) error. The MC-determined parameters are varied by $\pm 2\sigma$ to take into account possible imperfect modeling in the MC. We repeat the CP fit procedure with the new value, add the differences in S, \mathcal{A} quadratically, and then assign the result as the systematic error. The largest contribution to $S_{f_{CP}}$ comes from vertex reconstruction (0.026). This includes the uncertainties in the interaction point profile (the smearing used to account for the B flight length is varied by $-10\mu\text{m}$ and $+20\mu\text{m}$), the tag side track selection criteria, the helix parameter correction, the $|\Delta t|$ range (varied by ± 30 ps), the vertex quality cut ξ (changed to $\xi < 150$ and $\xi < 500$), the Δz measurement, and imperfect SVD alignment. The last two are obtained from a study of $J/\psi K_S^0$. Each physics parameter ($\tau_{B^0}, \Delta m_d$) is varied by the error in its world-average value [11]. Systematic errors due to uncertainties in wrong tag fractions are estimated by varying the parameters $w_l, \Delta w_l$ in each r region by their $\pm 1\sigma$ errors. Systematic errors due to uncertainties in the resolution function are estimated by varying each resolution parameter obtained from data (MC) by $\pm 1\sigma$ ($\pm 2\sigma$). The $\Delta E, M_{bc}$ parameters and signal fraction in each r region are varied to estimate the systematic errors. No significant bias is seen by fitting a large sample of MC events. The systematic errors from uncertainties in the peaking background are obtained by varying the peaking fraction, shape, as well as its CP asymmetry parameters. The systematic errors from uncertainties in the background Δt shape are estimated by varying each background parameter by its statistical error. We also include the effects of interference between CKM-favored and CKM-suppressed $B \rightarrow D$ transitions in the f_{tag} final state [18]. We add each contribution above in quadrature to obtain the total systematic uncertainty.

We perform various cross-checks for this measurement. A fit to the first data sample (SVD-I) results in the CP violation parameter, $S = 0.97 \pm 0.18$, which is consistent with our previous result [4]. A fit to the CP asymmetries of the control sample gives the CP violation parameters, $S = 0.02 \pm 0.05$ and $\mathcal{A} = -0.03 \pm 0.03$, which are consistent with no CP asymmetry. A fit to the sideband events in the

TABLE II. Systematic uncertainties.

Parameter	$\Delta S_{\psi(2S)K_S^0}$	$\Delta \mathcal{A}_{\psi(2S)K_S^0}$
Vertexing	0.026	0.028
Wrong tag fraction	0.006	0.023
Resolution function	0.007	0.005
Fit bias	0.012	0.011
Physics parameters	0.001	0.001
Peaking background	0.006	0.005
PDF shape and fraction	0.001	0.003
Background Δt shape	0.003	0.003
Tag side interference	0.001	0.036
Total	0.031	0.053

$B^0 \rightarrow \psi(2S)K_S^0$ data sample gives an asymmetry consistent with zero ($S = 0.02 \pm 0.21, \mathcal{A} = -0.04 \pm 0.10$). A lifetime fit to $B^0 \rightarrow \psi(2S)K_S^0$ and $B^+ \rightarrow \psi(2S)K^+$ gives $\tau_{B^0} = 1.51 \pm 0.05$ ps and $\tau_{B^+} = 1.62 \pm 0.03$ ps, respectively, which are consistent with the world-average values. We also examine the CP violation parameters separately for the $\psi(2S) \rightarrow l^+ l^-$ ($S = 0.84 \pm 0.13, \mathcal{A} = 0.14 \pm 0.09$) and $\psi(2S) \rightarrow J/\psi \pi^+ \pi^-$ ($S = 0.61 \pm 0.13, \mathcal{A} = -0.09 \pm 0.10$) decay modes. We find that all results are consistent within errors.

In summary, we have performed improved measurements of CP violation parameters $\sin 2\phi_1$ and $\mathcal{A}_{f_{CP}}$ for $B^0 \rightarrow \psi(2S)K_S^0$ using $657 \times 10^6 B\bar{B}$ events. These measurements supersede our previous result [4] and are in agreement with results from measurements of $B^0 \rightarrow J/\psi K^0$ [19]. Combining the results from $B^0 \rightarrow J/\psi K^0$ [5] and $B^0 \rightarrow \psi(2S)K_S^0$ decays, we obtain a new Belle average $\sin 2\phi_1 = 0.650 \pm 0.029 \pm 0.018$.

We thank the KEKB group for excellent operation of the accelerator, the KEK cryogenics group for efficient solenoid operations, and the KEK computer group and the NII for valuable computing and Super-SINET network support. We acknowledge support from MEXT and JSPS (Japan); ARC and DEST (Australia); NSFC (China); DST (India); MOEHRD, KOSEF, and KRF (Korea); KBN (Poland); MES and RFAAE (Russia); ARRS (Slovenia); SNSF (Switzerland); NSC and MOE (Taiwan); and DOE (USA).

- [1] N. Cabibbo, Phys. Rev. Lett. **10**, 531 (1963); M. Kobayashi and T. Maskawa, Prog. Theor. Phys. **49**, 652 (1973).
 [2] A. B. Carter and A. I. Sanda, Phys. Rev. D **23**, 1567 (1981); I. I. Bigi and A. I. Sanda, Nucl. Phys. **B193**, 85 (1981).

- [3] Another naming convention, $\beta(= \phi_1)$, is also used in the literature.
 [4] K. Abe *et al.* (Belle Collaboration), Phys. Rev. D **71**, 072003 (2005).
 [5] K-F. Chen *et al.* (Belle Collaboration), Phys. Rev. Lett. **98**, 031802 (2007).

H. SAHOO *et al.*

PHYSICAL REVIEW D **77**, 091103(R) (2008)

- [6] B. Aubert *et al.* (BABAR Collaboration), Phys. Rev. Lett. **99**, 171803 (2007).
- [7] This analysis is improved compared to our previous publication [4]. The peaking backgrounds are estimated directly from the data sidebands. The signal and peaking fraction in the time-dependent PDF are determined for each r bin. In addition to the lepton tracks from the J/ψ , we use the prompt $\pi^+\pi^-$ tracks in the vertex reconstruction for the $\psi(2S)(J/\psi\pi^+\pi^-)K_S^0$ decay mode. Only lepton tracks from the J/ψ were used in the previous analysis.
- [8] S. Kurokawa and E. Kikutani, Nucl. Instrum. Methods Phys. Res., Sect. A **499**, 1 (2003), and other papers included in this volume.
- [9] A. Abashian *et al.* (Belle Collaboration), Nucl. Instrum. Methods Phys. Res., Sect. A **479**, 117 (2002).
- [10] Z. Natkaniec (Belle SVD2 Group), Nucl. Instrum. Methods Phys. Res., Sect. A **560**, 1 (2006).
- [11] W.-M. Yao *et al.*, J. Phys. G **33**, 1 (2006).
- [12] K-F. Chen *et al.* (Belle Collaboration), Phys. Rev. D **72**, 012004 (2005).
- [13] G. C. Fox and S. Wolfram, Phys. Rev. Lett. **41**, 1581 (1978).
- [14] H. Kakuno *et al.*, Nucl. Instrum. Methods Phys. Res., Sect. A **533**, 516 (2004).
- [15] H. Tajima *et al.*, Nucl. Instrum. Methods Phys. Res., Sect. A **533**, 370 (2004).
- [16] H. Albrecht *et al.* (ARGUS Collaboration), Phys. Lett. B **241**, 278 (1990).
- [17] Throughout this paper, the inclusion of the charge-conjugate decay mode is implied unless otherwise stated.
- [18] O. Long, M. Baak, R. N. Cahn, and D. Kirkby, Phys. Rev. D **68**, 034010 (2003).
- [19] See <http://www.slac.stanford.edu/xorg/hfag/> for updated results.

Observation of radiative $B^0 \rightarrow \phi K^0 \gamma$ decays

I. Adachi,¹⁰ H. Aihara,⁵⁹ K. Arinstein,^{1,41} T. Aso,⁶³ V. Aulchenko,^{1,41} T. Aushev,^{26,19}
 T. Aziz,⁵⁴ S. Bahinipati,³ A. M. Bakich,⁵³ V. Balagura,¹⁹ Y. Ban,⁴⁵ E. Barberio,³⁰
 A. Bay,²⁶ I. Bedny,^{1,41} K. Belous,¹⁶ V. Bhardwaj,⁴⁴ B. Bhuyan,¹³ M. Bischofberger,³³
 S. Blyth,³⁵ A. Bondar,^{1,41} A. Bozek,³⁷ M. Bračko,^{28,20} J. Brodzicka,³⁷ T. E. Browder,⁹
 M.-C. Chang,⁴ P. Chang,³⁶ Y.-W. Chang,³⁶ Y. Chao,³⁶ A. Chen,³⁴ K.-F. Chen,³⁶
 P.-Y. Chen,³⁶ B. G. Cheon,⁸ C.-C. Chiang,³⁶ R. Chistov,¹⁹ I.-S. Cho,⁶⁵ S.-K. Choi,⁷
 Y. Choi,⁵² J. Crnkovic,¹² J. Dalseno,^{29,55} M. Danilov,¹⁹ A. Das,⁵⁴ M. Dash,⁶⁴
 A. Drutskoy,³ W. Dungel,¹⁵ S. Eidelman,^{1,41} D. Epifanov,^{1,41} M. Feindt,²² H. Fujii,¹⁰
 M. Fujikawa,³³ N. Gabyshev,^{1,41} A. Garmash,^{1,41} G. Gokhroo,⁵⁴ P. Goldenzweig,³
 B. Golob,^{27,20} M. Grosse Perdekamp,^{12,47} H. Guo,⁴⁹ H. Ha,²³ J. Haba,¹⁰ B.-Y. Han,²³
 K. Hara,³¹ T. Hara,¹⁰ Y. Hasegawa,⁵¹ N. C. Hastings,⁵⁹ K. Hayasaka,³¹ H. Hayashii,³³
 M. Hazumi,¹⁰ D. Heffernan,⁴³ T. Higuchi,¹⁰ Y. Horii,⁵⁸ Y. Hoshi,⁵⁷ K. Hoshina,⁶²
 W.-S. Hou,³⁶ Y. B. Hsiung,³⁶ H. J. Hyun,²⁵ Y. Igarashi,¹⁰ T. Iijima,³¹ K. Inami,³¹
 A. Ishikawa,⁴⁸ H. Ishino,^{60,*} K. Itoh,⁵⁹ R. Itoh,¹⁰ M. Iwabuchi,⁶ M. Iwasaki,⁵⁹ Y. Iwasaki,¹⁰
 T. Jinno,³¹ M. Jones,⁹ N. J. Joshi,⁵⁴ T. Julius,³⁰ D. H. Kah,²⁵ H. Kakuno,⁵⁹ J. H. Kang,⁶⁵
 P. Kapusta,³⁷ S. U. Kataoka,³² N. Katayama,¹⁰ H. Kawai,² T. Kawasaki,³⁹ A. Kibayashi,¹⁰
 H. Kichimi,¹⁰ C. Kiesling,²⁹ H. J. Kim,²⁵ H. O. Kim,²⁵ J. H. Kim,⁵² S. K. Kim,⁵⁰
 Y. I. Kim,²⁵ Y. J. Kim,⁶ K. Kinoshita,³ B. R. Ko,²³ S. Korpar,^{28,20} M. Kreps,²²
 P. Križan,^{27,20} P. Krokovny,¹⁰ T. Kuhr,²² R. Kumar,⁴⁴ T. Kumita,⁶¹ E. Kurihara,²
 E. Kuroda,⁶¹ Y. Kuroki,⁴³ A. Kusaka,⁵⁹ A. Kuzmin,^{1,41} Y.-J. Kwon,⁶⁵ S.-H. Kyeong,⁶⁵
 J. S. Lange,⁵ G. Leder,¹⁵ M. J. Lee,⁵⁰ S. E. Lee,⁵⁰ S.-H. Lee,²³ J. Li,⁹ A. Limosani,³⁰
 S.-W. Lin,³⁶ C. Liu,⁴⁹ D. Liventsev,¹⁹ R. Louvot,²⁶ J. MacNaughton,¹⁰ F. Mandl,¹⁵
 D. Marlow,⁴⁶ A. Matyja,³⁷ S. McOnie,⁵³ T. Medvedeva,¹⁹ Y. Mikami,⁵⁸ K. Miyabayashi,³³
 H. Miyake,⁴³ H. Miyata,³⁹ Y. Miyazaki,³¹ R. Mizuk,¹⁹ A. Moll,^{29,55} T. Mori,³¹ T. Müller,²²
 R. Mussa,¹⁸ T. Nagamine,⁵⁸ Y. Nagasaka,¹¹ Y. Nakahama,⁵⁹ I. Nakamura,¹⁰ E. Nakano,⁴²
 M. Nakao,¹⁰ H. Nakayama,⁵⁹ H. Nakazawa,³⁴ Z. Natkaniec,³⁷ K. Neichi,⁵⁷ S. Neubauer,²²
 S. Nishida,¹⁰ K. Nishimura,⁹ O. Nitoh,⁶² S. Noguchi,³³ T. Nozaki,¹⁰ A. Ogawa,⁴⁷
 S. Ogawa,⁵⁶ T. Ohshima,³¹ S. Okuno,²¹ S. L. Olsen,⁵⁰ W. Ostrowicz,³⁷ H. Ozaki,¹⁰
 P. Pakhlov,¹⁹ G. Pakhlova,¹⁹ H. Palka,³⁷ C. W. Park,⁵² H. Park,²⁵ H. K. Park,²⁵
 K. S. Park,⁵² L. S. Peak,⁵³ M. Pernicka,¹⁵ R. Pestotnik,²⁰ M. Peters,⁹ L. E. Piilonen,⁶⁴
 A. Poluektov,^{1,41} K. Prothmann,^{29,55} B. Riesert,²⁹ M. Rozanska,³⁷ H. Sahoo,⁹
 K. Sakai,³⁹ Y. Sakai,¹⁰ N. Sasao,²⁴ O. Schneider,²⁶ P. Schönmeier,⁵⁸ J. Schümann,¹⁰
 C. Schwanda,¹⁵ A. J. Schwartz,³ R. Seidl,⁴⁷ A. Sekiya,³³ K. Senyo,³¹ M. E. Sevier,³⁰
 L. Shang,¹⁴ M. Shapkin,¹⁶ V. Shebalin,^{1,41} C. P. Shen,⁹ H. Shibuya,⁵⁶ S. Shiizuka,³¹
 S. Shinomiya,⁴³ J.-G. Shiu,³⁶ B. Shwartz,^{1,41} F. Simon,^{29,55} J. B. Singh,⁴⁴ R. Sinha,¹⁷
 A. Sokolov,¹⁶ E. Solovieva,¹⁹ S. Stanič,⁴⁰ M. Starič,²⁰ J. Stypula,³⁷ A. Sugiyama,⁴⁸
 K. Sumisawa,¹⁰ T. Sumiyoshi,⁶¹ S. Suzuki,⁴⁸ S. Y. Suzuki,¹⁰ Y. Suzuki,³¹ F. Takasaki,¹⁰
 N. Tamura,³⁹ K. Tanabe,⁵⁹ M. Tanaka,¹⁰ N. Taniguchi,¹⁰ G. N. Taylor,³⁰ Y. Teramoto,⁴²
 I. Tikhomirov,¹⁹ K. Trabelsi,¹⁰ Y. F. Tse,³⁰ T. Tsuboyama,¹⁰ K. Tsunada,³¹ Y. Uchida,⁶
 S. Uehara,¹⁰ Y. Ueki,⁶¹ K. Ueno,³⁶ T. Uglov,¹⁹ Y. Unno,⁸ S. Uno,¹⁰ P. Urquijo,³⁰
 Y. Ushiroda,¹⁰ Y. Usov,^{1,41} G. Varner,⁹ K. E. Varvell,⁵³ K. Vervink,²⁶ A. Vinokurova,^{1,41}
 C. C. Wang,³⁶ C. H. Wang,³⁵ J. Wang,⁴⁵ M.-Z. Wang,³⁶ P. Wang,¹⁴ X. L. Wang,¹⁴

M. Watanabe,³⁹ Y. Watanabe,²¹ R. Wedd,³⁰ J.-T. Wei,³⁶ J. Wicht,¹⁰ L. Widhalm,¹⁵
J. Wiechczynski,³⁷ E. Won,²³ B. D. Yabsley,⁵³ H. Yamamoto,⁵⁸ Y. Yamashita,³⁸
M. Yamauchi,¹⁰ C. Z. Yuan,¹⁴ Y. Yusa,⁶⁴ C. C. Zhang,¹⁴ L. M. Zhang,⁴⁹ Z. P. Zhang,⁴⁹
V. Zhilich,^{1,41} V. Zhulanov,^{1,41} T. Zivko,²⁰ A. Zupanc,²⁰ N. Zwahlen,²⁶ and O. Zyukova^{1,41}

(The Belle Collaboration)

¹*Budker Institute of Nuclear Physics, Novosibirsk*

²*Chiba University, Chiba*

³*University of Cincinnati, Cincinnati, Ohio 45221*

⁴*Department of Physics, Fu Jen Catholic University, Taipei*

⁵*Justus-Liebig-Universität Gießen, Gießen*

⁶*The Graduate University for Advanced Studies, Hayama*

⁷*Gyeongsang National University, Chinju*

⁸*Hanyang University, Seoul*

⁹*University of Hawaii, Honolulu, Hawaii 96822*

¹⁰*High Energy Accelerator Research Organization (KEK), Tsukuba*

¹¹*Hiroshima Institute of Technology, Hiroshima*

¹²*University of Illinois at Urbana-Champaign, Urbana, Illinois 61801*

¹³*India Institute of Technology Guwahati, Guwahati*

¹⁴*Institute of High Energy Physics,*

Chinese Academy of Sciences, Beijing

¹⁵*Institute of High Energy Physics, Vienna*

¹⁶*Institute of High Energy Physics, Protvino*

¹⁷*Institute of Mathematical Sciences, Chennai*

¹⁸*INFN - Sezione di Torino, Torino*

¹⁹*Institute for Theoretical and Experimental Physics, Moscow*

²⁰*J. Stefan Institute, Ljubljana*

²¹*Kanagawa University, Yokohama*

²²*Institut für Experimentelle Kernphysik, Universität Karlsruhe, Karlsruhe*

²³*Korea University, Seoul*

²⁴*Kyoto University, Kyoto*

²⁵*Kyungpook National University, Taegu*

²⁶*École Polytechnique Fédérale de Lausanne (EPFL), Lausanne*

²⁷*Faculty of Mathematics and Physics, University of Ljubljana, Ljubljana*

²⁸*University of Maribor, Maribor*

²⁹*Max-Planck-Institut für Physik, München*

³⁰*University of Melbourne, School of Physics, Victoria 3010*

³¹*Nagoya University, Nagoya*

³²*Nara University of Education, Nara*

³³*Nara Women's University, Nara*

³⁴*National Central University, Chung-li*

³⁵*National United University, Miao Li*

³⁶*Department of Physics, National Taiwan University, Taipei*

³⁷*H. Niewodniczanski Institute of Nuclear Physics, Krakow*

³⁸*Nippon Dental University, Niigata*

³⁹*Niigata University, Niigata*

⁴⁰*University of Nova Gorica, Nova Gorica*

- ⁴¹*Novosibirsk State University, Novosibirsk*
⁴²*Osaka City University, Osaka*
⁴³*Osaka University, Osaka*
⁴⁴*Panjab University, Chandigarh*
⁴⁵*Peking University, Beijing*
⁴⁶*Princeton University, Princeton, New Jersey 08544*
⁴⁷*RIKEN BNL Research Center, Upton, New York 11973*
⁴⁸*Saga University, Saga*
⁴⁹*University of Science and Technology of China, Hefei*
⁵⁰*Seoul National University, Seoul*
⁵¹*Shinshu University, Nagano*
⁵²*Sungkyunkwan University, Suwon*
⁵³*School of Physics, University of Sydney, NSW 2006*
⁵⁴*Tata Institute of Fundamental Research, Mumbai*
⁵⁵*Excellence Cluster Universe, Technische Universität München, Garching*
⁵⁶*Toho University, Funabashi*
⁵⁷*Tohoku Gakuin University, Tagajo*
⁵⁸*Tohoku University, Sendai*
⁵⁹*Department of Physics, University of Tokyo, Tokyo*
⁶⁰*Tokyo Institute of Technology, Tokyo*
⁶¹*Tokyo Metropolitan University, Tokyo*
⁶²*Tokyo University of Agriculture and Technology, Tokyo*
⁶³*Toyama National College of Maritime Technology, Toyama*
⁶⁴*IPNAS, Virginia Polytechnic Institute and State University, Blacksburg, Virginia 24061*
⁶⁵*Yonsei University, Seoul*

Abstract

We report the first observation of radiative decay $B^0 \rightarrow \phi K^0 \gamma$ using a data sample of 772×10^6 $B\bar{B}$ pairs collected at the $\Upsilon(4S)$ resonance with the Belle detector at the KEKB asymmetric-energy e^+e^- collider. We observe a signal of 35 ± 8 events with a significance of 5.4 standard deviations including systematic uncertainties. The measured branching fraction is $\mathcal{B}(B^0 \rightarrow \phi K^0 \gamma) = (2.66 \pm 0.60 \pm 0.32) \times 10^{-6}$. We also precisely measure $\mathcal{B}(B^+ \rightarrow \phi K^+ \gamma) = (2.34 \pm 0.29 \pm 0.23) \times 10^{-6}$. The uncertainties are statistical and systematic, respectively. The observed $M_{\phi K}$ mass spectrum differs significantly from that expected in a three-body phase-space decay.

PACS numbers: 14.40.Nd, 13.25.Hw, 11.30.Er

Rare radiative decays of B mesons play an important role in the search for physics beyond the standard model (SM) of electroweak interactions. These flavor changing neutral current decays are forbidden at tree level in the SM, but allowed through electroweak loop processes. The loop can be mediated by non-SM particles (for example, charged Higgs or SUSY particles), which could affect either the branching fraction or the time-dependent CP asymmetry.

The current measured inclusive world average branching fraction for $B \rightarrow X_s \gamma$ ($(3.55 \pm 0.26) \times 10^{-4}$ [1]), is one standard deviation (σ) higher than the SM prediction at next-to-next-to-leading order (NNLO) $(3.15 \pm 0.23) \times 10^{-4}$ [2], and still allows significant new physics contributions to radiative B decays. Exclusive $b \rightarrow s \gamma$ decays have also been extensively measured, but their sum so far accounts only for 44% of the inclusive rate. Therefore, further measurements of branching fractions for exclusive $B \rightarrow \phi K \gamma$ modes will improve our understanding of the $b \rightarrow s \gamma$ process. The neutral mode $B^0 \rightarrow \phi K^0 \gamma$ [3] can be used to study time-dependent CP asymmetry, which is suppressed in the SM by the quark mass ratio ($2m_s/m_b$) [4, 5]. In several models beyond SM, the photon acquires an appreciable right-handed component due to the exchange of a virtual heavy fermion in the loop process, resulting in large values of time-dependent CP asymmetries. Due to the narrow width of the ϕ resonance, the decay $B \rightarrow \phi K \gamma$ is well separated from the background and can be effectively used for measurements of photon momentum over a wide interval. In addition, this mode can also be used to search for a possible contribution from kaonic resonances decaying to ϕK . Furthermore, we can probe the photon polarization using the angular distributions of the final state hadrons [6, 7].

The decay $B^0 \rightarrow \phi K_S^0 \gamma$ can be described by the conventional radiative penguin diagram with the creation of an additional $s\bar{s}$ pair as shown in Fig. 1.

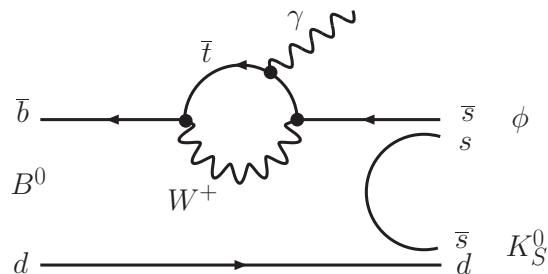


FIG. 1: Feynman diagram for the radiative penguin decay $B^0 \rightarrow \phi K_S^0 \gamma$ with $s\bar{s}$ pair creation.

The branching fractions for $B \rightarrow \phi K \gamma$ decays have already been reported by the Belle and BaBar collaborations. Belle measured $\mathcal{B}(B^+ \rightarrow \phi K^+ \gamma) = (3.4 \pm 0.9 \pm 0.4) \times 10^{-6}$ and $\mathcal{B}(B^0 \rightarrow \phi K^0 \gamma) < 8.3 \times 10^{-6}$ at the 90% confidence level (C.L.) using $96 \times 10^6 B\bar{B}$ pairs [8]. BaBar measured $\mathcal{B}(B^+ \rightarrow \phi K^+ \gamma) = (3.5 \pm 0.6 \pm 0.4) \times 10^{-6}$ and $\mathcal{B}(B^0 \rightarrow \phi K^0 \gamma) < 2.7 \times 10^{-6}$ at the 90% C.L. using $228 \times 10^6 B\bar{B}$ pairs [9]. BaBar also reported the direct CP asymmetry for $B^\pm \rightarrow \phi K^\pm \gamma$, $\mathcal{A}_{CP} = (-26 \pm 14 \pm 5)\%$. We report herein the first observation of radiative decay $B^0 \rightarrow \phi K^0 \gamma$ and an improved measurement of $B^+ \rightarrow \phi K^+ \gamma$ using a data sample of $772 \times 10^6 B\bar{B}$ pairs collected at the $\Upsilon(4S)$ resonance with the Belle detector at the KEKB asymmetric-energy e^+e^- collider [10]. This data sample is nearly eight times larger than the

sample used in our previous measurement [8].

The Belle detector is a large-solid-angle magnetic spectrometer that consists of a silicon vertex detector (SVD), a 50-layer central drift chamber (CDC), an array of aerogel threshold Cherenkov counters (ACC), a barrel-like arrangement of time-of-flight scintillation counters (TOF), and an electromagnetic calorimeter (ECL) comprised of CsI(Tl) crystals located inside a superconducting solenoid coil that provides a 1.5 T magnetic field. An iron flux-return located outside the coil is instrumented to detect K_L^0 mesons and to identify muons (KLM). The detector is described in detail elsewhere [11]. Two different inner detector configurations were used. For the first sample of 152×10^6 $B\bar{B}$ pairs, a 2.0 cm radius beampipe and a 3-layer silicon vertex detector (SVD-I) were used; for the latter 620×10^6 $B\bar{B}$ pairs, a 1.5 cm radius beampipe, a 4-layer silicon vertex detector (SVD-II), and a small-cell inner drift chamber were used. A GEANT-based simulation of the Belle detector is used to produce signal Monte Carlo (MC) [12] event samples.

The signal is reconstructed in the decays $B^+ \rightarrow \phi K^+ \gamma$ and $B^0 \rightarrow \phi K_S^0 \gamma$, with $\phi \rightarrow K^+ K^-$ and $K_S^0 \rightarrow \pi^+ \pi^-$. All the charged tracks used in the reconstruction (except for charged pions from K_S^0 's) are required to satisfy a requirement on the distance of closest approach to the interaction point (IP) along the beam direction, $|dz| < 5$ cm, and in the transverse direction, $dr < 2$ cm. This eliminates poorly reconstructed tracks or tracks that do not come from the interaction region. Charged kaons are identified using a likelihood ratio $\mathcal{L}(K/\pi) > 0.6$, based on information from the ACC, TOF and CDC (dE/dx) detectors. This requirement has an efficiency of 90% for kaons with a 8% pion fake rate. A less restrictive likelihood ratio requirement $\mathcal{L}(K/\pi) > 0.4$ is applied to the kaon candidates, which are used to reconstruct the ϕ meson. The invariant mass of the ϕ candidates is required to be within $-0.01 \text{ GeV}/c^2 < M_{K^+K^-} - m_\phi < +0.01 \text{ GeV}/c^2$, where m_ϕ denotes the world-average ϕ mass [13].

Neutral kaon (K_S^0) candidates are formed from the $\pi^+ \pi^-$ combinations with invariant mass in the range $0.482 \text{ GeV}/c^2 < M_{\pi^+ \pi^-} < 0.514 \text{ GeV}/c^2$. The selected candidates must pass a set of momentum-dependent requirements on impact parameter, vertex displacement, mismatch in the z direction, and the direction of the pion pair momentum as described in the Ref. [14].

The primary signature of this decay is a high energy prompt photon. These are selected from isolated ECL clusters within the barrel region ($32^\circ < \theta_\gamma < 129^\circ$, where θ_γ is the polar angle of the photon in the laboratory frame) and center-of-mass system (cms) energy (E_γ^{cms}) in the range 1.4 to 3.4 GeV. The selected photon candidates are required to be consistent with isolated electromagnetic showers, i.e., 95% of the energy in an array of 5×5 CsI(Tl) crystals should be concentrated in an array of 3×3 crystals and should have no charged tracks associated with it. We also suppress the background photons from $\pi^0(\eta) \rightarrow \gamma\gamma$ using a likelihood $\mathcal{L}_{\pi^0}(\mathcal{L}_\eta) < 0.25$, calculated for each photon pair consisting of the candidate photon and any other photon in the event [15].

We combine a ϕ meson candidate, a charged or neutral kaon candidate and the radiative photon to form a B meson. The B candidates are identified using two kinematic variables: the energy difference $\Delta E \equiv E_B^{\text{cms}} - E_{\text{beam}}^{\text{cms}}$ and the beam-energy-constrained mass $M_{\text{bc}} \equiv \sqrt{(E_{\text{beam}}^{\text{cms}})^2 - (p_B^{\text{cms}})^2}$, where $E_{\text{beam}}^{\text{cms}}$ is the beam energy in the cms, and E_B^{cms} and p_B^{cms} are the cms energy and momentum, respectively, of the reconstructed B candidate. In the M_{bc} calculation, the photon momentum is replaced by $(E_{\text{beam}}^{\text{cms}} - E_{\phi K}^{\text{cms}})$ to improve resolution. The events that satisfy the requirements $M_{\text{bc}} > 5.2 \text{ GeV}/c^2$ and $|\Delta E| < 0.3 \text{ GeV}$ (defined as the fit region) are selected for further analysis. Using MC simulations, we find nearly 12%

(3%) of events have more than one B candidate for the $B^+ \rightarrow \phi K^+ \gamma$ ($B^0 \rightarrow \phi K^0 \gamma$) mode. In case of multiple candidates, we choose the best candidate based on a series of selection criteria, which depend on a χ^2 variable using the candidate's ϕ mass (and the K_S^0 mass in the neutral mode) as well as the highest E_γ^{cms} and the highest $\mathcal{L}(K/\pi)$ in the charged mode. For events with multiple candidates, this selection method chooses the correct B candidate for the $B^+ \rightarrow \phi K^+ \gamma$ ($B^0 \rightarrow \phi K^0 \gamma$) mode 57% (69%) of the time. We define the signal region as $5.27 \text{ GeV}/c^2 < M_{bc} < 5.29 \text{ GeV}/c^2$ and $-0.08 \text{ GeV} < \Delta E < 0.05 \text{ GeV}$. The ΔE signal region is asymmetric in order to include the tail in the lower region due to photon energy leakage in the ECL.

The dominant background comes from $e^+e^- \rightarrow q\bar{q}$ ($q = u, d, s, \text{ or } c$) continuum events. We use two event-shape variables to distinguish the spherically symmetric $B\bar{B}$ events from the jet-like continuum events. A Fisher discriminant [16] is formed from 16 modified Fox-Wolfram moments [17] and the scalar sum of the transverse momenta. The second variable is the cosine of the angle between the B flight direction and the beam axis ($\cos\theta_B$) in the cms frame. For each variable, we obtain the corresponding signal and background probability density functions (PDFs) from large MC samples. A likelihood ratio $\mathcal{R}_{s/b} = \mathcal{L}_s/(\mathcal{L}_s + \mathcal{L}_b)$ is formed, where \mathcal{L}_s (\mathcal{L}_b) denotes the product of Fisher discriminant and $\cos\theta_B$ PDFs for the signal (background). The selection criteria on $\mathcal{R}_{s/b}$ are determined by maximizing the figure of merit, $N_S/\sqrt{N_S + N_B}$, where N_S (N_B) is the expected number of signal (continuum) events in the signal region. We require $\mathcal{R}_{s/b} > 0.65$, which removes 91% of the continuum while retaining 76% of the signal.

In addition to the dominant continuum background, various $B\bar{B}$ background sources are also studied. In the $B^0 \rightarrow \phi K_S^0 \gamma$ mode, some backgrounds from $b \rightarrow c$ decays, such as $D^0\pi^0$, $D^0\eta$ and $D^-\rho^+$ peak in the M_{bc} distribution. We remove the dominant peaking backgrounds by applying a veto to ϕK_S^0 combinations consistent with the nominal D mass [13]. Some of the charmless backgrounds, where the B meson decays to $\phi K^*(892)$, $\phi K\pi^0$ and $\phi K\eta$ also peak in M_{bc} . In these charmless modes, one of the photons from a π^0 or η may not be detected in the calorimeter while the other is reconstructed as the signal high-energy photon. Therefore, these backgrounds shift towards lower ΔE . Another significant background is non-resonant $B \rightarrow K^+K^-K\gamma$, which peaks in the ΔE - M_{bc} signal region. The fraction of such events is estimated to be $(12.5 \pm 6.7)\%$ using the ϕ mass sideband, $1.05 \text{ GeV}/c^2 < M_{K^+K^-} < 1.3 \text{ GeV}/c^2$, in data.

The signal yield is obtained from an extended unbinned maximum-likelihood fit to the two-dimensional ΔE - M_{bc} distribution in the fit region. We model the shape for the signal component using the product of a Crystal Ball line shape [18] for ΔE and a single Gaussian for M_{bc} . The continuum background is modeled with a product of first order Chebyshev polynomial for ΔE and an ARGUS [19] function for M_{bc} . The $b \rightarrow c$ background is modeled with a product of second order Chebyshev polynomial for ΔE and an ARGUS plus Gaussian function for M_{bc} . The small charmless backgrounds (except the non-resonant component) are modeled with a functional form that is the product of two Gaussians for ΔE and with a single Gaussian for M_{bc} [20]. In the final fit the continuum parameters are allowed to vary while all other background parameters are fixed to the values from MC simulation. The shape of the peaking backgrounds are fixed to that of signal in M_{bc} and ΔE . In the $B^+ \rightarrow \phi K^+ \gamma$ mode, the non-resonant background yield is fixed to the value from the ϕ sideband and assuming isospin symmetry, the same non-resonant fraction is used in the neutral mode. The signal shapes are adjusted for small differences between MC and data using a high statistics $B^0 \rightarrow K^*(892)^0(\rightarrow K^+\pi^-)\gamma$ control sample. The invariant mass of

the K^* candidates are required to satisfy $0.820 \text{ GeV}/c^2 < M_{K^+\pi^-} < 0.970 \text{ GeV}/c^2$. The fit yields a signal of $136 \pm 17 B^+ \rightarrow \phi K^+\gamma$ and $35 \pm 8 B^0 \rightarrow \phi K_S^0\gamma$ candidates. The projections of the fit results onto ΔE and M_{bc} are shown in Fig. 2. The signal significance is defined as $\sqrt{-2 \ln(\mathcal{L}_0/\mathcal{L}_{\text{max}})}$, where \mathcal{L}_{max} is the maximum likelihood for the best fit and \mathcal{L}_0 is the corresponding value with the signal yield fixed to zero. The additive sources of systematic uncertainty described below are included in the significance by varying each by its error and taking the lowest significance. The signal in the charged mode has a significance of 9.6σ , whereas that for the neutral mode is 5.4σ .

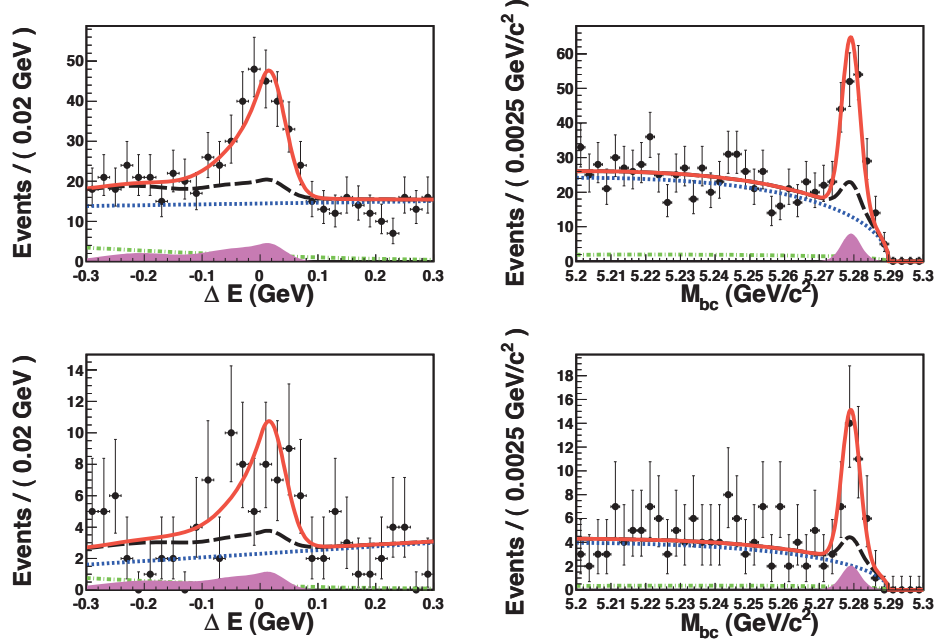


FIG. 2: The ΔE and M_{bc} projections for $B^+ \rightarrow \phi K^+\gamma$ (upper) and $B^0 \rightarrow \phi K_S^0\gamma$ (lower). The points with error bars represent the data. The different curves show the total fit function (solid red), total background function (long-dashed black), continuum component (dotted blue), the $b \rightarrow c$ component (dashed-dotted green) and the non-resonant component as well as other charmless backgrounds (filled magenta histogram).

We also examine the ϕK invariant mass distribution of the signal. To unfold the $M_{\phi K}$ distribution, we subtract all possible backgrounds and correct the ϕK invariant mass for the efficiency. The background-subtracted and efficiency-corrected $M_{\phi K}$ distributions are shown in Fig. 3. Nearly 72% of the signal events are concentrated in the low-mass region ($1.5 \text{ GeV}/c^2 < M_{\phi K} < 2.0 \text{ GeV}/c^2$). It is clear that the observed ϕK mass spectrum differs significantly from that expected in a three-body phase-space decay. The MC-determined reconstruction efficiencies (defined as the ratio of signal candidates passing all selection criteria to the total number of events generated) are corrected for this $M_{\phi K}$ dependence.

TABLE I: The signal yields, significances, weighted efficiencies and branching fractions for the $B^+ \rightarrow \phi K^+ \gamma$ and $B^0 \rightarrow \phi K^0 \gamma$ decay modes.

Decay mode	Yield	Significance (σ)	Efficiency (%)	Branching fraction (10^{-6})
$B^+ \rightarrow \phi K^+ \gamma$	136 ± 17	9.6	15.3 ± 0.1	$2.34 \pm 0.29 \pm 0.23$
$B^0 \rightarrow \phi K^0 \gamma$	35 ± 8	5.4	10.0 ± 0.1	$2.66 \pm 0.60 \pm 0.32$

From the signal yield (N_{sig}), we calculate the branching fraction (\mathcal{B}) as $N_{\text{sig}} / (\epsilon \times N_{B\bar{B}} \times \mathcal{B}_{\text{sec}})$, where ϵ is the weighted efficiency, $N_{B\bar{B}}$ is the number of $B\bar{B}$ pairs in the data sample, and \mathcal{B}_{sec} is the product of daughter branching fractions [13]. The results are summarized in Table I.

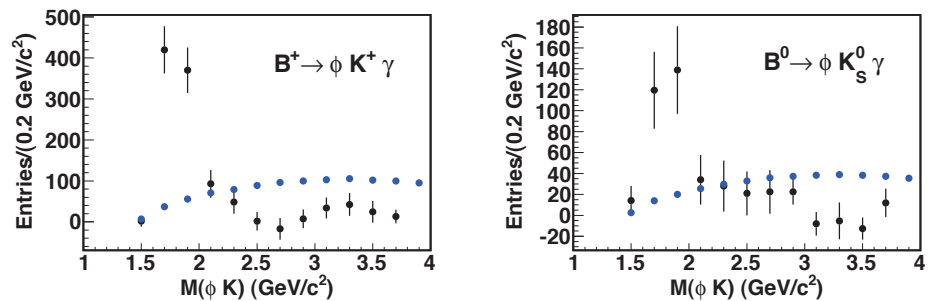


FIG. 3: The background-subtracted and efficiency-corrected ϕK mass distributions for $B^+ \rightarrow \phi K^+ \gamma$ (left) and $B^0 \rightarrow \phi K_S^0 \gamma$ (right). The points with error bars represent the data. The yield in each bin is obtained by the fitting procedure described in the text. The three-body phase-space model from the MC simulation is shown by the circles (blue) and normalized to the total data signal yield.

We fit the data with each fixed parameter varied by its $\pm 1 \sigma$ error, and then the quadratic sum of all differences from the nominal value is assigned as the systematic error on the signal yield. We checked for possible bias in the fitter by doing ensemble tests with MC pseudo-experiments. The statistical errors obtained from our measurements are within the expectations from the ensemble tests and a systematic error of 0.2% (2.7%) is assigned in the $B^+ \rightarrow \phi K^+ \gamma$ ($B^0 \rightarrow \phi K^0 \gamma$) mode. The largest contribution comes from the non-resonant yield (8.0%). The total systematic uncertainty assigned to the estimated yield is 8.2% (8.8%). We also assign a systematic error of 3.3% (4.6%) due to uncertainty on charged track efficiency, 1.4% due to particle identification, 2.4% due to photon detection efficiency, 1.4% due to uncertainty in the number of $B\bar{B}$ pairs in $B^+ \rightarrow \phi K^+ \gamma$ ($B^0 \rightarrow \phi K^0 \gamma$) mode. Furthermore, we assign a systematic error of 4.6% in the neutral mode due to K_S^0 reconstruction. The statistical uncertainty on the MC efficiency after reweighting is 0.9% (1.3%). The uncertainties due to daughter branching fractions account for a systematic contribution of 1.2%. We add each contribution above in quadrature to obtain the total systematic uncertainty of 9.9% (11.9%).

In summary, we report the first observation of radiative $B^0 \rightarrow \phi K^0 \gamma$ decays in Belle using a data sample of 772×10^6 $B\bar{B}$ pairs. The observed signal yield is 35 ± 8 with a significance of 5.4σ including systematic uncertainties. The measured branching fraction is $\mathcal{B}(B^0 \rightarrow \phi K^0 \gamma) = (2.66 \pm 0.60 \pm 0.32) \times 10^{-6}$. We also precisely measure $\mathcal{B}(B^+ \rightarrow \phi K^+ \gamma) = (2.34 \pm 0.29 \pm 0.23) \times 10^{-6}$ with a significance of 9.6σ . The signal events are mostly concentrated at low ϕK mass, which is similar to a two-body radiative decay. The neutral mode has enough statistics to measure time-dependent CP asymmetry in order to search for new physics from right-handed currents in radiative B decays.

We thank the KEKB group for the excellent operation of the accelerator, the KEK cryogenics group for the efficient operation of the solenoid, and the KEK computer group and the National Institute of Informatics for valuable computing and SINET3 network support. We acknowledge support from the Ministry of Education, Culture, Sports, Science, and Technology (MEXT) of Japan, the Japan Society for the Promotion of Science (JSPS), and the Tau-Lepton Physics Research Center of Nagoya University; the Australian Research Council and the Australian Department of Industry, Innovation, Science and Research; the National Natural Science Foundation of China under contract No. 10575109, 10775142, 10875115 and 10825524; the Department of Science and Technology of India; the BK21 and WCU program of the Ministry Education Science and Technology, the CHEP SRC program and Basic Research program (grant No. R01-2008-000-10477-0) of the Korea Science and Engineering Foundation, Korea Research Foundation (KRF-2008-313-C00177), and the Korea Institute of Science and Technology Information; the Polish Ministry of Science and Higher Education; the Ministry of Education and Science of the Russian Federation and the Russian Federal Agency for Atomic Energy; the Slovenian Research Agency; the Swiss National Science Foundation; the National Science Council and the Ministry of Education of Taiwan; and the U.S. Department of Energy. This work is supported by a Grant-in-Aid from MEXT for Science Research in a Priority Area ("New Development of Flavor Physics"), and from JSPS for Creative Scientific Research ("Evolution of Tau-lepton Physics").

* now at Okayama University, Okayama

- [1] E. Barberio *et al.*, Heavy Flavor Averaging Group (HFAG), arXiv:0808.1297.
- [2] M. Misiak *et al.*, Phys. Rev. Lett. **98**, 022002 (2007).
- [3] Throughout this paper, the inclusion of the charge-conjugate decay mode is implied unless otherwise stated.
- [4] D. Atwood, M. Gronau and A. Soni, Phys. Rev. Lett. **79**, 185 (1997).
- [5] D. Atwood, T. Gershon, M. Hazumi and A. Soni, Phys. Rev. D **71**, 076003 (2005).
- [6] V. D. Orlovsky, V. I. Shevchenko, Phys. Rev. D **77**, 093003 (2008).
- [7] D. Atwood, T. Gershon, M. Hazumi and A. Soni, hep-ph/0701021.
- [8] A. Drutskoy *et al.* (Belle Collaboration), Phys. Rev. Lett. **92**, 051801 (2004).
- [9] B. Aubert *et al.* (BaBar Collaboration), Phys. Rev. D **75**, 051102 (2007).
- [10] S. Kurokawa and E. Kikutani, Nucl. Instrum. Methods Phys. Res., Sect. A **499**, 1 (2003), and other papers included in this volume.
- [11] A. Abashian *et al.* (Belle Collaboration), Nucl. Instrum. Methods Phys. Res., Sect. A **479**, 117 (2002).
- [12] We use the EvtGen B meson decay generator, D. J. Lange, Nucl. Instrum. Methods Phys. Res., Sect. A **462**, 152 (2001). The detector response is simulated with GEANT, R. Brun *et*

- al.*, GEANT 3.21, CERN Report DD/EE/84-1 (1984).
- [13] C. Amsler, *et al.*, Physics Letters **B 667**, 1 (2008).
 - [14] K-F. Chen *et al.* (Belle Collaboration), Phys. Rev. D **72**, 012004 (2005).
 - [15] P. Koppenburg *et al.* (Belle Collaboration), Phys. Rev. Lett. **93**, 061803 (2004).
 - [16] R. A. Fisher, Annals of Eugenics **7**, 179 (1936).
 - [17] The Fox-Wolfram moments were introduced in G. C. Fox and S. Wolfram, Phys. Rev. Lett. **41**, 1581 (1978). The modified Fox-Wolfram moments used in this analysis are described in S. H. Lee *et al.* (Belle Collaboration), Phys. Rev. Lett. **91**, 261801 (2003).
 - [18] T. Skwarnicki, Ph.D. thesis, Institute for Nuclear Physics, Krakow, 1986; DESY Internal Report No. DESY F31-86-02, 1986. The function is widely used to describe asymmetric distributions caused by shower leakage in crystal calorimeters.
 - [19] H. Albrecht *et al.* (ARGUS Collaboration), Phys. Lett. B **241**, 278 (1990).
 - [20] $f(\Delta E, M_{bc}) = G_1(\Delta E - E_1) G(M_{bc} - M_0) + G_2(\Delta E - E_2) G(M_{bc} - M_0)$, where G_1 , G_2 and G_3 are Gaussian functions and E_1 , E_2 and M_0 are constants.

Bibliography

- [1] A. D. Sakharov, JETP Letters **5**, 24 (1967).
- [2] J. H. Christenson *et al.*, Phys. Rev. Lett. **13**, 138 (1964).
- [3] N. Cabibbo, Phys. Rev. Lett. **10**, 531 (1963).
- [4] M. Kobayashi and T. Maskawa, Prog. Theo. Phys. **49**, 652 (1973).
- [5] L. Wolfenstein, Phys. Rev. Lett. **51**, 1945 (1983).
- [6] I. I. Bigi and A. I. Sanda, *CP Violation*, Cambridge monographs on particle physics, page 207, nuclear physics and cosmology Vol. 9 (Cambridge University Press, Cambridge, 2000).
- [7] D. Atwood and G. Hiller, hep-ph/0307251.
- [8] BaBar Collaboration, B. Aubert *et al.*, Phys. Rev. D **79**, 072009 (2009).
- [9] Belle Collaboration, K. Abe *et al.*, Phys. Rev. D **71**, 072003 (2005).
- [10] E. Barberio *et al.*, Heavy Flavor Averaging Group (HFAG), arXiv:0808.1297.
- [11] M. Misiak *et al.*, Phys. Rev. Lett. **98**, 022002 (2007).
- [12] D. Atwood, M. Gronau, and A. Soni, Phys. Rev. Lett. **79**, 185 (1997).
- [13] D. Atwood, T. Gershon, M. Hazumi, and A. Soni, Phys. Rev. D **71**, 076003 (2005).
- [14] Throughout this paper, the inclusion of the charge-conjugate decay mode is implied unless otherwise stated.
- [15] V. D. Orlovsky and V. I. Shevchenko, Phys. Rev. D **77**, 093003 (2008).
- [16] D. Atwood, T. Gerson, M. Hazumi, and A. Soni, hep-ph/0701021.

- [17] Belle Collaboration, A. Drutskoy *et al.*, Phys. Rev. Lett. **92**, 051801 (2004).
- [18] BaBar Collaboration, B. Aubert *et al.*, Phys. Rev. D **75**, 051102 (2007).
- [19] S. Kurokawa and E. Kikutani, Nucl. Instrum. Methods Phys. Res., Sect. A **499**, 1 (2003).
- [20] C. Amsler, Physics Letters **B 667**, 1 (2008).
- [21] Belle Collaboration, A. Abashian *et al.*, Nucl. Instrum. Methods Phys. Res., Sect. A **479**, 117 (2002).
- [22] G. Alimonti *et al.*, Nucl. Instrum. Methods Phys. Res., Sect. A **453**, 71 (2000).
- [23] Y. Ushiroda, Nucl. Instrum. Methods Phys. Res., Sect. A **511**, 6 (2003).
- [24] H. Hirano *et al.*, Nucl. Instrum. Methods Phys. Res., Sect. A **455**, 294 (2000).
- [25] T. Iijima *et al.*, Nucl. Instrum. Methods Phys. Res., Sect. A **453**, 321 (2000).
- [26] H. Kichimi *et al.*, Nucl. Instrum. Methods Phys. Res., Sect. A **453**, 315 (2000).
- [27] H. Ikeda *et al.*, Nucl. Instrum. Methods Phys. Res., Sect. A **441**, 401 (2000).
- [28] Y. Makita *et al.*, Adv. Cryog. Eng. **37**, 401 (1992).
- [29] A. Abashian *et al.*, Nucl. Instrum. Methods Phys. Res., Sect. A **449**, 112 (2000).
- [30] R. Santonico and R. Cardarelli, Nucl. Instrum. Methods Phys. Res., Sect. A **187**, 377 (1981).
- [31] R. Akhmetshin *et al.*, Nucl. Instrum. Methods Phys. Res., Sect. A **455**, 324 (2000).
- [32] Tracking Group, Charged Particle Tracking in Belle, Belle Note **327** (Internal).
- [33] B. Casey, Hadron *B*, Belle Note **390** (Internal).
- [34] R. Itoh, BASF User's Manual, Belle Note **161** (Internal).
- [35] We use the EvtGen *B* meson decay generator, D. J. Lange, Nucl. Instrum. Methods Phys. Res., Sect. A **462**, 152 (2001). The detector response is simulated with GEANT, R. Brun *et al.*, GEANT 3.21, CERN Report DD/EE/84-1 (1984).

- [36] Information on the number of $B\bar{B}$ pairs collected by the Belle detector can be found in <http://belle.kek.jp/secured/nbb/nbb.html> (Internal).
- [37] F. Fang, Study of $K_S^0 \rightarrow \pi^+\pi^-$ Selection, Belle Note **320** (Internal).
- [38] ARGUS Collaboration, H. Albrecht *et al.*, Phys. Lett. B **241**, 278 (1990).
- [39] G. C. Fox and S. Wolfram, Phys. Rev. Lett. **41**, 1581 (1978).
- [40] The information regarding inclusive charmonium MC samples can be found in http://belle.kek.jp/secured/indirectcp/charmonium/mc/2004/incl_psi.html (Internal).
- [41] T. Affolder *et al.*, Phys. Rev. Lett. **88**, 071801 (2002).
- [42] H. Tajima *et al.*, Nucl. Instrum. Methods Phys. Res., Sect. A **533**, 370 (2004).
- [43] Belle Collaboration, K. Chen *et al.*, Phys. Rev. D **72**, 012004 (2005).
- [44] H. Kakuno *et al.*, Nucl. Instrum. Methods Phys. Res., Sect. A **533**, 516 (2004).
- [45] The errors on w_l and Δw_l can be found in <http://belle.kek.jp/secured/indirectcp/cpfit/> (Internal).
- [46] O. Long, M. Baak, R. N. Cahn, and D. Kirkby, Phys. Rev. D **68**, 034010 (2003).
- [47] Belle Collaboration, K. Chen *et al.*, Phys. Rev. Lett. **98**, 031802 (2007).
- [48] BaBar Collaboration, B. Aubert *et al.*, Phys. Rev. D **72**, 052004 (2005).
- [49] Belle Collaboration, P. Koppenburg *et al.*, Phys. Rev. Lett. **93**, 061803 (2004).
- [50] Belle Collaboration, S. H. Lee *et al.*, Phys. Rev. Lett. **91**, 261801 (2003).
- [51] R. O. Duda, P. E. Hart, and D. G. Stork, Pattern Classification, 2nd Edition (John Wiley and Sons, 2001).
- [52] C. Jacoby, PhD thesis, Lusanne, EPFL (2007).
- [53] T. Skwarnicki, Ph.D. thesis, Institute for Nuclear Physics, Krakow, 1986; DESY Internal Report No. DESY F31-86-02, 1986. The function is widely used to describe the asymmetric distributions caused by shower leakage in crystal calorimeters.
- [54] http://belle.kek.jp/group/pid_joint/kid/kid.html (Internal).

- [55] H. W. Kim, Study of High Energy Photon Detection Efficiency Using Radiative Bhabha, Belle Note **499** (Internal).
- [56] N. Joshi, K. Trabelsi, and T. Aziz, Study of D_s^*h decay, Belle Note **995** (Appendix C) (Internal).
- [57] Belle Collaboration, K. Abe *et al.*, Phys. Rev. D **68**, 012001 (2003).
- [58] Belle Collaboration, H. Sahoo *et al.*, Phys. Rev. D **77**, 091103 (2008).
- [59] Heavy Flavor Averaging Group, summer 2010 update. Check their webpage for updated results: <http://www.slac.stanford.edu/xorg/hfag/>.
- [60] S. Hashimoto *et al.*, Letter of intent for the KEK Super B Factory. KEK, 2004. KEK-REPORT-2004-4.
- [61] K. Hanagaki *et al.*, Nucl. Instrum. Methods Phys. Res., Sect. A **485**, 490 (2002).
- [62] A. Abashian *et al.*, Nucl. Instrum. Methods Phys. Res., Sect. A **491**, 69 (2002).